12-2016

Development of inverse methods for reconstruction of flight environments on ablators

A. Brandon Oliver
Purdue University

Graduate School Form
30 Updated 12/26/2015

PURDUE UNIVERSITY
GRADUATE SCHOOL
Thesis/Dissertation Acceptance

This is to certify that the thesis/dissertation prepared

By Anthony Brandon Oliver

Entitled

DEVELOPMENT OF INVERSE METHODS FOR RECONSTRUCTION OF FLIGHT ENVIRONMENTS ON ABLATORS

For the degree of Doctor of Philosophy

Is approved by the final examining committee:

Gregory A. Blaisdell
Co-chair

Anastasios S. Lyrintzis
Co-chair

Steven P. Schneider

Jonathan Poggie

To the best of my knowledge and as understood by the student in the Thesis/Dissertation Agreement, Publication Delay, and Certification Disclaimer (Graduate School Form 32), this thesis/dissertation adheres to the provisions of Purdue University's "Policy of Integrity in Research" and the use of copyright material.

Approved by Major Professor(s): Gregory A. Blaisdell

Approved by: Weinong Wayne Chen 10/12/2016

Head of the Departmental Graduate Program Date

DEVELOPMENT OF INVERSE METHODS FOR RECONSTRUCTION OF FLIGHT ENVIRONMENTS ON ABLATORS

A Dissertation

Submitted to the Faculty

of

Purdue University

by

A. Brandon Oliver

In Partial Fulfillment of the

Requirements for the Degree

of

Doctor of Philosophy

December 2016

Purdue University

West Lafayette, Indiana

For Kim.

And Joshua.

ACKNOWLEDGMENTS

I would like to gratefully acknowledge the assistance provided by many individuals in the development of this dissertation. First of all, I would like to thank my advisors Dr. Anastasios Lyrnitzis and Dr. Gregory Blaisdell for their guidance through my graduate studies. I would also like to thank Dr. Steven Schneider and Dr. Jonathan Poggie for serving on my thesis committee. I would like to thank Adam Amar and Randy Lillard for their friendship and technical mentoring over the years I have been working with NASA. Randy has been instrumental in guiding me to a career in aerothermodynamics at NASA and has encouraged me to stick with the Ph.D. through the years, and Adam's guidance and encouragement led me into the field of ablation modeling. I would also like to thank Milad Mahzari and Ben Blackwell for many valuable technical discussions on the subject matter, Todd White for his assistance in acquiring many of the materials necessary for the MEDLI reconstruction effort, Justin Droba for his help in reviewing parts of the manuscript in preparation for publication, Giovanni Salazar and Jay Hyatt for their help in testing and motivating improvements to *INHEAT*, and the rest of the Applied Aeroscience and CFD branch at the NASA Johnson Space Center for countless technical interactions over the years. I would also like to acknowledge the support provided by Adam Amar, Joe Olejniczak, Ben Kirk, and Jay LeBeau in affording me the time to dedicate to this effort. Megan MacDonald, Karen Minton, Alan Schwing, and my parents Tony and Belinda have provided endless encouragement in this pursuit for which I am grateful. And last but not least, I would like to thank my wife Kim for her love and support, and the many sacrifices she has endured during the development of this work.

TABLE OF CONTENTS

LIST OF TABLES

LIST OF FIGURES

Figure Page

Figure Page

SYMBOLS

a_h	h^{th}-order regularization scaling parameter
B	Trial-function mapping matrix
B'	Non-dimensional mass flux
B_n	Reaction model pre-exponential constant
C	Specific heat
C_h	Heat transfer coefficient (Stanton number)
C_h^*	Film coefficient ($\rho_e u_e C_h$)
C_m	Mass transfer coefficient
E_a	Activation energy
$\hat{g}_i$	Specific Gibbs function for species i
H	Mixture enthalpy
H_{rec}	Recovery enthalpy
H	Regularization matrix
ΔH_f^o	Latent heat of fusion
h_i^o	Heat of formation of species i
I	Identity matrix
j_k	Elemental diffusive flux
K_f	Forward reaction rate
K_p	Equilibrium constant
k	Thermal conductivity
L	Spatial domain length
$\mathcal{M}_k$	Atomic weight of element k
$\dot{m}''$	Mass flux
P	Pressure
P_i	Partial pressure of species i

$\dot{q}''$	Heat flux
$\mathbf{q}$	Boundary condition solution vector
$\tilde{\mathbf{q}}$	Trial-function vector
$\mathcal{R}$	Universal gas constant
$\vec{R}$	Net reaction rate
R_b	Effective nose radius
S	Objective function
$\dot{s}$	Surface recession rate
T	Temperature
$\mathbf{T}$	Modeled temperature vector
t	Time
t_{AST}	Accumulated simulated time
t_{FT}	Future time window length
t_{full}	Full time domain length
u	Streamwise velocity
v	Wall-normal velocity
$\mathbf{W}$	Regularization scaling matrix
$\mathbf{X}$	Pulse sensitivity coefficient matrix
x	One-dimensional spatial dimension
Y	Temperature measurement
$\mathbf{Y}$	Measurement vector

Greek symbols:

α_h	h^{th}-order regularization parameter
α	Thermal diffusivity, surface absorptivity
γ	Reaction probability
ϵ	Surface emissivity
$\tilde{\kappa}$	Permeability tensor
λ	Boundary condition interval time, blowing reduction parameter

μ	Gas viscosity
μ_{in}	Reaction stoichiometry of species i for reaction n
ν	Non-linear iterations
ν_{ki}	Element abundance coefficient for element k and species i
ρ	Density
σ	Stefan-Boltzman constant
ϕ	Step sensitivity coefficient
ϕ_n	Reaction model temperature exponent
$\mathbf{\Psi}$	Measurement covariance matrix
ω_k	Elemental composition

Subscripts:

$aero$	Net aerodynamic
$cond$	Conductive flux
e	Boundary layer edge
f	Fail recession
fl	Fluid component
g	Pyrolysis gas
n	Reaction index
rad	Shock-layer radiation
$rerad$	Thermal re-radiation
r	Reaction
s	Solid component
SSD	Sequential subdomain algorithm
w	Wall, ablation products
WD	Whole domain algorithm
x	Spatial term
0	Initial condition, Zeroth-order regularization
1	First-order regularization

∞	Far-field

Superscripts:

P	Reaction product
R	Reaction reactant
$*$	Dimensional value, linearizing value

Matrix indices:

f	Local solution boundary condition interval (max F)
i	Global measurement time (max I)
j	Global TC number (max J)
k	Unknowns in local solution (max $P = FN$)
m	Global boundary condition time interval (max M)
n	Distinct boundary conditions (max N)
r	Local measurement time (max R)

ABBREVIATIONS

ACE	Aerotherm Chemical Equilibrium code
AST	Accumulated Simulated Time (Equation 3.23)
BC	Boundary Condition
CFD	Computational Fluid Dynamics
EFT	Exploration Flight Test
FT	Future Time
IHCP	Inverse Heat Conduction Problem
IMU	Inertial Measurement Unit
MEADS	Mars Entry Atmospheric Data System
MEDLI	MSL Entry Descent and Landing Instrumentation
MISP	MEDLI Integrated Sensor Plugs
MPGFC	Multiphase Gibbs Function Continuation method
MSL	Mars Science Laboratory
NASA	National Aeronautics and Space Administration
PICA	Phenolic-Impregnated Carbon Ablator
RCG	Reaction Cured Glass
SEB	Surface Energy Balance (Equation 5.8)
SSD	Sequential Subdomain
TACOT	Theoretical Ablative Composite for Open Testing
TC	Thermocouple
TPS	Thermal Protection System
WD	Whole Domain

ABSTRACT

Oliver, A. Brandon PhD, Purdue University, December 2016. Development of Inverse Methods for Reconstruction of Flight Environments on Ablators. Major Professors: Gregory Blaisdell and Anastasios Lyrintzis.

Obtaining measurements of flight environments on ablative heatshields is both critical for spacecraft development and extremely challenging due to the harsh heating environment and surface recession. Thermocouples installed several millimeters below the surface are commonly used to measure the heatshield temperature response, but an ill-posed inverse heat conduction problem must be solved to reconstruct the surface heating environment from the embedded thermocouple measurements. The material properties of typical ablators make the reconstruction process more challenging when the measurements are deep, but measurements often must be located deep to allow for surface recession. Compounding the complexity of the surface reconstruction problem, surface recession can contribute substantially to the measurement response, but it is generally poorly predicted. Two methods are proposed in this dissertation to address these issues. To address reconstructions of deeply located measurements, a hybrid sequential/whole domain algorithm called the sequential subdomain algorithm is presented and demonstrated to show improved performance for applications similar to common low density carbon ablators used on the NASA Mars Science Laboratory and Orion capsules. To address uncertainty in surface recession prediction, a method for decoupling the surface recession evaluation from the inverse heat conduction problem is presented to allow more rapid and detailed analysis of different recession models. The decoupled method is shown in verification exercises to provide reconstructions of equivalent accuracy to the traditional coupled method but with reduced computational effort. These methods are applied to reconstruct the environments on the Mars Science Laboratory heatshield using several kinetically limited recession models.

1. INTRODUCTION

1.1 Motivation

Validation of aerothermal environments developed for atmospheric entry of a spacecraft can be incrementally performed in carefully scaled ground tests; however, only flight can capture all of the relevant physics and their interactions, making flight data extremely valuable to the design and development of a practical spacecraft. In a reentry environment database validation assessment, a number of terms in the energy balance equation are of interest to the aerothermodynamicist, but perhaps the most fundamental quantity of interest is the net heat flux from the environment to the surface of the heatshield. One of the primary purposes for predicting aerothermal environments is to size the thermal protection system (TPS) heatshield, and errors in the heat flux predictions can lead to heatshield failure or unnecessarily massive heatshields, which deprive the system of valuable payload mass. When flight data is obtained to validate predicted environments, measurement and processing errors can likewise contribute to the likelihood of heatshield failure or over-conservatism if they falsely 'validate' bad predictions or 'invalidate' good predictions. Care must be taken to reduce experiment errors to every extent possible.

Heat flux can be a difficult quantity to measure. It is not an intrinsic property, like temperature or pressure, and it can only be inferred from measurements of other properties. Commonly available sensors that 'directly' measure heat flux, such as Schmidt-Boelter and Gardon gages, actually use temperature measurements on either side of a material with known configuration and thermal properties, and the heat flux is inferred from the temperature difference. Other sensors, such as slug calorimeters, measure the time rate of change of temperature of a carefully-designed mass with known thermal properties to infer the influx of thermal energy. Still another family of sensors operate by measuring as near as possible the surface temperature, and as with the calorimeters, the heat flux is inferred

from the time rate of change of the surface temperature and heatshield thermal properties. This reliance on inference places considerable restrictions on the operational conditions of heat flux sensors. There are few sensors that can operate accurately at the conditions seen in atmospheric reentry.

A further complication in the effort to measure heat flux is the behavior of the heatshield on which the environments are being assessed. The windward side heatshields for NASA's Mars Science Laboratory (MSL) and Orion capsules, SpaceX's Dragon, and Boeing's Starliner capsules are all charring ablators, so it is expected that the heatshield will ablate, leaving anything embedded in the heatshield to protrude into the oncoming flow. A protruding sensor can amplify heating in the vicinity of the measurement and therefore measure heating higher than intended. Furthermore, the thermochemical state of the gas at the interface between a charring ablator and a high-temperature boundary layer is affected by a large number of physical processes. Most significantly for the issue of flight data interpretation, the gas mixture enthalpy at the surface and net chemical energy release via surface carbon oxidation can vary considerably with recession rate and chemical non-equilibrium effects. Since the mixture enthalpy is a key term in the film coefficient model frequently employed in scaling computational fluid dynamics (CFD) and engineering model environments to flight conditions for thermal analysis, uncertainties in the surface recession model can yield considerable uncertainty in heating estimates obtained from flight data.

The Apollo Program instrumented a few of the flight test vehicle ablative heatshields with sacrificial calorimeters [1], but this path was not followed for the Orion EFT-1 flight test, nor the MSL Entry Descent and Landing Instrumentation (MEDLI) program [2–5]. These vehicles used embedded thermocouples (TCs) inside their respective heatshields with the TCs set deep enough that they would survive through the relevant part of reentry. As with the other types of heat flux sensor, the surface heating must be inferred from the actual sensor measurements by solving a problem known as the inverse heat conduction problem (IHCP). The solution of the inverse problem, a process which is often referred to as *surface condition reconstruction*, is not always straightforward, and both the Orion

and MEDLI teams encountered a number of challenges in the reconstruction process. The MEDLI experience is considered further in this work.

1.2 MEDLI Flight Data

The phenolic-impregnated carbon ablator (PICA) heatshield of the MSL capsule was fitted [2, 3, 5] with seven instrumented plugs to gather temperature data during its August 2012 entry into the Martian atmosphere. These plugs contained four TCs embedded within the PICA plug at various depths, nominally $0.1\,\mathrm{in}$, $0.2\,\mathrm{in}$, $0.45\,\mathrm{in}$, and $0.7\,\mathrm{in}$ from the initial un-ablated surface. An unexpected result of the flight was that none of the near-surface TCs failed during the entry. This indicates that the surface recession was less than $0.1\,\mathrm{in}$, suggesting that the surface recession model used in design and post-flight analysis is notably over-conservative since it predicted that much more recession would occur. Given this observation and the potential benefit to payload capacity enabled by reducing TPS conservatism, it would be desirable to consider the recession assumptions more carefully to determine if the data supports the use of less conservative models on future missions.

The physical mechanisms of carbon ablation is an area of active research, and most models being proposed require tight coupling between CFD and ablation response. At the present time, this capability is not developed enough to be a feasible means of analysis on a problem of this scale and complexity. Instead, the MSL heatshield ablation analysis is performed using Apollo-era models of ablation. More detail is provided in Chapter 5; however, summarizing in order to motivate this work, these Apollo-era models introduce a number of assumptions to decouple the flowfield, ablation, and thermal response models. The decoupling relies on the film coefficient model given by

$$C_h^* = \frac{\dot{q}''_{aero}}{H_{rec} - H_w} \tag{1.1}$$

where $\dot{q}''_{aero}$ is the net heat flux from the boundary layer, C_h^* is the film coefficient, H_{rec} is the boundary layer recovery enthalpy, and H_w is the wall enthalpy. The film coefficient and recovery enthalpy are provided by separate CFD or boundary layer analysis, the wall

enthalpy is defined by the ablation response, and Equation 1.1 provides the resulting boundary layer heat flux contribution to the energy balance at the surface of the ablator. Using the same film coefficient as a non-dimensionalization parameter, it is possible to formulate a certain class of ablation problems in such a way that ablation rates and surface energy balance terms resulting from ablation can be pre-computed and passed to the thermal response code in table form. Solution of the surface energy balance then yields the boundary condition required for the thermal response analysis.

Mahzari et al. [6, 7] used inverse methods to reconstruct the flight aerothermal environment from the obtained data. Because the PICA surface recession model is formulated in the way described in the previous paragraph, they initially attempted to directly reconstruct the film coefficient. However, they encountered difficulties in this task because the recovery and wall enthalpies were too similar in magnitude (the reason this poses a challenge in the solution of the IHCP will be make clear in Section 4.3). When faced with this challenge, Mahzari et al. performed their reconstructions for the net heat flux into the surface assuming no recession occurred. They then assumed a surface recession profile (in this case, based on a uniformly-scaled profile predicted using CFD-derived estimates of heating) and evaluated a "heat rate" that contained the combined effects of environment heating (boundary layer diffusion, convection, and shock-layer radiation) and energy release due to the assumed ablation.

It is shown by Bose et al. [3] that predicted heating environments and the PICA thermal response model under-estimated the temperature near the stagnation point, with the predicted integrated heat load 33% below the reconstructed heat load determined by Mazhari et al. Cruden et al. [8] theorized that shock-layer radiation, which was not accounted for in the predicted environments, could be contributing to the discrepancy. Consequently, Cruden et al. performed some testing and analysis activities to generate shock-layer radiation estimates for the flight and show that nearly half of the discrepancy can be attributed to radiation by including their radiation estimates in the direct thermal analysis. They propose several different radiation profiles combined with different recession assumptions to show the temperature and load predictions improve, but it is unclear which profile is 'right'

and what other models used in the direct analysis could be contributing to the remaining discrepancy.

This highlights a key limitation of so-called *direct comparisons* to flight data. Especially on ablators, many models must be used in concert before a comparison may be made to available data. An error in a model applied early in the process could drive an otherwise accurate model applied later in the process to provide the wrong result. As a thought experiment, imagine the case of under-predicted environments that drive surface temperatures to a low enough value that an accurate temperature-dependent recession model does not predict enough recession. It would be easy to suggest that the recession model is inaccurate, especially if the environment prediction were difficult and costly (thereby implying a higher level of accuracy than may be truthfully warranted). If the recession model could have been applied with surface temperatures more representative of reality, it would be allowed to demonstrate its accuracy and the fault in the environments could more accurately be identified. A process is proposed in this work which permits this reverse application of the models, providing additional insight into the complicated problem of surface ablation.

1.3 Objectives

The objective of this work is to develop two aspects of the reconstruction process necessary to obtain useful heating measurements on ablative heatshields:

1. Develop an improved IHCP algorithm to permit accurate and largely automated reconstruction of the temperature field based on sub-surface thermocouples for materials exhibiting significant non-linearity in the material properties.

2. Develop a method to decouple surface thermochemistry assumptions from the IHCP reconstruction to permit a more focused evaluation of recession models in light of flight measurements.

This dissertation will describe the methods implemented to address the two objectives above. Numerical experiments are used to demonstrate each method. They are then used

together to reconstruct a subset of the MSL flight data to build on to the work of Mahzari et al. [6, 7].

Chapters 2-4 consider the first objective and discuss the inverse heat transfer algorithm implemented for this study neglecting surface recession. Chapter 5 introduces some background on the physical modeling of surface ablation and discusses the impact on environment reconstruction. Chapter 6 presents a proposed algorithm for addressing ablation in reconstructions and demonstrates its performance in numerical examples. The MEDLI data is addressed in Chapter 7 before a summary and conclusions are presented in Chapter 8.

2. RECONSTRUCTION BACKGROUND

2.1 Problem Definition

In an *inverse* heat conduction problem, the objective is to estimate the boundary conditions given temporally and spatially discrete solutions interior to the domain of a standard heat conduction problem. Stated mathematically [9]:

Given:

$$C\frac{\partial T}{\partial t} = \frac{\partial}{\partial x}\left(k\frac{\partial T}{\partial x}\right) \tag{2.1}$$

$$-k\frac{\partial T}{\partial x}\bigg|_{x=0} = q(t) \tag{2.2}$$

$$k\frac{\partial T}{\partial x}\bigg|_{x=L} = h(t)[T(L,t) - T_\infty] \tag{2.3}$$

$$T(x,0) = f(x) \tag{2.4}$$

$$T(x_i,t_j) = y_{ij} + \epsilon_{ij} \tag{2.5}$$

Find:

$$q(t) \text{ and } h(t) \text{ for } t > 0 \tag{2.6}$$

where coefficients C, k, L, and T_∞ are assumed known, as are the measurement locations x_j, times t_i, and values y_{ij} (to some limited accuracy because of unknown ϵ_{ij}), and the initial condition $f(x)$ is assumed known. Note that different boundary conditions than specified above can be used; these are included as common examples. By contrast, for a *direct* problem, $q(t)$ and $h(t)$ are known, and $T(x,t)$ is determined. Alternatively, Ozisik and Orlande [10] describe the problem as such:

> *In the direct problem the causes (heat flux) are given, the effect (temperature) is determined; whereas in the inverse problem the effect is given, the cause (or causes) is determined.*

The problem is an ill-posed problem, meaning that solutions are not guaranteed to be unique and that the solution does not always vary smoothly with small perturbations on the inputs. Frequently, optimization methods are used to obtain the desired boundary condition values. Given sufficiently accurate measurements and sufficient knowledge of the material thermal properties, very accurate estimates (sometimes termed reconstructions) of the boundary conditions can be obtained. However, the problem's ill-posedness means that the reconstruction will be very sensitive to measurement or modeling errors, and slight measurement noise could render an algorithm unstable. Any algorithm proposed to solve the IHCP must address the manner in which smoothing is applied to handle this tendency.

A class of problems similar to the IHCP are problems involving measured surface temperatures, such as those often employed in aerothermal ground testing. These problems have measurements on the domain boundary and therefore do not strictly fit the definition above. In many cases these problems can be well posed and solved by straightforward techniques such as the Cook-Felderman [11,12] method. However, limitations on measurement spatial and temporal resolution lead to an incompletely-defined or noisy boundary condition, which can introduce many problems similar to those introduced by the IHCP. Often, these problems can be solved with IHCP algorithms and so they frequently get lumped into the same class of problem.

Depending on the problem of interest, the unknown boundary conditions can take several forms. They can be temporally varying, spatially varying, or both. In most cases in the literature, IHCP algorithms tend to focus on problems for which the boundary conditions are temporally varying, sometimes defined as *function estimation* problems. If the boundary conditions are fixed in time and only vary in space (or are just simply constant) the problem is generally classified as a *parameter estimation* problem. The gulf between function and parameter estimation techniques is not very large, but IHCP algorithms are often built to explicitly address issues introduced by temporally varying boundary conditions.

A large number of approaches have been proposed to solve the IHCP. A fairly common and well characterized approach is to discretize the boundary condition (BC) in the time domain and compute BC values that minimize the least-squares difference of the measured and computed temperatures,

$$\underset{\mathbf{q}}{\text{Minimize}} \; (\mathbf{Y} - \mathbf{T}(\mathbf{q}))^T (\mathbf{Y} - \mathbf{T}(\mathbf{q})) \tag{2.7}$$

where $\mathbf{Y}$ is a vector of temperature measurements and $\mathbf{T}(\mathbf{q})$ is a vector of computed temperatures given the vector of boundary condition values $\mathbf{q}$. Frequently, the derivative of Equation 2.7 is taken with respect to the boundary condition values and set equal to zero to find the minimum value. This introduces the derivatives

$$\frac{\partial \mathbf{T}}{\partial \mathbf{q}^T} = \begin{bmatrix} \frac{\partial T_1}{\partial q_1} & \frac{\partial T_1}{\partial q_2} & \cdots & \frac{\partial T_1}{\partial q_{max}} \\ \frac{\partial T_2}{\partial q_1} & \frac{\partial T_2}{\partial q_2} & \cdots & \frac{\partial T_2}{\partial q_{max}} \\ \vdots & \vdots & \ddots & \vdots \\ \frac{\partial T_{max}}{\partial q_1} & \frac{\partial T_{max}}{\partial q_2} & \cdots & \frac{\partial T_{max}}{\partial q_{max}} \end{bmatrix} \tag{2.8}$$

which are known as sensitivity coefficients. As is shown in Section 2.3, the sensitivity coefficients drive IHCP algorithms, and depending on how they behave for certain problems, the ideal IHCP approach may change.

2.2 Common Algorithm Classifications

A review of the literature reveals many different algorithms and approaches that have been proposed for solving the IHCP. There are many different ways that these algorithms can be categorized to help identify which ones may work for a given problem. A brief overview of several methods of categorization is described.

The first, and perhaps easiest categorization metric describes the nature of the underlying direct problem. The spatial dimensions of the system (1-D, 2-D, or 3-D) can influence the choice of algorithm, particularly from a cost perspective. More selective for IHCP

algorithms, however, is whether the problem is linear or non-linear. If the sensitivity coefficients depend on any values in the the boundary condition vector, or if any of the boundary condition functions are affected by multiple elements of the boundary condition vector, the IHCP is non-linear. Temperature-dependent thermal properties introduce non-linearity, as do convective boundary conditions (through the dependence on surface temperature). Solutions to linear IHCPs are considerably faster and generally do not require iterations as non-linear IHCPs do.

There can be one or multiple boundary conditions to a given system at a given time that influence the sensor response (e.g. different heating levels to different parts of the domain). Given that many IHCP algorithms can handle spatially multiple dimensional systems with one or several unknown boundary conditions, the term *multi-dimensional inverse* can be ambiguous. In this work, the term *multi-component* is used to describe problems with multiple time-varying boundary conditions.

Another key categorization metric that strongly influences IHCP algorithms is the time in which a solution is required. Many applications require the solution of the IHCP in a control system feedback loop and need to obtain a solution as quickly as possible, whereas other applications are not as time-critical and can instead focus on accuracy in a detailed reconstruction. Algorithms for real-time applications, such as the future time filter coefficient method [13, 14], neural network algorithms [15], Kalman-filter methods [16], and the calibration integral method [17, 18], must attempt to infer the boundary conditions without use of extensive 'future time' data (temperature data at times *after* the time interval for which the boundary condition is being estimated) as this introduces a lag in time before the solution can be evaluated and used. This puts significant constraints on the physical system being analyzed as instrumentation locations become of critical importance [19]. Real-time applications often require assuming linear system response, although some methods such as the calibration integral method can handle non-linear problems by spending time upfront on detailed calibration efforts to achieve more accurate results in near-real-time. For post-test analysis applications, more leniency in instrumentation responsiveness and non-linear systems can be tolerated as all of the data is available to work with and time-to-solution is

generally not as important as solution accuracy. This work will focus on post-test analysis applications.

It was touched on earlier that the unknowns could be fixed or varying in time, with *function specification* problems handling time-varying unknowns and *parameter estimation* addressing time-invariant unknowns. An alternative interpretation of these terms in the literature [10] is that if the functional form of a boundary condition is known, then the problem is a parameter estimation problem for the function coefficients; otherwise it is a function estimation problem. This is a helpful interpretation, however as shown later, the introduction of spatial variation can confuse this interpretation, as time-varying coefficients of a functional form describing the boundary condition spatial distribution can be addressed. Furthermore, in the strictest sense, all IHCP algorithms make some form of assumption of the temporal functional form of the boundary condition, whether it is piecewise constant, piecewise linear, or some other functional (e.g.: polynomial or spline) with coefficients for these functionals forming the IHCP solutions.

One of the most quoted categorization metrics in the literature concerns how the temporally discretized values of the unknown boundary condition are evaluated. In *sequential* algorithms, they are estimated one at a time, in order, from the earliest time to the latest. By contrast, *whole domain* algorithms simultaneously estimate all of the values in one step. Each method has strengths and weaknesses. Sequential algorithms can be computationally more efficient for non-linear problems as less time is spent computing temperature estimates and sensitivity coefficients at times where the initial guess is poor. On the other hand, whole domain algorithms perform much better when measured temperatures take a substantial amount of time to respond to changes in the boundary condition. Neither is universally better than the other; the optimal choice comes down to the sensitivity coefficients of the specific problem. Some examples of sequential algorithms are the future time family of algorithms from Beck et al. [14] (which range from the Stoltz algorithm to the sequential function specification algorithm), and some examples of whole domain algorithms are the Gauss-Newton method [6] and conjugate-gradient methods (with and without the adjoint equation) [10,20]. Perhaps a bit tangent but still related to this metric, space marching tech-

niques [21, 22] swap a spatial dimension for time and compute temperatures sequentially in space from the sensor location to the boundary.

Because of the ill-posed nature of the IHCP and the inevitable presence of measurement noise (ϵ_{ij} in Equation 2.5), all practical IHCP algorithms require some form of smoothing, regularization, allowed bias, or other treatment of the solution sensitivity to data noise. One method that Beck's future time algorithms rely on is to integrate a BC interval over several measurements to average out noise. Probably the most common method of smoothing is *Tikhonov regularization* [9, 10, 14], where a penalty function is added to the minimization objective function (Equation 2.7) that penalizes when elements of the solution vector $\mathbf{q}$ vary in certain undesirable ways. For instance, adding the term $\alpha\mathbf{Hq}$ to Equation 2.7 (with α being the regularization parameter, and $\mathbf{H}$ being the regularization matrix) can bias the predicted temperatures when elements of $\mathbf{q}$ become unreasonably large or if they vary too rapidly, depending on the choice of $\mathbf{H}$. These are both examples of a *regularization operator*. An alternative approach is to *regularize the data*, as is done in the mollification method [22]. Alternatively, the *iterative regularization principle* of the conjugate-gradient-based methods does not bias the solution, however it uses an intricate iteration stopping criteria [10] to establish when the solution is close enough to the data that the gross character of the data is matched, but the noise is not.

Since sensitivity coefficients are often needed for IHCP algorithms, the manner in which these are computed can be a discriminator between different methods. Sometimes analytic formulations are available for simple linear problems, but more frequently they must be computed by *finite differences* or specially formulated *sensitivity equations*. The *adjoint* equation used in some conjugate-gradient based methods is an example of a sensitivity equation, but sensitivity equations can be defined even for regular non-linear heat conduction problems [23].

For completeness, it should be noted that the IHCP as it has been described so far (with the unknowns being boundary conditions that vary in time) is itself only a subset of related problems that have been investigated as inverse heat conduction problems. Many early efforts to define algorithms for the IHCP were directed at solving for an unknown

initial condition. Other problems that are often identified as IHCP problems attempt to estimate unknown source terms or varying geometry (a problem frequently addressed for solidification and material processing applications).

2.3 Sensitivity Coefficients

As stated in Section 2.1, IHCP algorithms are generally built on a least-squares optimization of the computed and measured temperatures,

$$\underset{\mathbf{q}}{\text{Minimize}}\, S = \sum_i \left(Y_i - T_i(\mathbf{q})\right)^2. \tag{2.9}$$

As this is a minimization problem, the objective function will be minimized at a stationary point. The derivative of Equation 2.9 with respect to q_m is

$$\frac{\partial S}{\partial q_m} = -\sum_i 2\left(Y_i - T_i(\mathbf{q})\right)\frac{\partial T_i}{\partial q_m}. \tag{2.10}$$

The terms $\frac{\partial T_i}{\partial q_m}$ are called the sensitivity coefficients and are often arranged into matrix form to produce the sensitivity coefficient matrix

$$\frac{\partial \mathbf{T}}{\partial \mathbf{q}^T} = \begin{bmatrix} \frac{\partial T_1}{\partial q_1} & \frac{\partial T_1}{\partial q_2} & \cdots & \frac{\partial T_1}{\partial q_{max}} \\ \frac{\partial T_2}{\partial q_1} & \frac{\partial T_2}{\partial q_2} & \cdots & \frac{\partial T_2}{\partial q_{max}} \\ \vdots & \vdots & \ddots & \vdots \\ \frac{\partial T_{max}}{\partial q_1} & \frac{\partial T_{max}}{\partial q_2} & \cdots & \frac{\partial T_{max}}{\partial q_{max}} \end{bmatrix}. \tag{2.11}$$

Physically, these represent the sensitivity of each temperature in the vector $\mathbf{T}$ to each model parameter or boundary condition value in the vector $\mathbf{q}$ that is sought in the IHCP solution. As most IHCP algorithms are fundamentally optimization algorithms, they often account for the physics of the problem through standard routines for evaluating $\mathbf{T}(\mathbf{q})$ and $\frac{\partial \mathbf{T}}{\partial \mathbf{q}^T}$. Evaluation of $\mathbf{T}$ is necessary for objective function evaluation, but the sensitivity coefficients are what really drive the updated estimates of the unknown parameters. As such, a close study

of the sensitivity coefficients can provide invaluable insight to how a particular IHCP algorithm will perform for a given problem.

With careful accounting of ordering (described in Section 3.2), temperatures at several distinct spatial locations x_j at multiple distinct times t_i can be included in the sensitivity coefficient matrix, with each time and location combination providing a row of the matrix. Likewise, the unknowns vector can contain elements that apply at multiple distinct locations (or represent different physical values) x_n at multiple distinct times t_m, with each combination providing a column of the matrix. There is no requirement that the time divisions of the temperatures match that of the times in the unknowns vector. Therefore, assuming J measurement locations sampled at I times for a problem described by N distinct boundary conditions each defined on M time intervals, the total size of the sensitivity coefficient matrix is $(JI) \times (NM)$.

Generalization of the sensitivity coefficient matrix can be difficult without putting constraints on it according to the problem of interest, but one general statement that can be made is that an IHCP is linear if: 1) the elements of the sensitivity coefficient matrix are independent of the unknowns vector, and 2) the boundary condition values at any given time are only dependent on a single element in the unknowns vector. In this instance, given a uniform initial temperature T_0, any temperature element in the **T** vector can be evaluated as

$$T(x_j, t_i) = T_0 + q_1 \frac{\partial T_{ji}}{\partial q_1} + q_2 \frac{\partial T_{ji}}{\partial q_2} + ... + q_{NM} \frac{\partial T_{ji}}{\partial q_{(NM)}} \tag{2.12}$$

for any given estimate of **q**. As in most cases, linear problems are much easier to solve, and many algorithms for non-linear IHCP problems linearize about a specific **q** inside an iteration loop to advance the solution.

However, to build intuition necessary for IHCP analysis, it is beneficial to simplify the problem. In the remainder of this section, we will limit ourselves to a transient, 1-D, semi-infinite solid heat conduction problem with temperatures evaluated at a single location at times consistent with the unknown values. The unknown values are a piecewise-constant

representation of a time-varying heat flux on the exposed boundary. In this case, the sensitivity coefficient matrix becomes a square lower-triangular matrix as the parabolic nature of the heat equation suggests that temperatures are unaffected at time t_i by a boundary condition applied at a later time t_m (i.e. $\frac{\partial T_i}{\partial q_m} = 0$ if $t_i < t_m$).

If we assume constant thermal properties and a constant heat flux boundary condition, the exact solution [24] of the posed problem is

$$T(x,t) = T_0 + \dot{q}_o'' \left[\frac{2\sqrt{\alpha t/\pi}}{k} \text{exp}\left(\frac{-x^2}{4\alpha t} \right) - \frac{x}{k} \text{erfc}\left(\frac{x}{2\sqrt{\alpha t}} \right) \right] \tag{2.13}$$

with α the thermal diffusivity ($\alpha = k/\rho C_p$, with k the thermal conductivity, ρ the density, and C_p the specific heat), T_0 the initial uniform temperature, and $\dot{q}_o''$ the applied heat flux. Because the heat equation with constant properties is a linear differential equation, the principle of superposition can be used to construct the solution corresponding to a transient piecewise-constant heat flux boundary condition. The building block solution used is the solution to a unit step heat flux

$$q(t) = \begin{cases} 0, & t < 0 \\ 1, & t > 0 \end{cases} \tag{2.14}$$

given by

$$\phi(x,t) = \begin{cases} 0, & t \leq 0 \\ \frac{2\sqrt{\alpha t/\pi}}{k} \text{exp}\left(\frac{-x^2}{4\alpha t} \right) - \frac{x}{k} \text{erfc}\left(\frac{x}{2\sqrt{\alpha t}} \right), & t > 0 \end{cases} \tag{2.15}$$

where $\phi(x,0)$ is defined to be 0 and T_0 is treated as a separate solution. Note that differentiation of Equation 2.13 with respect to q_o'' yields $\phi(x,t)$. Because of this, $\phi(x,t)$ is sometimes referred to as the *step* sensitivity coefficient.

The transient heat flux boundary condition function is approximated by a piecewise-constant function with interval boundaries defined by times $0, \lambda_1, \lambda_2, ..., \lambda_M$. The boundary flux values are denoted by $q_m = q(\lambda_{m-1/2})$, where $q(\lambda_{m-1/2})$ indicates the flux value

between times of λ_{m-1} and λ_m. With this definition, the contribution to the temperature of a flux value q_m at a specified time t_i is given by

$$\frac{\partial T_i}{\partial q_m} = \Delta\phi_{i-m} = \begin{cases} \phi(x, t_i - \lambda_{m-1}) - \phi(x, t_i - \lambda_m), & i \geq m \\ 0, & i < m \end{cases} \tag{2.16}$$

Equation 2.16 is known as the *pulse* sensitivity coefficient, though the word 'pulse' is often omitted in discussion. Given the linearity of the problem, the temperature at time t_i can be evaluated as

$$T(x, t_i) = T_0 + \sum_{m=1}^{M} q_m \frac{\partial T_i}{\partial q_m}. \tag{2.17}$$

This is consistent with the approximate numerical solution using the Duhamel method presented by Beck et al. [14]

Consider the case of a temperature $2\,\mathrm{mm}$ below the surface of a material with constant properties ($\rho = 280\,{}^{\mathrm{kg}}/_{\mathrm{m}^3}$, $k = 0.5\,{}^{\mathrm{W}}/_{\mathrm{mK}}$, and $C_p = 1860\,{}^{\mathrm{J}}/_{\mathrm{kgK}}$) shown in Figure 2.1. The heat flux profile for this case is shown in Figure 2.1(a) with the piecewise-constant flux intervals taken to be $1\,\mathrm{s}$ long. The sensitivity coefficients evaluated with Equation 2.16 are shown in Figure 2.1(b). The temperature evaluated by Equation 2.17 is shown in Figure 2.1(c) with the contributions from each flux interval index m indicated with different colored regions and $T_0 = 0\,\mathrm{K}$. Note that all three plots in Figure 2.1 are color-consistent, with each color representing an index m in Equation 2.17. For example, the first green curve represents $m = 3$: the heat flux interval active from $t = 2\,\mathrm{s}$ to $3\,\mathrm{s}$, the corresponding sensitivity coefficient which appears shortly after $t = 2\,\mathrm{s}$, and the corresponding temperature contribution, the lowest of the green bands.

Two observations can be made regarding the results of this example case. First of all, note that because this is a constant-property system, each of the sensitivity coefficient curves shown in Figure 2.1(b) is identical except for a time shift (this is not generally the case for non-linear problems). Indeed, as suggested by Equation 2.16, each coefficient is a function of the time difference between the current time t_i and the time that the respective

heat flux interval began λ_{m-1}. This time difference is termed the *development* time of the sensitivity coefficient. As is shown later, the development time required for the sensitivity coefficient to grow to substantial values is a strong function of the physical system and can have considerable impact on the performance of IHCP algorithms. For this case, the coefficients develop to a peak in approximately $2.5\,\mathrm{s}$, and decay slowly from there.

Secondly, Figure 2.1(c) breaks out the individual components of the summation in Equation 2.17 in this manner to show how long it can take for a particular flux interval to affect the overall temperature response relative to the contributions from all other flux intervals. The thickness of the bar at a particular time is the product of the developed sensitivity coefficient and the corresponding flux magnitude (in this regard, the width of the band is consistent with the *scaled* sensitivity coefficient). A careful study of this plot shows that for this case, it takes a short time for a particular intervals contribution to become visible, and the contribution can linger for a considerable time since the sensitivity coefficients do not decay rapidly, especially when the corresponding flux value is large.

The significance of both of these points can be seen in Figure 2.2. In this case, the same thermal properties are assumed, however temperatures at two different depths, $1\,\mathrm{mm}$ and $5\,\mathrm{mm}$, are considered. Both cases are exposed to the square-wave heating profile shown in Figure 2.2(a). Very different character is observed in the sensitivity coefficients ($1\,\mathrm{mm}$ in Figure 2.2(b) and $5\,\mathrm{mm}$ in Figure 2.2(c)), as the shallow location develops and decays rapidly, but the deep location develops much more slowly and does not significantly decay in the overall time domain. The impact this has on the temperature response is shown in Figure 2.2(d) for the shallow case and Figure 2.2(e) for the deep case. In the shallow case, the contribution from early components is seen to grow and decay rapidly, and when the step increase in heating arrives, the blue component (the first with elevated heating) leads the charge. In fact, the coefficients decay so rapidly that the total temperature response is shown to decrease at the end of the square wave without the flux going negative. By contrast, the deep case shows that it takes considerable time to even see the effect of the components with increased heating, and nearly all of the intervals are still contributing significantly to the total response at the end of the time domain.

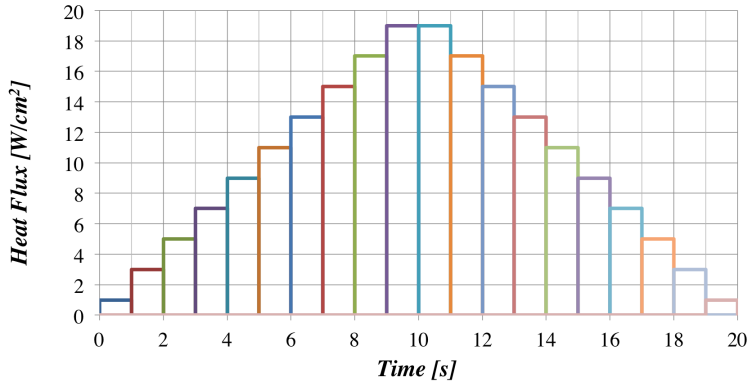

(a) Heat flux profile

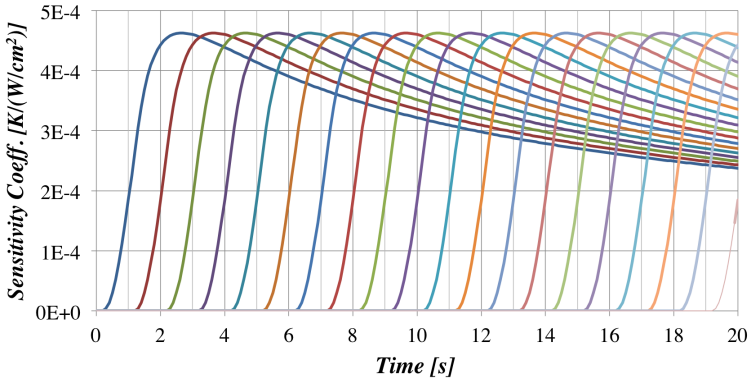

(b) Pulse sensitivity coefficients

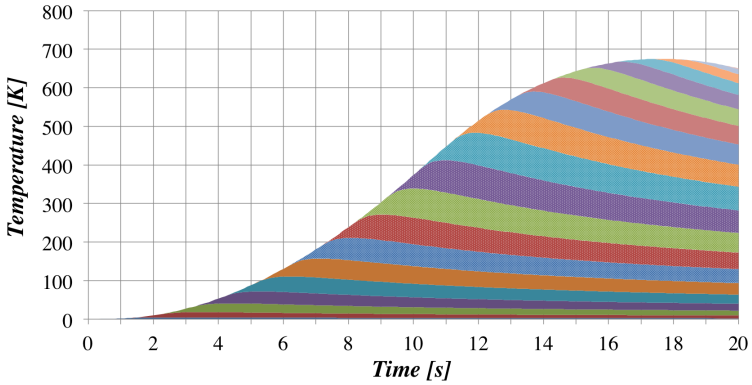

(c) Temperature Response

Figure 2.1. Duhamel solution for example case with $x = 2\,\mathrm{mm}$, $\rho = 280\,{}^{\mathrm{kg}}/_{\mathrm{m}^3}$, $k = 0.5\,{}^{\mathrm{W}}/_{\mathrm{mK}}$, and $C_p = 1860\,{}^{\mathrm{J}}/_{\mathrm{kgK}}$.

The practical implication of the differences between to two responses in Figure 2.2 to an IHCP is now considered. For a measurement at a given time (say $t = 8\,\mathrm{s}$), how strongly is the measurement (the total temperature response) affected by each of the unknown heat flux components being sought? In the case of the shallow measurement, nearly half of the temperature response at $t = 8\,\mathrm{s}$ is provided by the two intervals that immediately precede the measurement. For the deep measurement at $t = 8\,\mathrm{s}$, the two preceding intervals have only just become visible. An inverse algorithm trying to piece together the magnitude of these two heat flux components will have plenty of 'information' on the intervals of interest by looking at measurements near $8\,\mathrm{s}$ in the shallow case. However, for the deep case, it will need to use lots of measurements after $8\,\mathrm{s}$ to gather sufficient information, and it will have to try and untangle that information from the information on neighboring flux intervals. Furthermore, the sharp reduction in magnitude of the sensitivity coefficients as the measurement moves deeper means that any measurement noise (presumably at some fixed level of units K) will wipe out considerably more usable information in the deeper case than in the shallow case.

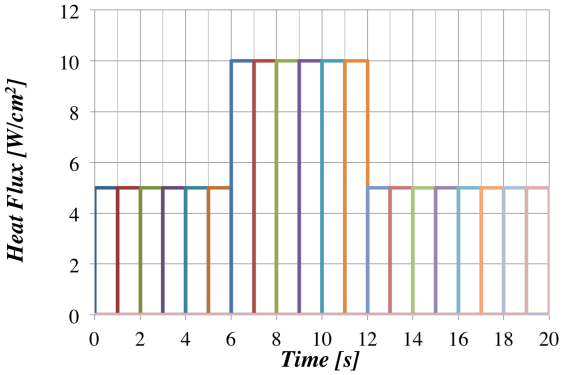

(a) Heat flux profile

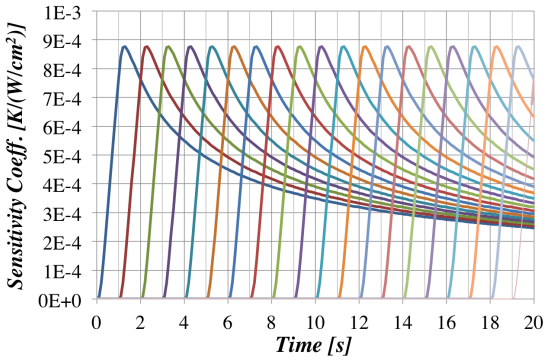

(b) Pulse sensitivity coefficients, shallow

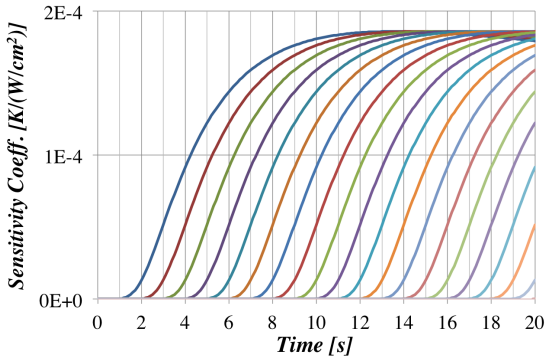

(c) Pulse sensitivity coefficients, deep

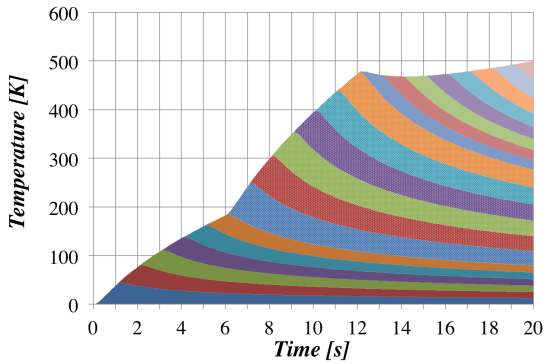

(d) Temperature Response, shallow

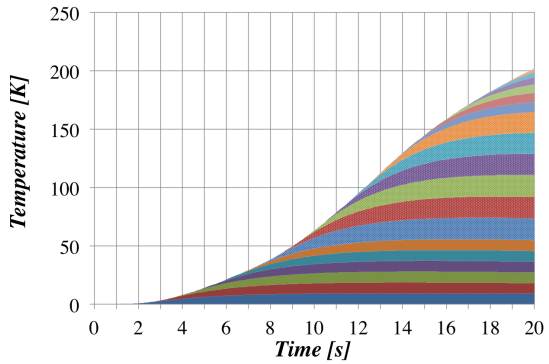

(e) Temperature Response, deep

Figure 2.2. Duhamel solution for example case with two TC depths ($x = 1\,\mathrm{mm}$ and $x = 5\,\mathrm{mm}$) exposed to the same heating profile to illustrate how different sensitivity coefficients will affect the thermal response.

2.4 Motivation for New Algorithm

As was indicated in Section 2.2, one common and significant discriminator between IHCP algorithms is the *sequential* vs. *whole-domain* approach to determining the unknown boundary condition values. The choice of approach primarily influences how the sensitivity coefficients are calculated and used. A whole domain algorithm computes the full sensitivity coefficient matrix and solves a system of equations similar to Equation 2.17 (one equation for each measurement) simultaneously for every unknown value. A sequential algorithm, however, will only compute the step sensitivity coefficient for the component being evaluated (only for a short development time known as the *future time window*) and solve for the temperatures (using Equation 2.17) that appear in this future time window.

From a cost perspective, sequential methods are considerably more desirable than whole domain methods. Recall that the sensitivity coefficient matrix will have dimensions of number of measurements by number of unknowns. If the problem is linear and exact solutions are available (like the example in the previous section), this may not be much of a problem. However, for many realistic problems, a finite-difference approximation to the sensitivity coefficients is used in the inverse algorithm which can become costly if the numerical model for the system is expensive. As an example (described in more depth in Seciton 3.4), a sequential reconstruction of the MSL dataset presented by Mahzari et al. [6] would require the ablator material response model integrating $1.95 \cdot 10^3\,\mathrm{s}$ of thermal response to complete the reconstruction. By contrast, the whole domain reconstruction presented by Mahzari et al. required the integration of $1.08 \cdot 10^6\,\mathrm{s}$ of thermal response, nearly three orders of magnitude more effort! With this sort of difference in cost, there must be a good reason to use a whole domain algorithm, and indeed there is a very good reason.

Conventional sequential algorithms make two key assumptions: 1) that the boundary condition values through the future time window follow an assumed pattern that is reduced to one unknown (typically the value is constant through the whole window), and 2) that there is a discernible amount of 'information' in the measurement due to the unknown BC (relative to measurement error) for the measurements in the future time window. With these

assumptions, the effect of the unknown BC can be identified and the value calculated. If the future time window is too short, assumption 2 breaks down and the algorithm becomes unstable and driven by measurement error. As such, the future time window must be chosen for each problem to ensure assumption 2 is valid. Recalling the example in Figure 2.2, if the sensitivity coefficients develop rapidly, the BCs will contribute significantly to measurements near the BC interval, but if they develop slowly, that may not be the case. If the coefficients develop too slowly, a long future time window is required and the first assumption begins to break down, yielding poor results that appear overly 'smoothed.' In this case, a whole domain algorithm performs much better since measurements can contribute their information to all of the BC values as they are all solved simultaneously.

The conditions used in the examples of Figures 2.1 and 2.2 are not completely arbitrary; they are approximations of the TACOT [25] material model, which is representative of a low density charring ablator similar to what is used on MSL and Orion. As such, the range of development times for sensitivity coefficients illustrated in these figures is representative of that which would be seen in flight. An effect of surface recession is that the measurement depth gets closer to the surface as the surface ablates, so to ensure survival, thermocouples (TCs) are typically embedded at a depth greater than $2\,\mathrm{mm}$. This required depth forces sequential algorithms to use a long future time window as sensitivity coefficients can develop slowly. The computational cost of solving the additional equations necessary in ablation simulations is non-negligible and properties are highly non-linear, so the reduced simulation time of a sequential algorithm is strongly desirable. Additionally, ablation simulations are only modestly robust (it is very easy to go out of bounds in one of many required tables of input properties), so wild excursions of boundary conditions that could be seen in a non-linear iteration of a whole domain algorithm can lead a reconstruction to fail. Finally, finite difference approximations to the sensitivity coefficients can become poor at times far from the perturbation due to accumulation of numerical error if highly stringent convergence tolerances are not imposed on the ablation simulation (generally well in excess of what is required for conventional ablation analysis). An algorithm that is predominantly sequential but draws from the whole domain algorithm to permit longer sensitivity coefficient devel-

opment time would be quite useful for reconstruction of heating environments on ablative materials.

Another situation that can arise in a practical flight experiment is a large, localized change in relevant timescales of the heating profile. An example of this would be a rapid spike in heating caused by a steering jet firing in an otherwise slowly changing heating profile. In this case, the sensitivity coefficients of a near-surface TC could develop rapidly enough compared to the rate change of the overall heating that a sequential algorithm would be quite satisfactory, but so slowly compared to the change in heating during the jet firing that a whole domain method would be required to characterize the jet heating augmentation. An algorithm that could seamlessly switch from a predominantly sequential algorithm to a predominantly whole domain algorithm in a local region would have considerable practical application.

Finally, both flight and wind tunnel applications could benefit from an inverse capability that will permit the reconstruction of heating environments on models too small, made of materials too conductive, or tested in facilities with run times long enough that lateral conduction errors prevent the use of conventional 1-D reconstruction methods like Cook-Felderman. In this case, the computational cost of a multi-dimensional simulation could make a pure whole domain reconstruction infeasible. However, if the traits of a sequential algorithm could be obtained with an algorithm that allows sensitivity coefficients to develop *enough* to account for lateral conduction, there is potential that existing test facilities could be used to obtain useful measurements on a wider range of model geometries than currently possible.

In the present work, a hybrid sequential/whole domain algorithm, named the *Sequential Subdomain* (SSD) algorithm, is proposed that permits the solution of multiple unknown boundary condition intervals on an otherwise sequential future time window. It is defined in such a way that allows the analyst to tailor the algorithm to the sensitivity coefficients of the physical system. Depending on the values of a few parameters, Beck's Future Time algorithm or a whole-domain Gauss-Newton method can be obtained. In the hybrid mode, it allows sequential specification of the unknown boundary condition values, allowing re-

duced computational effort than the pure whole domain approach without having to accept the excessive smoothing introduced for slowly responding sensors in the sequential function specification algorithm.

3. RECONSTRUCTION ALGORITHM FORMULATION

3.1 Derivation

The algorithm implemented here is based on the trial function specification algorithm of Beck et al. [14]. It is a least-squares optimization of the modeled temperature to the measured temperatures with a Tikhonov regularization term for stability. The function to be minimized is given by

$$S = (\mathbf{Y} - \mathbf{T})^T \boldsymbol{\Psi}^{-1} (\mathbf{Y} - \mathbf{T}) + \alpha_h \left[\mathbf{H}_h (\mathbf{q} - \tilde{\mathbf{q}})\right]^T \mathbf{W} \left[\mathbf{H}_h (\mathbf{q} - \tilde{\mathbf{q}})\right] \tag{3.1}$$

where $\mathbf{Y}$ is the vector of temperature measurements (the reconstruction target), $\mathbf{T}$ is the temperature resulting from the numerical model of the system, $\boldsymbol{\Psi}^{-1}$ is a covariance matrix describing $\mathbf{Y}$, α_h is the h^{th}-order regularization parameter, $\mathbf{H}_h$ the h^{th}-order regularization matrix, $\mathbf{W}$ is the regularization weighting matrix, and $\mathbf{q}$ is the vector of boundary condition values. The term $\tilde{\mathbf{q}}$ is a vector of expected boundary condition values that can be used to fine-tune regularization, if desired. It is assumed to have the form $\tilde{\mathbf{q}} = \mathbf{B}\mathbf{q} + \tilde{\mathbf{q}}^f$ with $\mathbf{B}$ and $\tilde{\mathbf{q}}^f$ specified by the user. Note that an arbitrary number of regularization terms of this form can be applied as desired, but only one is shown here to simplify the presentation. The specific structure of all of these matrices is described in Section 3.2. Depending on how they are defined, sequential function specification or whole domain solutions (or combinations in between those limits) can be obtained.

We seek to minimize the objective function S, so we take the derivative of Equation 3.1 with respect to each of the boundary condition values

$$\frac{\partial S}{\partial \mathbf{q}} = -2\mathbf{X}^T \boldsymbol{\Psi}^{-1} (\mathbf{Y} - \mathbf{T}) + 2\alpha_h \left[\mathbf{H}_h (\mathbf{I} - \mathbf{B})\right]^T \mathbf{W}\mathbf{H}_h (\mathbf{q} - \tilde{\mathbf{q}}) \tag{3.2}$$

where

$$\mathbf{X} = \left.\frac{\partial \mathbf{T}}{\partial \mathbf{q}^T}\right|_{\mathbf{q}^*} = \begin{bmatrix} \frac{\partial T_1}{\partial q_1} & \frac{\partial T_1}{\partial q_2} & \cdots & \frac{\partial T_1}{\partial q_L} \\ \frac{\partial T_2}{\partial q_1} & \frac{\partial T_2}{\partial q_2} & \cdots & \frac{\partial T_2}{\partial q_L} \\ \vdots & \vdots & \ddots & \vdots \\ \frac{\partial T_K}{\partial q_1} & \frac{\partial T_K}{\partial q_2} & \cdots & \frac{\partial T_K}{\partial q_L} \end{bmatrix}_{\mathbf{q}^*} \tag{3.3}$$

is the sensitivity coefficient matrix evaluated around the current solution vector $\mathbf{q}^*$ where K indexes the total number of measurements and L indexes the total number of unknowns[1]. Computation of the objective function requires temperatures corresponding to the new flux vector, so a Taylor series expansion about the current solution yields

$$\mathbf{T} = \mathbf{T}^* + \mathbf{X}\Delta\mathbf{q} \tag{3.4}$$

where $\mathbf{T}^*$ is the temperature evaluated with the solution vector $\mathbf{q}^*$, and $\Delta\mathbf{q} = (\mathbf{q} - \mathbf{q}^*)$ is the update to the estimated solution vector. Setting the objective function derivative (Equation 3.2) to zero, substituting in the Taylor series expansion (Equation 3.4), and rearranging yields the system

$$\mathbf{L}\Delta\mathbf{q} = \mathbf{R} \tag{3.5}$$

where

$$\mathbf{L} = \mathbf{X}^T\boldsymbol{\Psi}^{-1}\mathbf{X} + \alpha_h \left[\mathbf{H}_h \left(\mathbf{I} - \mathbf{B}\right)\right]^T \mathbf{W} \left[\mathbf{H}_h \left(\mathbf{I} - \mathbf{B}\right)\right] \tag{3.6}$$

$$\mathbf{R} = \mathbf{X}^T\boldsymbol{\Psi}^{-1} \left(\mathbf{Y} - \mathbf{T}^*\right) - \alpha_h \left[\mathbf{H}_h \left(\mathbf{I} - \mathbf{B}\right)\right]^T \mathbf{W}\mathbf{H}_h \left(\left(\mathbf{I} - \mathbf{B}\right)\mathbf{q}^* - \tilde{\mathbf{q}^f}\right) \tag{3.7}$$

The term containing $\mathbf{q}^*$ does not appear in the derivation of Beck et al. [14] as their derivation makes the assumption that $\mathbf{q}^* = \mathbf{0}$ when evaluating $\mathbf{T}^*$ (implicitly assuming that iteration is not required). For non-linear problems, this term is necessary for the regularization

[1]Recall that temperatures are measured at locations x_j and times t_i so $K = JI$. Unknowns are defined at x_n distinct locations and at times t_m, so $L = NM$. However, as described in the next section, K and L can be smaller if only a subset of the unknowns are evaluated.

to appropriately smooth the solution $\mathbf{q}$ if $\mathbf{T}^*$ and $\mathbf{X}$ are evaluated using non-zero values of $\mathbf{q}^*$. If this term is omitted, the regularization smooths the update $\Delta\mathbf{q}$. Introducing the Taylor series approximation (Equation 3.4) linearizes the problem about $\mathbf{q}^*$, so iteration will likely be required to converge the solution $\mathbf{q}$ if the problem is non-linear.

3.2 Matrix Definition

It is common in the literature to assume that boundary condition values are estimated on a uniform time scale that is consistent with measurement times. This is notationally convenient; however, it can cause difficulties in practical applications. As is shown in Section 3.4, the cost of a reconstruction scales with the number of unknowns estimated, so it may be desirable to reconstruct at a lower frequency than data is available. Additionally, reconstructing boundary conditions on a different time scale could also be motivated by missing or otherwise compromised data, changes in data rate near an expected transient event, or a mismatch in measurement times of data supplied by multiple sensors. In an attempt to make this as general and flexible as possible, the algorithm has been defined to allow measurement and boundary condition estimation times to be completely flexible, and it is up to the user to specify a reasonable problem for which a solution exists. This choice will make the notation more complex.

The algorithm presented in this work permits sequential evaluation of the terms in $\mathbf{q}$. Each of the sequential evaluation steps is referred to as a *local solution*. A local solution will solve the non-linear system of Section 3.1 for a subset of the $\mathbf{q}$ vector on an appropriate subdomain. Introduction of the local solution and keeping the global and local index systems distinct further complicates the notation. Furthermore, an arbitrary number of sensors can be providing data and multiple distinct unknown boundary conditions could be estimated at a given time, further complicating the notation.

Given the complexity of this system, the notation is explained in detail. Figure 3.1 presents an illustration of how time is indexed in this definition using two timelines. The top timeline describes the notation for the overall problem, and the red line below shows

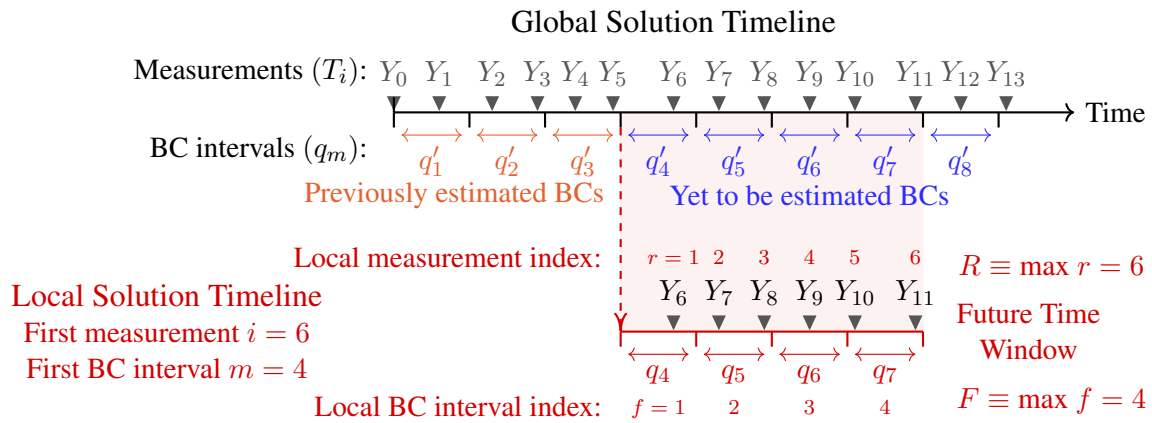

Figure 3.1. Summary of nomenclature describing the time-scales of the reconstruction. The top timeline represents the global problem, and the bottom line represents the timeline for a local solution starting with the global BC interval $m = 4$.

the nomenclature for a specific local solution. The top row of each timeline denotes the measurement times for which target data is provided to the algorithm, with the letter i identifying the global index and r identifying the local index. Note that the spacing between these times are not uniform, but the times in the local solution are a subset of the global measurement times. The bottom row of each line denotes the time *intervals* for which boundary condition (BC) values are to be estimated, with the letter m indexing the global set and f indexing the local set. There is no requirement that these intervals be regularly spaced, and the BCs defined in each interval are assumed to be constant through the interval (the estimated function is assumed to be piecewise-constant). The max measurement time in the global problem is denoted by I, the max measurement time index in a particular local solution is R, the max BC interval index in the global problem is M, and the max BC interval index in a particular local solution is F. Note that for different local solutions in the same global problem, R and F may change based on the length of the future time window (the length of the local solution) and the defined global measurement and BC intervals.

Beyond the times described in Figure 3.1, there may be input from multiple sensors at each measurement time (for instance, if there are several TCs in the system), and there may be multiple distinct BC values estimated on each interval. Multiple measurement locations

are indexed using the letter j (max J) in the matrix definitions, and multiple BCs on each interval are indexed with the letter n (max N). In the present derivation, it is possible to have only a subset of sensors providing data for a specific measurement time by using a special blanking matrix (whereby contributions from 'missing' data are ignored). However, at this time, it is not possible to define separate intervals for each of the distinct BCs; all distinct BCs are estimated on every BC interval. Given this, there will always be $(N \times F)$ BC values estimated in each local solution, and this dimension is given a special symbol P. A summary of the index system described is presented in Table 3.1.

Table 3.1. Summary of indices used in matrix definitions

Global Solution Indices:	
j	TC number (max J)
i	Global measurement times (max I)
m	Global boundary condition time intervals (max M)
n	Distinct boundary conditions (max N)

Local Solution Indices:	
r	Measurement times in current local solution (max R)
f	Boundary condition time intervals in current local solution (max F)
k	Boundary condition values in current local solution (max $P = FN$)

All of the matrices presented herein are built for a specific local solution with i referring to the first global measurement time in a local solution and m the first global BC interval in the local solution domain.

The vectors that represent temperature (either the target data **Y** or modeled temperatures **T**) have the following block form

$$\mathbf{T} = \overbrace{\begin{bmatrix} T(i) \\ T(i+1) \\ \vdots \\ T(i+R-1) \end{bmatrix}}^{1} \Bigg\updownarrow \begin{array}{l} R \text{ blocks} \\ (JR \text{ elements}) \end{array} \tag{3.8}$$

where each block is of the form

$$T(r) = \overbrace{\begin{bmatrix} T_1(r) \\ T_2(r) \\ \vdots \\ T_J(r) \end{bmatrix}}^{1} \Bigg\updownarrow J \quad . \tag{3.9}$$

If any data is unavailable from either **Y** (due to missing measurement) or **T** (possible due to surface recession in ablation problems), those elements in **Y** and the corresponding elements in the **T** matrix are both set to zero to prevent that time point from contributing to the objective function (Equation 3.1).

The vectors that represent the estimated boundary condition values have a similar block form

$$\mathbf{q} = \overbrace{\begin{bmatrix} q(m) \\ q(m+1) \\ \vdots \\ q(m+F-1) \end{bmatrix}}^{1} \Bigg\updownarrow \begin{array}{l} F \text{ blocks} \\ (P = FN \text{ elements}) \end{array} \tag{3.10}$$

where each block is given by

$$q(f) = \overbrace{\begin{bmatrix} q_1(f) \\ q_2(f) \\ \vdots \\ q_N(f) \end{bmatrix}}^{1} \Bigg\updownarrow N \quad . \tag{3.11}$$

The sensitivity coefficient matrix has the form

$$\mathbf{X} = \overbrace{\begin{bmatrix} \tilde{a}(i) \\ \tilde{a}(i+1) \\ \vdots \\ \tilde{a}(i+R-1) \end{bmatrix}}^{1 \text{ super block } (F \text{ blocks, } P = FN \text{ columns})} \Bigg\updownarrow \begin{array}{l} R \text{ blocks} \\ (JR \text{ rows}) \end{array} \tag{3.12}$$

where

$$\tilde{a}(r) = \overbrace{\begin{bmatrix} a_{11}(r) & a_{12}(r) & \dots & a_{1F}(r) \\ a_{21}(r) & a_{22}(r) & \dots & a_{2F}(r) \\ \vdots & \vdots & \ddots & \vdots \\ a_{J1}(r) & a_{J2}(r) & \dots & a_{JF}(r) \end{bmatrix}}^{F \text{ blocks } (P = FN \text{ columns})} \Big\updownarrow J \tag{3.13}$$

and each term in $\tilde{a}(r)$ is of the form

$$a_{jf}(r) = \overbrace{\begin{bmatrix} a(r,f,j,1) & a(r,f,j,2) & \dots & a(r,f,j,N) \end{bmatrix}}^{N} \Big\updownarrow 1 \tag{3.14}$$

and

$$a(r,f,j,n) = \frac{\partial T(\mathbf{x}_j, t_r)}{\partial q_n(t_f)} \tag{3.15}$$

Note that in Equation 3.15, t_f refers to the BC time interval f and not a specific time.

The regularization matrix $\mathbf{H}_h$ governs how the algorithm attempts to provide stability by smoothing the solution. Tikhonov regularization is a penalty function, where the penalized condition is defined by $\mathbf{H}_h$. One common regularization method is to penalize based on the absolute magnitude of the solution, $\alpha_0 \sum_{i=1}^{F} q_i^2$, which is often referred to as 0^{th}-order regularization. Alternatively, 1^{st}-order regularization penalizes based on the difference of one solution value compared to the next, $\alpha_1 \sum_{i=1}^{F-1} (q_{i+1} - q_i)^2$. For 0^{th}-order regularization, the definition of $\mathbf{H}_0$ is straightforward. However, for higher-order regularization where multiple solution terms are included, the structure of $\mathbf{H}_h$ will be different if the smoothing is applied to multiple BCs in space, multiple BC values in time, or both.

In a departure from the method described in Beck et al. [14], temporal and spatial regularization are handled in separate regularization terms, each with their own $\mathbf{H}$ (with dimensions $P \times P$) and α. Spatial regularization is highly problem dependent and requires

the user to input a matrix $\mathbf{h}_x$ of dimensions $N \times N$ that provides the desired mapping between uncertain components. The overall spatial regularization matrix is then given by organizing F copies of $\mathbf{h}_x$ in block diagonal form

$$\mathbf{H}_x = \text{diag}\Big[\mathbf{h}_x \quad \mathbf{h}_x \quad \dots \quad \mathbf{h}_x\Big]_{(P\times P)}. \tag{3.16}$$

Temporal regularization is a bit more straightforward given the known temporal connectivity of the solutions. 0^{th}-order temporal regularization is obtained by setting $\mathbf{H}_{0,t} = \mathbf{I}_P$. 1^{st}-order regularization is obtained by defining the temporal regularization matrix as the block $(F \times F)$ matrix of the form:

$$\mathbf{H}_{1,t} = \begin{bmatrix} -\mathbf{I}_N & \mathbf{I}_N & \mathbf{0} & \mathbf{0} & \dots & \mathbf{0} \\ \mathbf{0} & -\mathbf{I}_N & \mathbf{I}_N & \mathbf{0} & \dots & \mathbf{0} \\ \vdots & \vdots & \ddots & \ddots & \ddots & \vdots \\ \mathbf{0} & \dots & \mathbf{0} & \mathbf{0} & -\mathbf{I}_N & \mathbf{I}_N \\ \mathbf{0} & \dots & \mathbf{0} & \mathbf{0} & \mathbf{0} & \mathbf{0} \end{bmatrix}_{(P\times P)} \tag{3.17}$$

Selection of the value for the regularization parameter α_h is a common topic in the literature. A too-small value of α_h will not provide the desired smoothing effect, but a too-large value will overly smooth the solution and introduce too much bias in the reconstructed temperature vector. As pointed out by Mahzari et al. [6], the value of α_h will depend on the magnitude of the unknowns (in their case, small values of the heat transfer coefficient in their reconstructions required regularization parameters that were orders of magnitude greater than those needed for heat flux reconstructions in the literature). Many authors resort to a trial-and-error method for defining appropriate values for α_h. The "discrepancy principle" described by Woodbury [9] captures a commonly stated notion that α_h should be chosen as the minimum value that will yield an average difference between measured and modeled temperatures that is consistent with the expected accuracy of the measurements. The cross-validation method [22, 26, 27] is a commonly cited method to quantitatively define an optimum value. In the present implementation, it was observed that the α_h term

seemed to work the best when the two terms in Equation 3.6 contained elements of approximately the same magnitude. To this end, the user may indicate that α_h should be chosen for every local solution iteration to be a constant input factor `a_h` of the maximum element of the squared sensitivity coefficient matrix

$$\alpha_h = \texttt{a\_h} \cdot \left\| \mathbf{X}^T \mathbf{\Psi}^{-1} \mathbf{X} \right\|_\infty . \tag{3.18}$$

A degree of experimentation is still required as this metric does not fully take into consideration how much noise is present in the data to be fit (especially if $\mathbf{\Psi}^{-1}$ is neglected, as is often done in practice). However, a value of $\texttt{a\_h} = 1$ generally provides a good starting point considering the thermal properties of the system and the magnitude of the solution vector.

The regularization weighting matrix $\mathbf{W}$ has taken on a novel form to permit 'focusing' the regularization for sequential subdomain solutions. For pure whole domain solutions, shifting the emphasis of the regularization likely will not have any benefit. However for certain sequential problems, it appears that it may be advantageous to suppress the regularization at one end of the local solution time domain (different f indices) with the following:

$$\mathbf{W} = \text{diag}\Big[W(1) \quad W(2) \quad \dots \quad W(F) \Big]_{(P \times P)} \tag{3.19}$$

$$W(f) = \text{diag}\left[\frac{1}{10^{fW_f}} \quad \frac{1}{10^{fW_f}} \quad \cdots \quad \frac{1}{10^{fW_f}} \right]_{(N \times N)} \tag{3.20}$$

where W_f is a user input factor. For pure whole domain solutions, W_f can be set to 0 to obtain $\mathbf{W} = \mathbf{I}_P$ as desired. However, a positive value of W_f will result in less regularization at later f, whereas a negative W_f will yield less regularization on earlier f. Complete characterization of the behavior of this term is left to future work, so the parameter W_f is taken herein to be 0.

The covariance matrix $\mathbf{\Psi}$ describes the nonsystematic errors in the measurements provided to the algorithm. While this matrix can be of considerable concern in parameter

estimation and experiment design [28], the transient nature of the IHCP complicates the computation of this matrix. When several "standard" assumptions are made of the measurements, specifically that the measurement errors are uncorrelated, additive, normally distributed with zero mean, the inverse of this matrix reduces to the reciprocal variance matrix

$$\mathbf{\Psi}^{-1} = \text{diag}\Big[\Psi^{-1}(i) \quad \Psi^{-1}(i+1) \quad \dots \quad \Psi^{-1}(i+R-1)\Big]_{(JR\times JR)} \tag{3.21}$$

with

$$\Psi^{-1}(r) = \text{diag}\Big[\sigma_{Y_1}^{-2}(t_r) \quad \sigma_{Y_2}^{-2}(t_r) \quad \dots \quad \sigma_{Y_J}^{-2}(t_r)\Big]_{(J\times J)} \tag{3.22}$$

where $\sigma_Y(t)$ is the standard deviation of measurement Y at time t. In this form, this matrix effectively scales the difference between the measurements and numerical model in such a way that the least-squares objective function contribution is reduced if the difference is less than the measurement uncertainty, the least-squares contribution is increased if the difference is larger than the measurement uncertainty. If off-diagonal elements of $\mathbf{\Psi}$ are included, then additional contributions of $2\Psi_{kl}^{-1}(Y_k - T_k)(Y_l - T_l)$ for $k \neq l$ are added to the least-squares objective function to similarly weight contributions according to expected correlated deviations of the measurements.

For the present work, $\mathbf{\Psi}^{-1}$ is taken to be the identity matrix. It is shown by Beck et al. [14] that $\mathbf{\Psi}^{-1}$ cancels out under the "standard" measurement assumptions unless regularization terms are present. If regularization is present, neglecting $\mathbf{\Psi}$ will simply change the effective value of the regularization parameter. However, if the variance of measurements are not equal in space or time, then including $\mathbf{\Psi}$ will result in modeled errors at more precise measurements being weighted more heavily in the objective function and potentially reduce the reconstruction bias at those measurements.

At the present time, very little has been done to characterize the behavior of the $\mathbf{B}$ matrix enabling the trial function capability. For all presented results, $\mathbf{B} = \mathbf{0}_{(P\times P)}$ and $\tilde{\mathbf{q}}^f = \mathbf{0}_{(P\times 1)}$.

3.3 Algorithm Variants

The algorithm presented here has a number of parameters, set by the user, which significantly alter the behavior of the algorithm and yield performance ranging from pure whole domain Gauss-Newton to Beck's Future Time algorithm.

- **Length of the future time window**. This determines the length of time covered in a specific local solution. It affects how many measurements will inform this reconstruction step, and what period of time over which sensitivity coefficients must be calculated.

- **Discretization of BC interval times**. Determines how many boundary condition values must be estimated and how many measurements will inform each boundary condition interval. Note that having multiple measurements inside a boundary condition interval implicitly adds stabilization to the algorithm in the same manner as Beck's future time algorithm.

- **The number of considered BC intervals (parameter F)**. If the user specifies F to be lower than the number of intervals covered by the future time window, then it will ignore the intervals $f > F$. The $f = F$ interval is assumed to apply all the way to the end of the future time window (equivalently, all intervals $f > F$ are assumed equal to F). The step sensitivity coefficient is evaluated for interval F whereas pulse sensitivity coefficients are calculated for $f < F$.

- **The number of estimated BC intervals that are 'retained' after a local solution**. This algorithm allows the user to 'retain' a subset of the estimates calculated in a given local solution. In this way, solutions earlier in the future time window, which have sensitivity coefficients that have had time to develop, are retained as they are likely more accurate, and estimates at later times go towards improving the initial guess of those intervals.

- **Regularization parameters: α and W_f.** If $F > 1$, these options control solution stabilization beyond that implicitly included if multiple measurements are included in the defined solution intervals.

All of these options can be varied for different local solutions in a global problem if it is desirable for a particular reconstruction.

3.3.1 Beck's Future Time Algorithm

The Future Time (FT) algorithm of Beck et al. [14] can be obtained by setting $F = 1$, discretizing the boundary condition intervals to match the measurement times, and setting the length of the future time window to the appropriate number of 'future times' in Beck's algorithm. Since $F = 1$, the heat flux is assumed constant through the future time window (alternatively, the boundary condition intervals on the future time window are assumed equal to the first). A couple steps of this algorithm are illustrated in timeline form in Figure 3.2.

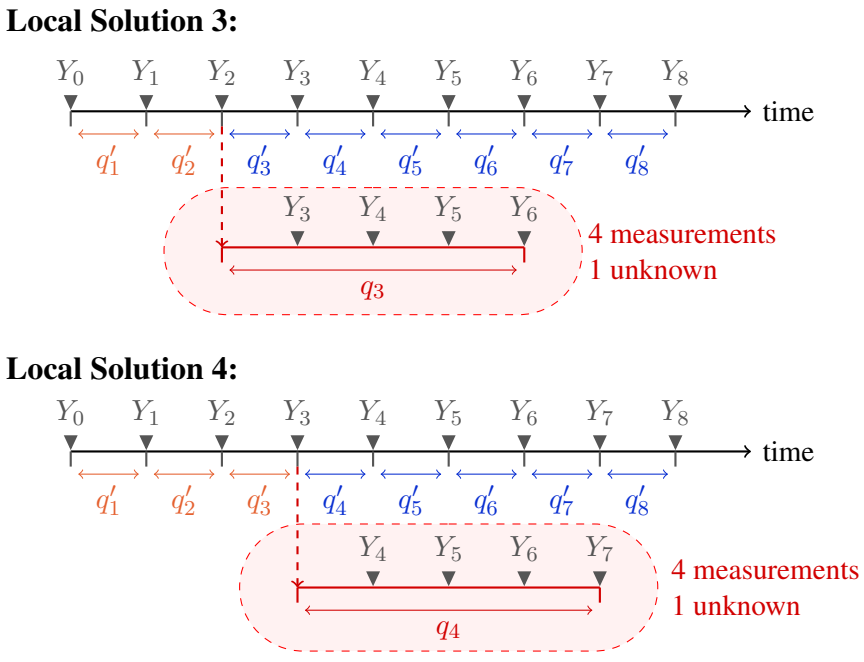

Figure 3.2. Timeline illustrating two local solutions of a Future Time reconstruction.

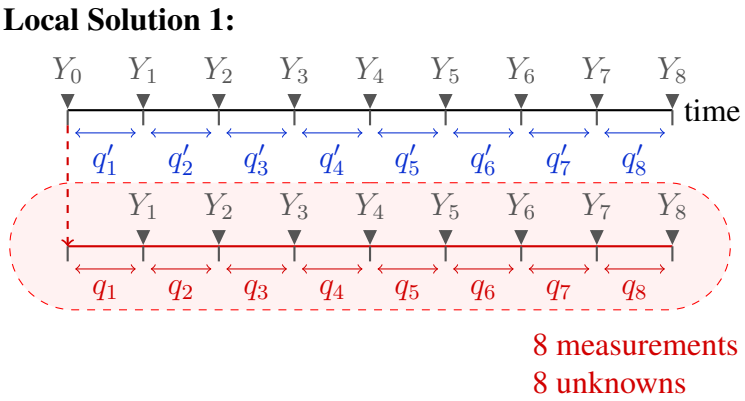

Figure 3.3. Timeline illustrating the local solution of a pure Whole Domain reconstruction.

3.3.2 Whole Domain Algorithm

On the other end of the spectrum, a pure Whole Domain (WD) algorithm solution can be obtained by setting $F = M$ to include all intervals, discretizing the boundary condition intervals to match the measurement times, and setting the length of the future time window to the whole problem domain. Regularization will need to be specified to stabilize the solution, and all solution values must be retained. This is illustrated in timeline form in Figure 3.3.

3.3.3 Sequential Subdomain Algorithm

An example illustrating the proposed hybrid algorithm, which we will refer to as the *Sequential Subdomain* (SSD) algorithm, is obtained by setting F to a value in the range $1 < F < M$, setting the length of the future time window long enough to cover the F boundary condition intervals, and setting the terms retained in each local solution to a desired value (typically 1). In Figure 3.4, the values of q_3 through q_6 are estimated in Local Solution 2, but only q_3 and q_4 are retained. The initial guess for q_5 and q_6 are updated based on the results of Local Solution 2, but they are re-estimated in Local Solution 3. This algorithm is proposed to address the concerns raised in Section 2.4. It was shown that the minimum length of the future time window is a constraint imposed by the material properties, the

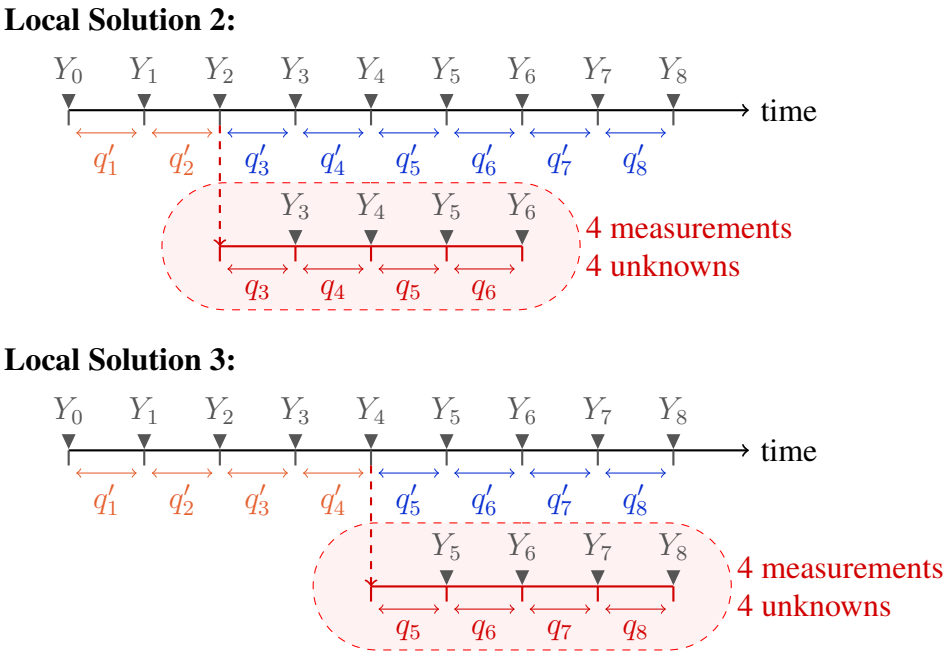

Figure 3.4. Timeline illustrating two local solutions of a Sequential Subdomain reconstruction with two retained terms.

measurement distance from the boundary, and the accuracy of the measurements. Given that constraint, Figure 3.2 shows why the future time algorithm can perform poorly if BC intervals necessary to capture the relevant behavior are short compared to the future time window: the estimated flux is essentially going to be the 'average' of the true solution over all solution intervals in the future time window. To get around this, the SSD algorithm draws on the whole domain approach of evaluating pulse sensitivity coefficients to the end of the future time window for all solution intervals in the future time window and performs a simultaneous estimation of all of the boundary condition values touched. Since the true 'whole domain' is not considered, the solution estimates at later times are not necessarily very accurate due to the shorter development time allowed for their sensitivity coefficients. As a result, these estimates are not retained for the final solution. They are, however, retained as an improvement to the initial guess for those intervals. If the problem is defined carefully, many problems using this approach will benefit from greatly improved

reconstructions compared to the future time algorithm and greatly reduced computation times compared to the whole domain algorithm.

The SSD algorithm appears similar in several aspects to Lamm's modified local Tikhonov regularization algorithm [29, 30]. Both methods utilize Tikhonov regularization on restricted 'local' domains and allow the extent of these local domains to vary in size throughout the overall problem domain. SSD seems to differ from Lamm's algorithm in that SSD considers only data at future times relative to the component being estimated (as opposed to applying the Tikhonov regularization considering data on an interval centered on the component being estimated), it estimates multiple components on the local domain, and it performs the overall estimation on a single sequential pass through the time domain as opposed to iterating with multiple passes over the full domain. There is quite a bit of material in the applied math community on problems of this nature, and more investigation of the literature is necessary to establish the novelty of the proposed algorithm.

3.4 Computational Cost

This implementation provides considerable flexibility for reconstruction problems. However, each option has an impact on the overall computational effort required to complete the reconstruction. Two metrics can be defined to compare the computational cost of different modes: linear system cost, and sensitivity coefficient cost.

The linear system cost describes the computational effort required to solve Equation 3.5 once it has been defined. General dense matrix algorithms such as LU or QR decompositions can be used to solve such a system. Generic implementation of these methods usually require order $\mathcal{O}(n^3)$ operations, though more efficient algorithms can provide some advantage. This is a fairly straightforward and intuitive metric: increasing the number of total unknowns rapidly increases the cost. For the algorithm modes described, all solve Equation 3.5 at the local solution level, so the linear system cost scales by the unknowns in a local solution. For the Future Time (FT) algorithm the number of unknowns is N. At the other end, the Whole Domain (WD) algorithm, the number of unknowns is NM. The

number of unknowns in the SSD algorithm is NF. However, each algorithm will compute a different number of local solutions, so the total cost will be higher.

The FT algorithm requires the solution of M local solutions; however, it generally does not require any non-linear iteration, so the total linear system cost of the FT algorithm is $\mathcal{O}(MN^3)$. The WD algorithm, on the other hand, only requires a single local solution, but it will most likely require iteration. If ν_{WD} iterations are assumed, the total linear system cost for the WD algorithm is $\mathcal{O}(\nu_{WD}(NM)^3)$. The SSD algorithm will likely require some non-linear iteration, though it is hoped that the sequential evaluation will reduce the number of non-linear iterations relative to the WD algorithm, so $\nu_{SSD} < \nu_{WD}$ iterations are assumed. The number of local solutions needed in the SSD algorithm is M/N_{ret}, where N_{ret} is how many solution intervals are retained from each local solution. With these assumptions, and neglecting that the linear system will be smaller for local solutions containing the end of the global problem, the linear system cost of the SSD algorithm is $\mathcal{O}(\nu_{SSD}\frac{M}{N_{ret}}(NF)^3)$.

Despite the cubic scaling of the linear system cost, far more time will generally be spent evaluating sensitivity coefficients, unless a problem is linear and special accounting is made for that fact. In this work, sensitivity coefficients are assumed to be computed by a finite-difference approximation, which means a number of direct material response simulations must be computed. Depending on the specific problem, the material response evaluation could be cheap (if, for instance, Equation 2.13 is used) or very expensive (if a multi-dimensional finite-element model must be evaluated). To generalize the cost of the methods, the sensitivity coefficient cost is measured by *accumulated simulated time* (AST). This measures the total amount of material response time integrated over the course of the reconstruction, both for sensitivity coefficient evaluation and temperature residual evaluation. For example, evaluating a finite-difference sensitivity coefficient on a $5\,\mathrm{s}$ future time window using central differences will require two evaluations of the $5\,\mathrm{s}$ domain (each referred to as a *future time track*) with perturbed boundary conditions, so $10\,\mathrm{s}$ is added to the accumulated system time for every non-linear iteration. This metric is not a direct measure of wall-time required to compute a reconstruction as wall-time per unit of simulated time will be problem specific. This metric also does not take into account differing par-

allel efficiencies of different reconstruction approaches. However, it provides a means of comparing to first-order the different costs of reconstruction algorithms.

The accumulated simulated time of any local solution is the number of required tracks multiplied by the length of each track. In the present implementation, one track must be evaluated in each local solution for residual evaluation ($\mathbf{T}^*$ in Equation 3.7), and two tracks for every unknown for sensitivity coefficient evaluation (one each for the positive and negative perturbations). For a generic solution, this yields an AST of $(1 + 2NF)t_{FT}$, where t_{FT} is the length of the future time window. As with the linear system time, the cost of a single local solution is scaled by the number of local solutions required, which gives a total AST of

$$t_{AST} = \nu \frac{M}{N_{ret}}(1 + 2NF)t_{FT}. \tag{3.23}$$

For the FT algorithm, this simplifies to $M(1 + 2N)t_{FT}$ as ν, N_{ret}, and F are all 1. For the WD algorithm, it simplifies to $\nu_{WD}(1 + 2NM)t_{full}$ as only one local solution is used, $F = M$, and $t_{FT} = t_{full}$. Note that in this implementation, the WD algorithm does not take advantage of the parabolic nature of the problem. A more optimal WD implementation could evaluate sensitivity coefficients using tracks that start at the first time for which the corresponding unknown can affect the solution. If a uniform discretization of the boundary conditions is assumed, this could theoretically reduce the cost of sensitivity coefficient evaluation by a factor of 2. The SSD algorithm AST takes the form of Equation 3.23 with $\nu = \nu_{SSD}$. These costs are summarized in Table 3.2.

Table 3.2. Summary of cost metrics for different algorithm modes.

Algorithm Mode	Linear System Cost	Accumulated Simulated Time (AST)
Future Time	$\mathcal{O}(MN^3)$	$M(1 + 2N)t_{FT}$
Whole Domain	$\mathcal{O}(\nu_{WD}(NM)^3)$	$\nu_{WD}(1 + 2NM)t_{full}$
Sequential Subdomain	$\mathcal{O}(\nu_{SSD}\frac{M}{N_{ret}}(NF)^3)$	$\nu_{SSD}\frac{M}{N_{ret}}(1 + 2NF)t_{FT}$

The formulae in Table 3.2 are not easily comparable due to the variable algorithm parameters. For some combinations of parameters, the SSD algorithm can provide significant computational savings over a pure WD algorithm. However, with other combinations of parameters, it is possible for the SSD to cost as much or more than a WD solution. For the sake of example, assume a problem with $N = N_{ret} = 1$ with uniform distribution of boundary condition intervals such that $t_{ft} \approx \frac{t_{full}}{M/F}$. With this, the ratio of accumulated simulated time of the WD and SSD algorithms is seen to reduce to

$$\frac{t_{AST,SSD}}{t_{AST,WD}} = \frac{\nu_{SSD} F(1+2F)}{\nu_{WD}(1+2M)}. \tag{3.24}$$

If $\nu_{SSD} < \nu_{WD}$ and $F^2 < M$, the SSD can be expected to provide a computationally cheaper result. However, if the local solution size (F) is too large relative to the total problem size (M), the SSD reconstruction could rapidly become the most expensive.

If we consider a numerical example, Mahzari et al. [6] considered a time domain of $t_{full} = 130\,\mathrm{s}$ with a reconstruction frequency of $1\,\mathrm{Hz}$ ($N = 1$, and $M = 130$) and $\nu = 30$ non-linear iterations for the MSL reconstruction[2]. This means that a whole domain reconstruction requires $1.08 \cdot 10^6\,\mathrm{s}$ of AST. If this were done with a sequential method with a future time of $t_{FT} = 5\,\mathrm{s}$, the AST would be $1.95 \cdot 10^3\,\mathrm{s}$–almost three orders of magnitude less. The SSD algorithm in this instance, with $F = 5$ and the same number of non-linear iterations, would have an AST of $2.2 \cdot 10^5\,\mathrm{s}$. However, if the future time window were $15\,\mathrm{s}$ with a corresponding $F = 15$, the AST would jump to $1.81 \cdot 10^6\,\mathrm{s}$. While the accuracy of an SSD reconstruction relative to a WD reconstruction must be taken into account, the potential for cost savings with SSD is clear.

3.5 Implementation

The IHCP algorithm presented in this chapter has been implemented as the *INHEAT* module in the *CHAR* code for general reconstruction activities. Furthermore, a stand-alone

[2]Reference [6] used 200 non-linear iterations for benchmark cases with poor initial conditions; however, per private communication with the authors, only 30 non-linear iterations were used for reconstructions of flight data.

IHCP code has been developed for linear inverse problems to take advantage of some computational efficiencies that are not available in the general case. This section will summarize the capabilities of the specific implementations used in this work.

3.5.1 *CHAR* Description

CHAR is a 1-D/2-D/3-D material thermal response code that solves general heat transfer problems on decomposing ablators as well as non-decomposing, non-ablating TPS materials. It uses a finite-element discretization with first- and second-order implicit time integrators. The pyrolysis gas and solid energy governing equations are solved fully-coupled and fully-implicit in serial or parallel. A rich and flexible suite of boundary conditions are implemented, and rigorous verification using the method of manufactured solutions is used to assure accurate implementation of the governing equations. It has been developed over several years in the NASA Johnson Space Center Applied Aeroscience and CFD Branch to improve methods of integrating products between the aerothermal environment and thermal protection disciplines. It is implemented in the C++ programming language and is built on the libMesh finite-element/adaptive mesh refinement library [31]. A more complete description can be found in Amar et al. [32, 33] and the *CHAR* modeling document [34].

3.5.2 *INHEAT* Capabilities

INHEAT has been developed and integrated with *CHAR* with the goal of maximizing the user's flexibility in specifying an inverse problem. Any time-varying boundary condition value that can be specified in a *CHAR* boundary condition file can be the unknown parameter estimated in an inverse run. This includes values that serve as input to runtime-evaluated expressions which themselves can be functions of time, space, 'spatial' BC input files, and temperature/pressure/location values at 'monitor points' defined at fixed or node-following locations. Any number of temperature targets can be specified and moving targets are permitted (in order to make use of data provided by isotherm tracking sensors). This places a fair bit of responsibility on the user to define a problem that can actually

be solved. However, this is believed to be a small cost compared to the flexibility provided. It has also been implemented in such a way as to put as few restrictions on standard *CHAR* capabilities as possible (adaptive mesh refinement is the key feature not permitted, dynamically variable time-stepping is permitted).

As the cost of computing required sensitivity coefficients can be significant, *INHEAT* has been implemented with a limited threading capability over and above *CHAR*'s own ability to solve a direct problem on multiple processors using MPI. The majority of time in an inverse solution is spent evaluating sensitivity coefficients. *INHEAT* has been implemented to compute sensitivity coefficients using finite-difference approximations. As previously noted, each direct simulation of the future time window with a perturbed BC value is referred to as a *future time track*. Evaluation of the future time tracks needed for sensitivity coefficient evaluation is an embarrassingly-parallel problem, so parallel efficiency is maximized by assigning minimum-sized 'threads' to solve the tracks in parallel as opposed to all processors working on one track at a time (which maximizes parallel communication inside the direct solver). The desired number of threads are specified, the available processors are divided up between the threads, and future time tracks are divided up between threads for evaluation. If a direct problem is too large to fit on a single processor, the threads may themselves use multiple CPUs managed by *CHAR*. At this time, *INHEAT* is not capable of dynamically adjusting the number of threads to optimally fit the specified problem. Since the future time window will generally be evaluated many times in a given local solution, *CHAR* has been given the ability to internally save the state of the numerical system at the beginning of the future time track, and return to this previously saved state once temperatures computed in a specific future time track have been retrieved. This internal restart capability saves a considerable amount of effort since the solution time prior to the start of the future time window does not need to be recomputed. It should be noted that solving sensitivity coefficients using dedicated sensitivity equations could be more computationally efficient, however this greatly complicates the addition of physical models. *CHAR* has been developed with the intention that physical models can be quickly added, so finite-difference sensitivity coefficients maintains this development paradigm.

INHEAT has been used for several recent flight and ground test data reconstruction activities and has a small user base that has assisted with identifying bugs and providing advice on desirable input options and capabilities. It is now a standard component included with the *CHAR* distribution.

3.5.3 Linear IHCP Solver

For a subset of IHCP problems, reconstructions can be evaluated much more rapidly using a different strategy than that implemented in *INHEAT*. For linear problems, the sensitivity coefficients do not need to be recomputed; they only need to be appropriately shifted in time (recall Equation 2.16). *INHEAT* does not have the mechanism implemented to save and shift coefficients in this manner, so a separate stand-alone code was implemented for these problems.

The linear IHCP solver is a C++ code that reads sensitivity coefficient information from a file and solves the inverse problem described in Section 3.1. The Eigen library[3] is used to simplify matrix math and solution of the linear system of Equation 3.5. The scope of problems that may be solved by this tool is somewhat limited, as time-scales of input measurements are expected to be uniformly distributed, and pulse sensitivity coefficients must be provided on a consistent time scale, with the pulse width identical to the time between measurements (implying solution intervals also consistent with time between measurements). To accommodate future time smoothing which needs step sensitivity coefficients (instead of pulse sensitivity coefficients), the sensitivity coefficient matrix must be adjusted.

The sensitivity coefficient matrix with solution intervals consistent with the measurement time scales is denoted by $\mathbf{X}_m$. It has the same structure as Equation 3.12 except that $F = R$, therefore has dimensions $(JR \times RN)$. It is populated with sensitivity coefficients read from a user-specified file, with the appropriate time-shifting performed to populate the columns representing the R different solution intervals. If reconstruction solution in-

[3]Freeware available at: `http://eigen.tuxfamily.org`

tervals are desired on a time-scale different from the measurement time scales, the required $(JR \times FN)$ sensitivity coefficient matrix can be obtained by

$$\mathbf{X} = \mathbf{X}_m \mathbf{A} \tag{3.25}$$

where the pulse integration matrix $\mathbf{A}$ is given by

$$\mathbf{A} = \begin{bmatrix} \bar{a}_{11} & \bar{a}_{12} & \dots & \bar{a}_{1F} \\ \bar{a}_{21} & \bar{a}_{22} & \dots & \bar{a}_{2F} \\ \vdots & \vdots & \ddots & \vdots \\ \bar{a}_{R1} & \bar{a}_{R2} & \dots & \bar{a}_{RF} \end{bmatrix}_{(RN \times FN)} \tag{3.26}$$

with

$$\bar{a}_{ij} = \begin{cases} \mathbf{I}_N, & \lambda_{j-1} < t_i \leq \lambda_j \\ \mathbf{0}_N, & \text{otherwise} \end{cases}. \tag{3.27}$$

Note that with this implementation, solution intervals are constrained to be integer multiples of the measurement time scales.

Any source may be used to generate sensitivity coefficients (both *CHAR* and Equation 2.13 are used in this work), and any number of uncertain BCs can be solved based on any number of supplied measurements (as long as measurement times are consistent). As this is only valid for linear cases, iteration is not used. Temperatures are evaluated with the Duhamel approximation (Equation 2.17), except that a time-varying 'initial' temperature, T_0, may be specified to permit solution on systems that begin with non-uniform temperatures. Time-varying T_0 values are computed using *CHAR* by starting with the non-uniform initial temperature and integrating in time with heat flux boundary conditions set to zero.

4. NON-ABLATING RECONSTRUCTION EXAMPLES

The behaviors of the different algorithms are perhaps best described by illustration. Two standard linear benchmark cases are considered to demonstrate the basic performance of the different algorithm modes. Following those, a reconstruction of a decomposing ablator is considered to assess the non-linear performance of the proposed algorithm. Next, a reconstruction of a highly-transient heating profile similar to steering jet augmented heating on a flight test is considered to demonstrate performance when representative time-scales change during a reconstruction. Finally, a multi-component/multi-dimensional benchmark case is shown to demonstrate *INHEAT*'s multi-component capability. All cases in this chapter neglect the effects of surface recession and leave that issue for Chapter 6.

4.1 Standard Benchmark Cases

Two commonly used [14] benchmark cases are considered: a square pulse heating profile and a triangular pulse heating profile. Both cases model 1-D semi-infinite slab of material with the constant properties ($\rho = 280\,{}^{\mathrm{kg}}/_{\mathrm{m}^3}$, $k = 0.4\,{}^{\mathrm{W}}/_{\mathrm{m\cdot K}}$, $C_p = 1000\,{}^{\mathrm{J}}/_{\mathrm{kg\cdot K}}$). A single thermocouple is placed at a depth of $3.8\,\mathrm{mm}$ below the heated surface and is sampled at $10\,\mathrm{Hz}$. This combination yields a sensitivity coefficient (evaluated using Equation 2.16) that peaks at approximately $5\,\mathrm{s}$, as seen in Figure 4.1. With this profile, the regularization parameter suggested by Equation 3.18 is approximately $2 \cdot 10^{-9}$. This is a relatively simple linear problem and therefore does not necessarily tax the different algorithms, but it does demonstrate the general characteristics of the converged result of a more realistic non-linear problem. The linear IHCP solver described in Section 3.5.3 is used for all results presented in this section.

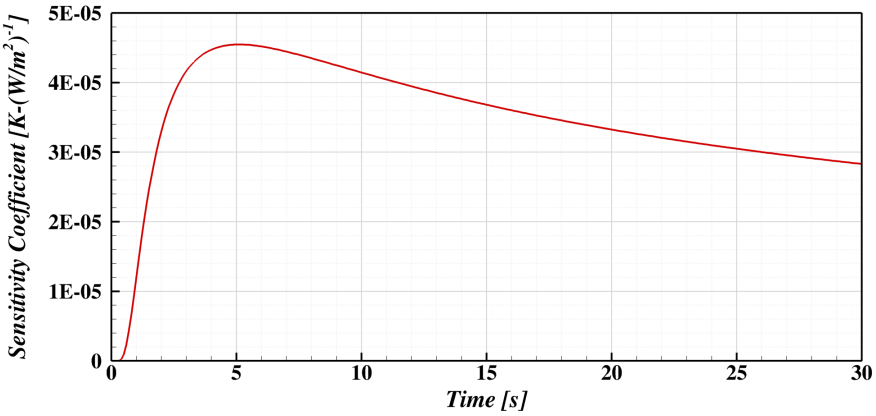

Figure 4.1. Sensitivity coefficient curve for example problem

4.1.1 Square Heating Pulse

The square heating profile shown in Figure 4.2 is used to generate artificial 'measurements' for reconstruction. The resulting temperature data is also shown in Figure 4.2. In addition to the 'clean' temperature profile (which is the direct thermal result of the applied heating profile), a 'noisy' profile is also generated from the clean profile by adding random samples from a normal distribution with zero mean and a standard deviation of 0.2% of the clean temperature at the sample time. This level of noise is somewhat larger than would be expected from most well-designed experiments. However, it will provide a stressing case to demonstrate how the various algorithms respond to random measurement errors. More realistic levels of noise are considered in later examples.

Reconstruction results using Beck's Future Time (FT) algorithm are shown in Figure 4.3. Errors introduced by measurement noise are clearly visible in the reconstructions with shorter future time windows (4.3(b)). While the errors are clearly reduced by increasing the future time window, the reconstructions also considerably smooth over the true discontinuities in the heating profile. This is consistent with expectations, as the constant flux through the future time window assumption that is central to the FT algorithm is essentially averaging the true heat flux over the future time window.

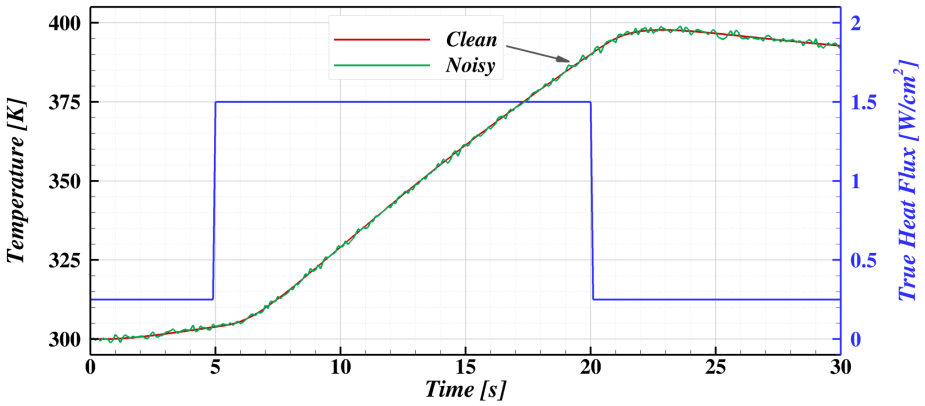

Figure 4.2. True heating profile and target temperature data for the square pulse example problem.

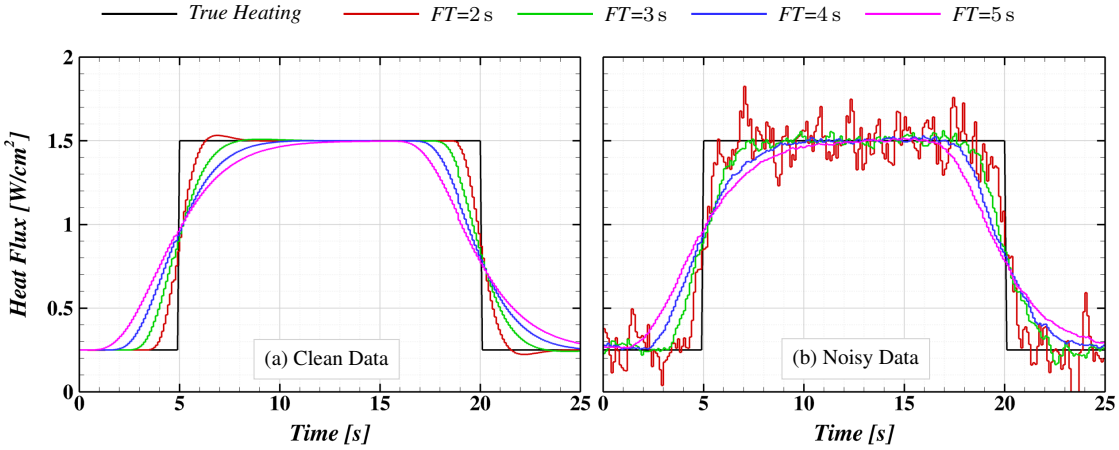

Figure 4.3. Reconstruction results using the Future Time algorithm for several future time window lengths

Reconstruction results using the Whole Domain (WD) algorithm are shown in Figure 4.4. Increasing the first-order regularization factor increases smoothness of the reconstruction in the presence of noise as expected, but significantly smooths out discontinuities in the solution relative to the true results, much like the FT algorithm. In this case though, the smoothing is more balanced before and after a discontinuity, though the noise seems to adversely affect the reconstructions more so for the WD reconstructions than the FT re-

constructions. The regularization parameter suggested by Equation 3.18 of $\alpha_1 = 2 \cdot 10^{-9}$ appears to be too small considering the relatively high level of noise.

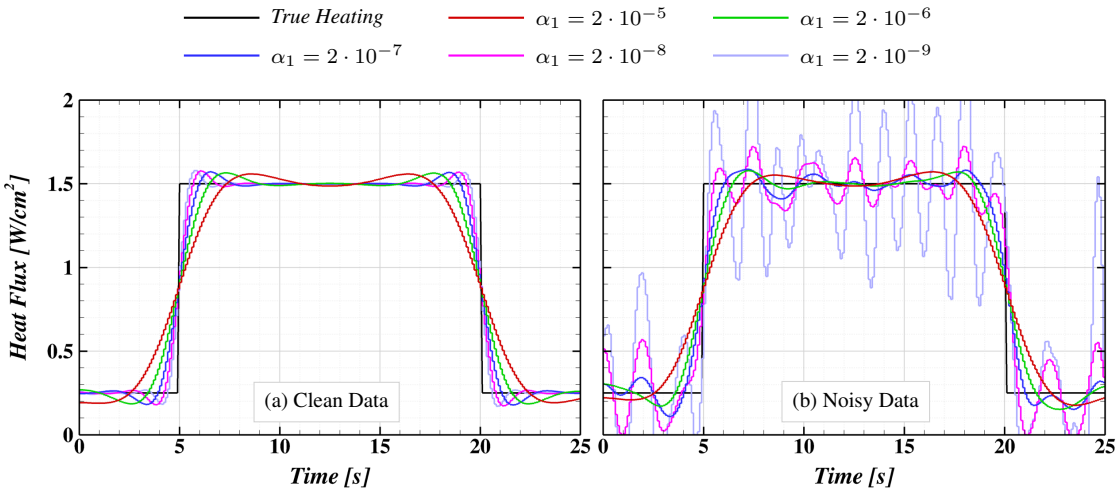

Figure 4.4. Reconstruction results using the Whole Domain algorithm for several values of the first-order regularization factor α_1

Reconstructions using the Sequential Subdomain (SSD) algorithm are shown in Figure 4.5. It is interesting to note that with a future time window of $2\,\mathrm{s}$ (before the peak in sensitivity coefficient), the SSD algorithm is largely unaffected by the regularization parameter. Conversely, for the longer future time windows, the solution becomes defined by the regularization parameter and independent of the future time window. Given the formulation of the SSD algorithm, it is to be expected that as the first-order regularization parameter is increased, the solution components on the future time window will be driven to a constant value. This is consistent with the assumptions of the FT algorithm, so FT behavior should be recovered. Similarly, if the future time window is long enough that the sensitivity coefficients develop sufficiently and regularization is low enough that the influence of later flux components in the future time window (which have poorly developed sensitivity coefficients) is sufficiently reduced, WD behavior should be recovered. Indeed, this is the trend that is seen when the three algorithms are compared on the same plot.

Figure 4.6 shows select reconstructions from each of the three algorithms on clean and noisy data. For both sets of results, SSD reconstructions with short future time windows and

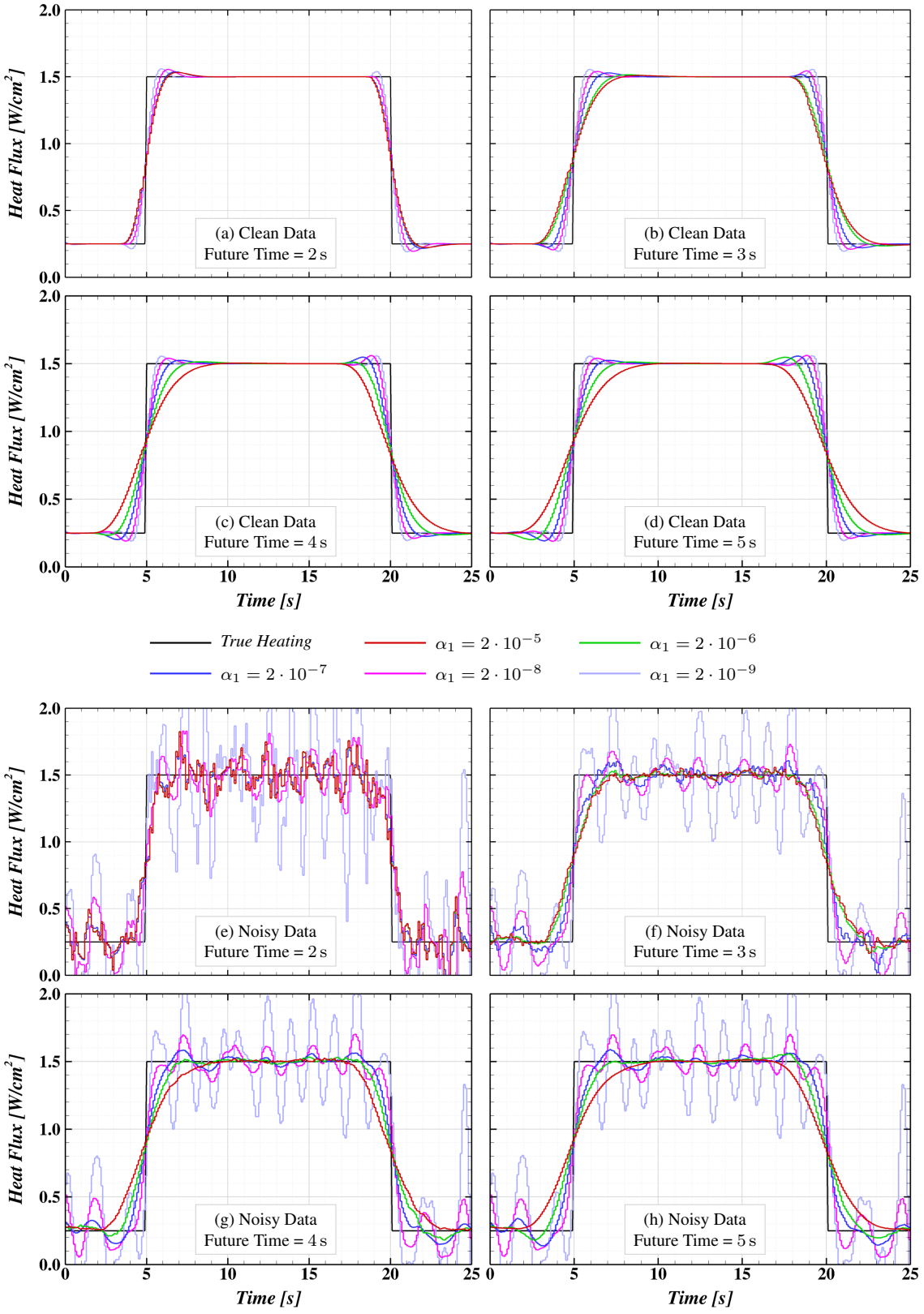

Figure 4.5. Reconstruction results using the Sequential Subdomain algorithm for various values of α_1

larger regularization parameters very closely match FT reconstructions (the FT results are completely hidden by the SSD results in both 4.6(b) and (f)). Similarly, for longer future time windows and smaller regularization parameters (4.6(c) and (g)), the SSD algorithm closely matches WD reconstruction. This exemplifies the point alluded to in the previous paragraph: the future time window in the SSD algorithm is not necessarily a smoothing parameter, it is a computational cost control. If the future time window is too short in the presence of data noise, it can do no better than the FT algorithm (4.6(f)). If the future time window is very long, the regularization parameter controls the smoothing and therefore the accuracy of the result, providing results consistent with the WD algorithm (4.6(g)). Further increasing the future time window from this point does not improve the result, it only increases the computational cost. The ideal future time window for an SSD reconstruction is as short as possible that still allows the sensitivity coefficients to develop sufficiently relative to the noise level. In this instance, a hybrid Tikhonov/future-time smoothing can be obtained that can provide better results (note the SSD results do not overshoot in Figure 4.6(h) as the WD results do) at an optimal cost.

To this point, reconstruction 'goodness' has only been qualitatively defined with regards to solution smoothness and how close the solution matches the true value. In practice, the true value will not be known and will not be available to guide the effort to select ideal reconstruction parameters. Quantitative comparisons of how well a reconstruction matches the provided temperature data can be made and can be quite useful. Two metrics are used here: the *residual temperature error* $(\mathbf{T} - \mathbf{Y})$ as a function of time, and the *sum-squared temperature error* $(\mathbf{T} - \mathbf{Y})^T(\mathbf{T} - \mathbf{Y})$. The sum-squared error is discussed in this example; the residual temperature error is demonstrated in the next section.

Figures 4.7 and 4.8 both show the value of the sum-squared temperature error for each reconstruction presented in two different ways: 4.7 plotting the FT and SSD solutions' response against the length of the future time window, and 4.8 plotting the WD and SSD solutions' response against the regularization parameter. The most obvious feature to note in these figures is the stark difference between clean and noisy data reconstructions. For most of the clean reconstructions in 4.7(a) and 4.8(a), the error is seen to decrease as the

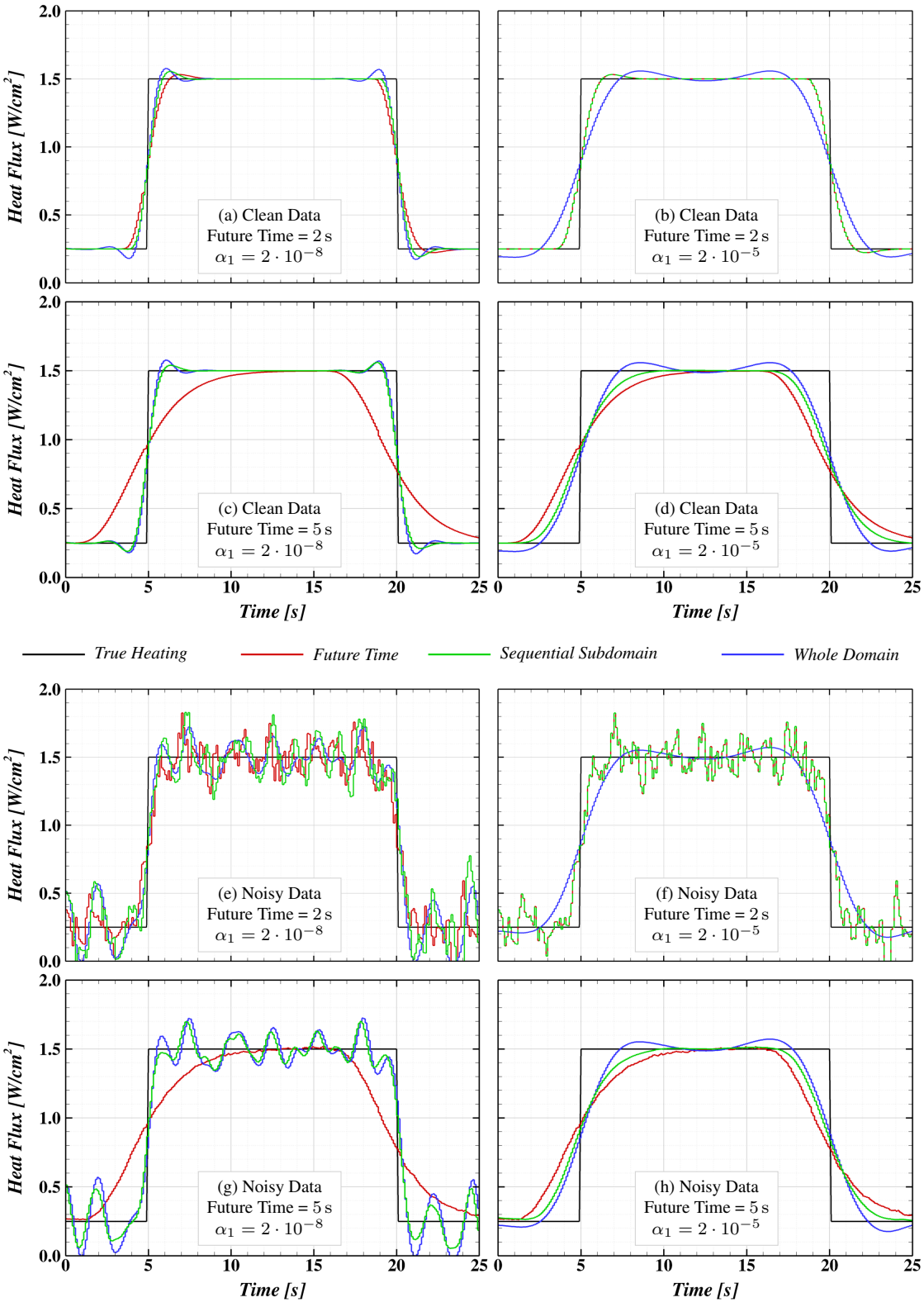

Figure 4.6. Comparison of algorithms on square heat pulse test case

smoothing parameters are reduced. For the noisy data reconstructions in 4.7(b) and 4.8(b), however, a level is reached below which the sum-squared temperature error does not significantly decrease. Recall that the 'noisy' data in this example was created by adding noise to the clean temperature profile. The clean profile would represent the reconstructed temperature of an ideal heating profile reconstruction, so the sum-squared error of the noisy temperature profile (Figure 4.2) can be calculated here and is found to be approximately $137.93\,\mathrm{K}^2$. A reconstruction with an error lower than this level is not necessarily better than another reconstruction closer to this level; it means that the reconstructed heating profile is departing from the true heating to follow the noise. Consulting Figures 4.4(b) and 4.5(h), it would seem that most of the oscillatory reconstructions also show sum-squared temperature errors lower than the error level of the noisy data trace (4.8(b)). From this, we can conclude that sufficient regularization is obtained when the error just reaches the plateau error level (in Figure 4.8(b), $\alpha_1 \approx 10^{-6}$ for the WD algorithm and 10^{-7} for the SSD algorithm).

Figure 4.7(a) provides further support for the earlier observation that the SSD is independent of the length of the future time window if the regularization parameter is small, and also corroborates the similarity of the temperature reconstructions to the FT algorithm if α_1 is large. Contrary to the qualitative observation earlier, this plot would seem to indicate that the regularization parameter sill has an effect even for the shortest future time window. In comparison to the WD algorithm, Figure 4.8(a) indicates that the SSD algorithm will introduce more error for a given α_1 if the future time window is long enough to be free of future time smoothing (seen when the SSD curves flatten out at higher α_1). This suggests that even with longer future time windows, truncating the sensitivity coefficients to only the future time window does introduce some additional bias in the reconstructed temperature. The slope of the SSD errors with respect to the regularization level parallels the WD slope quite well, again as long as the future time window is long enough to be free of significant future time smoothing.

To summarize this test case, a first demonstration of the three algorithms considered in this document has been presented, and it has been shown that the SSD algorithm provides additional control over the smoothing applied to reconstruct a heat flux profile when

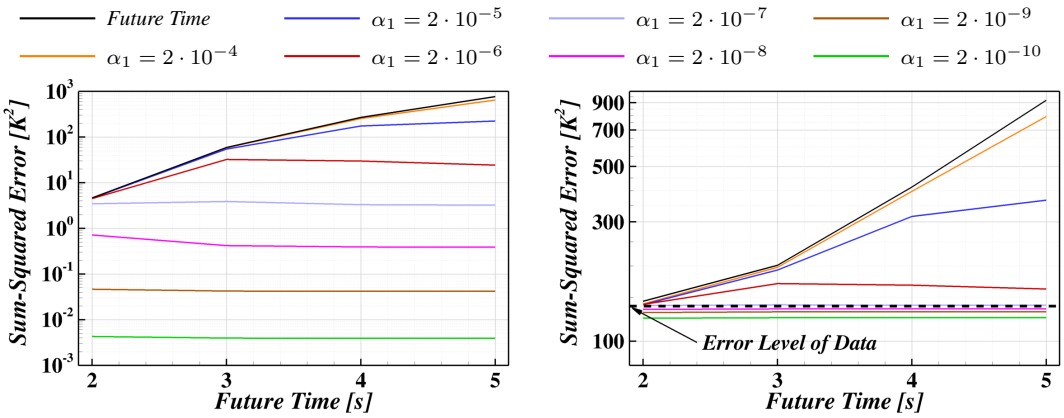

(a) Clean Data (b) Noisy Data

Figure 4.7. Effect of future time window on sum-squared temperature error in square pulse reconstructions for FT and SSD algorithms.

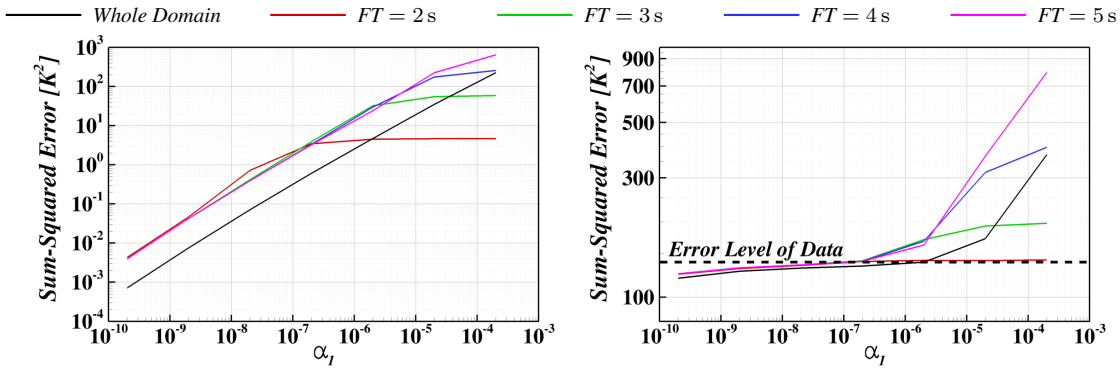

(a) Clean Data (b) Noisy Data

Figure 4.8. Effect of regularization parameter on sum-squared temperature error in square pulse reconstructions for SSD and WD algorithms.

substantial noise is present in the target temperature data. In this case, however, the noise applied is not particularly realistic, and the case of a step change in heating is much more difficult reconstruction task then typically present in flight data reconstruction efforts. The cases in the subsequent sections will introduce more smoothly varying heating profiles and more realistic noise levels to demonstrate the behavior of the three algorithms under these conditions.

4.1.2 Triangular Heat Pulse

The triangular heating profile defined in Figure 4.9 is another common benchmark case for IHCP evaluation as the slope is more representative of many realistic heating profiles, and reconstruction of the peak of the triangle can be challenging. In this section, the residual temperature error is plotted along with the reconstructed heat flux to demonstrate how characteristics of the solution can be identified by looking for certain features in the error plots.

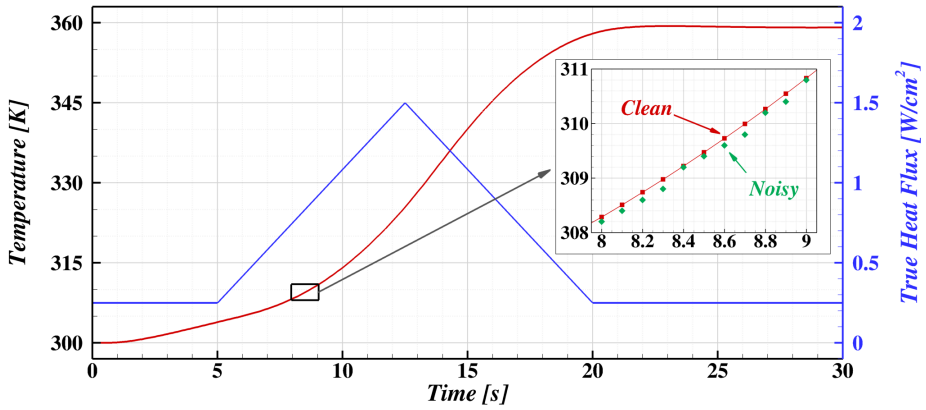

Figure 4.9. Truth heating profile and target temperature data for triangular heating profile example problem.

The temperature profile corresponding to this heating profile is also shown in Figure 4.9. For this case, the 'noisy' reconstructions will use temperature data that has been truncated to a resolution of $0.2\,\mathrm{K}$, simulating a low resolution data acquisition system. As with the square heating profile test case before, TC data is provided to each algorithm at $10\,\mathrm{Hz}$.

The FT algorithm results are presented in Figure 4.10. The more gradual change in heating subdues, to an extent, the early rise seen in the square pulse (Figure 4.3(a)). However, the smoothing from this algorithm strongly smooths over the peak of the triangle, yielding a general under-prediction of the peak heating that increases with increasing future time window. For this test case with a more realistic noise profile, the future time algorithm is seen to smooth the noise reasonably well, with significant deviations only visible for the shortest future time window. Since the future time window is not centered on

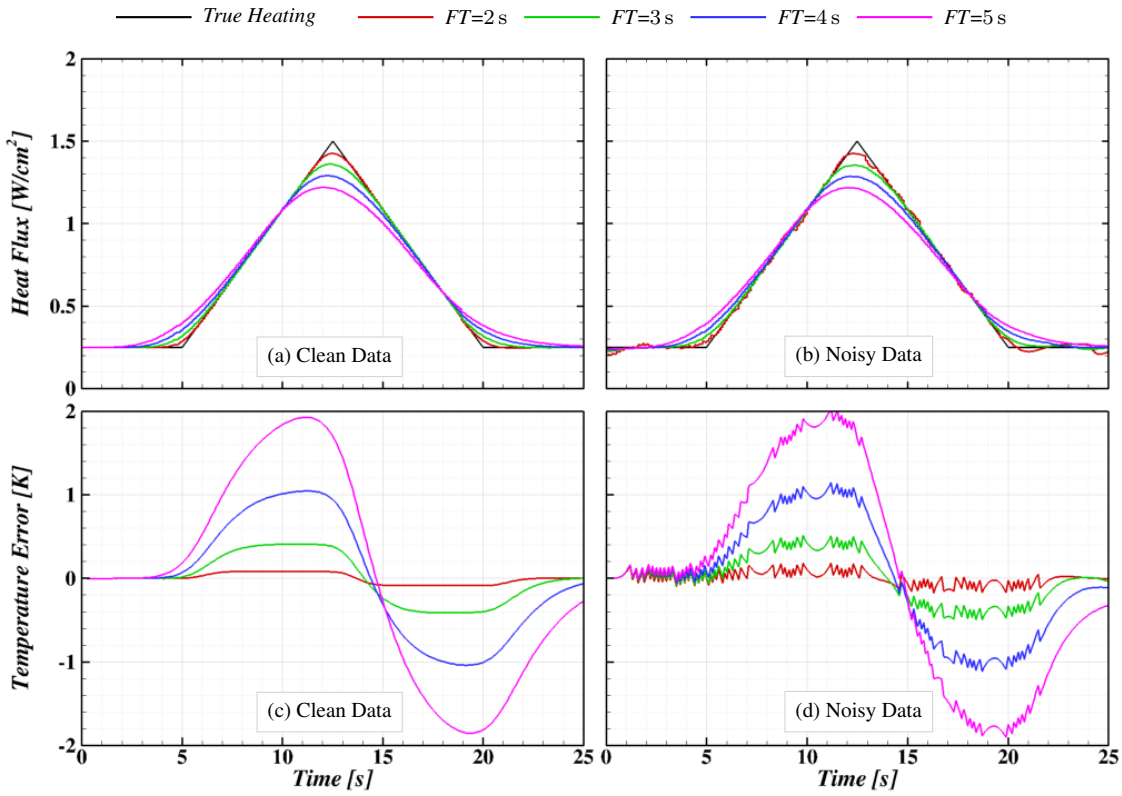

Figure 4.10. Reconstruction results of triangular heating profile using the Future Time algorithm for several future time window lengths, along with residual error in the reconstructed temperatures.

the solution interval that it defines, the FT smoothing produces a tendency for this algorithm to 'lead' a transient heating profile. This can be seen in Figure 4.10(a) and (b) as the peak reconstructed values are seen to gradually shift earlier in time as the future time window is increased. This effect can also be seen in the residual temperature errors shown in 4.10(c) and (d). Recall that the residual temperature error is the reconstructed temperature minus the target temperature, evaluated at each measurement time. The jagged shape of the temperature error in 4.10(d) is due to the finite resolution of the noisy target data, but of more interest is the larger trends seen in both clean and noisy data error plots. The larger departures from zero are referred to here as a *bias* in the reconstructed temperature. In general, the smaller the biases in the reconstruction, the more accurate the heat profile reconstruction is. The large positive bias when the slope of the heat flux profile is positive

and negative bias when the slope of the heat flux profile is negative is characteristic of the reconstruction being driven by behavior farther ahead in time. This character is clearly seen in both 4.10(c) and (d).

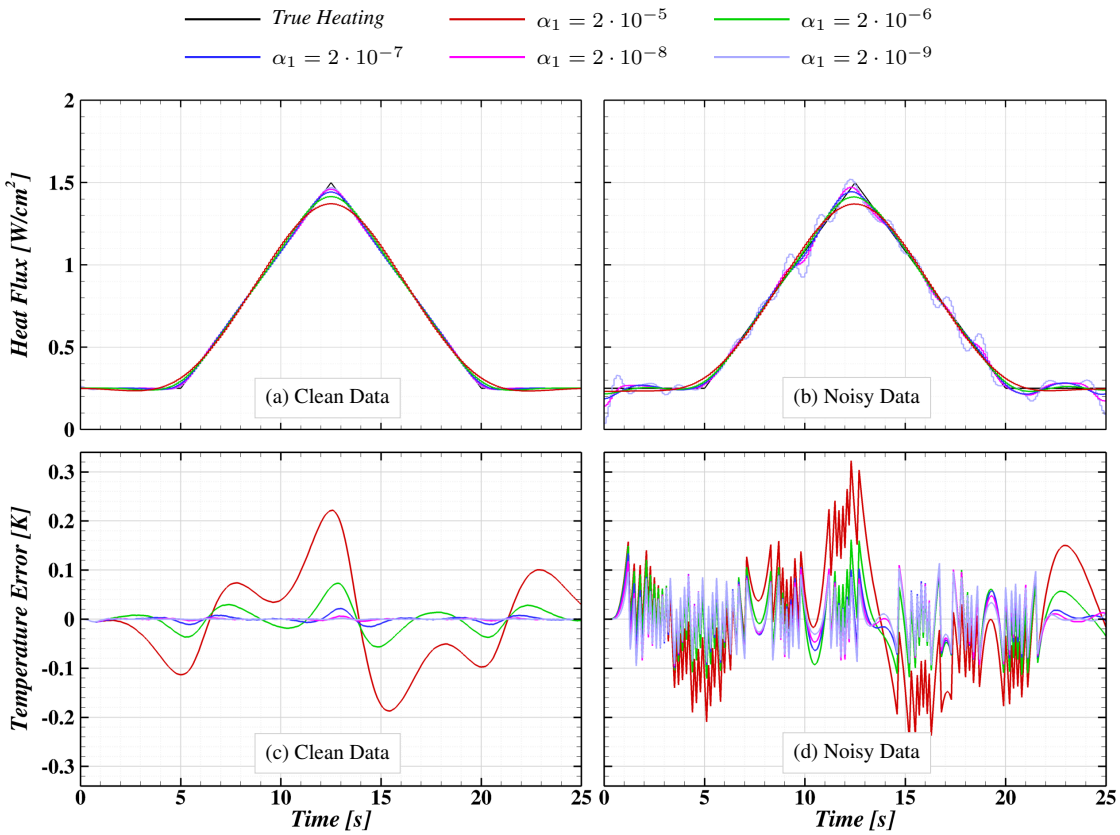

Figure 4.11. Reconstruction results of triangular heating profile using the Whole Domain algorithm for several values of the first-order regularization factor, along with residual error in the reconstructed temperatures. α_1

The WD algorithm results in Figure 4.11 show some interesting contrasts with the FT results. Even with fairly strong regularization, the peak heating is much more accurately resolved, and there is no apparent shift in time. These observations can also be noted in the residual temperature error, as the biases are relatively small for all regularization parameters and do not show the clear bias trends that were seen in the FT algorithm. The WD reconstructions appear to degrade more than the FT due to measurement noise. However, close examination of the higher values of the regularization parameter yield reasonable re-

constructions. This characteristic is identified in the temperature error plot (4.11(d)) by the overall collapse of multiple temperature error curves with no clearly identifiable bias; only regularization parameters greater than 10^{-6} seem to show errors in excess of the precision of the noisy data. Reducing α_1 much below this leads only to more accurate reconstruction of the noise, and spuriously noisy reconstructed flux profiles.

The SSD algorithm results are presented in Figures 4.12 and 4.13. Trends are consistent with before, as the SSD solution tends from the FT to WD solution as the regularization parameter is reduced. The 'S'-shaped nature of the clean data, high regularization WD solution is considerably reduced in the equivalent SSD solutions. For the longer future time window, even with a larger α_1, the time shift in the peak heating is largely removed. When noise is introduced, the SSD results show more effects of the noise than the FT results; however, for higher regularization parameters, they are a little bit smoother than the WD reconstructions. The residual temperature error in general shows the general character of the FT results, albeit at a greatly reduced magnitude, but there are some additional features in the longer future time window results (e.g. near $5\,\mathrm{s}$ and $13\,\mathrm{s}$ in 4.12(h)) that appear in the WD results.

Figure 4.14 shows select reconstructions from each of the three algorithms on clean and noisy data. For this heating profile, the tendency of the SSD to mimic the FT with large regularization and mimic the WD with small regularization is even more apparent than in the square heating pulse. It is also apparent in this figure that the time shift introduced by the FT algorithm is mitigated in the SSD algorithm (provided the regularization is not too strong).

Consideration of the sum-squared temperature error in Figures 4.15 and 4.16 yields many conclusions in common with the square heating case. The sum-squared error in the noisy data is approximately $3.872\,\mathrm{K}^2$ in this case. The WD solution errors are all lower than the error inherent in the noisy temperature trace, except for the case with $\alpha_i = 2 \cdot 10^{-4}$, as are most of the lower regularization SSD cases. The reconstructions in Figures 4.11 and 4.13 do not show the corresponding oscillations in these low-error reconstructions that were seen in the square heat pulse case. This is explained by the nature of the noise

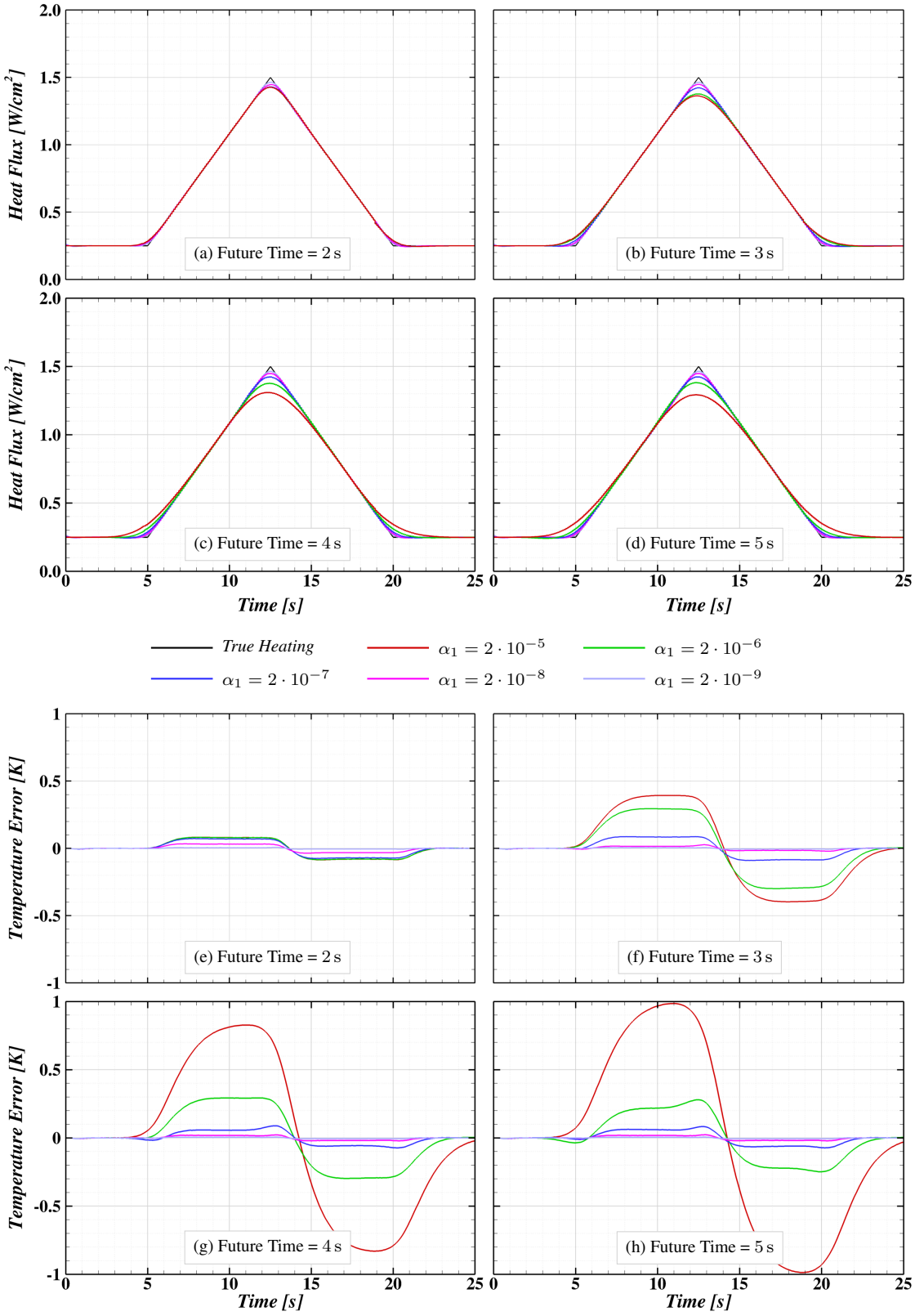

Figure 4.12. Reconstruction results of triangular heating profile using the Sequential Subdomain algorithm with clean temperature data for various values of α_1.

applied in the two cases: truncation of precision in the present case, and additive noise of magnitudes in excess of the precision limit in the square pulse case. The errors in the noisy temperature profile are not zero-biased, but the reconstruction algorithms are all treating them as such. This leads to the sum-squared error plateau appearing lower than the error level of the noisy temperature trace. Finally, the flattening of the WD curve at low α_1 in Figure 4.16(a) is likely due to the limited precision of the clean temperature data used for reconstruction (10 significant digits).

In this test case, with more realistic heating and noise profiles, the SSD algorithm is seen to provide improvements over both FT and WD reconstructions. With sufficiently long future time windows, it is seen to eliminate the tendency of the sequential FT method to 'lead' the true heating profile. It does not show considerable improvement over the WD reconstructions with sufficient regularization, however it does seem to be less affected by noise than the pure WD algorithm. This simple linear case is not optimal for assessing computational effort on real problems, so that is addressed in the next example.

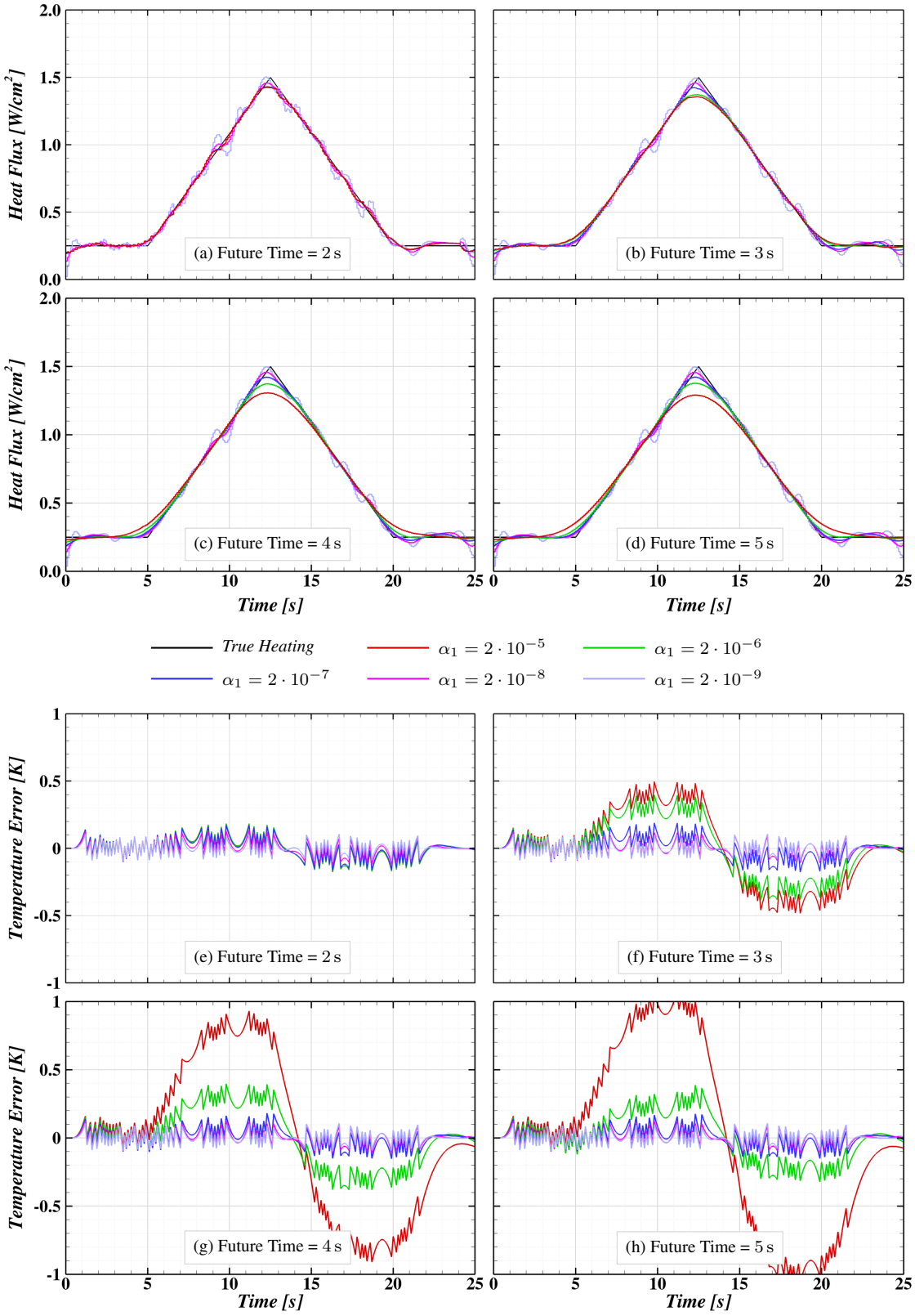

Figure 4.13. Reconstruction results of triangular heating profile using the Sequential Subdomain algorithm with noisy temperature data for various values of α_1.

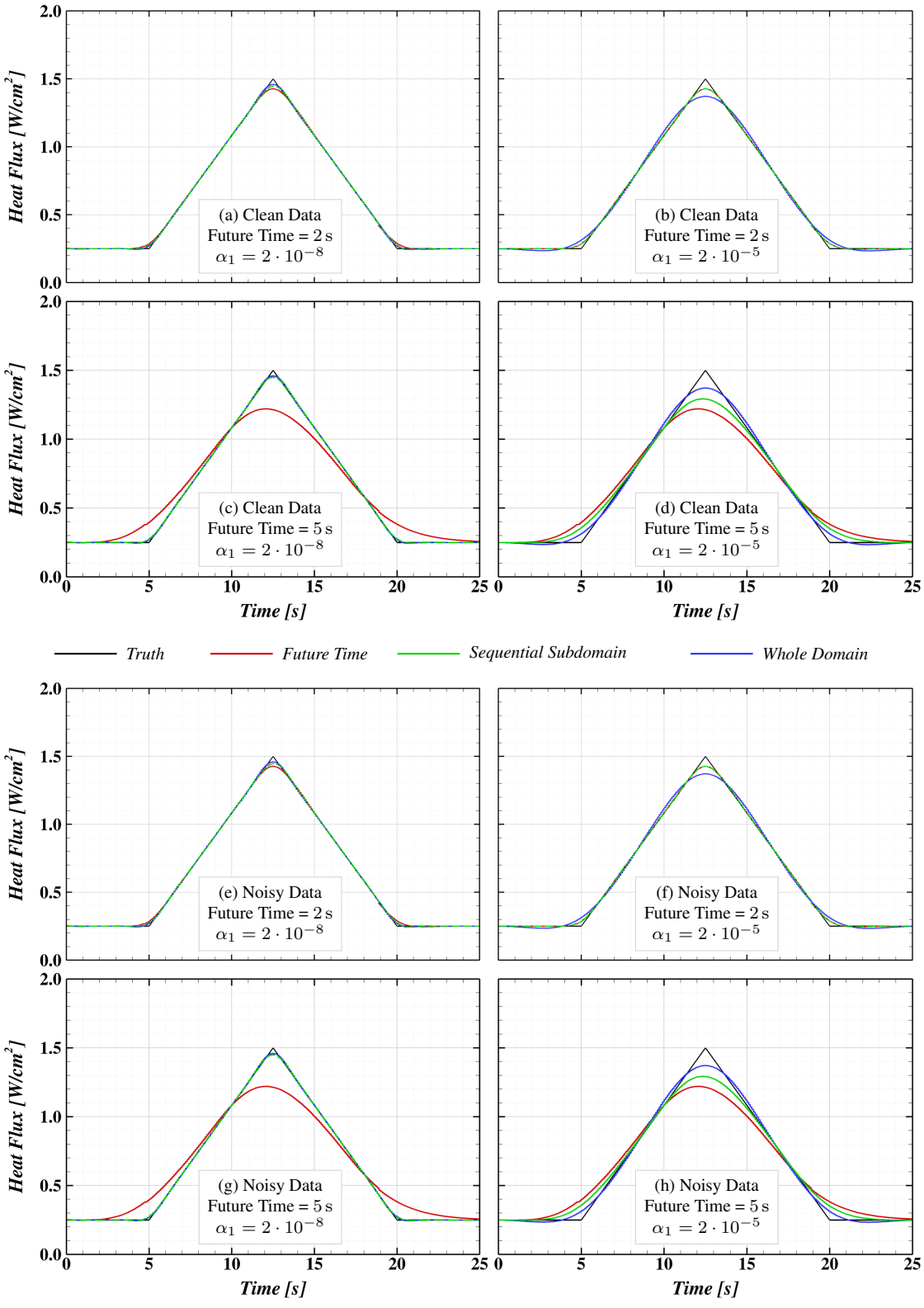

Figure 4.14. Comparison of algorithms on triangular heating profile test case

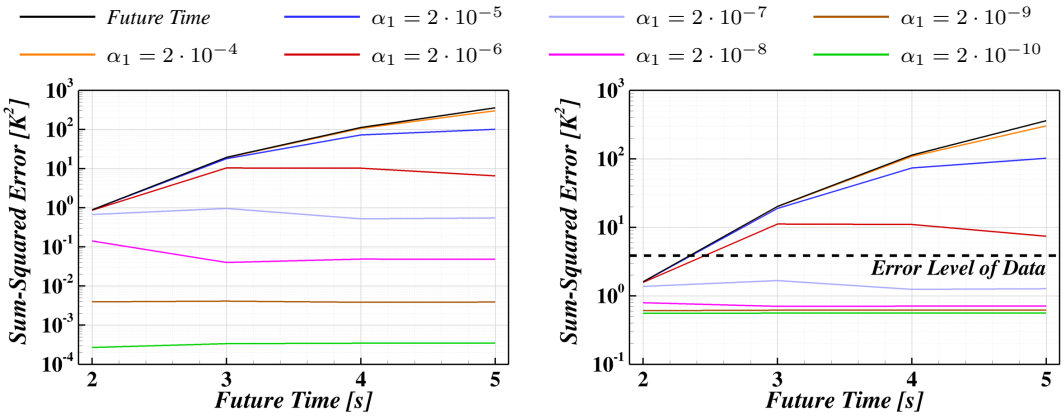

(a) Clean Data (b) Noisy Data

Figure 4.15. Effect of future time window on residual temperature error in triangular pulse reconstructions for FT and SSD algorithms.

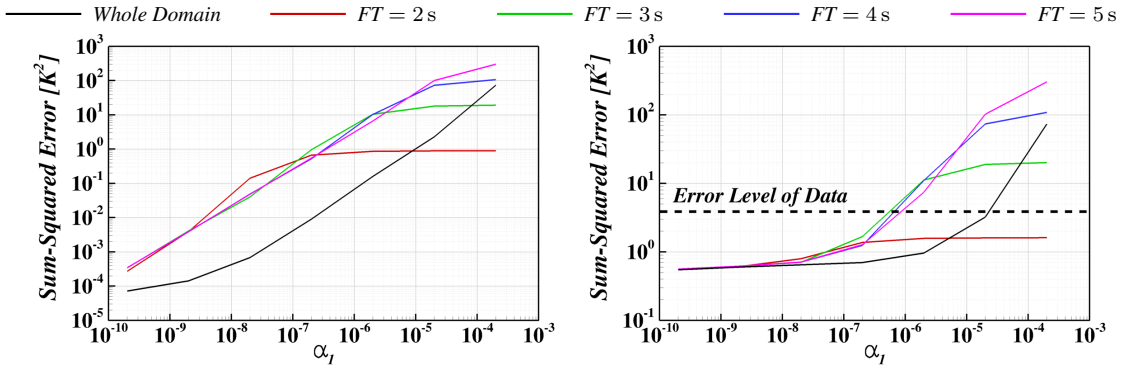

(a) Clean Data (b) Noisy Data

Figure 4.16. Effect of regularization parameter on residual temperature error in triangular pulse reconstructions for SSD and WD algorithms.

4.2 Decomposing TACOT Test Case

The problems considered so far have been linear and iteration has not been required of the SSD or WD algorithms. Recall that an inverse problem is non-linear if the sensitivity coefficients depend on the boundary condition solution. Sequential algorithms such as the FT algorithm generally do not require iteration as the sequential estimates provide an initial guess of the boundary condition solution sufficiently close to the correct value that the sensitivity coefficient evaluation is accurate. The SSD algorithm was designed to take advantage of this to reduce the number of required iterations in a non-linear problem.

To demonstrate the non-linear performance of the SSD algorithm, a 1-D decomposing ablator is considered. Temperature-dependent thermal properties introduce a degree of non-linearity, and decomposing ablators also experience a change of state in response to heating that further complicates the problem. As illustrated in Figure 4.17, a decomposing ablator starts out as a virgin composite material containing volatile and non-volatile constituents. After sufficient heating, volatile constituents begin to thermally decompose into pyrolysis gas in an endothermic reaction. The pyrolysis gas percolates through the remaining non-volatile material (referred to as char) and out of the domain. The thermal properties of the virgin and char states are typically quite different, and a mass-weighted interpolation of properties is generally used in the decomposition zone. All of these effects result in a highly non-linear thermal response, and sensitivity coefficients will have to be evaluated from perturbations very near the correct solution values in order to be accurate.

The domain in this example consists of $40\,\mathrm{mm}$ of TACOT [25] on $3.175\,\mathrm{mm}$ of aluminum ($\rho = 2700\,{}^{\mathrm{kg}}/_{\mathrm{m}^3}$, $k = 237\,{}^{\mathrm{W}}/_{\mathrm{mK}}$, and $C_p = 896.91\,{}^{\mathrm{J}}/_{\mathrm{kgK}}$). TACOT is a fictitious low density charring ablator model that was developed to permit open publication of ablation modeling results. However, the model responds similarly to models for real materials such as PICA and Avcoat and should be sufficiently realistic to assess the performance of *IN-HEAT* on those materials. An array of thermocouples are placed below the heated surface at depths of $3.175\,\mathrm{mm}$, $6.35\,\mathrm{mm}$, and $9.525\,\mathrm{mm}$. Surface recession is neglected in this example to avoid issues of missing data due to thermocouple burn-through.

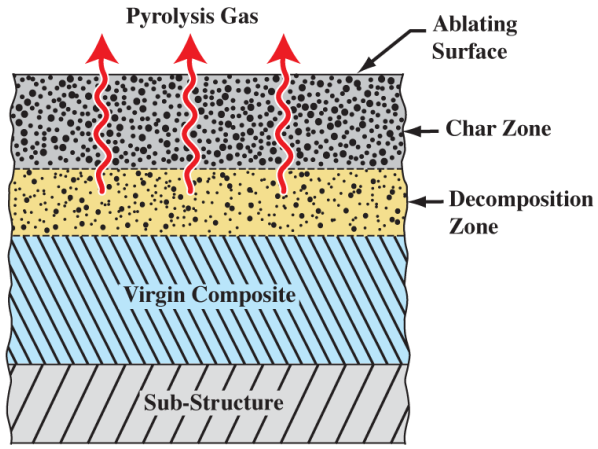

Figure 4.17. Regions of interest in a charring ablator. Used with permission [35].

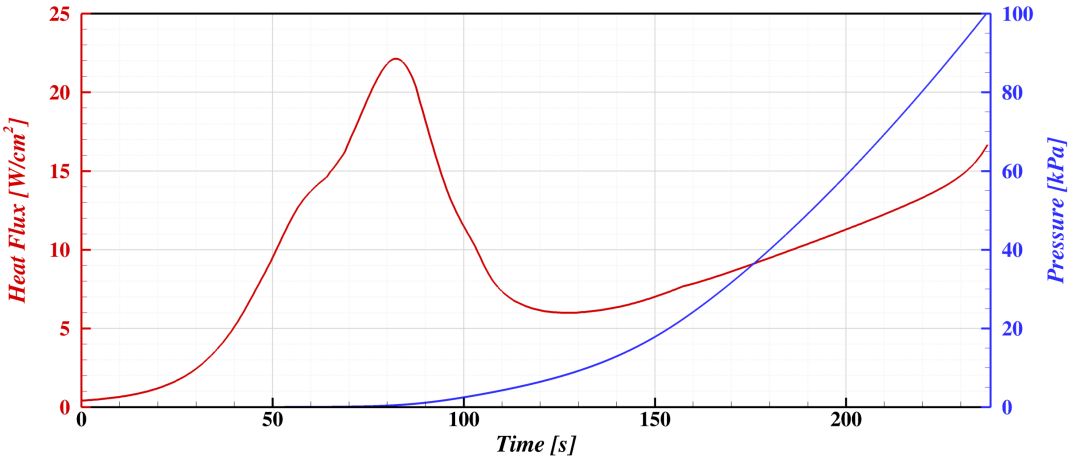

Figure 4.18. Heat flux and pressure boundary conditions for TACOT example problem.

Figure 4.18 shows the heating and pressure profile used as the reference in this example (the back face is assumed impermeable and insulated). The resulting simulated TC measurements are shown in Figure 4.19. Representative sensitivity coefficients for this problem are shown in Figure 4.20. Sensitivity coefficients for 1 s intervals starting every 50 s are shown to illustrate the extent to which the coefficients change through the entry. The heating profile and the decomposition state of the material at depth during the simulated entry (with TC depths indicated) are shown on the same time scale to provide context. Several observations can be made. First, note that TC #1 sensitivity coefficients peak after

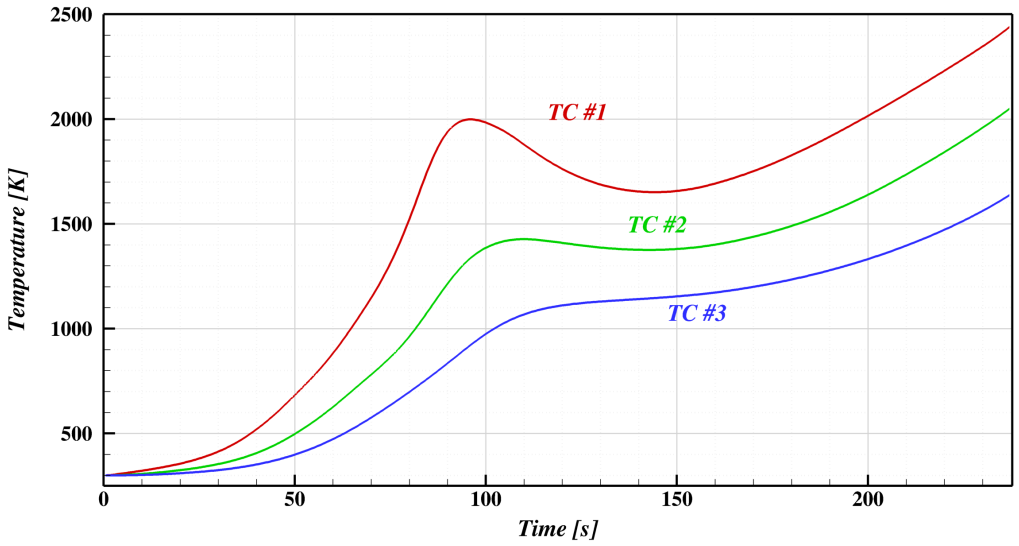

Figure 4.19. Simulated measured temperatures for TACOT example problem.

approximately $4\,\mathrm{s}$ of development time when the TC is in virgin material, and this reduces to approximately $3\,\mathrm{s}$ when the TC is in charred material. TC #2 shows a similar trend with the peak moving from $13\,\mathrm{s}$ in virgin to $10\,\mathrm{s}$ in char. TC #3 peaks after about $25\,\mathrm{s}$ but does not get into enough char by the end of the trajectory to see much of a shift in time. Secondly, the amplitude of the coefficients vary through time, with the TCs being generally more sensitive in virgin material than in charred material. The sensitivity coefficients that start at $50\,\mathrm{s}$ have a somewhat depressed nature because of the ablator decomposition process. Decomposition is typically modeled as a temperature driven endothermic reaction [36]. An increase in heat flux to a decomposing material element will increase the rate of decomposition, which leads to more heat being carried away in the pyrolysis gas and proportionally less heat available to heat up the material element and those below it. The TACOT material model assumes a two-reaction decomposition model, which leads to the two local minima in the TC #1 response (at shallow depths, the reactions advance fast enough for their effects to appear separate). Finally, though it may be intuitively obvious, it is worth repeating that a different heating profile would lead to decomposition occurring at different times and rates, which would yield significantly different sensitivity coefficients, making this inverse problem highly non-linear.

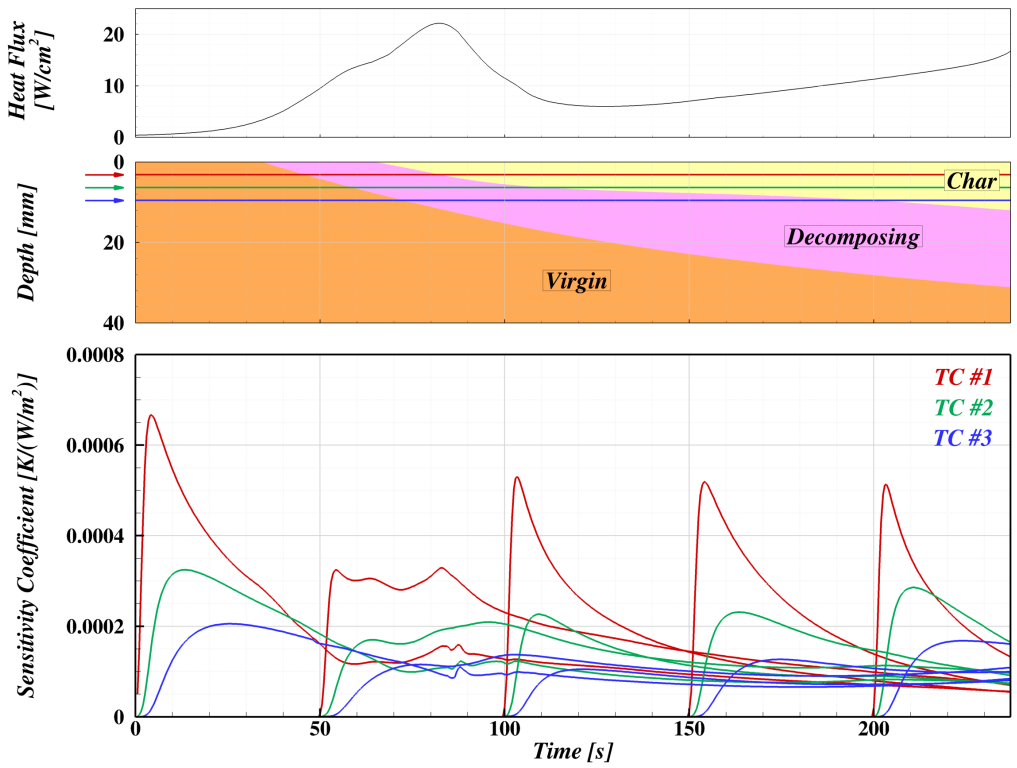

Figure 4.20. TACOT sensitivity coefficients for $1\,\mathrm{s}$ interval perturbations from the true environment relative to applied flux and material decomposition state.

INHEAT is used for the reconstructions presented. *CHAR* settings used in sensitivity coefficient evaluations are consistent with those in the direct problem. The TACOT domain is represented by 300 uniformly spaced elements and $0.5\,\mathrm{s}$ time steps are used in time integration. The domain was initialized to $300\,\mathrm{K}$ and $20\,\mathrm{Pa}$. *INHEAT* was set to use un-scaled sensitivity coefficients with regularization applied to the solution magnitude. All unknown boundary conditions values were initialized to $10\,\mathrm{W/m^2}$ with a minimum finite-difference perturbation of $5\,\mathrm{W/m^2}$ (nominal perturbations are 0.1% of the boundary condition value).

Reconstructions using the Future Time algorithm are shown in Figure 4.21. In Figure 4.21(a), reconstructions based on TC #1 are shown for several values of the future time window. As expected from previous examples, longer future time windows lead to overly-smoothed peaks. Figure 4.21(b) shows reconstructions based on the three different TCs holding the future time window constant at $8\,\mathrm{s}$. In this instance, the results may seem

counter-intuitive, as the deepest TC produces the most accurate reconstruction. However, if we consider the differences in development time of the sensitivity coefficients at each TC, it becomes apparent that $8\,\mathrm{s}$ is too long for the shallow TC, but more appropriate for the deeper ones.

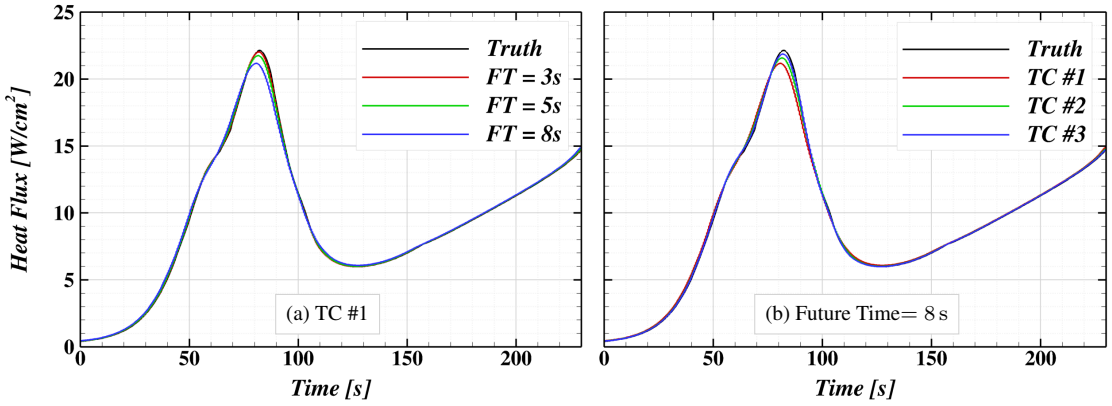

Figure 4.21. Reconstructions of TACOT test case using Future Time algorithm using different TCs and future time windows.

Reconstructions using the Whole Domain algorithm are shown in Figure 4.22. Given the dependance of the sensitivity coefficients on the unknown solution, the regularization parameter was specified using `a_1` from Equation 3.18 as 1^{st}-order regularization is used (recall that this means the actual regularization parameter is taken to be a factor of `a_1` of the largest element in the sensitivity coefficient matrix). Figure 4.22(a) shows the reconstructions obtained from each of the three TCs with `a_1` $= 1.0$. Visible differences are apparent, with the regularization having a much stronger effect on reconstructions based on the deeper TCs. Figure 4.22(b), in contrast, shows all three reconstructions collapsing to the resolution of the plot with `a_1` $= 0.001$ (three orders of magnitude less regularization).

Reconstructions using the Sequential Subdomain algorithm are shown in Figure 4.23. All successful reconstructions using future time windows of $3\,\mathrm{s}$, $5\,\mathrm{s}$, and $8\,\mathrm{s}$, each with values of the 1^{st}-order regularization scaling parameter `a_1` of 1.0, 0.1, 0.01, and 0.001, are shown on the plot with all virtually collapsing onto a single line at this resolution. Some combinations of future time window and regularization scaling parameter (noted later)

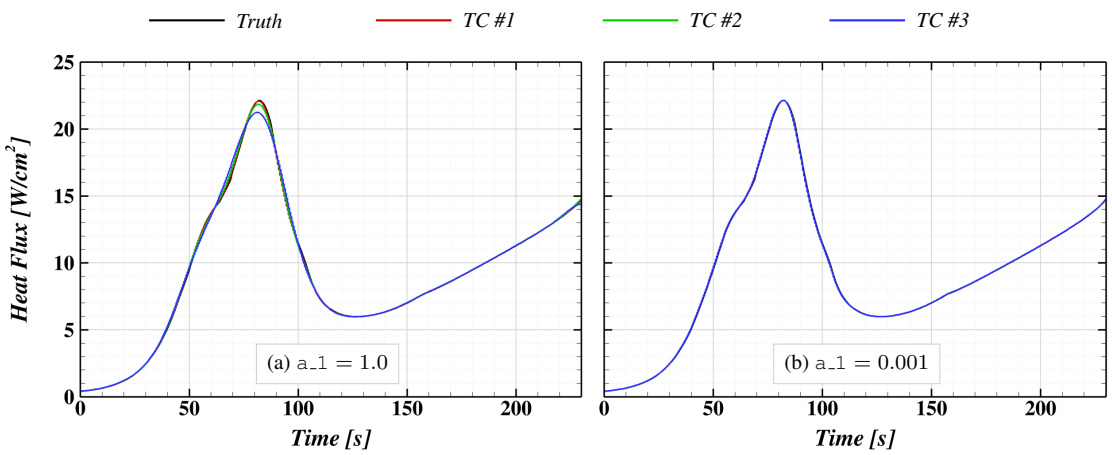

Figure 4.22. Reconstructions of TACOT test case using Whole Domain algorithm using different TCs and regularization scaling parameters.

yielded insufficient smoothing and were either clearly unstable or resulted in *CHAR/INHEAT* aborting when material property table bounds were exceeded. While both of the individual FT and WD algorithms show some sensitivity to the input parameters, it is perhaps interesting to note that the SSD is much less sensitive to the input parameters. This insensitivity is a desirable feature of the SSD, as this suggests that the reconstruction results may be less sensitive to the particular choices an analyst may make in performing the reconstruction. A common criticism of inverse reconstructions, particularly ones using algorithms with many variable parameters, is that two different analysts are likely to arrive at different results using the same data. Figure 4.23 suggests that the SSD algorithm with the regularization scaling method of Equation 3.18 reduces this likelihood, at least for cases with minimal data noise.

The sum-squared temperature error of each presented reconstruction is shown in Table 4.1 and the maximum instantaneous relative solution error, $\left\| \frac{q_{m,reconstructed}}{q_{m,truth}} - 1 \right\|_\infty$ over the first $200\,\mathrm{s}$ of the trajectory[1], is shown in Table 4.2. These tables show variation in the error metric as a function of the future time window length across the horizontal dimension (with the WD results in the red-highlighted column) and the regularization scaling

[1]The final $37\,\mathrm{s}$ of the trajectory were discarded for this assessment as the end of the reconstructions can become erratic as later coefficients do not have time to fully develop.

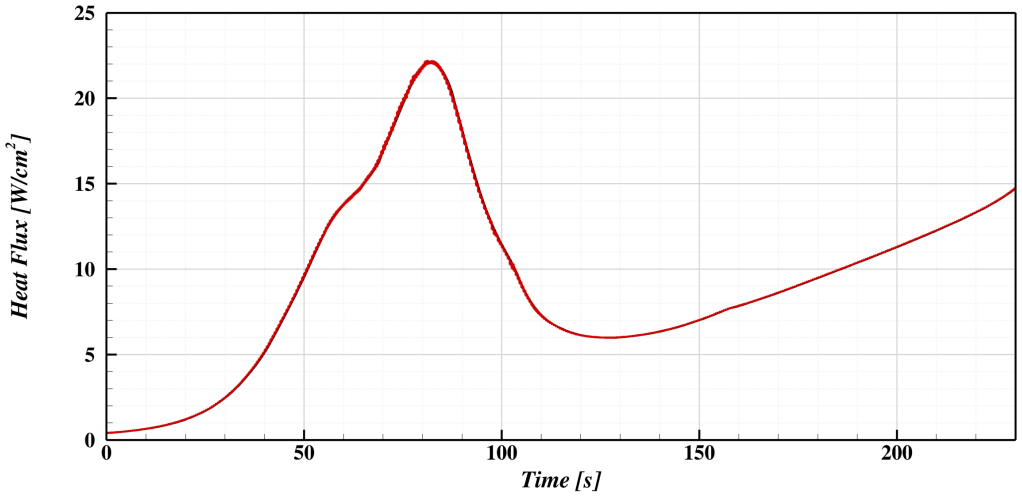

Figure 4.23. Reconstructions of TACOT test case using Sequential Subdomain algorithm. All successful reconstructions of TCs 1, 2, and 3 with future time windows of $3, 5,$ and $8\,\mathrm{s}$ and values of $\mathtt{a\_1} = 1.0, 0.1, 0.01,$ and 0.001 are included, with the collapse showing insensitivity to reconstruction parameters.

parameter in the vertical dimension (with the FT results in the gray-highlighted row), with a separate table for reconstructions based on each TC. In general, trends are as would be expected: increasing smoothing (either by increasing the future time window or regularization parameter) increases the error for this case with no measurement noise. Even without explicitly added noise[2], reconstructions based on the deeper TCs became unstable and failed to complete for FT and SSD reconstructions with shorter future time windows. A stark observation from these tables is that the SSD–if it converges–produces a result that is more accurate than WD and FT solutions with the same reconstruction inputs. Furthermore, there is less variation in the accuracy of the results across the same spread of reconstruction inputs for the SSD reconstructions than for the FT and WD algorithms.

Part of the reason that the SSD performs better than the other algorithms is that the actual regularization parameter derived from Equation 3.18 is different for the SSD and the WD algorithms for the same value of $\mathtt{a\_1}$. Because α_1 is made a function of the sensitivity coefficients, differences in the development time for the different algorithms (and different

[2]Note that even though explicit noise is not added, there is still some noise introduced by rounding the measurement data to 10 significant digits as was done in this example

Table 4.1. Sum-squared temperature error [K^2] in reconstructions of TACOT example.

(a) Reconstructions using TC 1

		WD	$FT = 3\,\mathrm{s}$	$FT = 5\,\mathrm{s}$	$FT = 8\,\mathrm{s}$
FT algorithm			18.90	73.36	211.5
SSD	a_1 = 0.001	0.102	0.076	0.094	0.144
	a_1 = 0.01	0.377	0.169	0.534	0.703
	a_1 = 0.1	1.514	1.600	2.012	3.119
	a_1 = 1.0	7.889	9.696	10.58	11.91

(b) Reconstructions using TC 2

		WD	$FT = 3\,\mathrm{s}$	$FT = 5\,\mathrm{s}$	$FT = 8\,\mathrm{s}$
FT algorithm			1.086	8.333	41.22
SSD	a_1 = 0.001	1.464	Failed	0.035	0.058
	a_1 = 0.01	0.292	0.043	0.055	0.294
	a_1 = 0.1	1.463	0.385	0.520	0.858
	a_1 = 1.0	8.826	0.923	3.584	4.283

(c) Reconstructions using TC 3

		WD	$FT = 3\,\mathrm{s}$	$FT = 5\,\mathrm{s}$	$FT = 8\,\mathrm{s}$
FT algorithm			Failed	0.744	5.424
SSD	a_1 = 0.001	0.062	Failed	Failed	0.022
	a_1 = 0.01	0.306	Failed	Failed	0.053
	a_1 = 0.1	1.828	Failed	Failed	0.199
	a_1 = 1.0	8.405	Failed	0.540	1.602

future time windows within the SSD) can lead to different values of α_1. Furthermore, the SSD will derive α_1 based only on sensitivity coefficients within the future time window, whereas the WD will derive α_1 based on the whole time domain. As is seen in Figure 4.20, the peak values occur early and drive the values for the WD reconstructions, but the SSD can pick a value based on the solution intervals it is dealing with in a particular local solution. The actual values of α_1 used in the reconstructions using $\texttt{a\_1} = 1.0$ are shown in Figure 4.24. For all three TCs, the SSD regularization parameter is one to three orders of magnitude lower than the WD regularization parameter, with greater discrepancies at deeper TCs where the shorter future time windows do not allow the sensitivity coefficients to fully develop. The SSD regularization parameter is also seen to vary by an order of

Table 4.2. Maximum instantaneous error in reconstructed heat flux for TACOT example.

(a) Reconstructions using TC 1

		WD	$FT = 3\,\mathrm{s}$	$FT = 5\,\mathrm{s}$	$FT = 8\,\mathrm{s}$
FT algorithm			2.3%	4.7%	10.0%
SSD	a_1 = 0.001	0.3%	0.1%	0.2%	0.2%
	a_1 = 0.01	0.4%	0.2%	0.3%	0.3%
	a_1 = 0.1	0.9%	0.7%	0.4%	0.6%
	a_1 = 1.0	2.4%	1.7%	2.2%	1.4%

(b) Reconstructions using TC 2

		WD	$FT = 3\,\mathrm{s}$	$FT = 5\,\mathrm{s}$	$FT = 8\,\mathrm{s}$
FT algorithm			1.9%	3.1%	6.7%
SSD	a_1 = 0.001	0.5%	Failed	0.3%	0.3%
	a_1 = 0.01	0.8%	0.9%	0.3%	0.4%
	a_1 = 0.1	1.8%	0.9%	1.0%	0.5%
	a_1 = 1.0	3.7%	1.0%	2.5%	2.8%

(c) Reconstructions using TC 3

		WD	$FT = 3\,\mathrm{s}$	$FT = 5\,\mathrm{s}$	$FT = 8\,\mathrm{s}$
FT algorithm			Failed	2.3%	4.5%
SSD	a_1 = 0.001	0.6%	Failed	Failed	1.1%
	a_1 = 0.01	1.4%	Failed	Failed	0.5%
	a_1 = 0.1	2.7%	Failed	Failed	0.9%
	a_1 = 1.0	5.2%	Failed	1.7%	3.6%

magnitude or more during the course of a reconstruction. Note that all presented results were taken from the final non-linear iteration of a given local solution. As the sensitivity coefficients change through the non-linear iterations, different α_1 values are used in each iteration. Understanding this fact, it perhaps makes more sense to compare the accuracy of the SSD reconstruction of TC 1 with an $8\,\mathrm{s}$ future time window and $\mathtt{a\_1} = 1.0$ to the WD reconstruction of TC 1 with $\mathtt{a\_1} = 0.1$ which brings the accuracy of the SSD more in line with observations from the previous sections.

A goal of the SSD was to reduce the computational expense of non-linear inverse problems. Thus we will now consider the convergence behavior of the SSD and WD implementations in *INHEAT*. Figure 4.25 shows the non-linear convergence of the residual temper-

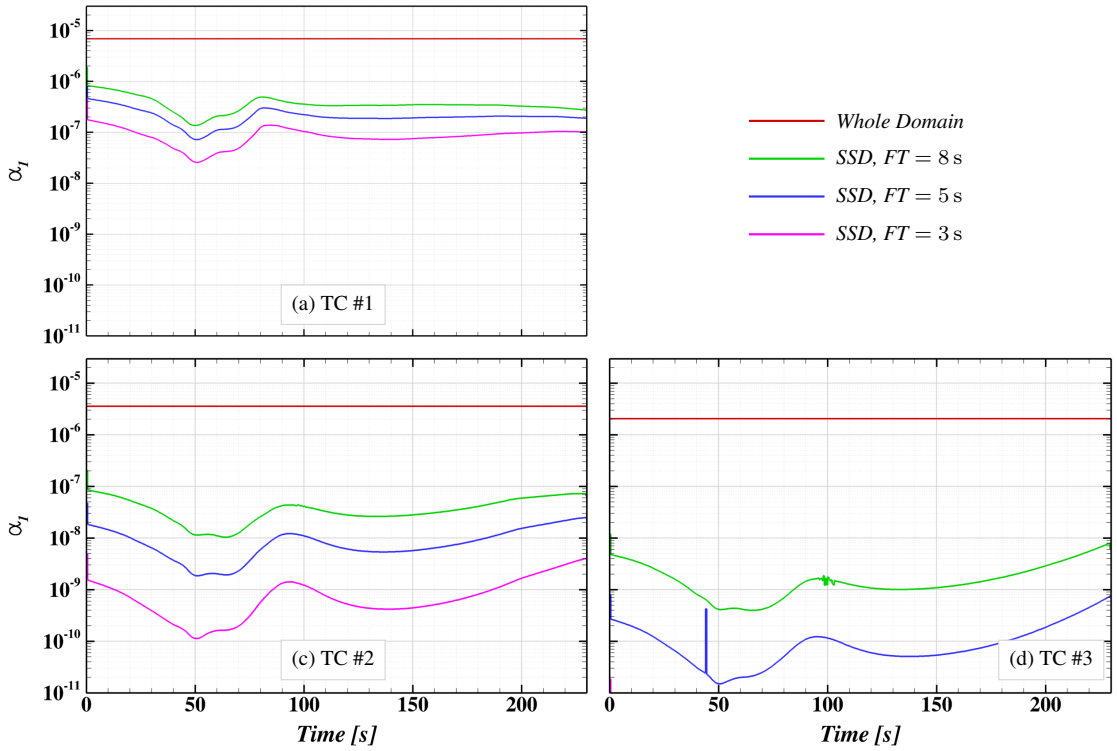

Figure 4.24. Regularization parameter value for WD and SSD reconstructions for `a_1` = 1.0.

ature error and the normalized update vector $\|\Delta\mathbf{q}\|_2$ (normalized by the value at the first iteration). All local solutions are run for 30 iterations regardless of convergence level to show the full behavior. Both plots show the error metric at the next iteration plotted against the error metric at the current iteration. As the Taylor series approximation for the modeled temperature (Equation 3.4) which introduces the sensitivity coefficients that form the Jacobian matrix is 2^{nd}-order accurate, it is expected that points on this plot for a solution in the asymptotic range with exact Jacobians should move down and to the left parallel to the 2^{nd}-order reference line until the precision limit is reached.

For the sum-squared temperature error convergence in Figure 4.25(a), the early iterations loosely follow the 2^{nd}-order reference line until the limit allowed by the regularization is reached, at which point the iterations stall (denoted by points on the diagonal of the plot). It is expected that the final converged level of residual error varies according the magnitude

of the regularization scaling parameter as the sum-squared temperature error is only a part of the non-linear system residual (Equation 3.7) which is actually being driven to zero in the iteration loop. The normalized update vector trend in Figure 4.25(b), however, does not show any significant difference in convergence behavior based on the regularization scaling parameter. Similar nearly 2^{nd}-order behavior is seen in the normalized update vector, however all solutions appear to have a larger error at the second iteration than the first, before beginning to converge at nearly 2^{nd}-order rates. Neither error metric shows inconsistent or distinct behavior for reconstructions based on different TCs.

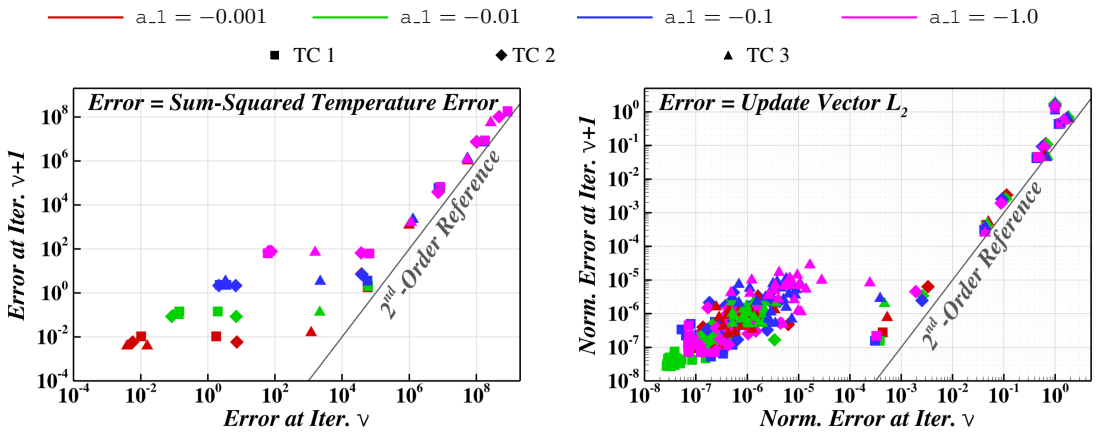

(a) Temperature Error

(b) Update Vector Magnitude

Figure 4.25. Non-linear convergence for WD reconstructions.

Exact 2^{nd}-order convergence is expected if Jacobians are exact; however, the sensitivity coefficients that compose the Jacobian matrix are evaluated by a finite-difference approximation, so it is not anticipated that exact 2^{nd}-order convergence can be obtained. The default method used for reconstructions in Figure 4.25 is to perturb the current boundary condition estimate by $\pm 0.1\%$ of the currently estimated value. To assess the sensitivity of this assumption, results using two additional perturbation levels are shown in Figure 4.26, with $\pm 5\%$ perturbations in green and $\pm 0.01\%$ perturbations in blue. Neither perturbation level significantly changes the rate of convergence. However, the normalized update vector appears to stall at a different value in Figure 4.26(b) as the magnitude of the first iteration (the normalizing iteration) is different for the three cases. As the final accuracy of the three

cases are virtually identical (Figure 4.26(a)), the reconstruction is not strongly dependent on the perturbation sizes of this range.

The smaller perturbation appears to suffer more of a setback at the first iteration than the others do, although it still reaches convergence in a similar number of iterations. This can be explained by the second requirement of well-behaved 2^{nd}-order convergence: the solution must be "close" to the correct answer before 2^{nd}-order convergence is expected. In this example, the solution is initialized to a uniform value of $10\,\mathrm{W/m^2}$, which is not very near the correct solution. At this low level of heating, decomposition does not begin at the appropriate time, and most of the sensitivity coefficients are more like virgin coefficients than decomposing or char coefficients. However, the heat flux profile that results from that iteration *is* sufficient to cause decomposition to occur, so the sensitivity coefficients computed in the second iteration are more representative of the true converged coefficients and well-behaved non-linear convergence results. This can be seen in Figure 4.27, where the solutions obtained on the first three iterations are plotted relative to their respective initial guess. Using an initial guess with enough heating to cause decomposition yields much more rapid convergence. The convergence behavior of the solution shown in Figure 4.27(b) is shown in Figure 4.26 as the magenta line, where the initial increase in the solution update vector magnitude is seen to be absent.

Now that the general non-linear convergence trends of an inverse ablation problem are better understood, the specific behavior of the SSD is considered. Figure 4.28 shows the sum-squared temperature error and normalized update vector convergence plots for the SSD case with $\boldsymbol{FT} = 8\,\mathrm{s}$ and $\mathtt{a\_1} = -0.001$. These plots show the accumulated behavior of all local solutions (recall the SSD involves 473 sequential non-linear solutions of up to 16 unknowns instead of 1 non-linear solution with 473 unknowns) as points on these plots. One particular solution, $m = 83$, has been shown with lines connecting the iterations to show the general behavior. Even with all the data plotted in this way, it is apparent that there are only a few local solutions that experience much of any improvement with more than one or two non-linear iterations. The update vector generally sees greater than 3 orders of magnitude reduction between the first and second iteration and the solutions move out

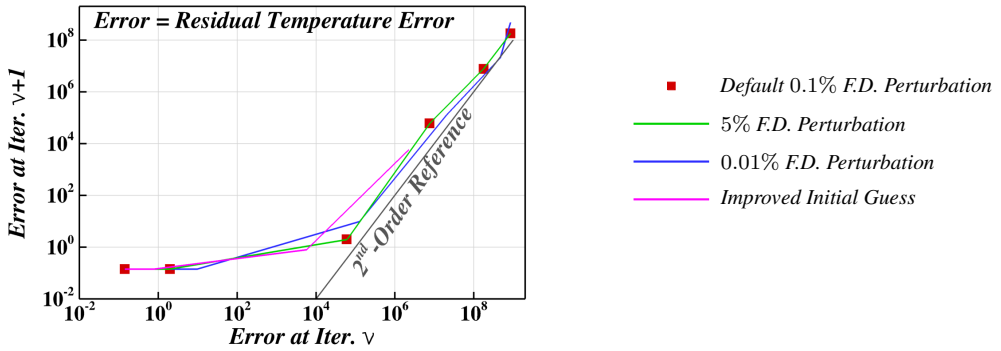

(a) Temperature Error

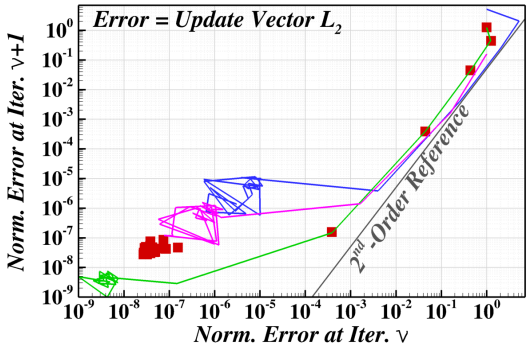

(b) Update Vector Magnitude

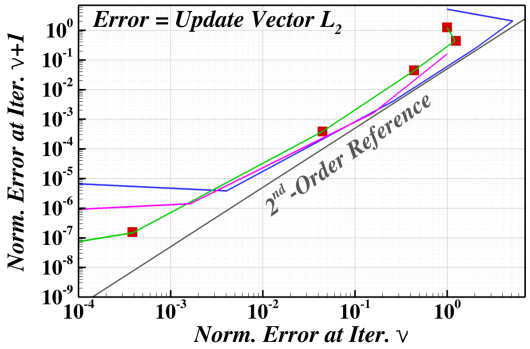

(c) Update Vector Magnitude Detail

Figure 4.26. Non-linear convergence sensitivities for WD reconstruction of TC 1 with $\texttt{a\_1} = 0.01$.

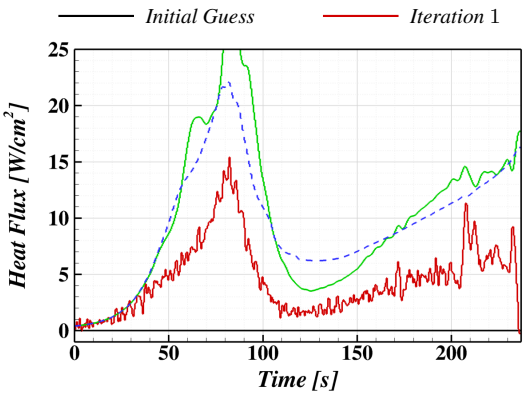

(a) Constant Initial Guess

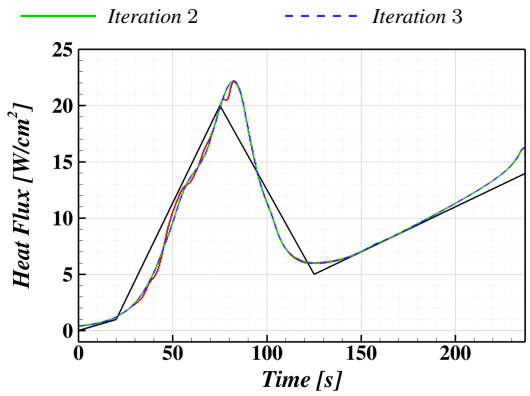

(b) Improved Initial Guess

Figure 4.27. Solution convergence for WD reconstruction of TC 1 with $\texttt{a\_1} = 0.01$.

to the diagonal. This interpretation is confirmed by looking at Figure 4.29 which shows the number of iterations required at each step to reach different levels of convergence (defined by $\left\| \frac{\Delta \mathbf{q}}{\mathbf{q}} \right\|_2$ dropping below the specified level). It indicates that for nearly every non-linear solution, three iterations are all that is required to converge the solution to better than 6 significant digits.

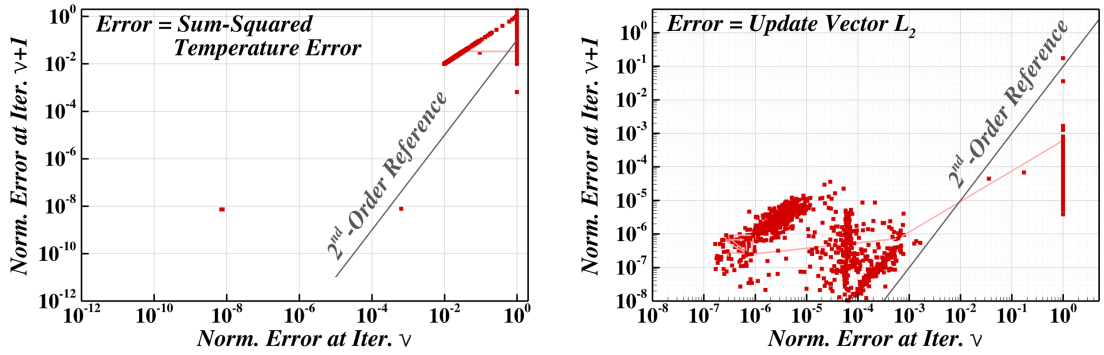

(a) Temperature Error

(b) Update Vector Magnitude

Figure 4.28. Non-linear convergence for SSD reconstruction of TC 1 with a_1 = 0.001.

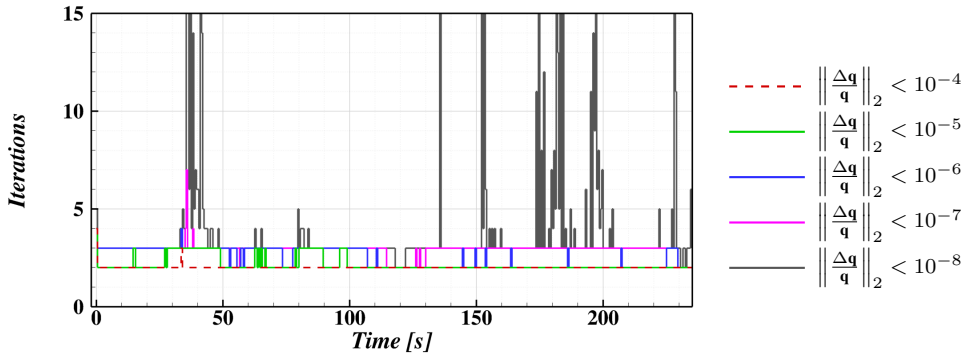

Figure 4.29. Non-linear iterations used in SSD reconstruction of TC 1 with a_1 = 0.001 as a function of the scaled solution convergence tolerance.

The final aspect the SSD was developed to improve is the amount of computational effort required to perform a reconstruction. Figure 4.30 shows the accumulated simulated time (AST) for each of the reconstructions presented in this section. Recall that the AST quantifies the total amount of time (simulation time, not CPU or wall time) that must be

computed by the direct solver to evaluate the sensitivity coefficients. Figure 4.30(a) compares the FT, SSD, and WD algorithms as a function of the length of the future time window. For this case, the SSD required fewer simulated seconds than the WD algorithms when both algorithms take the same number of non-linear iterations (30 in this instance). Figure 4.30(b) shows the AST required for sensitivity coefficient evaluation if convergence tolerances are used to limit iteration. The WD solutions plateau to a value of $\left\| \frac{\Delta \mathbf{q}}{\mathbf{q}} \right\|_\infty$ between 10^{-5} and 10^{-6} in 6 iterations, so cases with tolerances of 10^{-5} and greater see a factor of 5 reduction in effort (from 30 to 6 non-linear iterations). The SSD algorithm shows a wider spread in the plateau levels, but iterations can be limited with convergence tolerances above 10^{-8}.

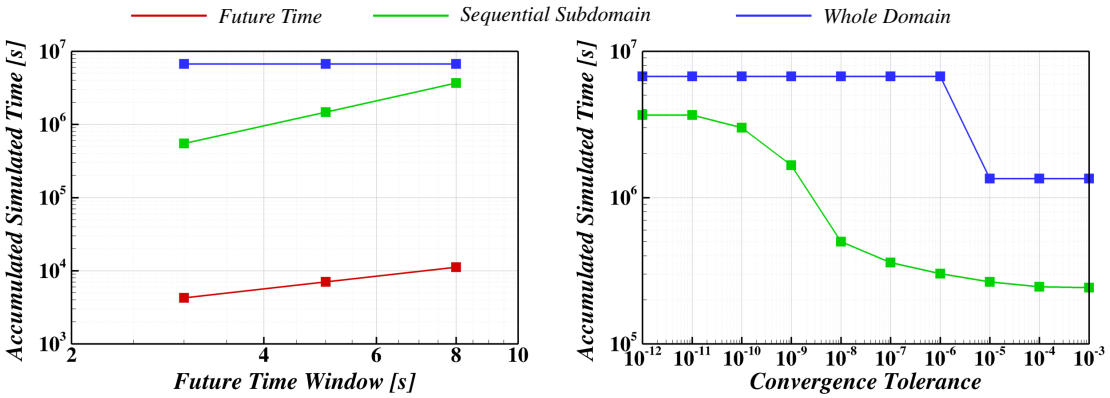

(a) Algorithm Comparison

(b) SSD, $FT = 8\,\mathrm{s}$

Figure 4.30. Amount of time simulated to evaluate sensitivity coefficients.

For this example, the SSD clearly requires less overall computational effort. This is not necessarily reflected in Table 4.3 which shows the wall time in hours for WD and SSD reconstructions with loose and tight non-linear convergence tolerances. For the loose convergence tolerance of 10^{-3}, the difference in simulated time results in faster SSD reconstructions; however, for the tighter tolerance where both WD and SSD run the full 30 non-linear iterations, the WD is a bit faster. This can be attributed to the embarrassingly-parallel nature of the WD algorithm and the limited parallel scalability of the SSD algorithm due to its sequential nature. Recall that in the present implementation, the sensitivity

coefficient matrix for any local solution includes an independent column for each unknown considered in the local solution. The present implementation utilizes a threading approach to parallelize the sensitivity coefficient matrix evaluation whereby a user-specified number of threads independently evaluate future time tracks needed to compute each column of the matrix (for central finite-differences, two independent future time track evaluations produce a single column of the matrix). For the WD reconstructions, there are 473 columns (946 future time tracks) that can be each evaluated using a single CPU, thereby eliminating parallel communication during the evaluation of an individual track. For SSD reconstructions with a future time window of $8\,\mathrm{s}$, there are only 16 independent columns (32 tracks), so no more than 32 threads can be used. Assigning more CPUs than threads means that multiple CPUs are assigned to some threads introducing parallel communication in the solution of each future time track. Furthermore, the local solution must be completed before the sensitivity coefficients for the next local solution can be processed[3]. As such, if a large number of CPUs are available and the total number of unknowns is manageable (the present implementation solves the linear system of each local solution on a single CPU, limiting the total number of unknowns), a WD reconstruction could end up more computationally efficient, even if it is not computationally cheaper.

Table 4.3. TACOT example reconstruction wall time [hours].

(a) Reconstructions using $\left\| \frac{\Delta \mathbf{q}}{\mathbf{q}} \right\|_2 < 10^{-3}$

CPUs	WD	SSD	
		32 threads	16 threads
16	2.2	-	0.63
32	1.12	0.43	0.40
64	0.59	0.26	0.27

(b) Reconstructions using $\left\| \frac{\Delta \mathbf{q}}{\mathbf{q}} \right\|_2 < 10^{-12}$

CPUs	WD	SSD	
		32 threads	16 threads
16	11.4	-	9.7
32	5.9	6.4	5.9
64	3.1	3.9	4.0

Computed on cluster utilizing Intel Westmere X5650 processors (12 per node) running at 2.67 GHz with 24 GB of RAM per node.

[3]One additional un-perturbed track evaluation is needed for each local solution, and this must be evaluated before sensitivity coefficient evaluations can begin. The CPU/thread allocation is not altered for this evaluation, so a single thread performs this. This additional serial operation leads to the 32 thread, 32 CPU computations taking longer than the 16 thread, 32 CPU reconstructions in Table 4.3, since only a single CPU performs the serial operation as opposed to two.

This example investigated the performance of the *INHEAT* implementation on a non-linear inverse problem. The SSD algorithm using the regularization scaling parameter `a_1` (Equation 3.18) is shown to provide accurate reconstructions with a higher degree of input parameter independence than the FT or WD algorithms due to the ability to scale the regularization to the level needed in each local solution. The non-linear convergence behavior of the *INHEAT* implementation is shown to have nearly second-order convergence, as would be expected, and the SSD algorithm is shown to require fewer non-linear iterations in each local solution than the WD requires. The resulting increase in computational efficiency is shown, although it is noted that due to the limited parallel scalability of the SSD algorithm, this efficiency may not lead to reduced wall-time if many CPUs are available for the analysis.

4.3 High-frequency Transient Event Reconstruction

Transient events which significantly decrease the representative time-scale of a heating profile are not uncommon in flight testing, and in some instances it would be desirable to be able to accurately characterize the heating profile during these events. In this example, the transient event in question is the aerodynamic heating augmentation due to the firing of a nearby steering jet.

Rapid changes in relevant time-scale can pose a challenge to IHCP algorithms, particularly with regards to the regularization approaches employed. Transient events of this nature can increase the required reconstruction frequency and greatly increase the overall number of unknowns. While a WD algorithm would generally be most able to cope with the changing time-scales, the number of total unknowns can increase to a point that would make solution of the problem infeasible without special treatment of the numerical solution. In this situation, the SSD algorithm provides a means of obtaining a nearly WD-quality result without the computational expense or complexity of solving the whole problem simultaneously.

In examples shown to this point, the heat flux on the boundary has been the parameter evaluated in the inverse solution, as this is generally how the IHCP is presented in the literature. However, for practical problems, the boundary heat flux can be taken as the result of a model combining a number of parameters, one of which may be the solution variable for the inverse problem. In this instance, the boundary condition is defined in terms of the film coefficient model given by

$$\dot{q}'' = C_h^*(H_{rec} - H_w), \tag{4.1}$$

where $\dot{q}''$ is the heat flux, C_h^* is the film coefficient, H_{rec} is the recovery enthalpy, and H_w is the wall enthalpy. The film coefficient is the reconstructed term. The recovery enthalpy is assumed to be known, and the wall enthalpy is taken to be the enthalpy of an equilibrium mixture of air at the surface pressure (assumed known) and temperature (a result of the thermal response). Aside from the requirement that the other terms in the model (recovery enthalpy, surface pressure) be known, it is shown that this model affects the IHCP regularization in a manner that makes standard WD algorithms yield undesirable results that can be mitigated by the SSD algorithm.

The material properties assumed in this example are representative of a reusable silica tile like those used on the heatshield of the Space Shuttle Orbiter ($25.4\,\mathrm{mm}$ of LI-900 coated with $0.5\,\mathrm{mm}$ of black reaction-cured glass (RCG), with material properties obtained from Williams et al. [37]). A film coefficient boundary condition is assumed on the RCG surface with the film coefficient and recovery enthalpy shown in Figure 4.31. Each of the film coefficient spikes represent augmented heating levels caused by steering jet firings. The firings are arbitrarily assumed to augment the nominal film coefficient by a factor of 2 for $0.5\,\mathrm{s}$, with the middle $0.1\,\mathrm{s}$ being augmented by a total factor of 3.2 to simulate an overlapping firing of a second jet. The surface is assumed to reradiate to a $300\,\mathrm{K}$ far field, and the surface pressure used in the wall enthalpy calculation is shown in Figure 4.18. The simulated thermocouple is placed at a depth of $0.5\,\mathrm{mm}$ at the interface between the RCG and LI-900. The TC is sampled at $50\,\mathrm{Hz}$, and a noisy trace is constructed by truncating

the resolution of the sampled TC data to approximately $0.45\,\mathrm{K}$, a level representative of a 12-bit data acquisition system often used in practice (Figure 4.32).

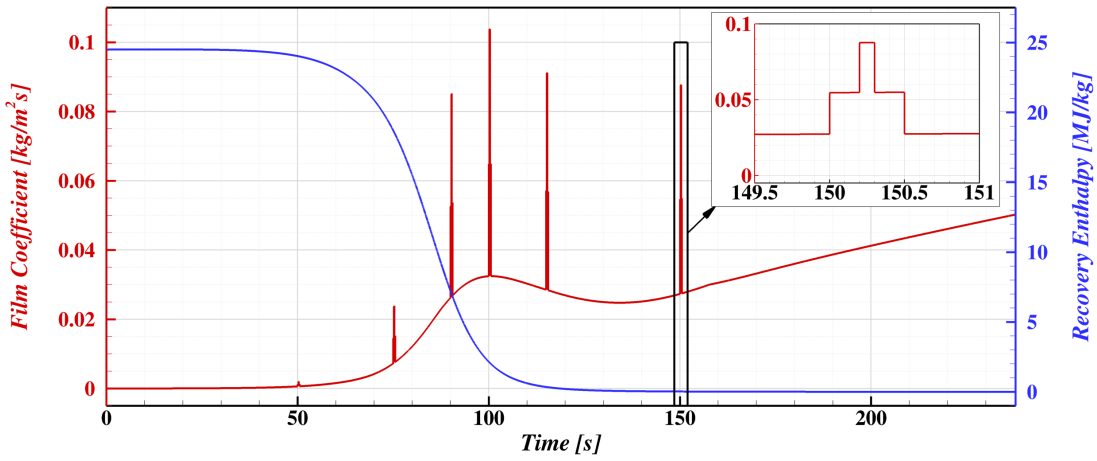

Figure 4.31. Film coefficient and recovery enthalpy for jet augmentation example problem. Inset figure shows film coefficient detail of typical steering jet firing.

The sensitivity coefficients that result for this case are shown in Figure 4.33. Note that, unlike those shown previously, these coefficients represent the sensitivity of the in-depth temperatures to the film coefficient. Consequently, they are markedly different than those from earlier problems, and the effects of this is seen in the results. The coefficients at early times show a very rapid rise (peaking approximately $0.3\,\mathrm{s}$ from the start of the interval) followed by a slow decay. The magnitude of the peaks is observed to decrease rapidly in time, with the coefficients for intervals after $100\,\mathrm{s}$ becoming very small by comparison. This reduction is due to the fact that the aerodynamic heat flux in Equation 4.1 is scaled by the recovery enthalpy. The TC responds to the heat flux, and the heat flux and TC response become less sensitive to changes in the film coefficient because the recovery enthalpy drops during the entry profile. The slight variation of the peaks relative to the recovery enthalpy profile is caused by non-linearities in the thermal properties and reradiation which is a strong function of surface temperature.

Reconstructions are performed with the same integration time as the direct problem ($0.1\,\mathrm{s}$) and the same grid. The reconstructed film coefficient profile is assumed to be com-

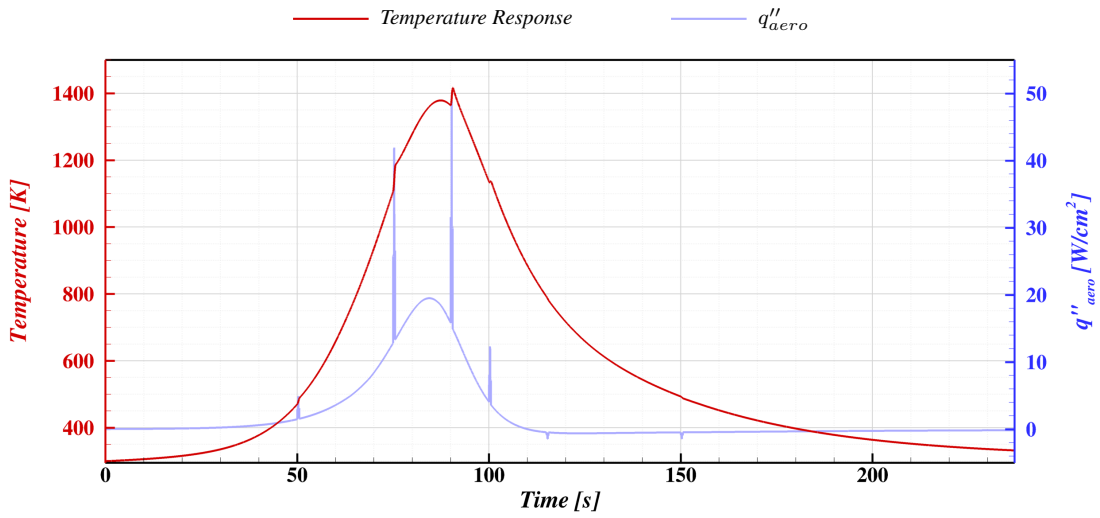

(a) Overall Response

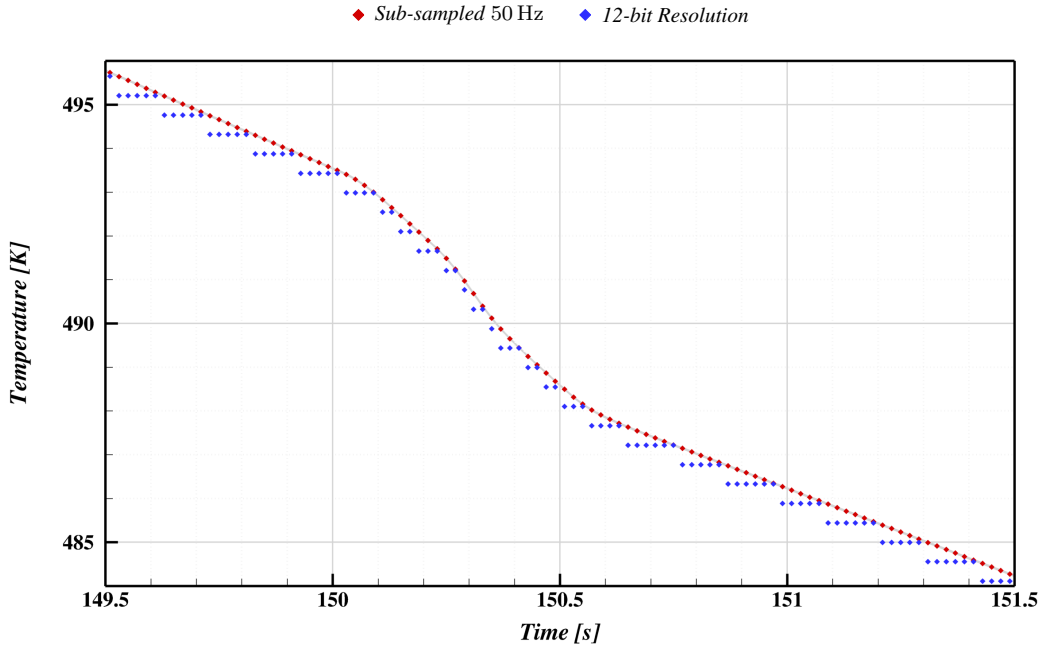

(b) 150 s Firing Detail

Figure 4.32. Aeroheating flux and temperature response at thermocouple location for jet augmentation case. In the detail plot, symbols denote sub-sampled (red) and 12-bit resolution quantized (blue) representations of temperature response for use as reconstruction target temperatures.

posed of uniformly distributed 0.1 s intervals, so there is an implicit factor of 5 future-time smoothing since the data rate is higher than the reconstruction rate.

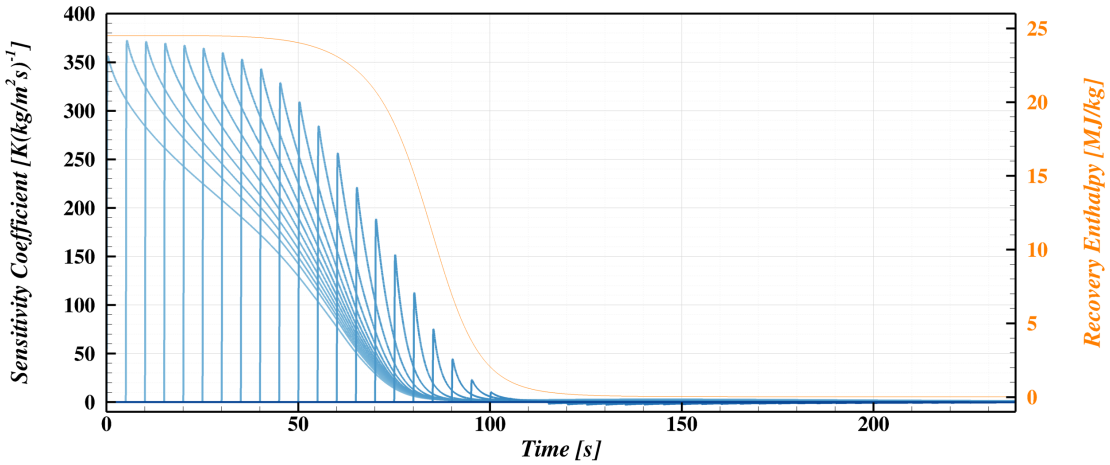

Figure 4.33. Sensitivity coefficients for jet augmentation example problem.

Figure 4.34 shows the reconstructions produced by the FT algorithm for several future time window lengths. Two features of the overall solution stand out: the spurious oscillatory spike seen at approximately $110\,\mathrm{s}$ and the growing instability of the noisy reconstructions at later times. The spike at $110\,\mathrm{s}$ occurs at the time that the aerodynamic heat flux passes through zero (when the recovery enthalpy drops below the wall enthalpy at the onset of cooling, see the flux in Figure 4.32). At this point, the term $(H_{rec} - H_w)$ is very near zero, so the TCs become very insensitive to the film coefficient, making the IHCP particularly ill-conditioned. The growing noise later in time is caused by a combination of the small sensitivity coefficients for later time and the relatively large amount of noise introduced by quantizing the temperature measurements to a 12-bit level. As the nominal signal is slowly decaying, the truncation operation yields correlated errors in the noisy trace, which the reconstruction algorithm tries to reproduce. The reconstruction with a future time window of $1\,\mathrm{s}$ is seen to significantly smooth out the transient profile of the jet firing and significantly lead the actual heating profile, and even the shortest future time window of $0.3\,\mathrm{s}$ under-predicts the magnitude of the peak augmentation. The general character of the reconstructions are consistent between the $75\,\mathrm{s}$ firing and the $150\,\mathrm{s}$ firing.

Reconstructions using the WD algorithm are shown in Figure 4.35. In contrast to the FT reconstructions, the spike at $110\,\mathrm{s}$ and the instabilities at later times do not occur. Also

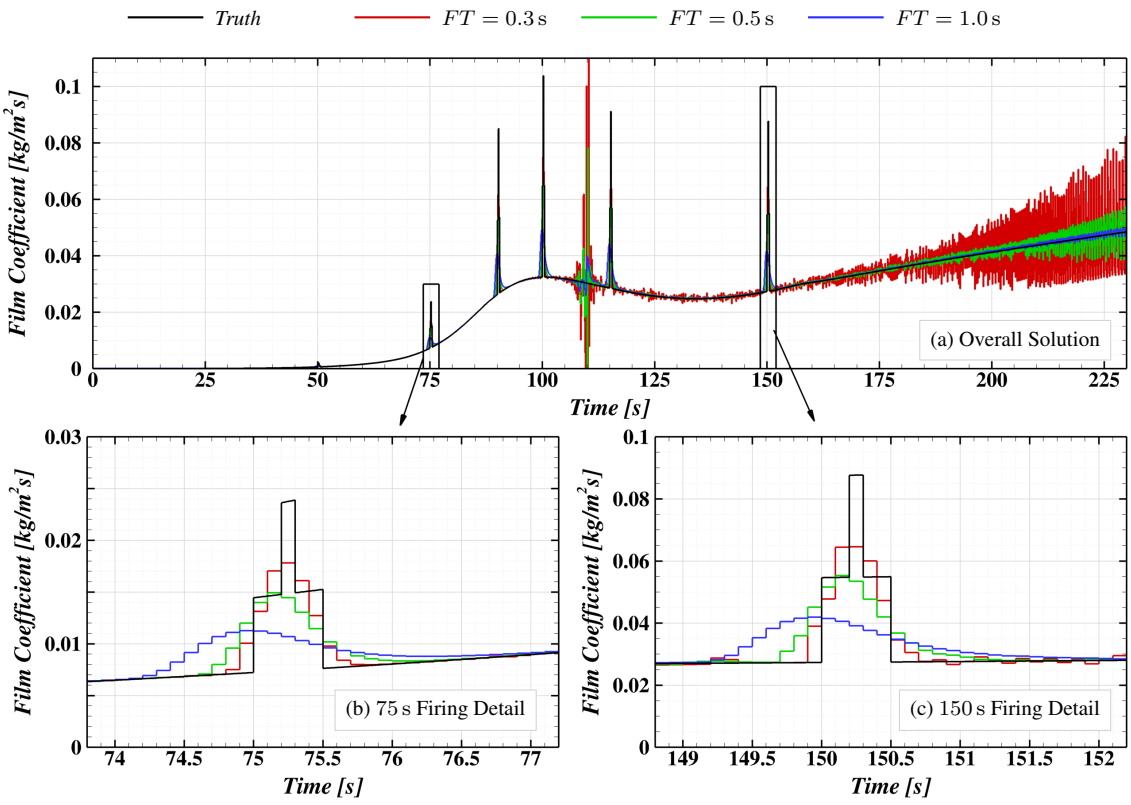

Figure 4.34. Reconstructions of jet augmentation test case using Future Time algorithm.

in contrast to the FT reconstructions, the nature of the reconstructions of the $75\,\mathrm{s}$ firing are quite different from the reconstructions of the $150\,\mathrm{s}$ firing. The increased smoothing observed in the later firing is a direct result of the reduced sensitivity coefficients at later times. Recall that the WD algorithm as-implemented uses a single regularization parameter across the whole time domain. As a result, the regularization term in the objective function (Equation 3.1) is quite a bit larger than the sensitivity coefficient term for the later firing, while the difference is not as large for the earlier firing. It is also the increased smoothing at later times that suppresses the onset of the instabilities noted in the FT reconstructions. It is notable that the WD reconstruction of the earlier firing is quite good, with no clear bias in time and a reasonable prediction of the peak for the lowest regularization parameter value considered.

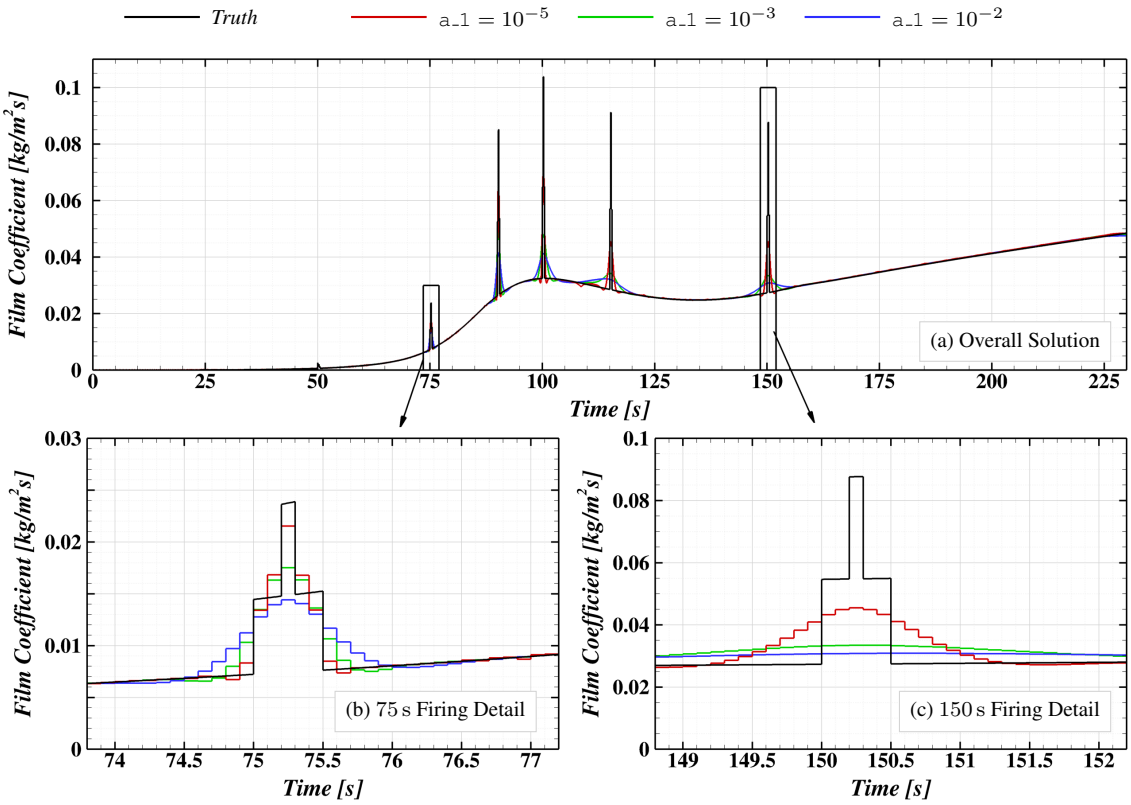

Figure 4.35. Reconstructions of jet augmentation test case using WD algorithm.

Reconstructions using the SSD with a future time window of $1\,\mathrm{s}$ are shown in Figure 4.36. The overall solutions show similar behavior as the FT reconstructions, however the detail views show significantly improved reconstructions of the two firings. The consistent reconstructions of the two firings, and also the increased sensitivity to noise later in time, are enabled by the local regularization scaling parameter approach that scales the regularization to follow the magnitude of the sensitivity coefficients. The instabilities later in time imply that the sensitivity coefficients alone are not sufficient for defining the optimal regularization parameter; the noise level must be considered as well. From the trend of the reconstructions in the detail views with increasing regularization scaling parameter, is reasonable to expect that increasing the regularization to address the later instabilities would lead to a poorer reconstruction of the $150\,\mathrm{s}$ firing, so there is a limit to what may be

obtained with the available data. Should this sort of reconstruction be desired in practice, higher resolution measurements are likely needed.

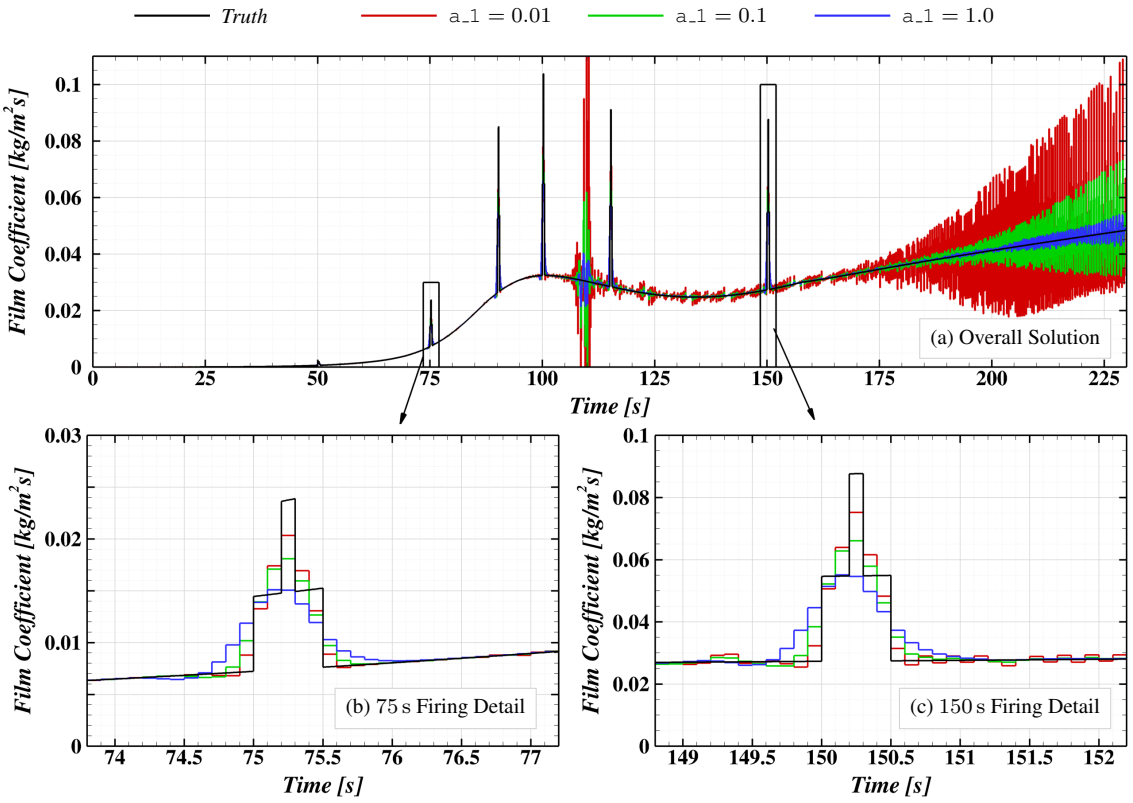

Figure 4.36. Reconstructions of jet augmentation test case using SSD algorithm with a 1 s future time window.

The different reconstruction algorithms are compared in Figure 4.37. In this case, the minimum-regularization reconstruction from each method has been chosen for comparison to estimate the best each method could do at resolving the transient event heating profiles. The WD reconstruction performs clearly better than the other two at predicting the peak heating of the 50 s firing but worse than the other algorithms for the 150 s firing. With the short future time window, the FT reconstruction does not introduce too much of a time shift, however the SSD still performs marginally better at predicting the peak heating level. It is worth noting, however, that the accuracy of the FT and SSD reconstruction of the transient heating events comes at the cost of unstable reconstructions of the nominal heating profile at later times. For this test case and level of noise, none of the algorithms as-presented are

capable of providing good reconstructions of all aspects of the present heating profile in a single reconstruction.

Run times for the results presented in Figure 4.37 were taken from computations performed on a cluster utilizing Intel Westmere X5650 processors (12 cores per node) running at $2.67\,\mathrm{GHz}$ with 24GB of RAM per node. The FT reconstruction required $5.6\,\mathrm{min}$ of wall-time using only 2 cores, the SSD reconstruction required $0.90\,\mathrm{hr}$ of wall-time using 20 cores, and the WD reconstruction required $4.9\,\mathrm{hr}$ of wall-time using 120 cores. To more directly compare the WD and SSD performance, the WD reconstruction required $14.3\,\mathrm{hr}$ of wall-time to complete the reconstruction using only 20 cores (only 10 cores per node were used since more than 2GB of memory was required for the construction and solution of the IHCP linear system). A notable qualification of these comparisons is that the WD reconstruction assumed one-sided differences in the sensitivity coefficient evaluation (reducing the computational effort of evaluating the sensitivity coefficient matrix by a factor of two) while the SSD and FT reconstructions used central-differences. For this problem, the computational efficiency of the SSD algorithm relative to the WD algorithm is clearly apparent. The FT algorithm is considerably cheaper than the SSD algorithm, though, as is noted in the previous paragraph, the transient event reconstruction is not as accurate.

This test case demonstrates some of the complexities in reconstructing transient events with a realistic level of measurement noise. Furthermore, it demonstrates some some practical issues in attempting to reconstruct the film coefficient during a typical reentry as opposed to the heat flux usually discussed in the literature. In regards to reconstructions of the transient event profiles, the WD algorithm appears to perform well for jet firings early in the entry trajectory; however, the reduced sensitivity of the measurement to the film coefficient caused by the decreasing recovery enthalpy leads to considerable over-smoothing of later firings. The SSD algorithm with the local solution regularization scaling does not suffer from this change in behavior and produces consistent reconstructions of the jet firings. The level of data noise applied is seen to be too large relative to the sensitivity coefficient magnitudes for the IHCP to yield stable reconstructions at later times without over-smoothing the transient events. The FT and SSD algorithms both provide unstable reconstructions

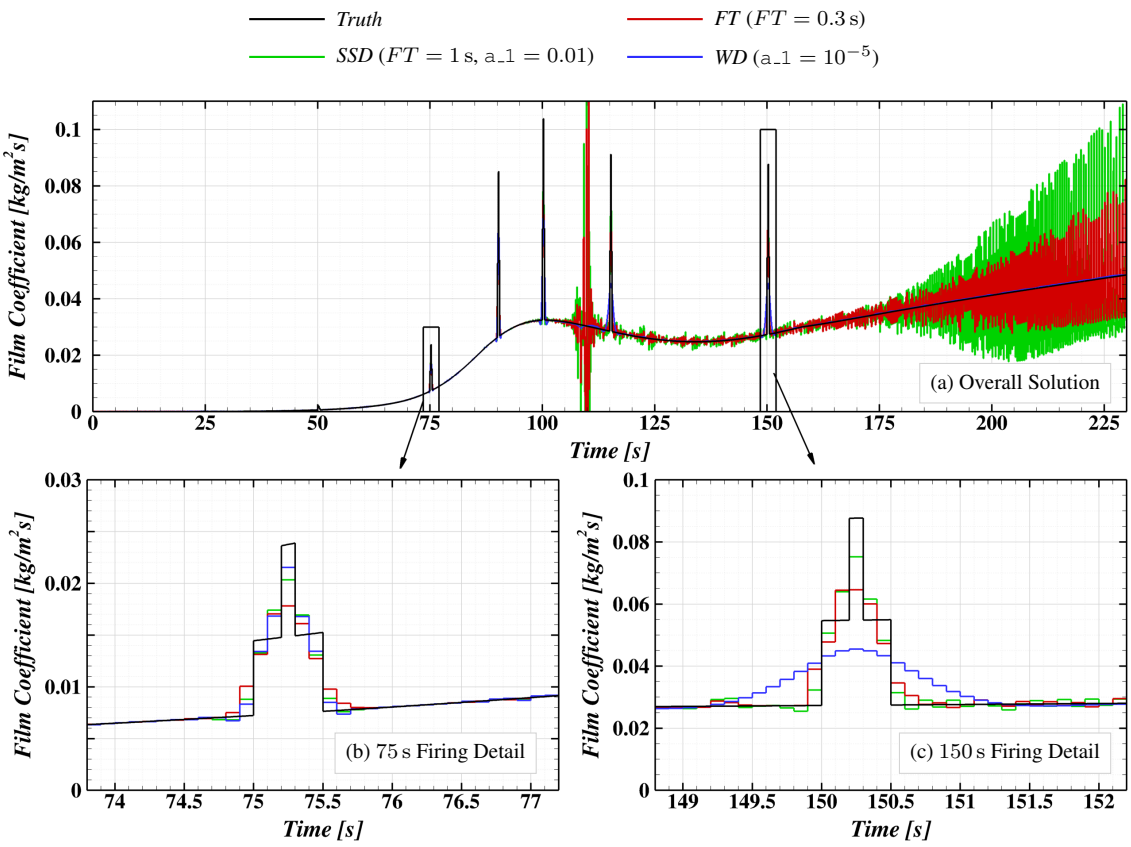

Figure 4.37. Comparisons of jet augmentation test case reconstructions using 'best' regularization combinations for each algorithm.

unless smoothing is increased to the point that the transient features lose most of the detail of the event. The high level of smoothing applied at later times for the WD algorithm that over-smooths the later firings eliminates the instability at later times.

It should be noted that in instances like this where the cause of the change in sensitivity coefficient is well known prior to the reconstruction, the regularization applied in a WD reconstruction can be made to scale in a manner similar to the SSD algorithm. Achieving this, however, involves a custom defined regularization weighting matrix, $\mathbf{W}$ in Equation 3.1. This has not been pursued in this work as the same effect can be achieved much more simply with the SSD algorithm.

4.4 Multi-Component Reconstruction

To demonstrate the algorithm performance in the presence of multiple BCs with spatial regularization, the system illustrated in Figure 4.38 is considered. The planar 2-D domain is $20\,\mathrm{mm}$ wide and $25.4\,\mathrm{mm}$ deep with constant properties used in the example of Section 4.1. The top surface is exposed to a time- and space-varying heat flux boundary condition, while the remaining three boundaries are insulated. The heating boundary condition is assembled by the linear combination of 21 'tent' basis functions. Each basis function is invariant in time, but in the linear combination, each is scaled by the time-varying (piecewise constant) value of the heat flux at the node of the function. The nodes are uniformly distributed along the heated surface. As a result, the boundary condition is a piecewise linear function in space, and a piecewise constant function in time[4].

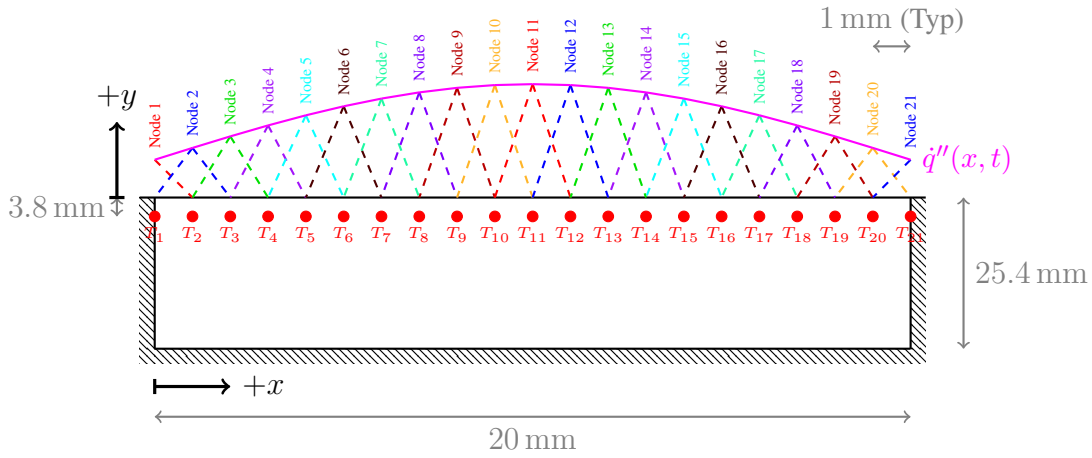

Figure 4.38. Schematic of physical domain for spatial reconstruction example case.

An array of 21 thermocouples are placed $3.8\,\mathrm{mm}$ below the heated surface, and each is centered under the boundary condition nodes. The sensitivity coefficients for these locations are evaluated in *CHAR* and presented in Figure 4.39 (as the domain is symmetric

[4]To simplify the presentation, only the value at the end of a solution interval is plotted in the results, which makes the results appear piecewise linear in time. However, the actual solution is evaluated assuming piecewise constant temporal variation of the boundary condition nodal values in the sensitivity coefficient evaluation.

about $x = 10\,\mathrm{mm}$, only nodes located on $0\,\mathrm{mm} \leq x \leq 10\,\mathrm{mm}$ are shown). As these properties and thermocouple depths are identical to those used in Section 4.1, it might be expected that the coefficients for TCs directly beneath a node would be consistent with those in Figure 4.1. However, due to relief from conduction in the additional spatial dimension, the coefficients in this instance peak earlier, at about $3\,\mathrm{s}$, and to a much lower level. As would be expected, the peak is observed to occur later and to lower levels at TCs farther from the node that is being perturbed, and the coefficients for node 11 display symmetry about the center of the domain. The sensitivity coefficient peak is much higher for the nodes near the boundaries because of the influence of the insulated boundary condition limiting the lateral conduction. The nodes on the boundaries (1 and by symmetry 21) are lower due to the fact that the surface area for which their basis functions are non-zero is half of that of all the other nodes. Given the linearity of the material properties, the sensitivity coefficients were evaluated using a one-sided finite-difference assumption. Perturbed temperatures were computed assuming an applied flux pulse-width of $0.1\,\mathrm{s}$ on a grid of quad elements 149×74 (149 elements in the x-direction) with $0.15\,\mathrm{mm}$ thick elements at the heated surface. *CHAR* defaults for the numerical tolerances were used, but the timestep was set to be $0.005\,\mathrm{s}$ to improve the accuracy of the solution.

CHAR was used to generate simulated measurements based on the heating profile shown in Figure 4.40. The 5 nodes closest to the edges of the domain are exposed to constant heating and the remaining nodes are exposed to the triangular heating profile from Section 4.1.2. The heating profile is symmetric about node 11. The spatial variation of heating to the nodes is a step function, however the basis functions used to construct the boundary condition provide a linear change from constant heating at node 5 to the full triangular profile at node 6. Temperatures obtained with this heating profile are shown in Figure 4.41, along with profiles with white noise superimposed to test the regularization of the reconstruction algorithms (given the symmetry of the profile, only the unique TC traces are shown). While *CHAR* was used to generate the simulated data, the linear IHCP solver is used in the reconstructions presented in this section. For all results, reconstruction is performed at $2\,\mathrm{Hz}$, so all reconstructions will have an additional $0.5\,\mathrm{s}$ of implicit future time smoothing.

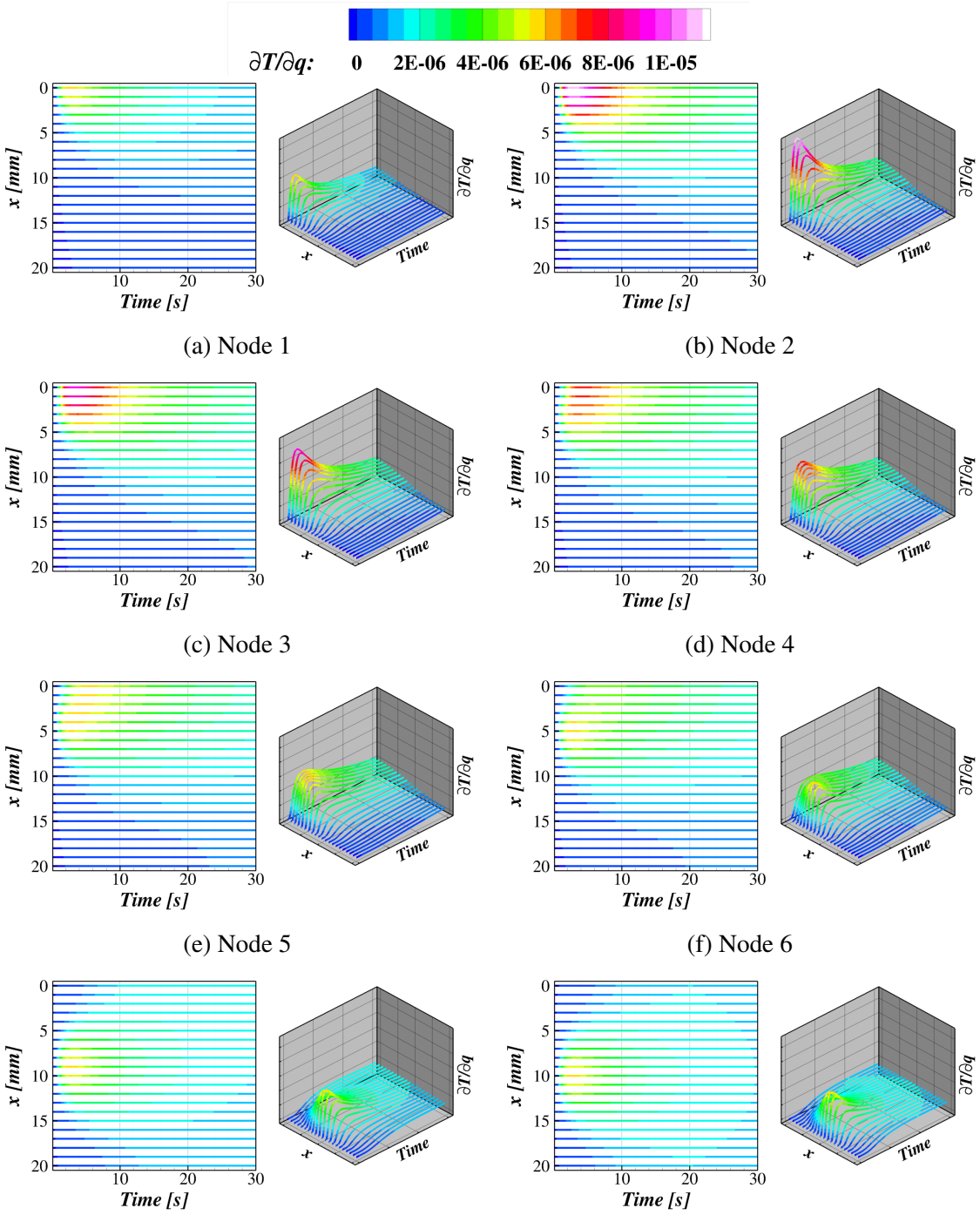

(a) Node 1 (b) Node 2

(c) Node 3 (d) Node 4

(e) Node 5 (f) Node 6

(g) Node 10 (h) Node 11

Figure 4.39. Representative sensitivity coefficients for spatial reconstruction example.

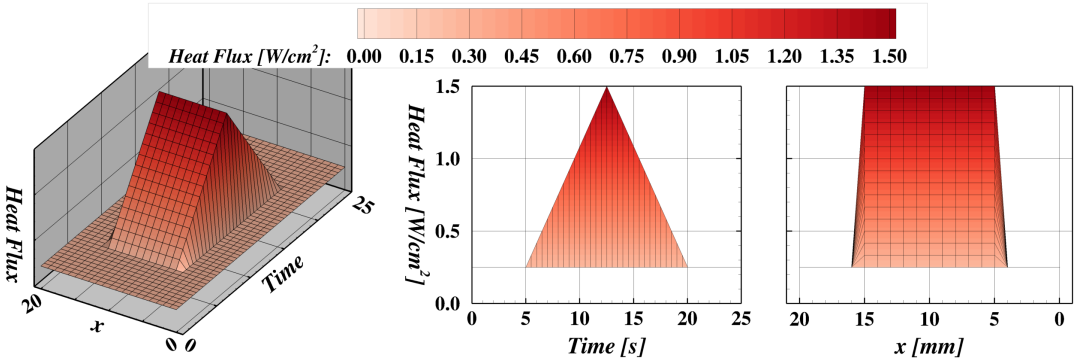

Figure 4.40. Applied heat flux profile for spatial reconstruction example.

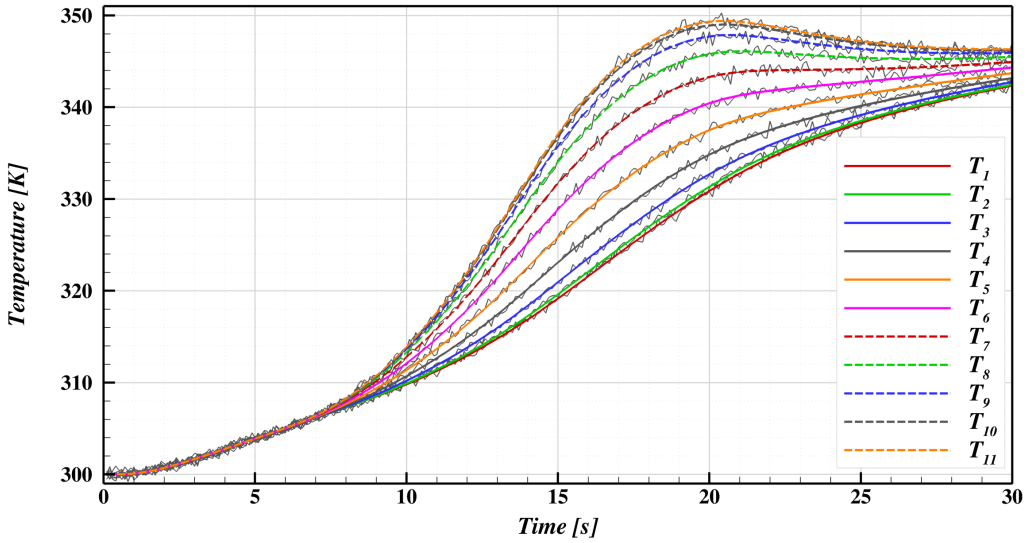

Figure 4.41. Simulated temperature data for spatial reconstruction example. 'Clean' temperatures superimposed on corresponding 'noisy' temperature traces. Only half of the temperatures shown given the symmetry of the problem.

The key difference between this case and those in Section 4.1 is that multiple distinct BCs are considered (in this case, the nodes). Just as some form of regularization is necessary to maintain smoothness between temporally-adjacent elements of the solution vector $\mathbf{q}$, some regularization is necessary between spatially-adjacent elements of the solution

vector to maintain an overall smooth and stable solution. For this example, the spatial regularization component matrix of Equation 3.16 has been set to

$$\mathbf{h}_x = \begin{bmatrix} -1 & 1 & 0 & 0 & \dots & 0 \\ 0 & -1 & 1 & 0 & \dots & 0 \\ \vdots & \vdots & \ddots & \ddots & \ddots & \vdots \\ 0 & \dots & 0 & 0 & -1 & 1 \\ 0 & \dots & 0 & 0 & 0 & 0 \end{bmatrix}_{(21\times 21)} \tag{4.2}$$

in order to provide first-order spatial regularization. Figure 4.42 shows the effect of varying the spatial regularization parameter α_x when used with the FT algorithm. In these figures, the translucent blue surface is the 'true' heating profile and is included for reference. Furthermore, each grid line on the reconstruction surface corresponds to a reconstructed node and time interval. As expected, larger values of the spatial regularization parameter lead to smoothed out reconstructions of the spatial distribution of heating. Reducing the regularization increases the sharpness of the spatial distribution, though over- and under-shoots, leading to the multimodal surfaces, are still present on either side of the heating profile discontinuity. This spatial distribution is qualitatively consistent with the WD temporal reconstructions of the square heating pulse example considered earlier (Figure 4.4(a)). This should be expected since the first-order spatial regularization of Equation 4.2 used here is identical to the first-order temporal regularization used in the previous example, and both are subjected to a step change in the target heating profile.

The temporal behavior of the node at the center of the domain is very similar to what would be expected from the FT algorithm (recall that due to similar properties and heating profile definitions, the temporal reconstruction of the centerline should be similar to that in Figure 4.10(a)). This point is supported by the results in Figure 4.43, which shows equivalent reconstructions using the FT, WD, and SSD algorithms. The temporal reconstruction of the center of the profile follows expectations for each algorithm (FT: Figure 4.10(a), SSD: Figure 4.12(b), and WD: Figure 4.11(a)), and spatial reconstructions are similar,

with the SSD and WD reconstructions slightly smoother due to additional smoothing provided by the temporal regularization parameter. For completeness, Figure 4.44 shows how the mulit-component algorithm responds to noisy TCs. Keeping in mind that the spatial terms are always evaluated in a whole-domain sense with Tikhonov regularization (this algorithm does not support 'sequential' evaluation of components within a single solution time interval), results are consistent with single component reconstructions. Because the present formulation limits all spatial boundary conditions to be defined on a consistent time scale (with all being estimated at the same frequency), the number of total unknowns can become very large. This can pose a challenge for the WD algorithm as the linear system can become quite large, so the SSD algorithm provides a means of achieving improved results over the FT algorithm without the special handling of a very large numerical system. The WD algorithm required $147\,\mathrm{s}$ of wall-time[5] to evaluate the linear system, whereas the SSD algorithm was able to perform the reconstruction in only $13.6\,\mathrm{s}$ of wall-time (recall that this is performed with the linear IHCP tool, so sensitivity coefficient evaluation time is negligible here). The FT algorithm required $5.4\,\mathrm{s}$ of wall-time to complete the reconstruction.

[5]Computed on a single core using a MacBook Pro 2.8 Ghz Intel Core i7 CPU (8 cores) with 16 GB of 1600 MHz DDR3 RAM.

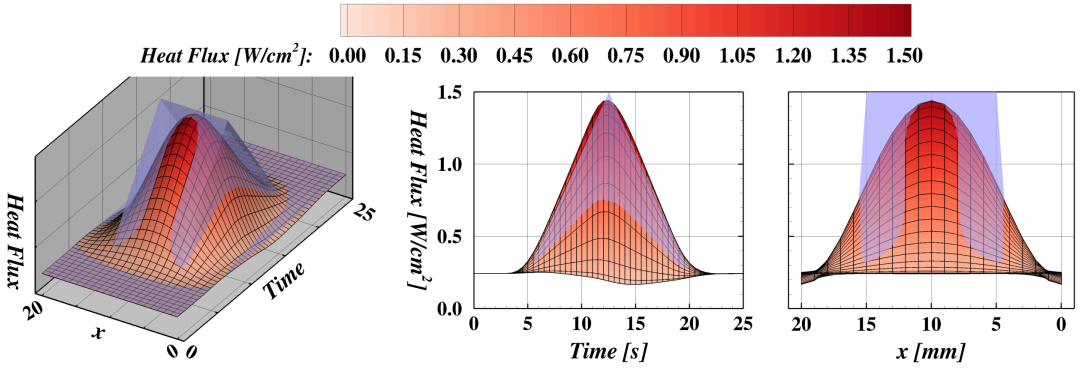

(a) $\alpha_x = 10^{-5}$

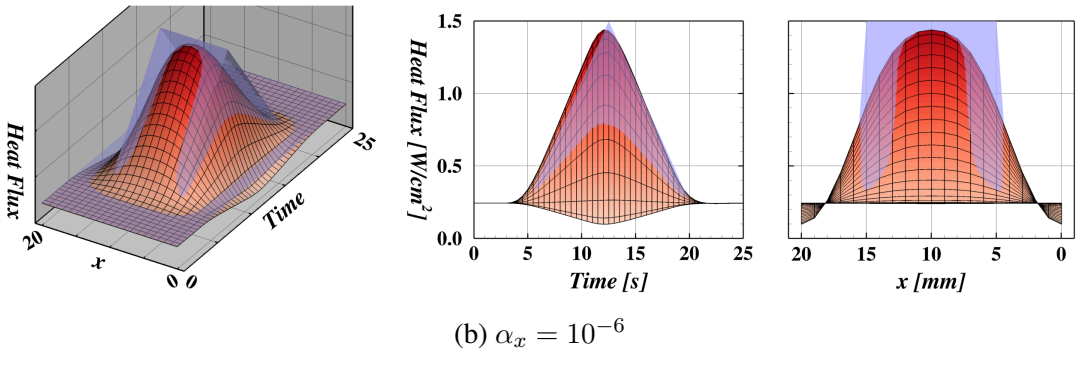

(b) $\alpha_x = 10^{-6}$

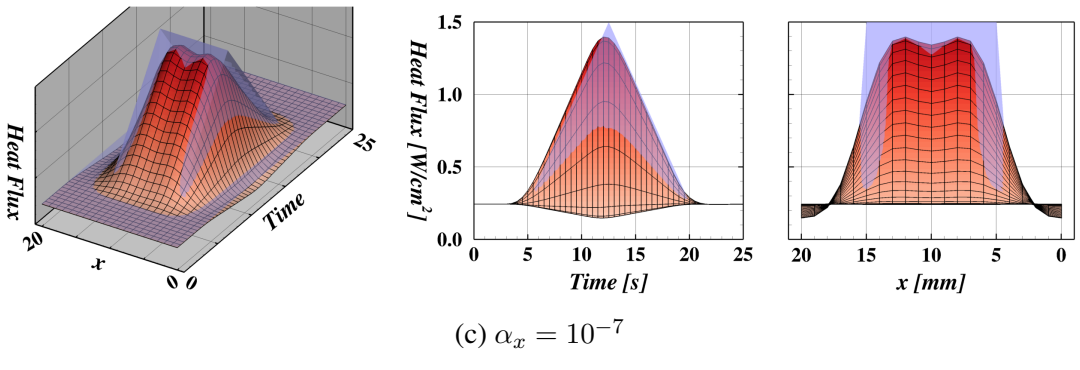

(c) $\alpha_x = 10^{-7}$

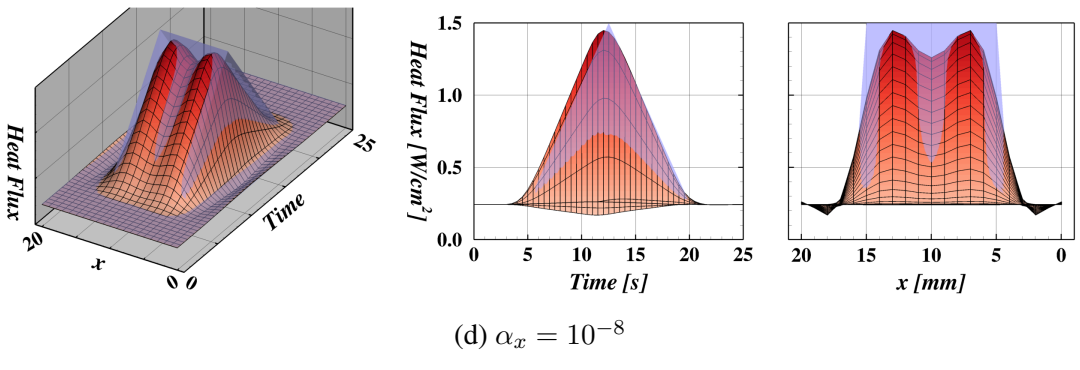

(d) $\alpha_x = 10^{-8}$

Figure 4.42. Spatial reconstruction results for Future Time algorithm with a 3 s future time window and various values of the spatial regularization parameter α_x.

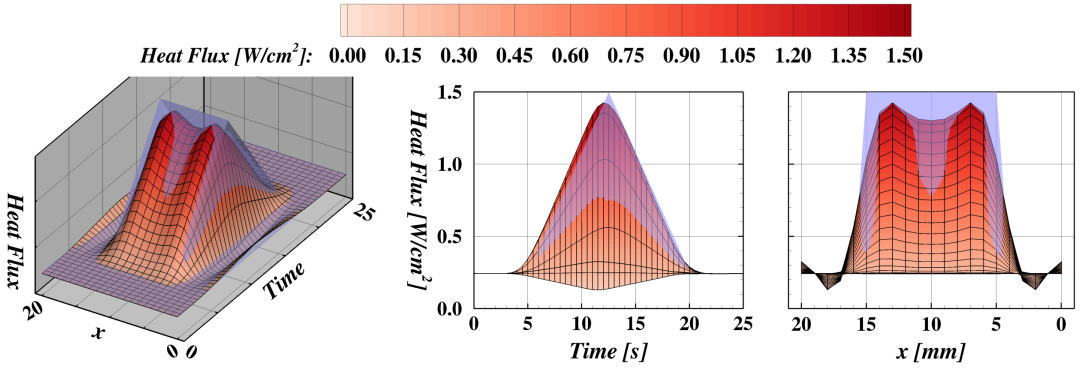

(e) $\alpha_x = 10^{-9}$

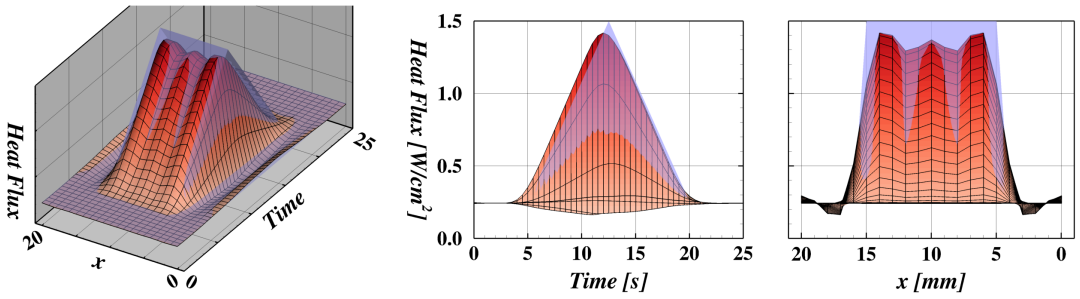

(f) $\alpha_x = 10^{-10}$

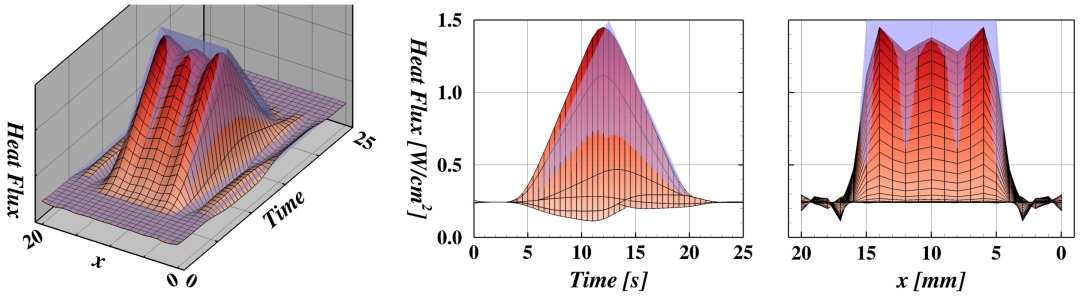

(g) $\alpha_x = 10^{-11}$

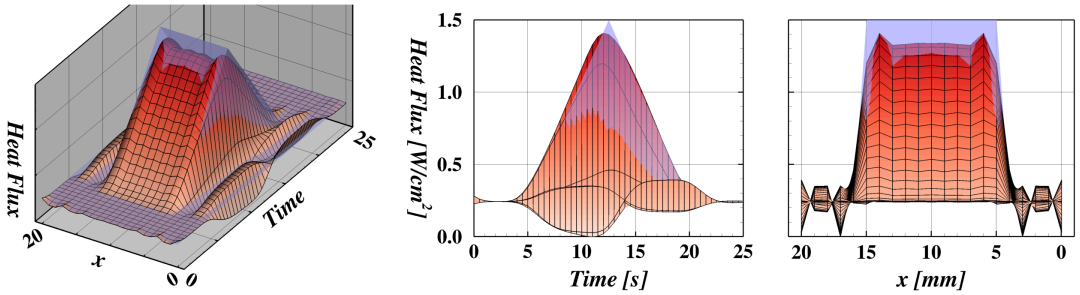

(h) $\alpha_x = 10^{-12}$

Figure 4.42. *(continued)* Spatial reconstruction results for Future Time algorithm with a 3 s future time window and various values of the spatial regularization parameter α_x.

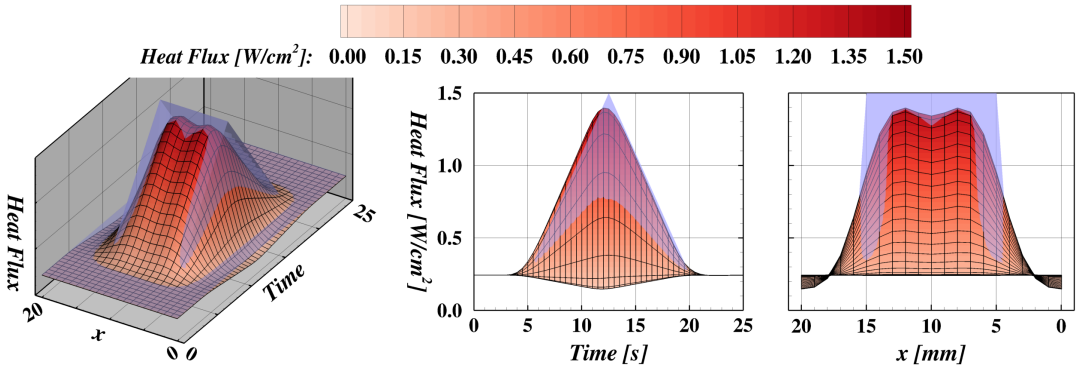

(a) Future Time: FT window 3 s

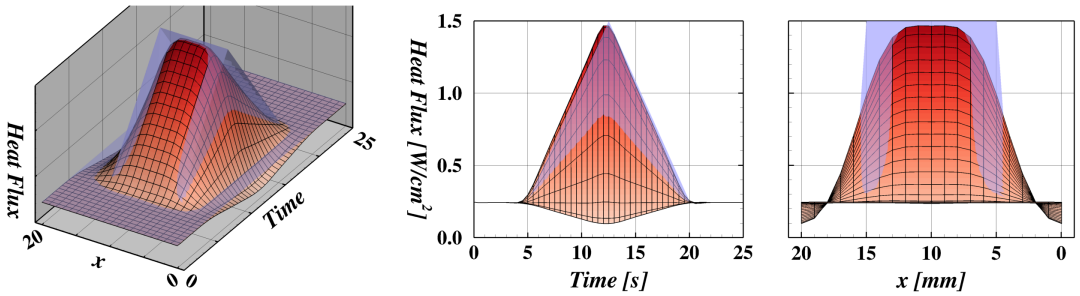

(b) Sequential Subdomain: FT window 3 s and $\alpha_1 = 10^{-8}$

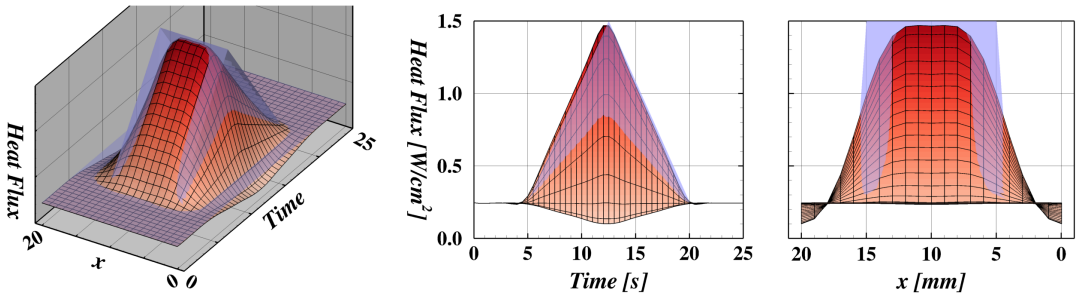

(c) Whole Domain: $\alpha_1 = 10^{-8}$

Figure 4.43. Spatial reconstruction of clean TC data for different algorithms with $\alpha_x = 10^{-7}$.

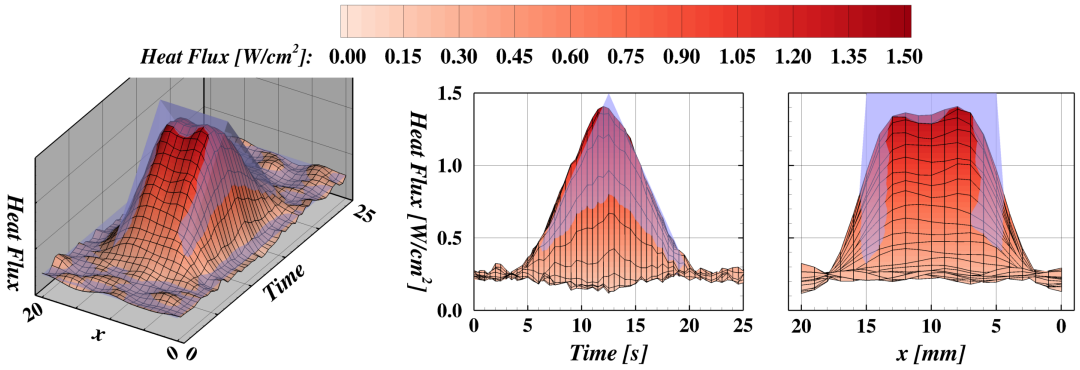

(a) Future Time: FT window 3 s

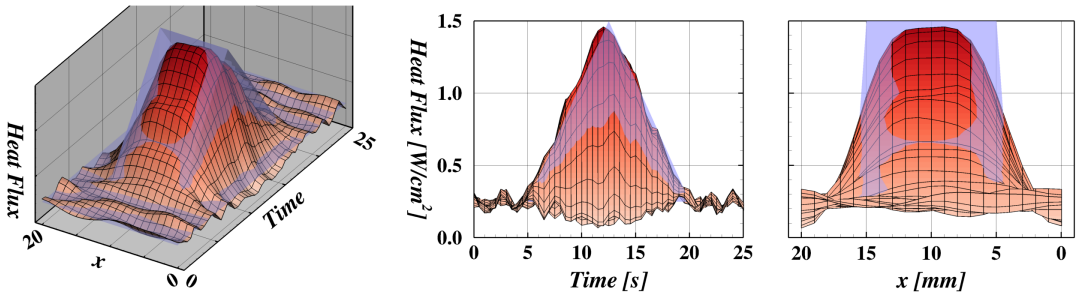

(b) Sequential Subdomain: FT window 3 s and $\alpha_1 = 10^{-8}$

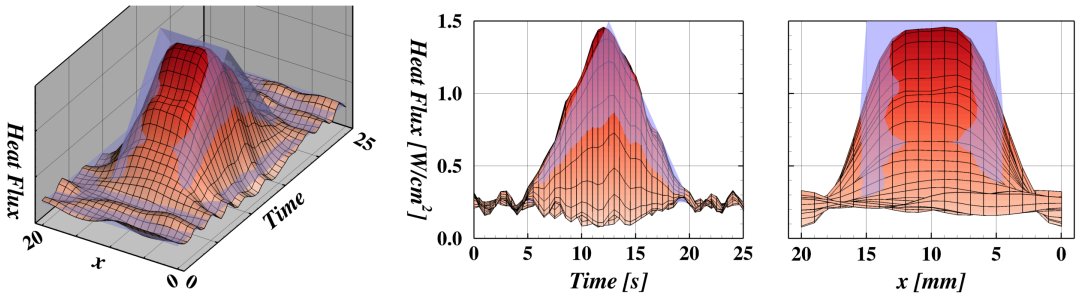

(c) Whole Domain: $\alpha_1 = 10^{-8}$

Figure 4.44. Spatial reconstruction of noisy TC data for different algorithms with $\alpha_x = 10^{-7}$.

5. ABLATION CONSIDERATIONS IN ENVIRONMENT RECONSTRUCTION

5.1 Background

Figure 5.1 shows an illustration of the two-step process that a decomposing ablator experiences upon sufficient heating. In the first step (described earlier in Section 4.2), the virgin composite material thermally *decomposes* (or more precisely, *pyrolyzes*), producing char and pyrolysis gas which percolates through the char to the surface. Second, a number of physical processes may occur at the surface to consume or otherwise remove char from the surface leading to surface recession, a process generally referred to as *ablation*. These two processes are separate and distinct. Most low density ablative TPS materials (e.g. PICA, SLA, and Avcoat) experience both decomposition and ablation. However, not all ablators decompose (graphite and teflon are common examples) and nor do all decomposing materials ablate under design conditions (e.g. SIRCA). If decomposition is present, it will affect ablation by the introduction of pyrolysis gas.

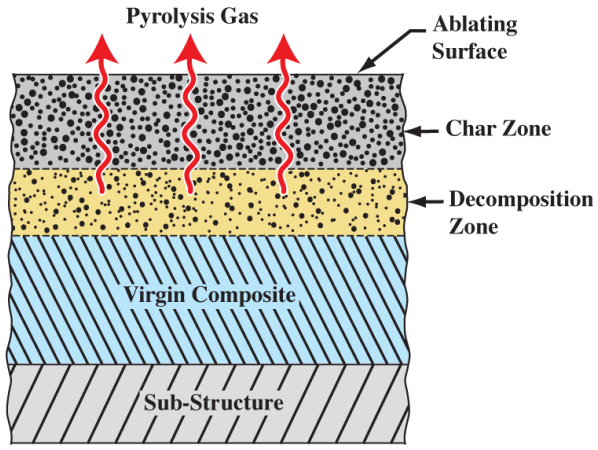

Figure 5.1. Illustration defining regions of interest in a charring ablative TPS. From [35], used with permission.

Ablation can be caused by a number of physical processes. Several mechanical failure modes (i.e. erosion, spallation, and structural failure) can result in char removal without any change of phase occurring. With sufficient heating, surface char may undergo a phase change through melting or sublimation before being swept away by the boundary layer. Finally, surface material can be consumed through heterogeneous chemical reactions (e.g. oxidation) with the boundary layer gas in a process called *thermochemical ablation*. Depending on the specific composition of a given TPS material, one or more of these modes are generally dominant. For instance, teflon is generally regarded as a melter/sublimer [38], and low density carbon ablators tend to oxidize with limited spallation. Each physical process is governed by different parameters and has a different net effect on the heat conduction into the TPS.

Regardless of the dominant ablation mode, two balances must be maintained: a mass balance and an energy balance. The surface *elemental* mass balance can be given by

$$\tilde{j}_{k_w} + \dot{m}''_g \tilde{\omega}_{k_g} + \dot{m}''_c \tilde{\omega}_{k_c} - (\rho v)_w \tilde{\omega}_{k_w} - \dot{m}''_f \tilde{\omega}_{k_f} = 0 \tag{5.1}$$

where $\tilde{j}_{k_w}$ is the rate of diffusion of atoms of element k to the surface per unit area through the boundary layer; $\dot{m}''$ and $\tilde{\omega}_k$ are the mass flux rates and elemental mass fractions of the pyrolysis gas (subscript g), ablating char (subscript c), and mechanically failing char (subscript f); and $(\rho v)_w$ is the mass flux of the combined ablation products leaving the surface with an elemental mass fraction of $\tilde{\omega}_{k_w}$. All fluxes in Equation 5.1 are positive per orientations in Figure 5.2. The elemental formulation here does not place restrictions on the particular species in each term, allowing chemical reactions to occur between constituents in the infinitesimal volume of the surface.

Kendall et al. [39] pointed out that if the boundary layer species are assumed to have equal diffusion coefficients and unity Lewis and Prandtl numbers, the boundary layer diffusive flux of element k at the surface can be modeled by

$$\tilde{j}_{k_w} = \rho_e u_e C_m (\tilde{\omega}_{k_e} - \tilde{\omega}_{k_w}), \tag{5.2}$$

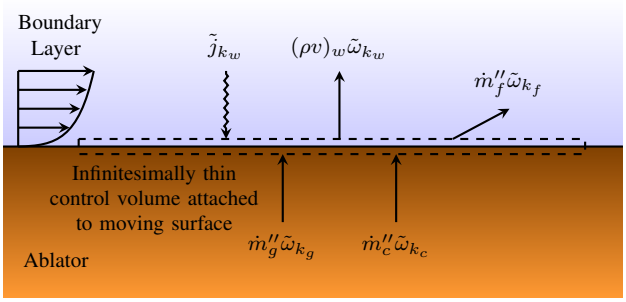

Figure 5.2. Elemental mass fluxes into the surface control volume.

where ρ_e is the boundary layer edge density, u_e the edge velocity, C_m the mass transfer coefficient, and $\tilde{\omega}_{k_e}$ is the elemental mass fraction at the boundary layer edge. Substituting into the mass balance equation, setting $(\rho v)_w = \dot{m}''_g + \dot{m}''_c - \dot{m}''_f$ to balance the total mass flux, and rearranging yields the elemental composition of the ablation products

$$\tilde{\omega}_{k_w} = \frac{\tilde{\omega}_{k_e} + B'_c \tilde{\omega}_{k_c} + B'_g \tilde{\omega}_{k_g} - B'_f \tilde{\omega}_{k_f}}{1 + B'_g + B'_c - B'_f} \tag{5.3}$$

where

$$B' = \frac{\dot{m}''}{\rho_e u_e C_m} = \frac{\dot{m}''}{C^*_m} \tag{5.4}$$

is a nondimensionalized mass flux. This indicates that, under the assumptions of Equation 5.2, the elemental composition of the ablation products is a mass-weighted average of the edge, pyrolysis gas, and char elemental compositions.

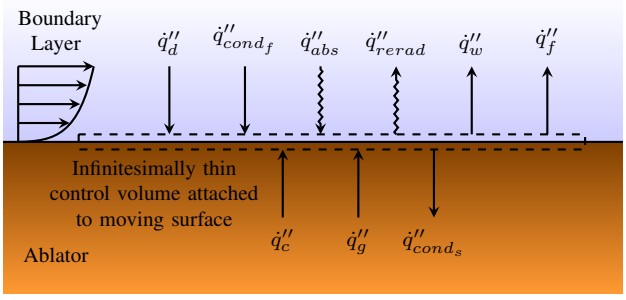

Figure 5.3. Energy fluxes into the surface control volume.

The surface energy balance (SEB) is given by

$$\dot{q}''_d + \dot{q}''_{cond_{fl}} + \dot{q}''_{abs} - \dot{q}''_{rerad} + \dot{q}''_c + \dot{q}''_g - \dot{q}''_w - \dot{q}''_f - \dot{q}''_{cond_s} = 0, \tag{5.5}$$

where the energy fluxes in each term are attributed to

$$\text{Species mass diffusion in fluid: } \dot{q}''_d = \sum_i j_{i_w} h_i^o \tag{5.6a}$$

$$\text{Conduction on the fluid side: } \dot{q}''_{cond_{fl}} = -k_{fl} \frac{\partial T_{fl}}{\partial x} \tag{5.6b}$$

$$\text{Absorbed shock layer radiation: } \dot{q}''_{abs} = \alpha \dot{q}''_{rad} \tag{5.6c}$$

$$\text{Surface reradiation: } \dot{q}''_{rerad} = \sigma \epsilon (T_s^4 - T_\infty^4) \tag{5.6d}$$

$$\text{Mass flux of char material: } \dot{q}''_c = \dot{m}''_c H_c \tag{5.6e}$$

$$\text{Mass flux of pyrolysis gas: } \dot{q}''_g = \dot{m}''_g H_g \tag{5.6f}$$

$$\text{Mass flux of ablation products: } \dot{q}''_w = \dot{m}''_w H_w \tag{5.6g}$$

$$\text{Mass flux of failed species: } \dot{q}''_f = \dot{m}''_f H_f \tag{5.6h}$$

$$\text{Conduction on solid side: } \dot{q}''_{cond_s} = -k_s \frac{\partial T_s}{\partial x} \tag{5.6i}$$

with $\dot{q}''$ a heat flux per unit area, x the wall-normal direction, h_i^o the heat of formation of species i, k the thermal conductivity of the near-surface fluid (subscript fl) or solid (subscript s), α the surface absorptivity, ϵ the surface emissivity, and H a mixture enthalpy. All flux terms are positive if oriented according to Figure 5.3. The first two terms collectively represent the convective heating to the surface by the boundary layer. Using film coefficient models, assuming equal diffusion coefficients, and assuming the heat and mass transfer coefficients are equal, Kendall et al. [39] show that these terms can be simplified to

$$\sum_i j_{i_w} h_i^o - k_{fl} \frac{\partial T_{fl}}{\partial x} = \rho_e u_e C_h (H_{rec} - H_w), \tag{5.7}$$

the form commonly used in engineering-level ablation analysis, where $\rho_e u_e C_h = C_h^*$ is the commonly referred to *film coefficient*, H_{rec} is the recovery enthalpy of the boundary layer, and H_w is the mixture enthalpy of the ablation products at the wall. Substitution of these terms back into Equation 5.5 yields

$$\dot{q}''_{cond_s} = \overbrace{C_h^*(H_{rec} - H_w) + \alpha \dot{q}''_{rad}}^{Environment} - \overbrace{\sigma\epsilon(T_s^4 - T_\infty^4)}^{Reradiation} + \overbrace{\dot{m}''_c H_c + \dot{m}''_g H_g - (\dot{m}''_c + \dot{m}''_g) H_w - \dot{m}''_f H_f}^{Ablation\ Terms}. \quad (5.8)$$

The terms highlighted in blue are typically provided by separate CFD or boundary layer analysis, and the red terms are material properties and assumed known (possibly functions of temperature and pressure). The remaining terms must be determined by the ablator response model and the recession model.

Generally, in a direct solution of an ablator response, the SEB is solved to obtain $\dot{q}''_{cond_s}$ and $\dot{m}''_c$. The first term is the actual flux boundary condition for the governing heat equation, and the other determines the surface recession rate. The enthalpy of the ablation products, H_w, depends on the state and composition of the ablation products (Equation 5.3), so it will be strongly dependent on the mass fluxes, including $\dot{m}''_c$. Since $\dot{m}''_c$ varies, the solution of the SEB requires a non-linear approach.

To reduce the computational cost of this solution, Moyer et al. [36] and Kendall [40] non-dimensionalized the ablation terms in the SEB using B' (Equation 5.4) so that recession model solutions could be pre-computed and packed into a so-called B' *table* that provides B'_c and H_w as a function of temperature, pressure, pyrolysis gas rate B'_g. Given these terms, $\dot{m}''_c$ and $\dot{q}''_{cond_s}$ can be readily evaluated. Though convenient, this approach places some constraints on the physical recession models that can be considered.

5.2 Recession Models

Recession model is the term used here to describe the physical model that determines the rate of char mass loss, $\dot{m}''_c$, and the corresponding enthalpy of the ablation products,

H_w, at a given time in an ablation simulation. As described earlier, a number of different physical processes can cause ablation, so recession models can take a wide range of forms, many of which are not compatible with the B' table approach described above.

The Diffusion Limit

The B' table approach was developed for materials that primarily experience thermochemical ablation (recall that this is driven by heterogeneous chemical reactions with the boundary layer gas) at conditions where reaction rates are fast enough that the char and ablation products are in a state of chemical equilibrium. Under this assumption, the mass balance equation (Equation 5.3) defines the elemental composition of the ablation products, and the gas species concentrations are calculated by minimizing the Gibbs free energy at a given temperature and pressure [40–45]. The largest amount of B'_c which does not result in condensation is determined, meaning that the gaseous ablation products will be saturated in at least one element that makes up the char (this can be complicated if the char is composed on multiple constituents [44]). As the film coefficient is the nondimensionalizing factor, the rate of surface mass loss scales directly by the rate that boundary layer edge species diffuse to the surface. Thus this recession model is called the *diffusion limit*. It represents the maximum recession rate possible at a specific condition in the absence of mechanical failure. As the enthalpy of the equilibrium mixture is an intrinsic property for a given composition, it can be tabulated along with B'_c for each chosen combination of temperature, pressure, and B'_g.

Plots of two B' tables are shown in Figure 5.4. Figure 5.4(a) shows the diffusion limit recession solution for graphite for several pressure values. Graphite does not pyrolyze, so these solutions are not a function of B'_g. This plot shows the typical solution for carbon ablation, with a plateau in the recession rate at the low temperatures (where the primary ablation product is CO_2), followed by a transition to the higher CO plateau at mid-range temperatures, before rapid recession begins as temperatures approach the sublimation asymptote (with sublimation temperature increasing with pressure). Note that when sublimation

is occuring, B'_c evaluated in this manner would be infinite, and a separate modeling approach is required (Section 5.2). Figure 5.4(b) shows the corresponding enthalpy of the ablation products, with the key point being the predominantly negative enthalpies (due to the negative heat of formation of CO and CO_2). Figure 5.4(c) shows the B'_c solution for the TACOT material for a pressure of $1\,\mathrm{atm}$, and Figure 5.4(d) shows the matching ablation product enthalpy. This material does decompose, so different solutions are obtained with different pyrolysis gas blowing rates, B'_g. Several curves associated with B'_g values of 0, 0.25, 1.0, and 10 are shown in different colors so that trends with increasing B'_g may be identified. In general, increasing the blowing rate will decrease the recession rate since carbon in the pyrolysis gas reduces the amount of carbon from the char that is needed to saturate the ablation products (note that if the ablation products become over-saturated in carbon, carbon would condense back onto the surface instead of ablate away). At some point, recession will not occur as the pyrolysis gas is capable of saturating the ablations products on its own. Closer to sublimation, hydrogen introduced by pyrolysis allows the ablation products to hold more carbon before condensation, so recession increases.

Kinetic Limiting

The diffusion limit model works well at high temperatures and pressures where chemical reactions proceed at a rapid rate. At lower temperatures, heterogeneous reactions may progress at a rate that is slow relative to the rate that species diffuse across the boundary layer, and will consume char slower than the diffusion limit rate. This condition is generally referred to as *kinetically limited* recession. Many different models have been proposed to predict kinetically limited recession and summarizing them is beyond the scope of this work. However, the model used in the present MEDLI analysis is discussed.

The Kinetic Limit

At the lowest temperatures where ablation occurs, the boundary layer is able to diffuse reactant species to the surface much faster than the reactions can consume them. This is

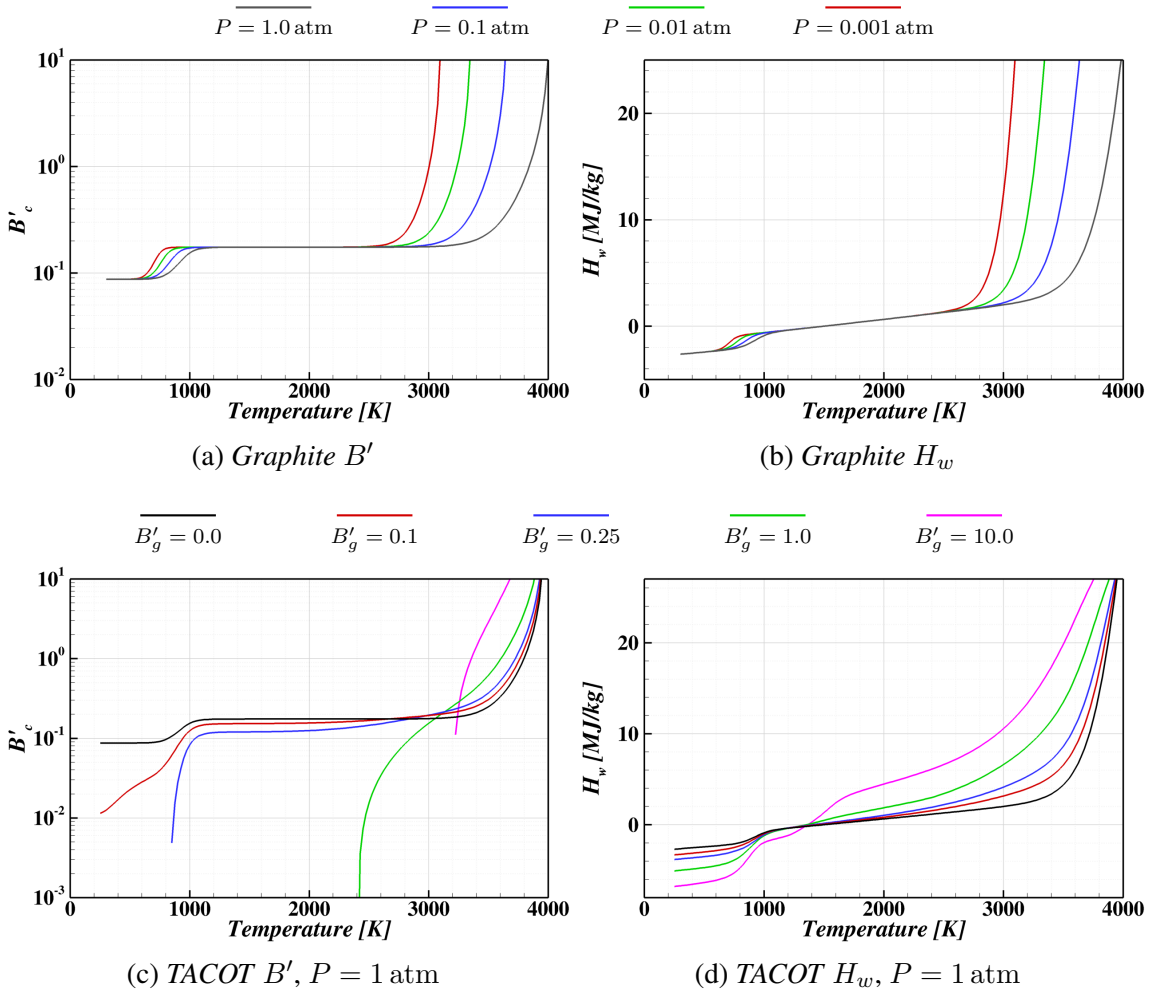

(a) *Graphite* B' (b) *Graphite* H_w

(c) *TACOT* B', $P = 1$ atm (d) *TACOT* H_w, $P = 1$ atm

Figure 5.4. Example B' tables for two carbon ablators.

called the *kinetic limit*. This case can provide simple recession models as the boundary layer solution will not be significantly altered by the recession rate. A commonly cited model for carbon stagnation point ablation in air is that of Scala [46] and takes the form

$$\dot{m}''_c = k_o \sqrt{R_b} P_{O_2}^{1/2} \exp\left(\frac{-E_a}{\mathcal{R}T}\right) \tag{5.9}$$

where k_o is the pre-exponential factor, R_b is the reference nose radius, P_{O_2} is the partial pressure of molecular oxygen at the surface, E_a is the reaction activation energy, $\mathcal{R}$ is the universal gas constant, and T is the surface temperature. Based on the initial as-

sumption that diffusion is much more rapid than the reactions, the partial pressure of oxygen at the wall is the same at the edge. Scala notes that the reaction rates suggested by experiment vary widely based on the type graphite tested. He proposed rate coefficients that bounded "fast" and "slow" variants of graphite with values of $E_a = 184\,{}^{\mathrm{kJ}}/_{\mathrm{mol}}$ and $k_o = 10.321 \cdot 10^6\,{}^{\mathrm{kg}}/_{\mathrm{m}^{3/2}\mathrm{sPa}^{1/2}}$ for "fast" reactions, and $E_a = 177\,{}^{\mathrm{kJ}}/_{\mathrm{mol}}$ and $k_o = 686.1\,{}^{\mathrm{kg}}/_{\mathrm{m}^{3/2}\mathrm{sPa}^{1/2}}$ for "slow" reactions[1]. Note that since this model is a function of temperature and partial pressure of oxygen, and not a function of the film coefficient, the mass loss rate cannot be packed into a B' table without assuming a normalizing film coefficient. In the true kinetic limit, the enthalpy will be defined by the edge gas composition (neglecting the influence of pyrolysis gas) as rapid diffusion equilibrates the composition. Often, this will be assumed to be in chemical equilibrium as dissociated species are likely to recombine at the low temperatures where the kinetic limit applies, especially in the presence of highly catalytic condensed carbon surface.

Transition Regime

In the *transition regime*, heterogeneous reaction rates are high enough relative to boundary layer diffusion rates that the reactions will be limited to a certain extent by the availability of gas phase reactants, but the rates are not high enough to completely consume the reactants as in the diffusion limit. Analysis of the transition regime generally focuses on reacting CFD or boundary layer analysis coupled with a heterogeneous reaction mechanism driving the surface boundary condition (i.e. neglecting surface shape change). Two early examples are those of Scala [46] and Welsh and Chung [47]. Many modern reaction mechanism studies build on the model of Zhulktov and Abe [48]. Due to the complexity of analysis required, this regime will not be considered in the present MEDLI reconstructions and is left as an opportunity for future work.

[1]Tim Risch pointed out in private communication that there was an error in the units published by Scala and their subsequent use in the ACE manual sample problem set. This can be attributed to a missing R_b term in the text of [46], which has been included in Equation 5.9.

ACE Kinetics Model

In seeking to obtain an approximate solution for kinetically-limited recession, Kendall proposed a model in the Aerotherm Chemical Equilibrium (ACE) code [40] (later extended by Milos and Chen [45]) assuming that one or a small number of heterogeneous reactions are slow relative to all of the other homogeneous and heterogeneous reaction rates. In this scenario, the gas phase ablation products are assumed to be in chemical equilibrium, but only a portion of the char atoms (determined by the slow reactions) are able to "react" with atoms from the boundary layer and pyrolysis gas. To simplify the following discussion, it is assumed that the char is pure carbon.

Limiting the amount of char that can enter the ablation products is enabled by defining a new element of *non-reactive carbon* (denoted here by atomic symbol $C^{(nr)}$) with the same atomic weight as normal *reactive carbon* (denoted with the conventional atomic symbol C). Most carbon-containing species in the chemical equilibrium solution, such as CO and CO_2, are defined to exist with reactive carbon and reactive carbon can only exist in gas phase. Non-reactive carbon can exist in condensed and gas phase, but only exists in gas phase as sublimation species (species containing only carbon such as $C^{(nr)}$ and $C_3^{(nr)}$). With this chemical system established, the carbon content in char is defined to be non-reactive carbon in $\tilde{\omega}_{k_c}$. The heterogeneous reaction model then converts an appropriate amount of non-reactive carbon to reactive carbon through the $\tilde{B}'_r$ term in a modified mass balance equation (Equation 5.3)

$$\tilde{\omega}_{k_w} = \frac{\tilde{\omega}_{k_e} + B'_c\tilde{\omega}_{k_c} + B'_g\tilde{\omega}_{k_g} - B'_f\tilde{\omega}_{k_f} + \tilde{B}'_r}{1 + B'_g + B'_c - B'_f}. \tag{5.10}$$

Using this mass balance, the typical diffusion limit solution approach is followed, whereby B'_c is determined such that non-reactive carbon is saturated in the ablation products. Keeping in mind that non-reactive carbon can only exist as sublimation species, only a small amount of non-reactive carbon will be present, and B'_c will be largely driven by the carbon called for by the heterogenous reaction. This will leave the ablation products undersaturated in reactive carbon and the recession rate will be less than the diffusion limited value.

The heterogeneous reaction model for $\tilde{B}'_r$ takes the form

$$\tilde{B}'_r = \frac{\mathcal{M}_k}{C^*_m} \sum_n \sum_i \left(\mu^P_{in} - \mu^R_{in}\right) \nu_{ki} \vec{R}_n \tag{5.11}$$

where $\mathcal{M}_k$ is the atomic weight of the limited element, μ^R_{in} is the reaction stoichiometric coefficient for reactant species i of reaction n, μ^P_{in} is the reaction stoichiometric coefficient for product species i of reaction n, ν_{ki} is the number of atoms of element k in species i, and $\vec{R}_n$ is the rate of reaction n. The rate of reaction for reaction n is given by

$$\vec{R}_n = K_{f_n} \left[\prod_{i,g} P_i^{\mu^R_{in}} - \frac{1}{K_{p_n}} \prod_{i,g} P_i^{\mu^P_{in}} \right] \tag{5.12}$$

where the products are only evaluated over gaseous species, and P_i is the partial pressure of species i. The forward rate coefficient is given by the Arrhenius model [40]

$$K_{f_n} = B_n T^{\phi_n} \exp\left(\frac{-E_{a_n}}{\mathcal{R}T}\right) \tag{5.13}$$

with modeling coefficients B_n $\left[{}^{\mathrm{mol}}/_{\mathrm{m^2 s Pa^{\mu^R_{gas}}}}\right]$, ϕ_n $[-]$, and E_{a_n} $\left[{}^{\mathrm{J}}/_{\mathrm{mol}}\right]$. The equilibrium constant is given by

$$K_{p_n} = \exp\left(-\frac{\sum_i \left(\mu^P_{in}\hat{g}_i - \mu^R_{in}\hat{g}_i\right)}{\mathcal{R}T}\right) \tag{5.14}$$

with $\hat{g}_i$ is the standardized Gibbs function for species i, and the sum is over gaseous and condensed species. If the reaction is considered irreversible, the second term in Equation 5.12 is neglected.

Considering Equation 5.12, it is apparent that the reaction rate is controlled by the quantity of available reactants. The quantities of these reactants depend on the equilibrium composition and not on any limits imposed by the rate of diffusion through the boundary layer. As such, this model is a kinetic limit model and not a true transition regime model. However, it does incorporate, to some extent, the competition between reaction rate

and available reactants, so it sometimes is used in place of much more complex transition regime models.

Since an explicit film coefficient is present in the definition of $\tilde{B}'_r$ which must be computed to evaluate the mass balance, a non-dimensionalizing film coefficient must be provided to obtain a recession solution. Propagating the non-dimensionalizing film coefficient term from Equation 5.11 into Equation 5.13, this coefficient is seen to essentially scale the pre-exponential constant, B_n, in the Arrhenius model. Therefore, even though the result of this model is a B'_c and corresponding H_w that can be put into a B' table, the evaluated solutions are only valid for the film coefficient used to compute the table (the film coefficient is not scaled out of the problem as it is in the diffusion limit). Accurate implementation of this model requires that either the table dimensions be increased to include the film coefficient, or the evaluation of the recession rate must be incorporated directly into the ablation simulation.

Figure 5.5 shows the recession predicted by the ACE kinetic model with coefficients defined to match the Scala "fast" and "slow" models. For comparison, the equivalent diffusion limit and pure kinetic limit solutions are also shown. A number of features can be identified. First of all, note the perhaps obvious difference between the two Scala models, with the "fast" model showing more recession at a given temperature than the "slow" model. Also note that the ACE model yields the same results as Equation 5.9 plotted with green lines when the reaction model is defined consistently. Note, however, that the ACE model departs from Equation 5.9 as the recession rate approaches B'_c of about 10^{-2}. This is caused by the ablated carbon reducing the partial pressure of O_2 in the equilibrium ablation products mixture from the value of $P_{O_2} = 0.21\,\mathrm{atm}$ used in the Scala model. Once this happens, the ACE models show similar two-plateau responses as the diffusion limit model does, albeit with transitions at increasingly higher temperatures as the heterogeneous reaction rates are decreased. In this regard, the ACE model is a desirable practical implementation of a kinetics model as it provides a smooth transition to a diffusion limit-like solution at higher temperatures, as opposed to the unreasonably high recession rates predicted by Equation 5.9 at high temperatures.

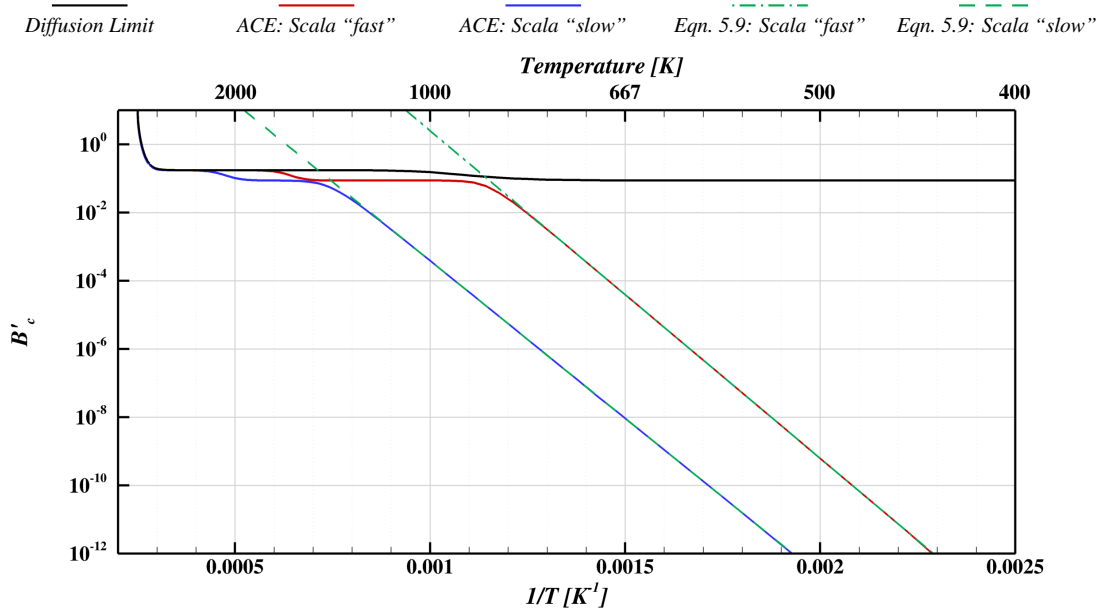

Figure 5.5. ACE implementation of Scala "fast" and "slow" carbon kinetics. Nondimensionalized by $C_m^* = 0.14647\,{}^{\mathrm{kg}}/_{\mathrm{m^2 s}}$ and $R_b = 1\,\mathrm{m}$.

Fail and Phase Change Recession

Fail recession is the term used to describe recession that does not alter the thermochemical state of the gaseous ablation products. This includes mechanical failure (spallation, erosion) and melting followed by melt flow. Fail recession, melting notwithstanding, will not alter the enthalpy of the recessing material. The fail enthalpy, H_f, in this case is set to match the char enthalpy to offset the additional energy flux in the $\dot{m}_c'' H_c$ term. The fail recession rate, B_f', can be set to a function of shear stress if desired, or it can also be modeled as a percentage of the thermochemical B_c'.

Recession due to phase change is generally assumed to occur at a constant temperature for a given pressure, and the mass loss rate is given by

$$\dot{m}_c'' = \frac{\dot{q}_{inc}'' - \dot{q}_{cond_s}''}{\Delta H_f^o}, \tag{5.15}$$

where ΔH_f^o is the latent heat of fusion, $\dot{q}_{inc}''$ is the net incident heat flux into the surface, and $\dot{q}_{cond_s}''$ is the solid conductive heat flux necessary to maintain the constant surface tem-

perature. Melting is considered a form of fail recession, so it leaves the surface as $\dot{m}''_f$ with an enthalpy of H_f. Sublimation is not typically considered a form of fail recession as the mixture enthalpy of the ablation products will be affected. However, if sublimation is the dominant recession mechanism, Equation 5.15 is used to define the recession rate given the heat flux and the heat of sublimation. For both melting and sublimation, the mass loss rate does not scale uniformly with film coefficient, and cannot be reasonably represented with a B' table.

5.3 Roughness and Blowing Effects

In conventional engineering-level ablation analysis, the evaluation of the environment terms in the SEB (Equation 5.8) is decoupled from the ablation analysis. However, the physical fluid and solid systems are strongly coupled. Some of the species diffusion effects are addressed by the assumptions that go into the B' recession model, and will not be addressed here. Of interest here is the fact that the convection of the ablation products from the surface, generally referred to as *blowing*, changes the wall boundary condition for the boundary layer analysis from an impermeable wall condition to one with a specified wall-normal velocity. This has an impact on the heat and mass transfer film coefficient of the boundary layer, generally reducing it. Furthermore, an ablated surface will generally be rough, so heat and mass transfer coefficients can be further augmented if the boundary layer becomes turbulent. Finally, the film coefficient may also be a function of surface temperature. In order to decouple the analysis, models must be used to account for these effects.

The effects of surface roughness and hot wall corrections will not be explicitly addressed in this work and are only mentioned here for completeness. Blowing, on the other hand, is addressed by the blowing model used in the CMA code [36], described further by Kays et al. [49], and given by

$$\frac{C_h^*}{C_h^*|_o} = \frac{2\lambda B'_o}{e^{2\lambda B'_o} - 1} \tag{5.16}$$

where

$$B'_o = \frac{\dot{m}''_g + \dot{m}''_c}{C^*_h|_o} \tag{5.17}$$

and $C^*_h|_o$ is the film coefficient evaluated by boundary layer analysis with a smooth and impermeable wall (sometimes referred to as the *unblown film coefficient*). The variable λ is the blowing reduction parameter and is taken to be 0.5 for laminar flow and 0.4 for turbulent flow. All instances of C^*_h mentioned previously in this chapter use the film coefficient corrected for the effects of blowing (sometimes referred to as the *blown film coefficient*). The dependence of the film coefficient on the blowing rate (and roughness model, if included) introduces further non-linearity to the SEB which must be accounted for in the solution.

5.4 Reconstruction Considerations

Much of the discussion in this chapter has focused on typical *forward*, as opposed to inverse, analysis used to predict material response given boundary conditions. In this section, complications introduced in inverse analysis is discussed.

In reconstruction problems to this point, it has been generally assumed that the IHCP boundary condition is the heat flux as that is typically how the problem is addressed in the literature. However, as was shown in Section 4.3, it is possible to formulate the IHCP to reconstruct the film coefficient (or any other environment term in Equation 5.8) as long as the other environment variables are known. If a B' recession model is used, the film coefficient must be determined since it is needed to define the dimensional mass flux for the surface recession calculation. Since the film coefficient is likely the most uncertain term in the SEB, it will generally be the environment variable of interest in a reconstruction on an ablator. Contributions from other terms and from surface recession can have a considerable effect on the behavior of the sensitivity coefficients and the stability of the IHCP problem.

First of all, an ablating surface can recess past an embedded thermocouple (sometimes referred to as burn-through), either in the physical experiment or in the material response model. This is not necessarily a problem if the recession model is physically accurate.

However, the recession model is generally inaccurate and introduces non-negligible modeling errors that lead to a difference in burn-through times. Once burn-trough occurs, comparisons between measurement and model cannot be made and the reconstruction will be unable to continue unless other measurements at greater depth are available to inform the reconstruction.

Secondly, variations in the other terms of the SEB, such as the radiation and net ablation energy release, can lead the TC response to be more or less sensitive to the film coefficient at different times in the reconstruction, the extent of which can be dependent on the film coefficient. This can increase the non-linearity of the IHCP. In extreme cases, such as those experienced on MSL, the TCs can become completely insensitive to the film coefficient. Recall that the film coefficient is multiplied by the term $(H_{rec} - H_w)$ in Equation 5.8. If this goes to zero, the TCs will become insensitive to C_h^* and the reconstruction will likely become unstable (recall the example in Section 4.3).

However, in a reconstruction the SEB does not have to be evaluated in the traditional forward sense. In a forward problem, the desired result of the SEB is the solid conductive heat flux. The solid conductive heat flux is the term that the TCs actually respond to, because this is the actual boundary condition driving the governing heat equation. If an IHCP reconstruction algorithm were able to define the conductive heat flux on the surface, the SEB could be solved in a separate step for the environment term of interest, and could possibly recover from the film coefficient becoming momentarily undefined due to modeling errors.

As was mentioned in Section 1.2, the nominal recession model used for the MEDLI analysis was demonstrated to over-predict the recession seen in flight, which means that reconstructions will be challenged by the near surface TC burning out earlier than it should in most models. The fact that the recovery enthalpy and wall enthalpy are of similar magnitude shortly after peak heating means that the film coefficient will likely become insensitive at this point as well. In order to provide a means of working around these issues and robustly reconstructing the film coefficient from the MEDLI data, a decoupled approach is proposed herein in which the IHCP will determine the solid conductive heat flux and the

SEB will be solved in a separate step for the film coefficient. It is also shown how this approach can be used to evaluate the feasibility of different recession models based on a single IHCP reconstruction.

6. DECOUPLED SEB RECONSTRUCTION APPROACH

To address some of the limitations mentioned in Section 5.4, a method is proposed in this chapter whereby the surface energy balance solution (and any associated surface recession) is decoupled from the IHCP reconstruction and solved in a separate step following the IHCP reconstruction. The theoretical basis for this method is presented, the code implementation is briefly described, and finally two verification examples and a comparison to a conventional coupled reconstruction are presented to demonstrate the level of error introduced by the decoupling.

6.1 Decoupling Theory

Consider the non-linear 1-D heat equation

$$C\frac{\partial T}{\partial t} - \frac{\partial}{\partial x}\left(k\frac{\partial T}{\partial x}\right) = 0 \tag{6.1a}$$

on the domain

$$x_0 \leq x \leq L \tag{6.1b}$$

with boundary and initial conditions given by

$$-k\frac{\partial T}{\partial x}\bigg|_{x_0} = \dot{q}''(t) \tag{6.1c}$$

$$T(L,t) = g(t) \tag{6.1d}$$

$$T(x,0) = f(x) \tag{6.1e}$$

that satisfy all conditions necessary to yield a unique solution for $T(x,t)$ for $t > 0$. Two time-varying locations on the domain are defined such that

$$x_0 \leq x_s(t) \leq x_m(t) \leq L, \tag{6.2}$$

for $t > 0$ (the temporal dependance is omitted from subsequent nomenclature for clarity). If a second similar problem is defined as

$$C\frac{\partial Y}{\partial t} - \frac{\partial}{\partial x}\left(k\frac{\partial Y}{\partial x}\right) = 0 \tag{6.3a}$$

on the restricted spatial domain

$$x_s \leq x \leq L \tag{6.3b}$$

with boundary and initial conditions given by

$$Y(x_s,t) = T(x_s,t) \tag{6.3c}$$

$$Y(L,t) = g(t) \tag{6.3d}$$

$$Y(x,0) = f(x), \tag{6.3e}$$

and C, k, g, and f identical to those in the first problem (only Equation 6.3c changes), then the uniqueness of the solution to Equation 6.1 implies that

$$Y(x_m,t) = T(x_m,t) \tag{6.4}$$

for any x_m on $[x_s, L]$ for $t > 0$. In the subsequent discussion, the system given by Equation 6.1 is referred to as the *full system*, and the system given by Equation 6.3 is referred to as the *restricted system*.

Taken one step further, if the two problems are identical except for the extent of the spatial domain and if the equality of Equation 6.4 is enforced, then the uniqueness proper-

ties of the heat equation solution require that the boundary condition on the surface of the restricted system must be given by Equation 6.3c (or the Neumann equivalent). Notice that stated this way, the problem takes the general form of an inverse problem. Also notice that the only restrictions on the interior points x_s and x_m above are that they are on the domain and that $x_s \leq x_m$. The implication of this is that an IHCP reconstruction is not only a reconstruction of the boundary condition, but a reconstruction of the whole temperature field *consistent with the governing equation and measurements at a point, x_m, on the domain.*

This result can be used in the reconstruction of boundary conditions when the location of the true boundary is unknown at the time of reconstruction. The restricted system represents the true physical system with the surface at x_s and the measurements describing $Y(x_m, t)$. IHCP algorithms are used to reconstruct an appropriate boundary condition at x_0 ($\dot{q}''(t)$ in Equationn 6.1c) for the full system that yields $T(x_m, t) = Y(x_m, t)$. The resulting solution of the full system can then provide the T and $\frac{\partial T}{\partial x}$ needed to compute $\dot{q}''_{cond_s}$ in the surface energy balance (Equation 5.8) for any possible surface location on $x_0 \leq x_s \leq x_m$ that is consistent with the measurements. Any information regarding the location of x_s can then be incorporated to define the boundary conditions, or a separate model describing the motion of x_s with time (even one that is a function of T and $\frac{\partial T}{\partial x}$ at x_s) can be evaluated separate from the IHCP solution. The key is that the temperature field reconstruction is decoupled from the surface recession evaluation.

These concepts are illustrated graphically in Figures 6.1 and 6.2. Figure 6.1 shows the temperature solution at time t_1 of the full system that has been reconstructed to provide the measured temperature at the measurement location x_m. Two potential values of x_s are shown as x_1 and x_2. Under a set of assumptions that specifies x_1 as the true surface location, the surface temperature must be $1200\,\mathrm{K}$ in order to provide the proper response at the sensor. In this case, the temperature at x_2 is simply an internal temperature. Alternatively, under a different set of assumptions that suggest x_2 is the true surface location, the surface temperature must be $900\,\mathrm{K}$ to satisfy the governing equation and match the sensor measurement. In this case, the temperature at x_1 is outside the true domain and is un-physical under these recession assumptions. Figure 6.2 shows a plot of the entire temperature field, with

contours of both full (thin black lines) and restricted (colored lines) systems co-plotted. The thick black line indicates the location of the true surface defining the restricted system. A slice through this surface at constant depth (magenta line) shows the temperature profile that defines the field (i.e. the embedded TC measurement) along with the governing equations.

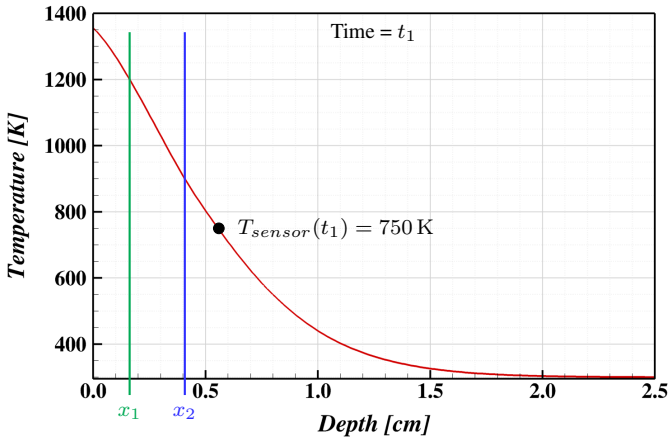

Figure 6.1. Illustration of a heat equation solution at a specific time showing how different combinations of boundary location and boundary value could yield an internal temperature value consistent with measurement.

These two figures highlight a significant caveat that should be addressed: the solutions on the extended domain ($x_0 \leq x < x_s$) are fictitious with respect to the real system and they can include physically impossible temperatures (for example on a melting material, temperatures in this region will exceed the melt temperature). The uniqueness property only requires that the restricted system solution and any full system solution be equal on the restricted domain. If C and k are functions of temperature and the full system solution on the extended domain includes values of T that are outside the range of Y, then it may be possible to obtain multiple different solutions to the full system that differ only on the extended domain if different functions for $C(T)$ and $k(T)$ are used (clearly, these functions will only differ for values of T outside the range of Y). Since material properties at fictitious temperatures are fictitious themselves, they may be carefully chosen to improve the stability of the full system inverse reconstruction.

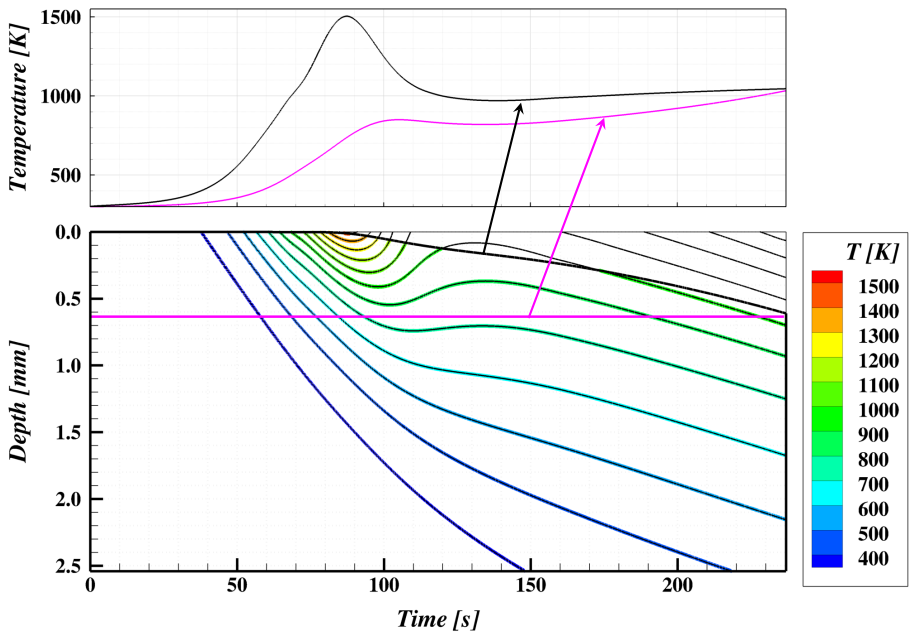

Figure 6.2. Illustration of a temperature field with a recessed surface shown relative to the fictive non-recessed surface. Note that a cut at a constant depth gives a temperature trace that corresponds to the expected response of a TC at that depth (shown as magenta lines), while the thick black line indicates the location of and conditions on the recessing surface.

6.1.1 Pyrolysis Gas Decoupling

It has been shown that the temperature field reconstruction can be computed without knowledge of the exact surface location. Decomposing ablators will have an additional partial differential equation governing the flow of pyrolysis gas. In order to fully reconstruct the behavior of these materials, additional constraints must be addressed. Development of models for the true physical nature of the pyrolysis gas flow is an area of open research and is beyond the scope of this work. However, there are two common modeling assumptions made regarding the flow of pyrolysis gas relevant here: zero residence time and steady porous flow.

Older ablation models used for the majority of engineering-level ablation analysis (such as CMA [36] and FIAT [50]) assume that the pyrolysis gas residence time in the interior of the ablator domain is negligible. The decomposition models are integrated through

the domain and any pyrolysis gas produced is assumed to be immediately present at the surface. With this assumption, there is no additional partial differential equation required, and a reconstruction can be completed as previously discussed.

As modeling capability is developing to handle multi-dimensional problems, this assumption becomes difficult to implement since it is not clear where on the surface the pyrolysis gas should emerge from. Consequently, governing equations for the pyrolysis gas flow are necessary. The *CHAR* code used here assumes that the pyrolysis gas adheres to the steady Darcy's law for flow in porous media which relates the gas flow rate to the gradient of the pressure in the ablator pore space (the *internal pressure gradient*) according to

$$\dot{m}''_g = -\rho_g \frac{\tilde{\kappa}}{\mu} \nabla P, \tag{6.5}$$

where $\dot{m}''_g$ is the local mass flux of pyrolysis gas, ρ_g is the gas density, μ is the gas viscosity, $\tilde{\kappa}$ is the permeability tensor of the porous medium, and P is the internal pressure. While the details of derivation are left to reference [34], *CHAR* solves an additional parabolic partial differential equation for the internal pressure field that satisfies the gas continuity (conservation of mass) equation. With this approach, the pyrolysis gas can stay resident in the ablator for a finite amount of time, and the flow rate (and direction in multi-dimensional problems) is dependent on permeability. The permeability is generally defined to be a function of the state of decomposition, with higher permeability in decomposed char than in virgin material. When *CHAR* is used to calculate the response of a material for which the model was developed with the zero residence time assumption, the permeability of the virgin and char states are set as low and as high as possible, respectively, that provide stable solutions. In this way, the pyrolysis gas residence time is minimized.

For the decoupled SEB approach proposed here, the pyrolysis gas mass flow rate at the surface must be determined since that will likely influence any thermochemical ablation model. For a reconstruction where pyrolysis gasses are handled with the zero residence time assumption, the surface pyrolysis gas mass flux can be determined by integrating the

decomposition model on the restricted domain $[x_s, L]$. For a model that implements additional governing equations, the pyrolysis mass flux must be determined from the coupled solution of the governing equations. This introduces a scenario in which the decoupling approach may break down.

Depending on the material permeability, the internal pressure gradient can be large and non-linear. By itself, this does not invalidate the decoupling theory, at least for the steady porous flow assumption, as the pressure field is governed by a parabolic PDE like the temperature field. However, in most reconstructions, the pressure will not be known at an internal location like the temperature will, the pressure will generally only be known on the true surface. Using the known pressure boundary condition on the full system boundary with a material having low permeability will yield internal pressures that are too high relative to the case where the known pressure boundary condition is applied on the boundary of the restricted system. If the pyrolysis gas enthalpy or the solid thermal conductivity are functions of pressure, errors will be introduced (although they will likely be small as these properties generally vary with the $\log$ of pressure). More significantly for this case, though, is that if the mass flux field is not uniform in the vicinity of x_s, then the decoupled reconstruction may not be able to define $\dot{m}''_g$ with sufficient accuracy.

To illustrate this, Figure 6.3 shows an example of a full system reconstructed pressure field overlaid on a true restricted system pressure field with "low" char permeability (using values recommended for the TACOT material of $\tilde{\kappa}_c = 2.0 \times 10^{-11}\,\mathrm{m}^2$ and $\tilde{\kappa}_v = 1.6 \times 10^{-11}\,\mathrm{m}^2$). Although the differences are not very large, some differences are seen between the contour lines in the region of most rapid decomposition ($70\,\mathrm{s}$-$130\,\mathrm{s}$). At a fixed depth, the top plot indicates that the full system reconstruction pressure exceeds that of the true system. However, if the permeability values are set to artificial values to mimic CMA ($\tilde{\kappa}_c = 1.0 \times 10^{-8}\,\mathrm{m}^2$ and $\tilde{\kappa}_v = 5.0 \times 10^{-14}\,\mathrm{m}^2$), the pressure field comparison in Figure 6.4 is obtained. In this case, the full system reconstruction pressure matches the true restricted system pressure very closely.

For the MEDLI data being addressed in this work, the PICA material model was developed in FIAT using the zero residence time assumption. As such, the *CHAR* implementa-

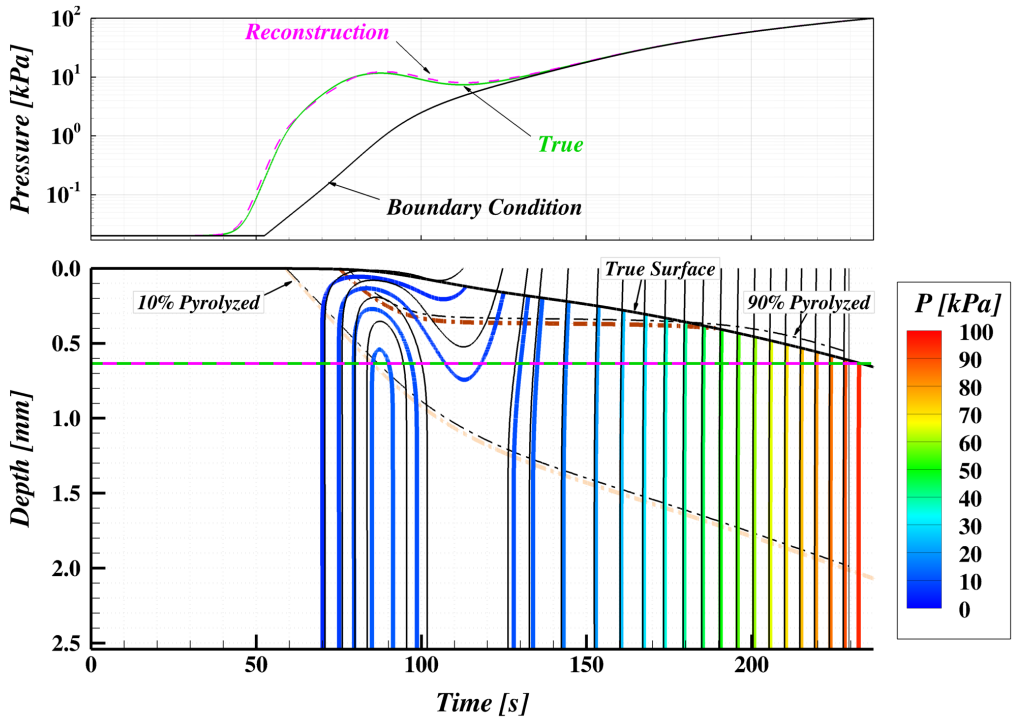

Figure 6.3. Illustration of pressure field with a full system reconstruction overlaid on a true restricted system solution. TACOT recommended permeability values of $\tilde{\kappa}_c = 2.0 \times 10^{-11}\,\mathrm{m}^2$ and $\tilde{\kappa}_v = 1.6 \times 10^{-11}\,\mathrm{m}^2$. Note that line contours are not uniformly spaced. The thick black line indicates conditions on the recessing surface, the indicated 10% pyrolysis line denotes the boundary between virgin and pyrolyzing material, and the indicated 90% pyrolysis line denotes the boundary between the pyrolyzing and char material.

tion of the model uses an artificially high permeability in the char, which leads to a low and linear pressure gradient that minimizes the effect of this modeling assumption. However, a different approach may be required to perform this sort of analysis with future material models that use more realistic permeability models.

6.1.2 Previous Uses of Decoupled SEB Reconstruction

This approach of decoupling the surface recession calculation from the IHCP solution has been used to some extent in two previous studies of reconstruction of environments on ablative heatshield materials. These are presently described and the differences proposed in this study are outlined.

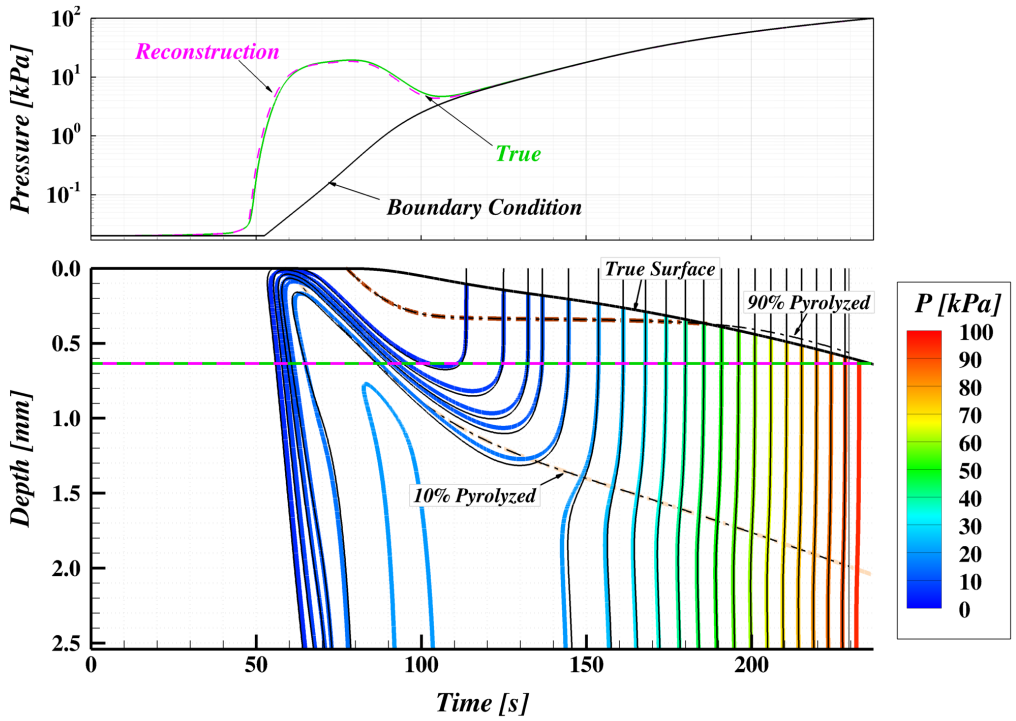

Figure 6.4. Illustration of pressure field with a full system reconstruction overlaid on a true restricted system solution. CMA-like behavior of pyrolysis gas flow obtained with permeability values of $\tilde{\kappa}_c = 1.0 \times 10^{-8}\,\mathrm{m}^2$ and $\tilde{\kappa}_v = 5.0 \times 10^{-14}\,\mathrm{m}^2$. Note that line contours are not uniformly spaced. The thick black line indicates conditions on the recessing surface, the indicated 10% pyrolysis line denotes the boundary between virgin and pyrolyzing material, and the indicated 90% pyrolysis line denotes the boundary between the pyrolyzing and char material.

As was described in Section 1.2, the team reconstructing the MEDLI flight data encountered problems with the recession model in their reconstructions. After discussions and collaboration among several individuals at NASA (present author included), it was proposed that reconstructing on a system with suppressed recession would be a meaningful bounding case, and the decoupling approach above was identified. Mahzari et al. used this idea in [7] to show bounding environments and assessed the sensitivity of a combined convection and ablation "heat rate" given by $\dot{q}_s'' = C_h^*(H_{rec} - H_w) + \dot{m}_c'' H_c + \dot{m}_g'' H_g - (\dot{m}_c'' + \dot{m}_g'') H_w$ for several assumed recession profiles using the temperature derivative evaluated from the no-recession reconstruction. The assumed recession profiles were defined by using uniformly-scaled pre-flight recession estimates. As they did not evaluate a recession model needed to

calculate the ablation terms, they could not isolate the film coefficient in their reconstructions.

Frankel et al. [18] have recently proposed a similar two-step reconstruction process, albeit with a different approach on the IHCP algorithm. However, in their paper, they provide very little discussion about how the surface energy balance affects recession and environment reconstruction. They only consider melting materials, so the surface location is easily identified by the isotherm corresponding to the material melt temperature.

The current work advances this concept by incorporating the thermochemical ablation surface energy balance into the process for reconstruction of environments on materials with more complicated oxidation recession mechanisms. It is also shown how this approach can be used to assess the feasibility of proposed recession models.

6.2 Implementation

A code has been developed to evaluate the SEB and recession model given a set of *CHAR* solution files. A number of support modules are implemented to manage the large array of data required. Each module reads in files in the same format that *CHAR* either reads or writes to enable seamless integration, and the material model routine has been built to provide consistent behavior with the model implemented in *CHAR* (refer to [34] for details of the model form). For the data structures that fulfill largely tabulation and lookup functions (trajectory, material model, and temperature field), routines have been implemented to verify the accuracy of the interpolation and computation routines. It is implemented in the C++ language and utilizes approximately 5,000 lines of code.

While many aspects of the code focus on managing data from other codes and models, the thermochemical ablation model is the core element of this code. The ACE kinetics model presented in Section 5.2 is the primary physics-based kinetics model implemented. Several attempts have been made to implement a stand-alone chemical equilibrium solver (based on [41–43]) with the reaction model and its analytical Jacobians built into the solver. However, the chemical equilibrium problem is well known to be somewhat unstable [41,

42, 51] and the algorithms implemented could not obtain solutions with enough reliability to work in this application. The multiphase Gibbs function continuation method (MPGFC) presented by Scoggins and Magin [43] is purported to be completely robust in solving the chemical equilibrium problem. This algorithm fundamentally requires that the elemental composition of the mixture under consideration be constant through the solution process[1]. Unfortunately, the elemental composition in the ACE recession model varies based on the solution species composition, which will vary through the solution[2].

In order to implement the ACE kinetics model with sufficient reliability to complete this work, some simplifications were required. First of all, the implementation of the MPGFC in the *Mutation++* library [52] was used, with only minor modifications, to evaluate the multi-phase chemical equilibrium solutions. Secondly, to get around the requirement that the elemental composition remain fixed, the solver must be formulated in such a way that the *Mutation++* algorithm can be used to compute the diffusion limited recession solution for an elemental composition defined by estimated values of B_c' and $\tilde{B}_r'$, after which the solution is used to update the estimates of B_c' and $\tilde{B}_r'$ until convergence is obtained. The process is slow but reliable; however, it limits problems to a single limiting kinetic reaction. Finally, this implementation presently limits problems to those with the char being composed of pure carbon.

The algorithm to evaluate a kinetically limited recession rate is shown graphically in Figure 6.5. Each of the three colors denotes a different logical routine in the code, with blue denoting the solution of B_c', red denoting solution of $\tilde{B}_r'$ given a B_c', and green denoting evaluation of the diffusion limit solution using the *Mutation++* library given B_c' and $\tilde{B}_r'$. This final step performed by *Mutation++* provides an evaluated B_c' and a corresponding vector of species mole fractions. The species mixture is used to evaluate $\tilde{B}_r'$ according to Equation 5.11 which is then compared to the guessed value. Once the red routine has converged to a value of $\tilde{B}_r'$, the B_c' value provided by *Mutation++* is compared to the

[1] In order to solve for B_c' in Equation 5.3, the MPGFC algorithm defines the wall gas elemental composition containing a large amount of char and solves for multi-phase equilibrium. At the conclusion of the iteration, the amount of char that was actually taken into gas phase is computed and used to determine B_c'.

[2] It seems likely that this additional non-linearity undermines the solution robustness for the Gibbs free energy minimization algorithms tested as kinetic solutions are generally more unstable than diffusion limit solutions.

B'_c guess in the blue routine and updated until convergence. Both of these convergence routines use a bisection-limited Newton solver (if the Newton update is undesirable, the update is chosen to halve the bounding interval) since natural bounds are inherent in the problem ($0 \leq \tilde{B}'_r \leq B'_c$, and $0 \leq B'_c \leq 100$, where $B'_c = 100$ is an unrealistically large value). Finite-difference approximations of the function residual derivative are used, and if the derivative evaluates to zero, the guess is updated by bisection. In Figure 6.5, the boxes "Compute B'_c" and "Compute $\tilde{B}'_r$" are evaluated twice with perturbed values of B'_c and $\tilde{B}'_r$ respectively for the finite difference derivative calculation.

Verification of the surface thermochemistry module was performed by code-to-code comparison and comparison to an analytic solution. For the diffusion limit case, comparison was made to the TACOT B' table, which is shown in Figure 6.6, with excellent agreement seen[3]. To verify the kinetic reactions, comparison was made to the models of Scala, and were shown previously in Figure 5.5, again with excellent agreement at low temperatures where it is expected to agree.

Recession models are specified by chemistry files (which define the permissible species in the gas phase and the mole fractions of the edge and pyrolysis gases) and the ACE model inputs. The pre-exponential factor in the ACE model, B_n, can optionally be entered as a function of temperature. In addition to these model parameters, the code can compute recession based on a "scaled" recession model. This model evaluates the diffusion limit recession rate, scales B'_c down by a constant percentage, and then recomputes the corresponding enthalpy of the ablation products.

The code is setup to compute SEB reconstructions for a range of recession model inputs in a single execution. After reading input and data structure initialization, the trajectory is reconstructed for each combination of recession model inputs specified. Two options are

[3]A comment on the physics modeled in the presented table: in order to match the enthalpy at the higher B'_g values in the published TACOT table, it was necessary to allow excess carbon in the pyrolysis gas to condense. Technically this means that B'_c was negative, however the value of B'_c was simply zeroed out. This is a physical inconsistency in the published TACOT tables as the enthalpy of the condensed pyrolysis carbon is not accounted for. On the other hand, algorithms which solve for B'_c without explicitly solving for a condensed species mole number will not suffer from this, but will instead have an ablation product mixture that is over-saturated in carbon. In reality, this carbon likely would have condensed out inside the char layer through a process known as "coking", so the real modeling failure is in the assumption that $\tilde{\omega}_{k_g}$ is constant.

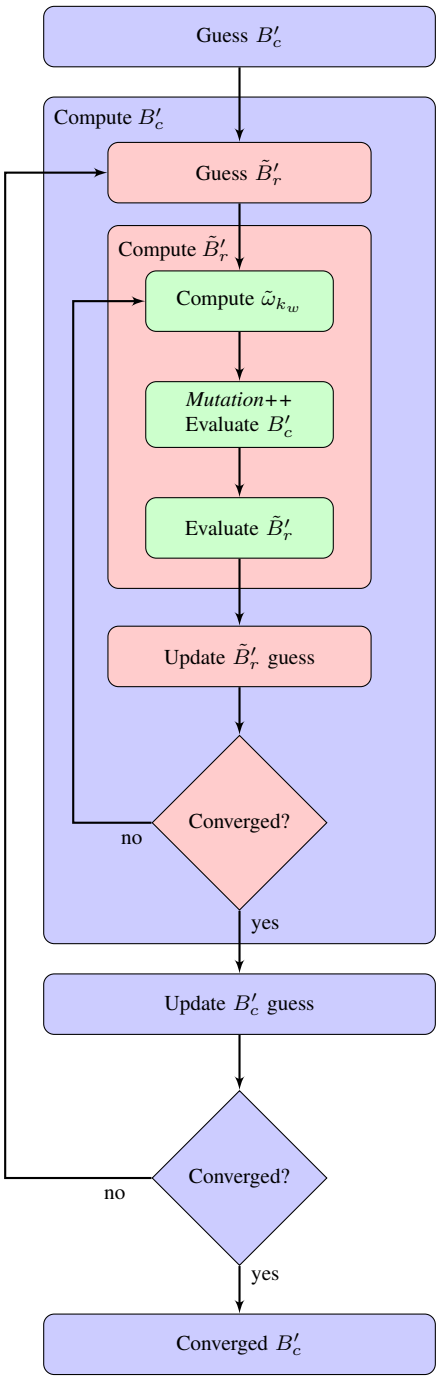

Figure 6.5. Flowchart for present implementation of ACE kinetic recession model.

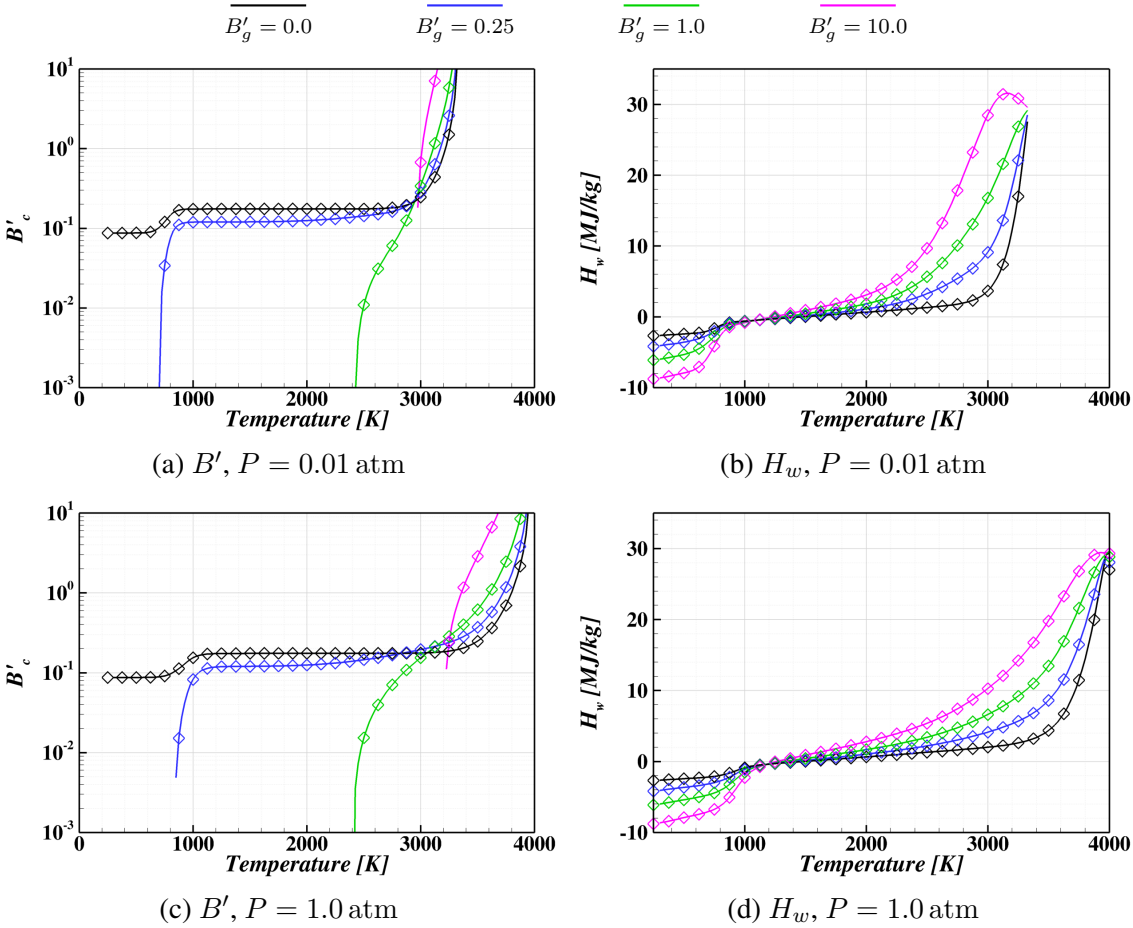

(a) B', $P = 0.01\,\text{atm}$ (b) H_w, $P = 0.01\,\text{atm}$

(c) B', $P = 1.0\,\text{atm}$ (d) H_w, $P = 1.0\,\text{atm}$

Figure 6.6. Verification of surface thermochemistry module by comparison to existing TACOT 3.0 B' table [25]. Lines evaluated by present implementation and symbols represent published table.

available for computing the SEB reconstructions, one explicit and the other implicit. The primary difference between the two options is the handling of the surface location (where properties are extracted for use in computing the recession and balance the SEB). The explicit algorithm determines the recession rate using properties from the surface location from the *previous* time step, whereas the implicit algorithm determines recession rate based

on properties that result from recession predicted in the *current* time step. This could alternatively be expressed as

$$\text{Explicit solution: } \dot{s}^{\nu=i}\big|_{x_s^{\nu=i-1}} \tag{6.6a}$$

$$\text{Implicit solution: } \dot{s}^{\nu=i}\big|_{x_s^{\nu=i}} \tag{6.6b}$$

where $\dot{s}$ denotes the surface recession rate (and represents here all variables evaluated to balance the SEB) and ν denotes the time step index.

In the explicit algorithm, the surface location x_s from the previous time step is used to extract the temperature, conduction flux, pressure, $\dot{m}_g''$, and solid density from the appropriate time solution in the temperature field data structure. The remaining material properties are evaluated at the corresponding conditions and time-dependent trajectory parameters are obtained. With that information, the explicit SEB kernel is called to find C_h^* which, along with the ablation terms determined from the specified recession model, balances the SEB. At this point, the computed C_h^* and ablation terms are written to an output buffer, the surface recession is calculated, and the loop repeats on the next time step. If the surface recession is seen to exceed a user-specified depth constraint prior to a specified time, the trajectory reconstruction is terminated.

The explicit SEB solution is obtained using an under-relaxed Newton method that seeks to sum all of the terms in Equation 5.8 to a tolerance of less than $10^{-8}\,\mathrm{W/m^2}$. The solver contains logic to detect and attempt to recover from an oscillating solution, and if the Newton solver fails, it will attempt to bracket the solution and converge using a bisection method. If the solver fails to find a solution, the trajectory reconstruction is terminated.

The implicit algorithm is similar, though instead of iterating on C_h^*, it iterates on $\dot{m}_c''$. By doing this, the surface location at the end of the time step can be defined, allowing solution and material properties to be extracted for use in balancing the SEB. Balancing the SEB in this manner, however, requires two nested Newton solvers, as C_h^* must be determined at the $\dot{m}_c''$ specified in each iteration of the external solver seeking to satisfy the SEB. As a result, the implicit algorithm requires considerably more computational effort than the

explicit algorithm, but it is believed that it may be more stable and accurate if the recession rate becomes large.

In an effort to minimize errors resulting from using the pressure boundary condition on a non-recessed surface when the char permeability is low, the temperature data structure has been designed to read in multiple fixed surface reconstructions, with each reconstruction having a different surface location. When properties are requested at a specific depth, the structure will provide results from the deepest surface reconstruction for which the requested point is in the domain.

6.3 Examples

The decoupled SEB reconstruction approach is demonstrated with two benchmark cases. A simulated graphite test case is considered first to point out several characteristics of the method without having to consider the contribution of pyrolysis gas. A similar TACOT case is then considered to address the complications introduced by pyrolysis gas. Both cases use the boundary conditions[4] shown in Figure 6.7; however, the film coefficient for the TACOT case is taken to be 20% of the value shown to maintain similar recession levels on the lower density material.

The task of verifying[5] the decoupled SEB tool is a challenging one. In this instance, much like IHCP examples presented earlier, verification is performed by producing simulated thermocouple data with *CHAR*, and comparing the reconstructed boundary conditions (based on the simulated data) to the original boundary conditions. An implicit assumption of this process is that *CHAR* is capable of producing simulated data consistent with the proposed physical model. Unfortunately, this is not strictly true, and in some cases the modeling fidelity of the decoupled SEB tool exceeds that of *CHAR*.

[4]Representative of the stagnation point of a ballistic low Earth orbit reentry of a blunt sphere-cone approximately the size of a CubeSat.

[5]Note that the nomenclature of Roache [53] is used here, with *verification* demonstrating an accurate implementation of a presented mathematical model. Whether or not the presented model accurately represents the physical system is the subject of *validation* and requires comparison to carefully designed experiments.

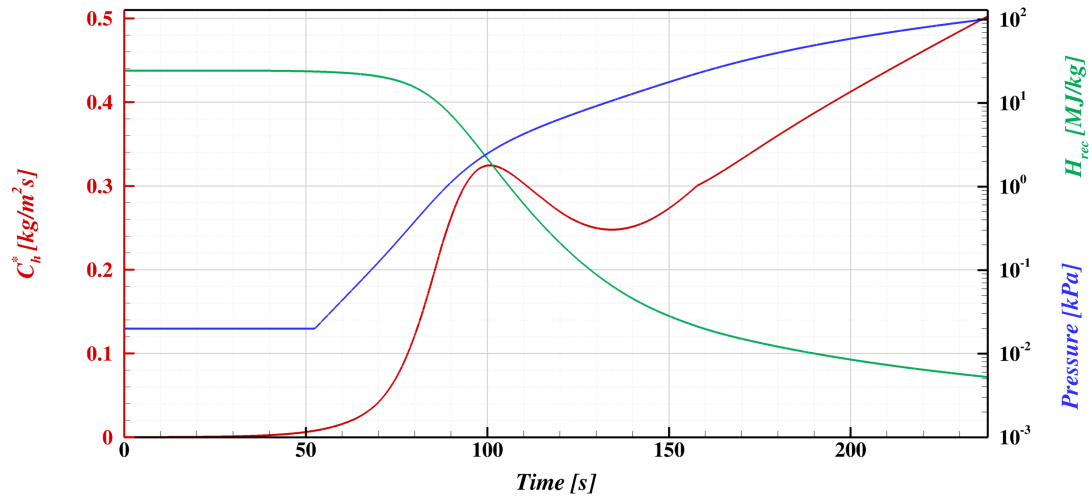

Figure 6.7. Boundary conditions for decoupled SEB example problems.

CHAR uses the B' table approach to compute surface recession, so all of the assumptions and limitations associated with that approach are contained in the simulated data of this exercise. One problem introduced here is that *CHAR* interpolates between solutions provided in the B' table to obtain terms needed to solve the SEB at the specific surface conditions. The decoupled SEB tool, on the other hand, computes the surface recession at the local conditions on the boundary, making interpolation between previous solutions unnecessary. In this regard, the decoupled SEB tool can more faithfully represent the proposed recession model than *CHAR* can. The effect of this inconsistency can be minimized by using an extremely refined B' table when generating the simulated data.

The other problem introduced by *CHAR*'s reliance on the B' model is that a kinetically-limited recession model cannot be faithfully represented. Recall from Section 5.2 that a B' table is formulated specifically to scale out the influence of the film coefficient, however kinetic models depend on film coefficient in a manner that cannot be scaled out. In order to faithfully represent a kinetically-limited recession model, *CHAR* would need to be modified to compute the recession thermochemical solutions needed to evaluate the SEB at each iteration of the thermal response solution. This capability is a goal of the *CHAR* development team and the thermochemistry module of the decoupled SEB tool has been designed

with eventual inclusion in *CHAR* in mind. As such, implementing this capability would not be beneficial for the present exercise as the module would essentially be used to verify itself. However, it is important to note that the goal of the present verification exercise is not to verify the accuracy of the recession thermochemical solution, but to verify the concept of evaluating recession based on solution of the SEB using inputs from a recession model and conditions from a non-recessing reconstruction of thermocouple data. It is possible to complete this verification using a diffusion limited recession model that can be placed in a B' form for *CHAR* to use in generating the simulated data.

Other limitations in *CHAR* affect the present exercise, but these are addressed as they are encountered in the following discussion.

6.3.1 Graphite

The material properties used in this case ($\rho = 1610\,{}^{\mathrm{kg}}/_{\mathrm{m}^3}$, $k = 8.7\,{}^{\mathrm{W}}/_{\mathrm{m\cdot K}}$, $C_p = 697\,{}^{\mathrm{J}}/_{\mathrm{kg\cdot K}}$, and $\epsilon = 0.9$) approximately represent graphite, a commonly considered ablator. It does not thermally decompose internally, so the effects of pyrolysis gas are not modeled. As it is pure carbon, the surface recession model shown in Figures 5.4(a) and (b) is representative of this material. However, the B' table used was much more refined than that presented in Figure 5.4, containing solutions on $5\,\mathrm{K}$ temperature intervals at 275 different pressure levels (approximately $2 \cdot 10^5$ individual thermochemical solutions) to minimize the error introduced by interpolation in *CHAR*. In order to similarly reduce the numerical error introduced by *CHAR*, 1000 elements are used to discretize the $40\,\mathrm{mm}$ domain, and the solution is integrated through time with $0.05\,\mathrm{s}$ time steps. Figure 6.8 shows the temperatures at depths of $3.175\,\mathrm{mm}$, $6.35\,\mathrm{mm}$, and $9.525\,\mathrm{mm}$. Since the IHCP solution is not the objective of the present verification, the simulated TC data was recorded with 16 significant figures to minimize quantization error. The similarity of the three TC traces is attributable to the relatively high thermal conductivity of the material. Note that recession in this case exceeds the depth of TC #1 at approximately $180\,\mathrm{s}$, thus TC #2 is used for reconstruction.

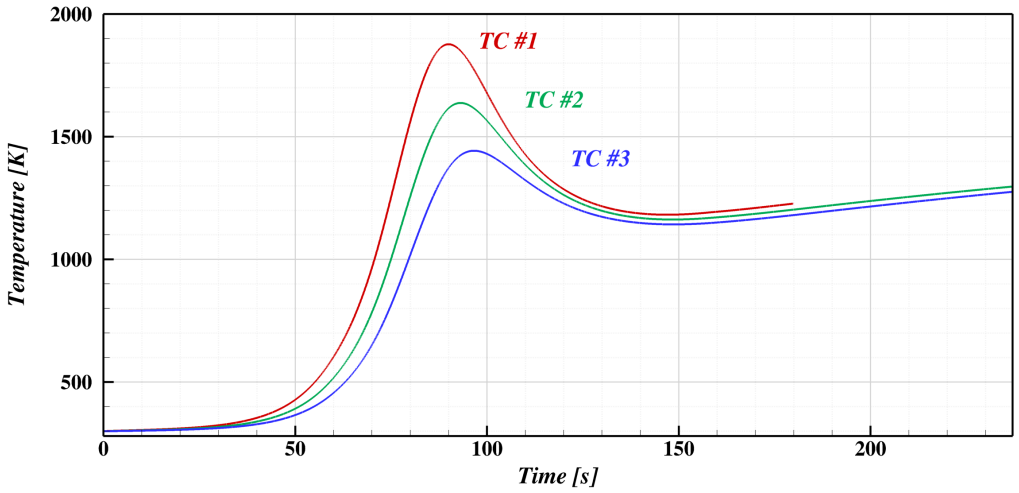

Figure 6.8. Simulated measured temperatures for graphite example problem reconstruction.

The non-recessing reconstructed temperature field is shown in Figure 6.9 (black lines) overlaid on the true temperature field (colored lines). Reconstruction of the heat flux on the surface of the non-recessing domain was performed using the SSD algorithm with a future time window of $3\,\mathrm{s}$, a regularization scaling parameter $\mathtt{a\_1} = -0.01$, and solution intervals of $0.05\,\mathrm{s}$. Since the material properties are not functions of temperature and heat flux was the reconstructed value, the inverse problem is linear and iterations were not used. Reconstruction was performed using a grid with 301 uniformly distributed elements, and the boundary of the non-recessing domain was located such that the restricted system initial surface location of $x = 0\,\mathrm{mm}$ was one element into the domain. Padding the reconstructed domain in this regard is done for two reasons, but the reason relevant to this case is that the decoupled SEB tool computes the conduction flux on the reconstructed domain using a finite difference approximation of

$$\dot{q}''_{cond_s} = -k_s \frac{\partial T_s}{\partial x}, \tag{6.7}$$

with T_s defined on the mesh nodes. Second-order central differences are used on most of the domain, but first-order one-sided differences must be used in the boundary elements. Padding the domain in this regard ensures that only the higher accuracy approximation

of $\dot{q}''_{cond}$ are used in the SEB reconstruction. The additional reason to pad the domain is discussed in Section 6.3.2.

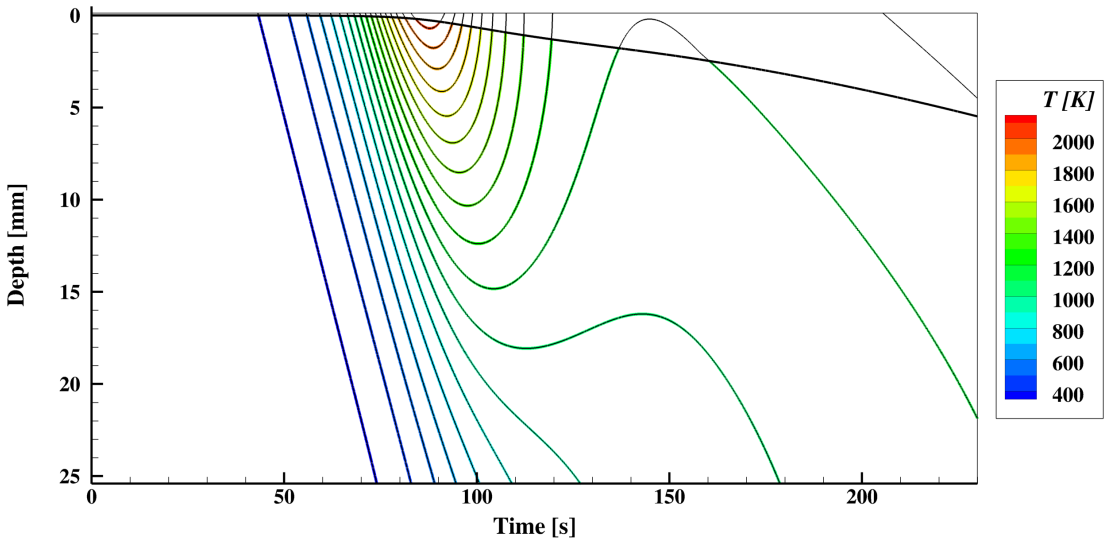

Figure 6.9. Reconstructed temperature field overlaid on the true temperature field. Thick black line indicates true recessed surface location.

Given the reconstructed temperature field shown in Figure 6.9, a number of options are available to the analyst with regards to reconstructing the recession profile with the decoupled SEB tool. First of all, explicit and implicit algorithms are available. Secondly, the time between SEB evaluations (i.e. the SEB reconstruction time step) can be varied. In this case, the temperature field is available with a resolution of $0.05\,\mathrm{s}$, but a coarser resolution could be used in reconstruction to assess the convergence behavior of the decoupled SEB algorithms and to approximate the results of using a temperature field evaluated at a coarser resolution[6].

Results of the SEB reconstruction are shown in Figure 6.10, with the film coefficient shown in 6.10(a), the surface location shown in 6.10(b), the enthalpy of ablation products shown in 6.10(c), and the aeroheating flux (Equation 5.7, the combination of the fluid conduction and boundary layer diffusion terms) shown in 6.10(d). For all of these quantities, plots of the reconstructed values differ from the true values by less than the line with of a

[6]The tool does not support interpolation in time, so only integer multiples of coarsening can be used.

legible plot, so separate plots are not made. Instead, this figure presents the percent error in each reconstructed value, and the absolute reconstructed values are shown qualitatively with the desaturated lines and symbols in these plots (symbols represent the true values). Both implicit and explicit solutions are included, and solutions with SEB reconstruction time steps of $0.5\,\mathrm{s}$, $0.1\,\mathrm{s}$, and $0.05\,\mathrm{s}$ are shown for each. Two qualifications on the presented results are the following: the relative error in the enthalpy of ablation products spikes as the nominal value passes through zero (high temperatures at peak heating are enough to offset the low heat of formation of ablation products to yield a positive value in this time period), and the high relative errors in surface recession at early times are due to the true value being very near zero.

Several observations can be made. It can be seen in all four plots that for both explicit and implicit algorithms, reducing the SEB reconstruction time step reduces the reconstruction error, as expected. Note particularly that the error in the finest explicit solution of the surface recession in 6.10(b) shows virtually no error, whereas the equivalent resolution implicit solution still shows errors reaching 0.75%. Even though the implicit algorithm is presumably more physically accurate since the recession depth and recession rate are time-consistent, *CHAR* is explicit in mesh motion. The explicit decoupled SEB algorithm makes that same assumption and yields the same result as *CHAR*. The better physical accuracy of the implicit algorithm is demonstrated by the improved accuracy and relative insensitivity of the implicit $\dot{q}''_{aero}$ solution (one of the terms directly balanced in the SEB) compared to the explicit algorithm. Recall from Figure 5.4 that B'_c for this material exhibits a dual-plateau behavior, with the transition between plateau levels being pressure and temperature dependent. The peak in SEB reconstruction errors observed at $59\,\mathrm{s}$ appears because the temperature and pressure at this time place B'_c in this transition regime, and interpolation error was introduced by *CHAR* when simulated data was generated.

Of the four quantities presented, only the film coefficient in 6.10(a) is an actual boundary condition (the others are the result of boundary condition and thermal response). Given that, it is fortunate that the decoupled SEB produces reconstructions accurate to better than 0.1% for both algorithms and all temporal resolutions. In general, the explicit algorithm

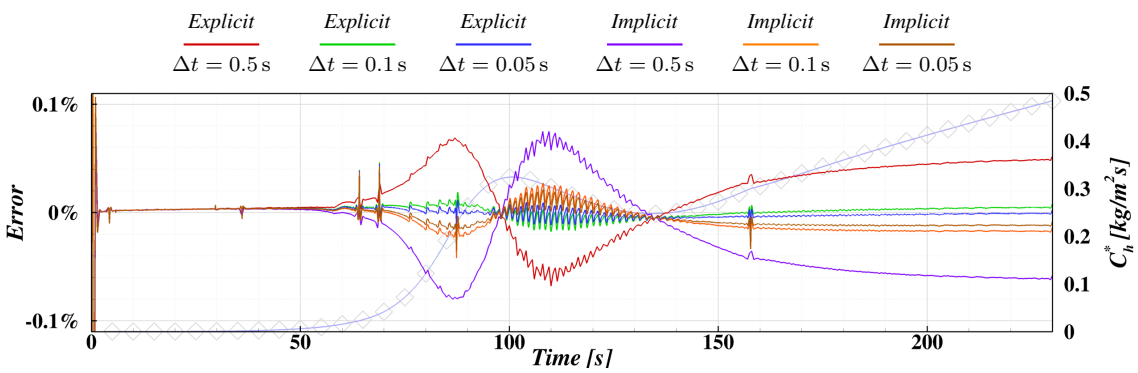

(a) Film Coefficient

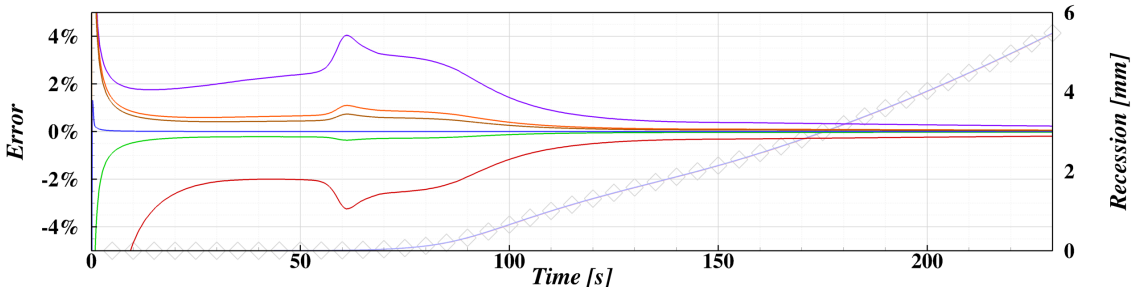

(b) Recession

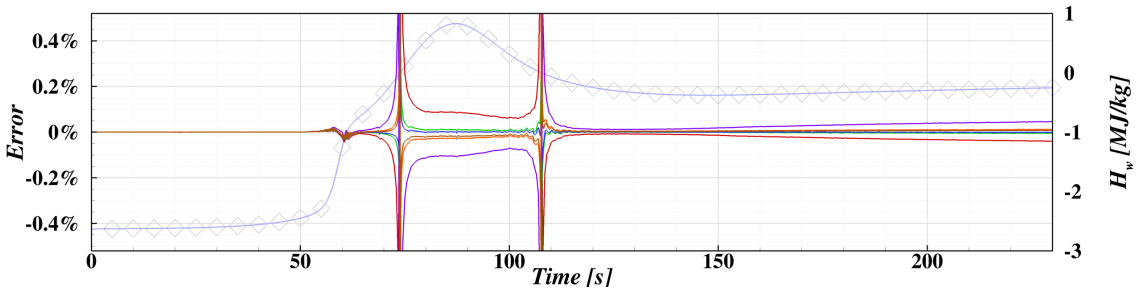

(c) Wall Enthalpy

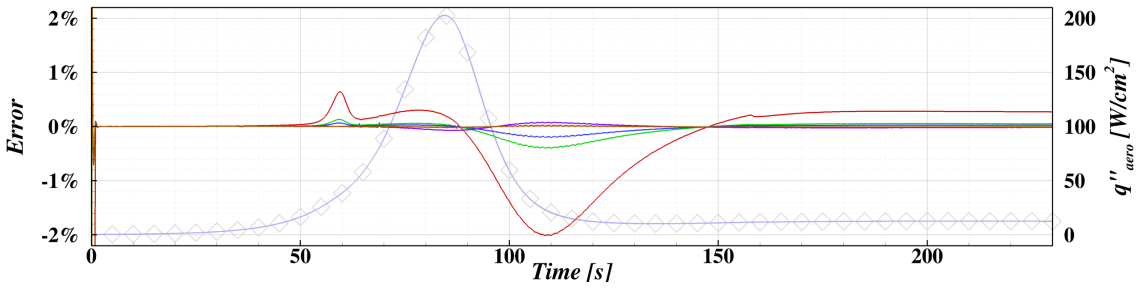

(d) Aeroheating Flux

Figure 6.10. Percent error in reconstructions performed with decoupled SEB method on diffusion limited graphite case for both explicit and implicit algorithms for different reconstruction time steps. Reconstructed values shown with desaturated colors and true values shown as symbols.

does a better job at reproducing the true film coefficient, probably because *CHAR* is explicit in recession, as noted earlier. Both algorithms yield slightly high values of the film coefficient (but still less than 0.01%) before the heating reaches significant levels at around $70\,\mathrm{s}$. Interestingly, the explicit and implicit algorithms yield errors of opposite sign, and both appear to change sign based on the sign of the first derivative of the film coefficient. Recall from the definition of B' (Equation 5.4) that recession rate scales with film coefficient; when the film coefficient is increasing, recession rate is increasing as well. The decoupled SEB tool holds recession rate constant over the time between SEB reconstructions, with the explicit algorithm using the recession rate at the start of this interval and the implicit algorithm using the recession rate at the end of this interval. For a large time step when the film coefficient is increasing, the explicit algorithm will use a the lowest recession rate in the integration, leading to an under-prediction of total recession. The film coefficient must then be larger to compensate for the shortfall of energy released by the exothermic recession reaction. The reverse of this is true for the implicit algorithm, leading to the opposite behavior for those results.

The high frequency waviness that is observed in each curve is an artifact that results from numerical issues in the direct *CHAR* solution[7]. The larger spikes in all of the reconstructions correspond to discontinuities in the first derivative of the film coefficient (see Figure 6.11). The first-order regularization in the temperature field reconstruction will make it difficult to perfectly resolve these discontinuities, introducing the slight errors that are present at these times.

This example demonstrates that the decoupled SEB process and tool is capable of accurately reconstructing environments on a recessing ablator without considering the effects of pyrolysis gas. Some implications of the implicit/explicit assumption have been discussed, particularly in light of the SEB reconstruction time step. The next example will address the effects of pyrolysis gas in this process.

[7] *CHAR* uses a compressing-mesh approach to modeling the spatial domain with recession. The spikes correspond to times when the point specified for temperature extraction for use as the simulated TC trace (which is fixed in space) moves across a gridline and into a neighboring element, changing the interpolation basis nodes. Using coarser meshes for the direct problem yielded fewer spikes in the reconstructed film coefficient, however the spikes were larger.

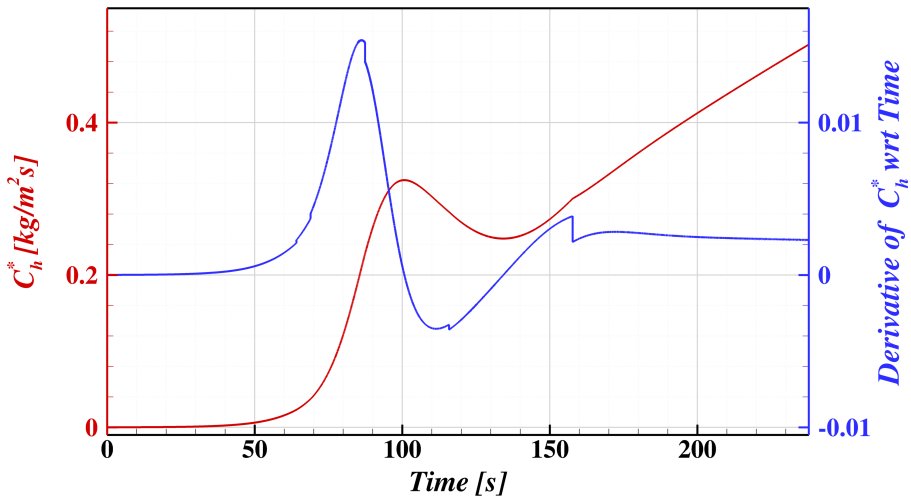

Figure 6.11. Film coefficient and first derivative with respect to time for decoupled SEB example problems.

6.3.2 TACOT

The effect of the ablator permeability on the validity of the decoupling assumptions on the pyrolysis gas flow field were described in Section 6.1.1. The TACOT material model has been defined with permeability values that support modest internal pressure gradients, which undermines the decoupling assumptions given that only the true surface pressure is known. However, the PICA material model for which the decoupled method is applied was built assuming negligible pyrolysis gas residence time. In this section, the TACOT model is used with both pyrolysis gas assumptions to show the validity of the method when assuming negligible residence time, as well as the potential errors introduced with more realistic physical assumptions. Furthermore, two methods of incorporating the zero residence time assumption into a 1-D *CHAR* solution is presented to determine the best strategy for reconstructions using the proposed decoupled approach.

The three permeability models considered in this example are provided in Table 6.1. Model A is the realistic permeability model assumed in the standard TACOT model, with the virgin permeability slightly lower than the char permeability. Model B is the model typically used when the CMA zero-residence-time assumption is used in a *CHAR* solution,

with a small permeability in virgin and a large permeability in char. Model C is introduced in this work to attempt to improve decoupled SEB reconstructions and assumes that both virgin and char use the same large value for the permeability. The motivation for this model is explained later.

Table 6.1. Permeability models used in TACOT example problem in units of m^2

Material State	Model A	Model B	Model C
Virgin	$1.6 \cdot 10^{-11}$	$5.0 \cdot 10^{-14}$	$5.0 \cdot 10^{-9}$
Char	$2.0 \cdot 10^{-11}$	$5.0 \cdot 10^{-9}$	$5.0 \cdot 10^{-9}$

The direct thermal response to generate simulated TC data was integrated using $0.05\,\mathrm{s}$ time steps. To minimize interpolation error introduced by *CHAR* relying on the B' table recession model, the TACOT B' table was recomputed with 139 logarithmically-distributed pressure tables, each with 244 linearly-distributed B'_g entries, each containing temperature solutions at $5\,\mathrm{K}$ intervals (totaling more than $25{\cdot}10^6$ individual solutions, occupying $1.2\,\mathrm{GB}$ on disk and $603\,\mathrm{MB}$ in memory). The Kays blowing reduction model (Equation 5.16) was used. The $40\,\mathrm{mm}$ domain was represented by geometrically stretched elements with the first element size being $10^{-4}\,\mathrm{mm}$ and a stretching ratio of 1.005 (approximately 1500 elements), with 13 more elements for $3.175\,\mathrm{mm}$ of aluminum backing. Whereas the graphite example shown previously could use a uniformly-spaced grid, this example requires the use of a stretched grid because of an implementation limitation in *CHAR* regarding the pyrolysis gas. Recall from Equation 6.5 that *CHAR* defines the pyrolysis gas mass flux using the gradient of pressure, which is evaluated at element nodes. In the finite-element method, derivatives of field variables are defined on the element interiors, but are undefined on nodes. The boundary is on a node, so in order to obtain the mass flux at the surface (necessary to solve the SEB and evaluate the recession model), a projection is performed to extrapolate the mass flux field onto the nodes from quadrature points interior to the elements. This projection yields a first-order finite difference approximation of the mass flux on the boundary. The first-order nature of the result necessitates the use of a very fine mesh at the surface in order to obtain grid-converged results.

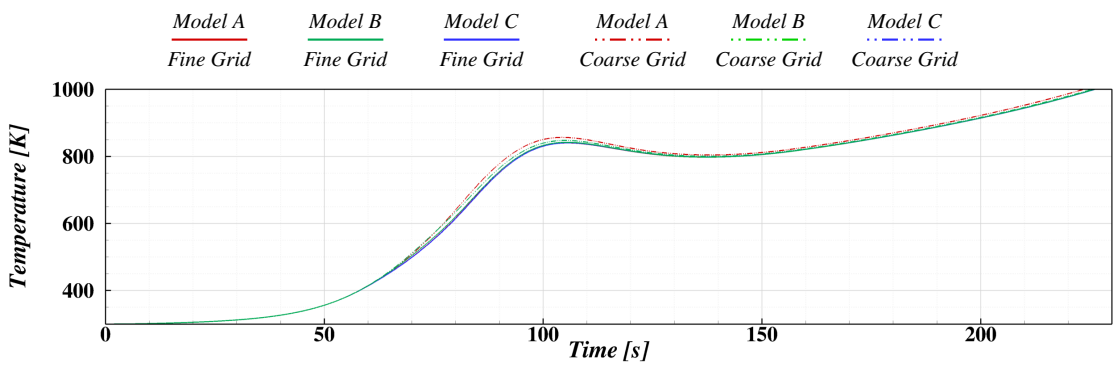

(a) *Temperature at* 6.35 mm

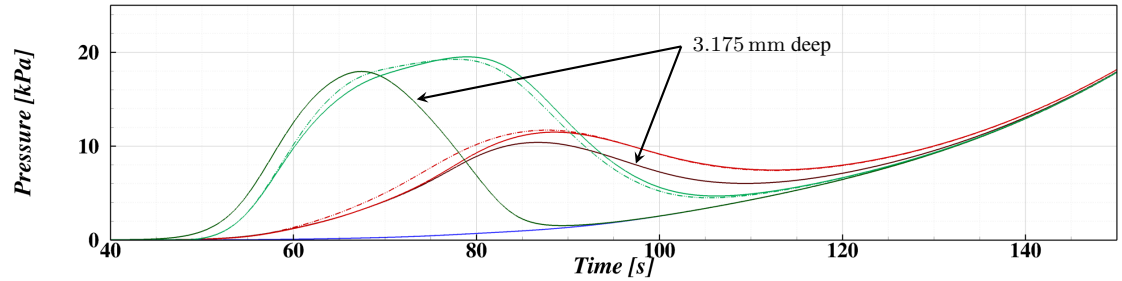

(b) *Pressure at* 6.35 mm

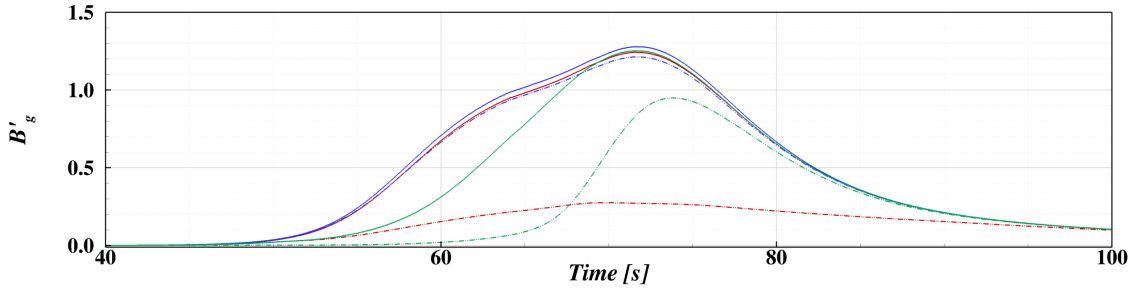

(c) *Surface* B'_g

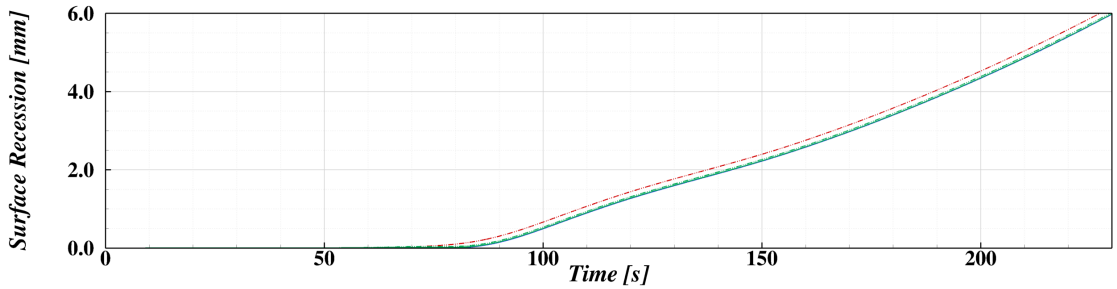

(d) *Surface Recession*

Figure 6.12. Effect of permeability and grid resolution on the direct problem.

Figure 6.12 shows comparisons of the temperature and pressure $6.35\,\mathrm{mm}$ below the surface, the surface pyrolysis gas blowing rate, and the surface recession of the direct problem using two mesh levels: the fine grid is described in the previous paragraph and the coarse grid is the 1000 element uniformly-spaced grid used in the graphite example. Furthermore, these results are presented for all three permeability models shown in Table 6.1. First of all, the grid resolution does have a small but noticeable effect in the temperature and pressure at the internal thermocouple location as well as in the surface recession. The pyrolysis gas blowing rate at the surface is strongly affected by the refined resolution at the surface in the fine grid. With regards to the effect of the permeability assumptions, note that the temperature and surface recession solutions with the different permeability models converge to nearly identical solutions on the fine grid. The solutions for the internal pressure make sense given the permeability values in Table 6.1: the low virgin permeability of Model B leads to higher internal pressures until that depth decomposes to char (since large pressure gradients are needed to provide the mass flux driven by decomposition); the high permeability of Model C yields very low pressure gradients so the internal pressure is very nearly the same as the pressure enforced at the boundary; and Model A responds in-between the other two. Note that for the pressure plot in 6.12(b), the pressure at $3.175\,\mathrm{mm}$ on the fine grid is also shown for models A and B, and both support the observation that lower permeabilities support larger internal pressure gradients.

The pyrolysis gas blowing rate in Figure 6.12(c) is interesting for two reasons. First, as expected from the discussion in the previous paragraphs, this parameter is the most sensitive of those shown to grid resolution. More importantly, though, is the differing behavior among the three permeability models on the fine grid. Both models A and C show an earlier increase in B'_g than model B, though all three collapse to virtually the same result after $68\,\mathrm{s}$. Figure 6.13 shows that this may be attributed to the permeability of the material at the surface. Models A and C have high virgin permeability and therefore provide little resistance to the initial gasses produced in decomposition. Model B, however, has a very low permeability and substantial decomposition must occur before the permeability

increases enough that gas may freely flow from the surface. As discussed later, this affects the reconstruction problem setup.

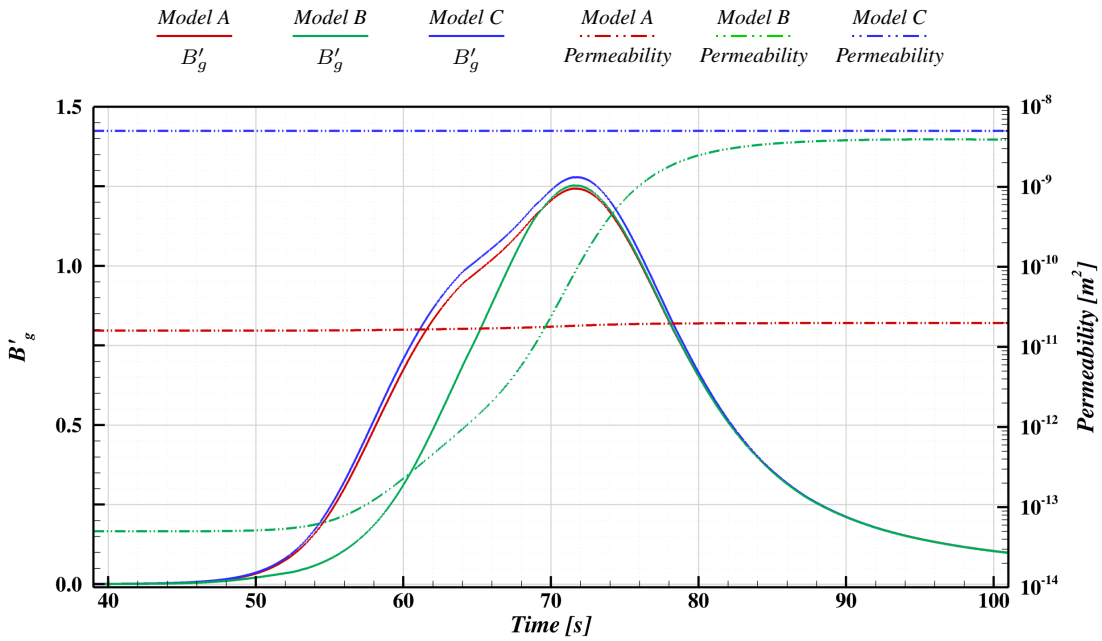

Figure 6.13. Pyrolysis gas blowing rate and permeability of the direct problem.

To assess the performance of the three different permeability models in the decoupled SEB reconstruction approach, the simulated TC data at $6.35\,\mathrm{mm}$ produced by permeability model A are used as the reconstruction target since that is believed the most realistic of the three models. Whole domain reconstructions of the surface heat flux are performed with solution intervals of $0.5\,\mathrm{s}$, a regularization scaling parameter of $\mathtt{a\_1} = -0.001$, and a relative L_∞ convergence tolerance of 10^{-5} yields convergence in approximately 6 non-linear iterations. The $40\,\mathrm{mm}$ TACOT domain is discretized using 900 uniformly spaced elements, with the first six elements located outside of the true domain initial surface (recall that the domain was padded by one element in the graphite example). Multiple elements are used for padding to avoid numerical artifacts of the mass flux projection process. Figure 6.14 shows contours of the reconstructed mass flux fields overlaid on the true mass flux contours at the times when the surface is decomposing from virgin to char. Vertical grid lines denote times at which the reconstruction solutions are available, the horizontal grid lines denote

nodes on the reconstruction grid, and the thick black line denotes the recessing surface of the direct problem. The reconstructed mass flux contours appear discontinuous in the first two elements, but generally continuous in the remaining elements. Because the discontinuity appears to be more severe for Models A and B with lower virgin permeabilities, model C is proposed here in an attempt to reduce spurious reconstruction results from the discontinuity. Beyond the numerical artifacts in the first two elements of the reconstruction, all of the permeability models show slight discrepancies between the reconstructed and true mass flux fields. In general, Model A is better before the peak around $80\,\mathrm{s}$, Model B is better after, and Model C leads the true values most of the time.

Figure 6.15 shows the reconstructed values (desaturated colored lines) of film coefficient (6.15(a)), surface recession (6.15(b)), aeroheating flux (6.15(c)), pyrolysis gas blowing rate (6.15(d)), and surface temperature (6.15(e)) with the true values plotted with symbols. The percent error of each reconstruction is shown using saturated colored lines. The red, green, and blue lines denote results utilizing thermochemical solutions computed at the local conditions, whereas the magenta dashed line utilizes thermochemical solutions in the highly-refined B' table used in the direct problem. The thermochemical solution algorithm at early times where temperatures are very low is not robust enough to yield a solution to the SEB. To work around this issue, the reconstructions are started at $30\,\mathrm{s}$ assuming that no recession has occurred to that point. The reconstruction utilizing the B' table did not suffer from this limitation, so it is started at $0\,\mathrm{s}$. This is the source of the large errors noted in surface recession in Figure 6.15(b), as a very small amount of recession occurs early in the direct problem. Once significant recession begins around $80\,\mathrm{s}$, the reconstructions quickly come back in line with the true values. The difference in recession does not significantly affect the reconstructed film coefficient values, as can by seen by the close agreement between magenta and red lines in Figure 6.15(a).

For each permeability model, over- or under-prediction of the film coefficient or aeroheating flux tends to correlate with similar over- or under-prediction of the reconstructed surface temperature. Since the general trend is to over-predict prior to peak heating and under-predict after peak heating, the errors are likely the result of the reconstructed tem-

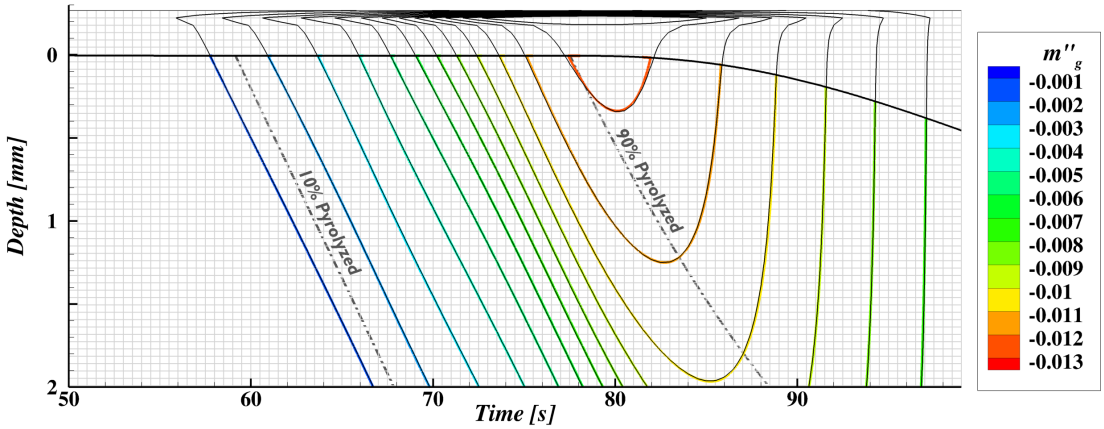

(a) *Permeability Model A*

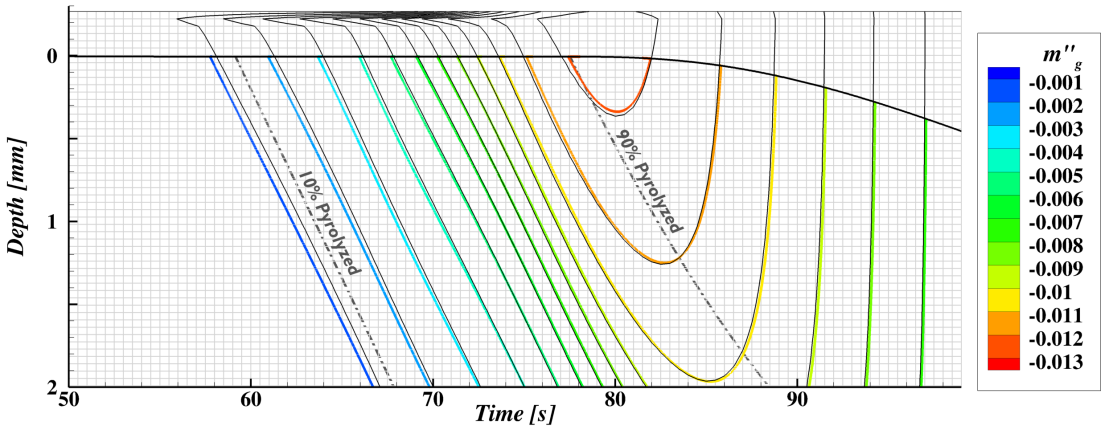

(b) *Permeability Model B*

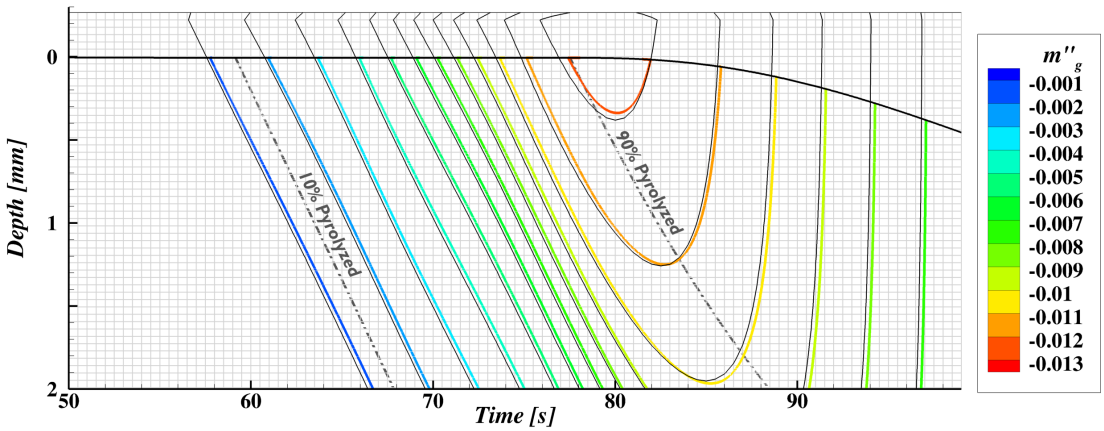

(c) *Permeability Model C*

Figure 6.14. Reconstructed pyrolysis gas mass flux field (black lines) for each permeability model overlaid on the true flux field (colored lines) for permeability model A. Grid indicates reconstructed times and mesh density, thick black line indicates true recessed surface location, and dash-dot line denotes extend of pyrolysis zone in true domain.

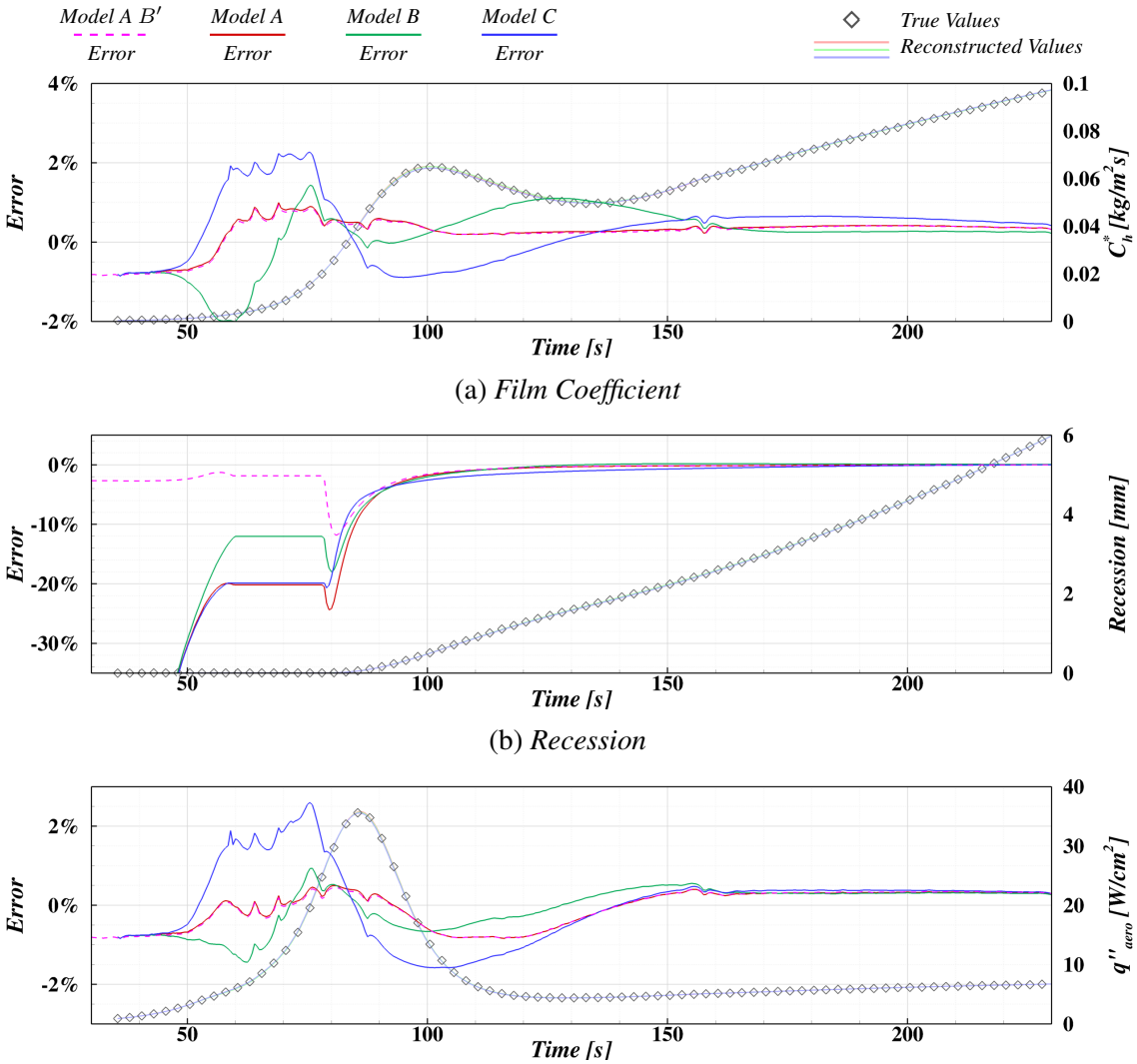

(a) *Film Coefficient*

(b) *Recession*

(c) *Aeroheating Flux*

Figure 6.15. Percent error in reconstructions performed with the explicit decoupled SEB method on diffusion limited TACOT case for each permeability model. The Model A permeability model is used to generate the simulated data and provide the basis for the error calculation. The curve denoted with B' interpolates in a highly-refined B' table for the thermochemical solutions, the remainder of the reconstructions evaluate the solution at each point.

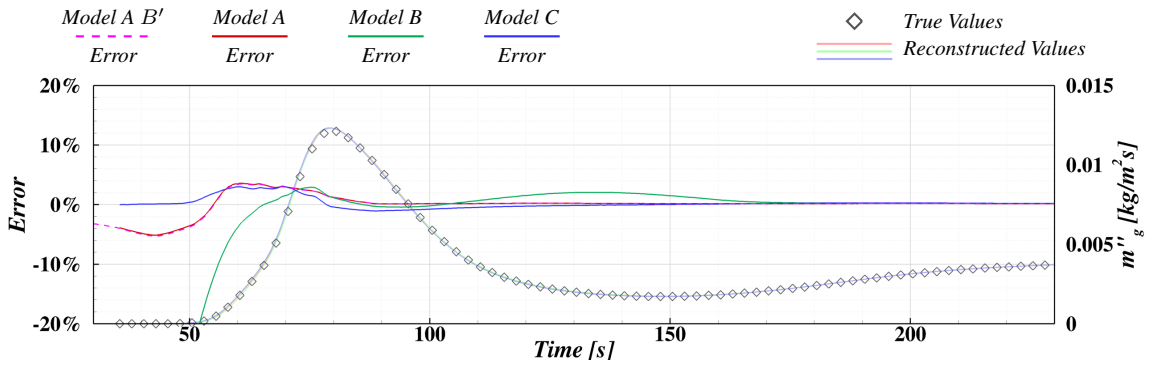

(d) *Dimensional Pyrolysis Gas Blowing Rate*

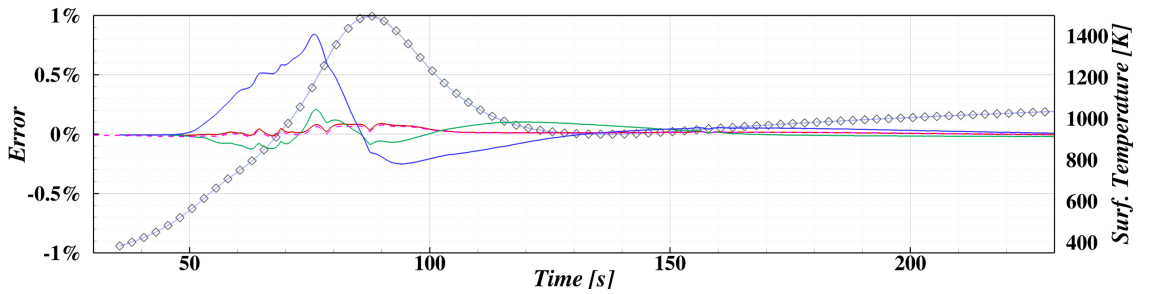

(e) *Surface Temperature*

Figure 6.15. (*continued*) Percent error in reconstructions performed with the explicit decoupled SEB method on diffusion limited TACOT case for each permeability model. The Model A permeability model is used to generate the simulated data and provide the basis for the error calculation. The curve denoted with B' interpolates in a highly-refined B' table for the thermochemical solutions, the remainder of the reconstructions evaluate the solution at each point.

perature field leading the true temperature field due to the long solution intervals. This explanation is supported by the generally positive bias in the reconstructed temperatures relative to the target temperature (Figure 6.16)[8] in this time period. The under-prediction in the aeroheating flux shortly after peak heating can be explained in the same manner.

[8]The oscillatory temperature errors presented in Figure 6.16 can be explained by the assumptions that go into simplifying the boundary condition profile in the reconstruction problem. In general, the reconstruction algorithm will maintain the 'heat load', $\int \dot{q}''\mathrm{d}t$, of the true heating profile. Simplifying a smoothly increasing heating profile to piecewise-constant steps that maintain the heat load of the true heating profile will result in temperatures that over-predict the true temperatures early in a solution interval. The converse is true for an overall decreasing heating profile. The reconstruction algorithm is attempting to drive errors down taking sensitivity coefficients into account. Since the coefficients are better developed later in the solution intervals, these errors are more effectively driven to zero, leading to the relative lack of bias seen by the solid-line bounding curves that represent these later times.

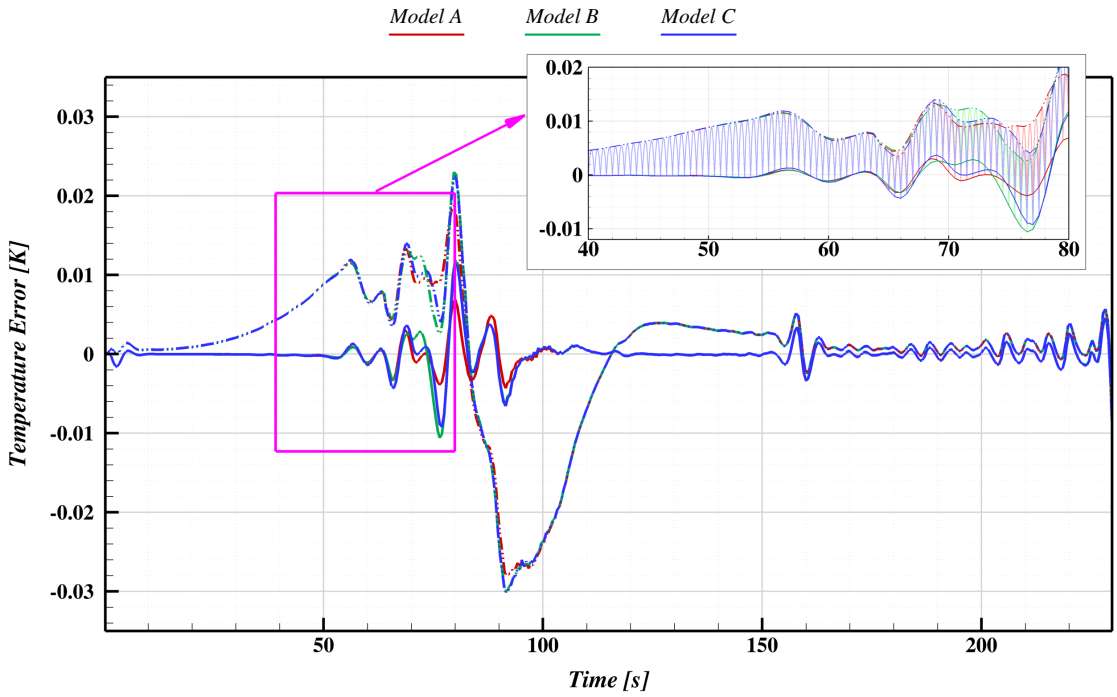

Figure 6.16. Error in reconstructed temperatures at $6.35\,\mathrm{mm}$ depth. Note that the temperature is evaluated every $0.05\,\mathrm{s}$ but the reconstructed boundary condition is assumed constant over $0.5\,\mathrm{s}$ intervals, which leads to the oscillatory behavior of the temperature error shown in the inset plot. The main plot shows the bounding curves over the full reconstruction time with the solid line denoting times consistent with the end of reconstructed solution intervals and the dash-dot line consistent with the middle of the reconstructed solution intervals.

The reconstructed pyrolysis gas mass flux in Figure 6.15(d) does not seem to show the same trends noted before, as Model C performs generally better over the time considered and Model A shows some notable (4%) error prior to $100\,\mathrm{s}$. Though not clearly visible in Figure 6.14 due to the much finer grid resolution, the "true" mass flux field also contains the discontinuity in mass flux in the two elements nearest the surface, making the "true" mass flux used to calculate the errors in Figure 6.15(d) somewhat different that the contour lines visible in Figure 6.14. Note also that Figure 6.14 only shows a small portion of the time range considered in Figure 6.15(d) and that the dimensional pyrolysis gas blowing rate is shown instead of B' to remove the error introduced by the estimated film coefficient.

Recall from the discussion earlier in this section that the direct problem required approximately 1500 geometrically-distributed elements, whereas the reconstruction was per-

formed on 900 uniformly-distributed elements. To assess the adequacy of this assumption, a grid refinement study is performed on reconstructions of permeability model A TC data. The reconstruction obtained using four increasingly refined uniformly-distributed element grids is presented in Figure 6.17. The introduction of the pyrolysis gas mass flux field increases the necessary grid resolution for this example to at least 600 uniformly-spaced elements, and the present resolution is sufficiently grid converged.

The performance of the three different permeability models in this reconstruction problem varies and there is no clear 'best' model. It is clear, however, that using the proposed Model C to improve the pyrolysis gas decoupling does not lead to better overall reconstructions. The SEB is highly non-linear, so the errors introduced by the temperature field reconstruction and errors introduced by errors in the pyrolysis gas blowing rate combine to yield the net error in the film coefficient. However, these errors in the final result are small; none of the reconstructions considered exceeds 3% (1% if Model C is excluded).

6.4 Comparison to Film Coefficient Reconstruction

The proposed decoupled SEB reconstruction approach is an alternative to performing an inverse reconstruction directly for the film coefficient, with the recession model evaluation involved in the sensitivity coefficient evaluation. For recession models provided in B' table form, *INHEAT* is capable of performing a reconstruction in this manner; however, the decoupled reconstruction approach provides a number of advantages for some problems. These advantages are discussed in this section as these two approaches are compared on the graphite and TACOT examples from the previous section.

Direct reconstruction of the film coefficient requires sensitivity coefficients for the film coefficient. As was shown in Section 4.3, the recovery enthalpy affects the sensitivity of the TC to the film coefficient. Surface recession also affects the sensitivity coefficients as the distance between the surface and the TC decreases. On charring ablators, the decomposition state further alters the sensitivity coefficients, introducing even more non-linearity into the inverse problem. Illustrative sensitivity coefficients for the present problem are shown

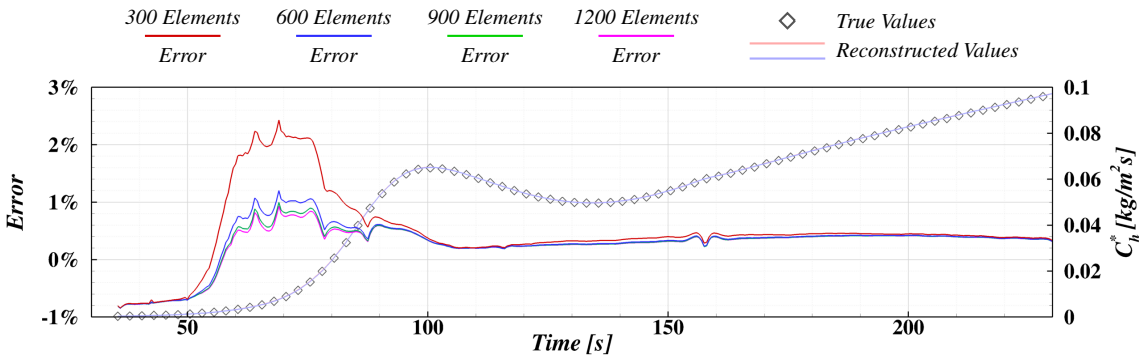

(a) *Film Coefficient*

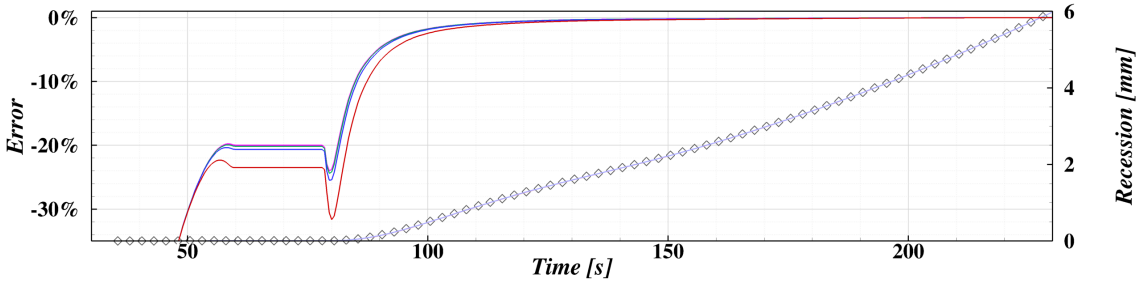

(b) *Recession*

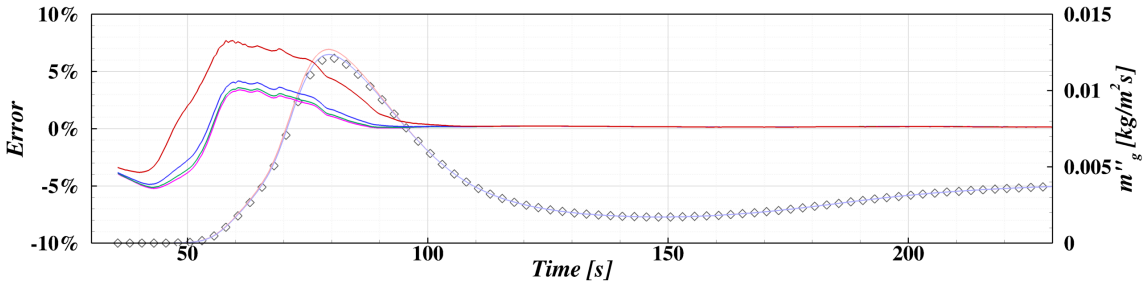

(c) *Dimensional Pyrolysis Gas Blowing Rate*

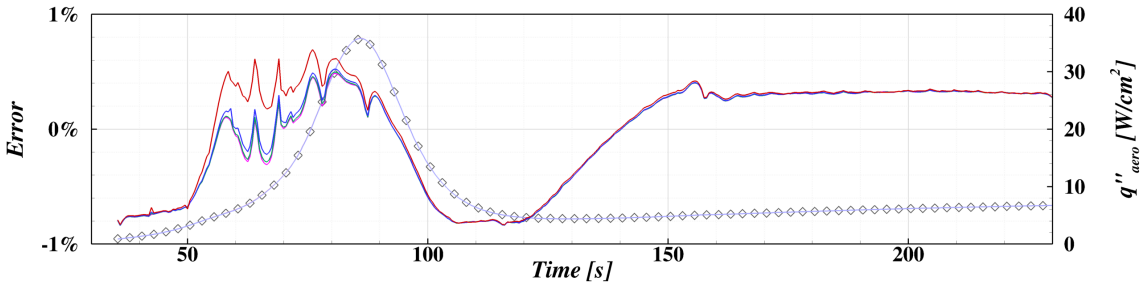

(d) *Aeroheating Flux*

Figure 6.17. Comparison of permeability model A reconstructions on four levels of grid refinement. The Model A permeability model is used to generate the simulated data and provide the basis for error calculation.

in Figure 6.18, with the graphite coefficients in 6.18(a) and TACOT coefficients in 6.18(b). A minimum in the peak value of the sensitivity coefficients is seen for boundary condition intervals in the vicinity of $t = 115\,\mathrm{s}$. This minimum occurs because the decreased sensitivity due to the dropping recovery enthalpy is offset by the increased sensitivity due to the surface moving closer to the measurement location. With this wide variation, it is not expected that a WD reconstruction would perform well. Furthermore, the coefficients take a relatively long time to develop, so a FT reconstruction will also likely perform poorly. As a result, the SSD algorithm is used for this effort. Considering the more rapid growth of the graphite coefficients, a smaller future time window is justified.

In order to isolate the differences between the two reconstruction approaches, the direct reconstruction and the decoupled temperature field reconstruction are performed with the same algorithm and regularization parameters. The graphite case uses a future time window of $3\,\mathrm{s}$ with solution intervals of $0.05\,\mathrm{s}$ to compare to the more accurate decoupled SEB result from the previous section. For the TACOT case, the future time window is taken to be $5.5\,\mathrm{s}$ with solution intervals of $0.5\,\mathrm{s}$ to represent a more practical engineering case. Both cases use a regularization scaling parameter of $\mathtt{a\_1} = -0.01$ and one-sided finite-differences for sensitivity coefficient evaluation. Graphite cases are computed with a single non-linear iteration and the TACOT cases are allowed 4 non-linear iterations if the L_∞ norm of the relative update vector does not drop below 10^{-5}. TACOT reconstructions use permeability Model A and both TACOT cases included in the timing comparison were run using 12 threads on 12 processors[9]. The temperature errors for the reconstructions are shown to be very small in Figure 6.19, with all reconstructions showing consistent results with those in the previous section. The direct film coefficient reconstructions begin to become unstable in the final $2\,\mathrm{s}$ of the problem, leading to the oscillations on the far right side of the plots in Figure 6.19.

Although the *INHEAT* parameters are consistent, the TACOT temperature field reconstruction for the decoupled SEB method is performed on the 900 element uniform mesh described before, whereas the direct film coefficient reconstruction must use the 1500 ele-

[9]The Thinkmate VSX R5 760V3 workstation used has 2 Intel Xeon™ E5-2697 v3 2.60 GHz CPUs (a total of 28 cores) with 128 GB of DDR4 2133 MHz ECC RAM.

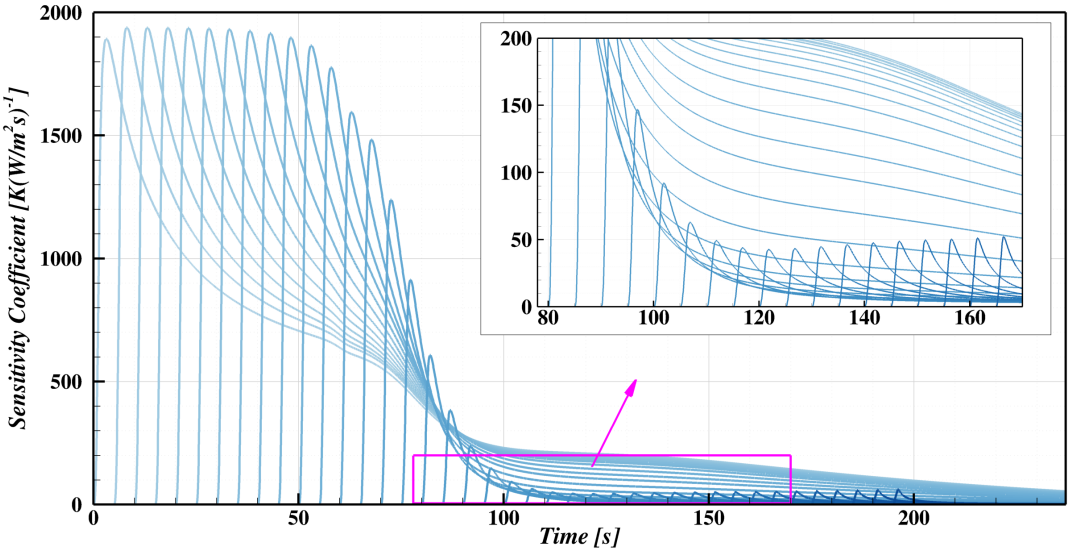

(a) *Graphite*

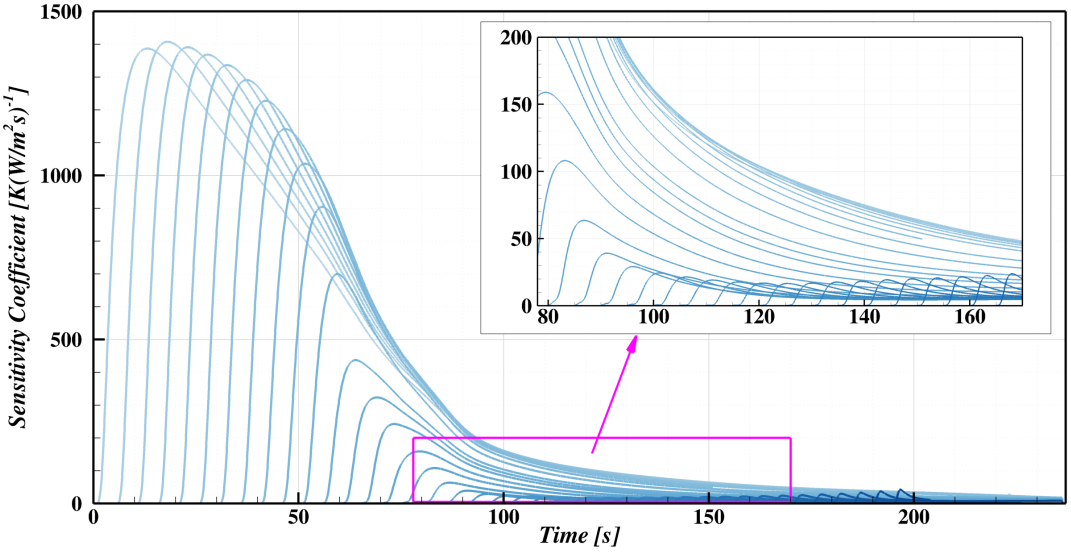

(b) *TACOT*

Figure 6.18. Film coefficient sensitivity coefficients for TC $6.35\,\mathrm{mm}$ below the surface.

ment stretched mesh since the pyrolysis gas mass flux at the surface must be resolved. This contributed to an increase in the computational cost of the direct film coefficient reconstruction. Table 6.2 shows the accumulated simulated time and the wall time that each solution required. The accumulated simulated time is similar, but that should be expected with the

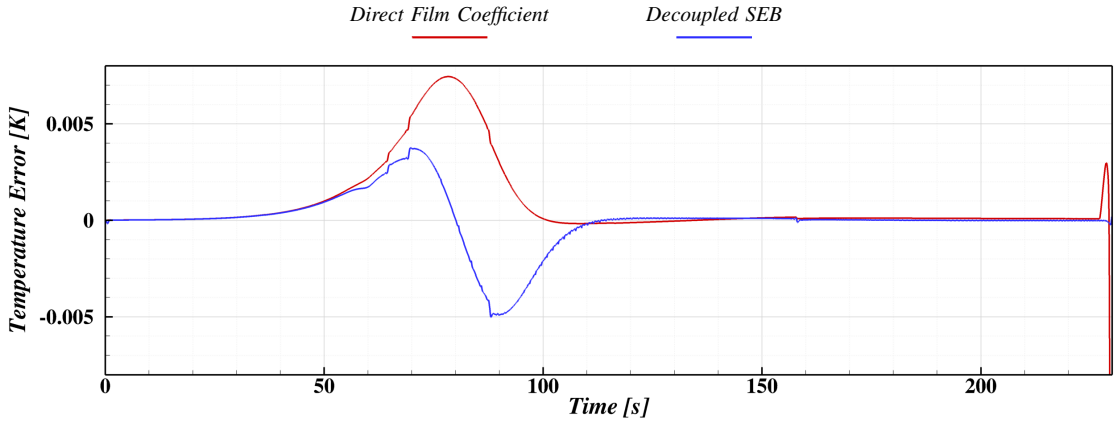

(a) *Graphite*

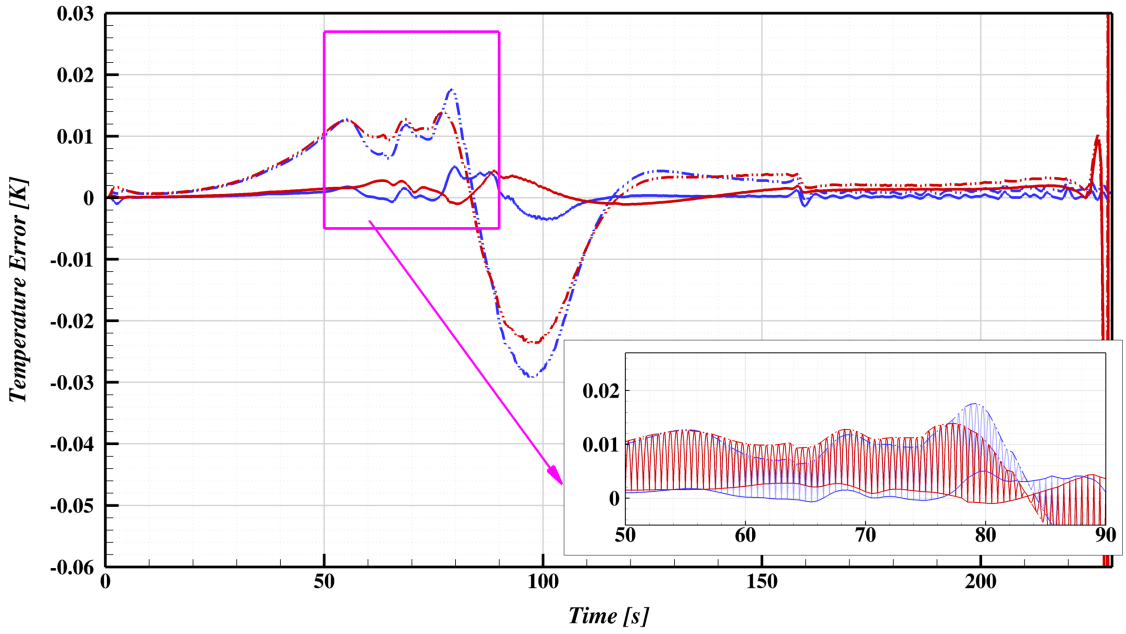

(b) *TACOT*

Figure 6.19. Residual error in reconstructed temperatures at $6.35\,\mathrm{mm}$ depth.

Table 6.2. Computational cost metrics for direct film coefficient and decoupled SEB reconstruction methods on TACOT example problem

Method	Accumulated Simulated Time	Wall Time
Decoupled SEB	187 hr	3.0 hr
Direct film coefficient	194 hr	5.8 hr

same *INHEAT* parameters. The slight increase in accumulated simulated time for the direct film coefficient reconstruction is attributed to the increased non-linearity of the sensitivity coefficients, as that method evaluated more non-linear iterations than the decoupled SEB temperature field reconstruction. More importantly, the wall time required to complete the direct film coefficient reconstruction is higher than the decoupled SEB temperature field reconstruction. The difference in mesh size certainly contributes to this difference. However, the direct problem solutions for the decoupled SEB temperature field reconstructions are considerably cheaper due to the linearity of the boundary conditions, the boundary condition not needing to iterate on the blowing correction, and mesh motion not needing to be considered.

To keep the recession models on similar terms for comparison, the decoupled SEB results are evaluated using the same high-density B' tables used by the direct film coefficient reconstructions. Figure 6.20 shows the comparison of the reconstructed surface conditions for the graphite example. While generally very similar with very little reconstruction error, the direct film coefficient reconstruction results are less accurate than the decoupled SEB results, likely due to the fact that the regularization is directly applied to the film coefficient which impacts the other parameters through the recession model. Figure 6.21 shows the comparison of the reconstructed surface conditions for the TACOT example. Both algorithms have large errors at the very beginning of the problem when the true film coefficient is small, but have come to reasonable values before the heating rate becomes significant. The direct film coefficient reconstruction performs markedly better in computing the pyrolysis gas blowing rate and surface recession. Presented this way, the spike in recession error around 80 s for the decoupled SEB method appears likely due to delayed onset of recession

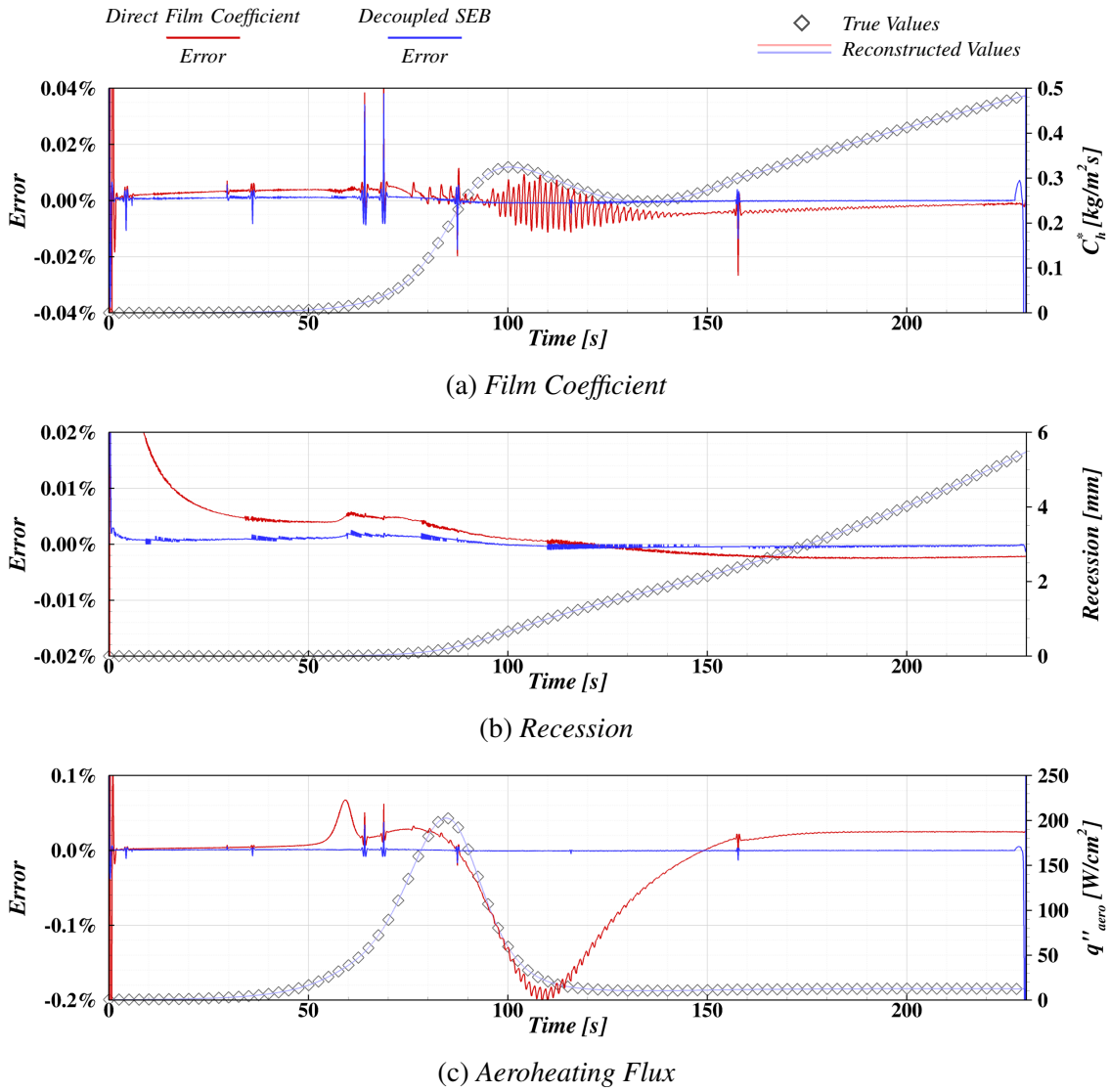

(a) *Film Coefficient*

(b) *Recession*

(c) *Aeroheating Flux*

Figure 6.20. Comparison of reconstruction method results on the diffusion limited graphite case.

caused by the over-prediction of surface blowing. The improved accuracy in blowing and recession for the direct film coefficient method does not translate to more accurate film coefficients or aeroheating fluxes, with the latter two quantities being more relevant for flight vehicle design. The decoupled SEB method tends to provide a more consistently accurate estimate of the aeroheating flux. In terms of the film coefficient estimate, neither method is obviously better than the other, and errors are generally less than $\pm 2\%$.

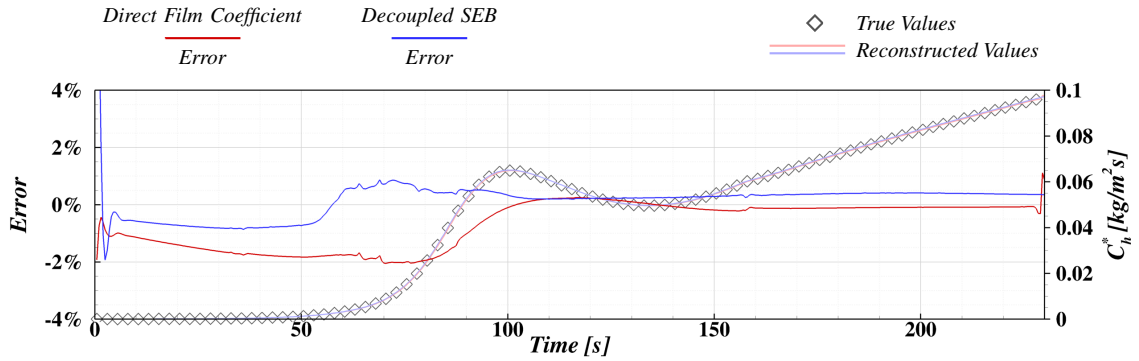

(a) *Film Coefficient*

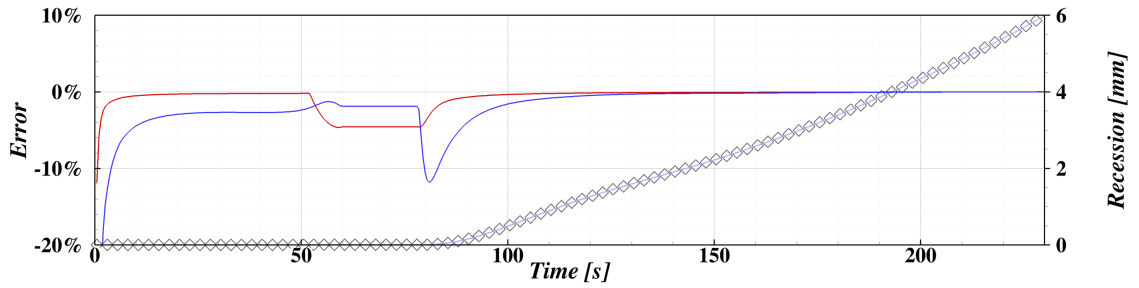

(b) *Recession*

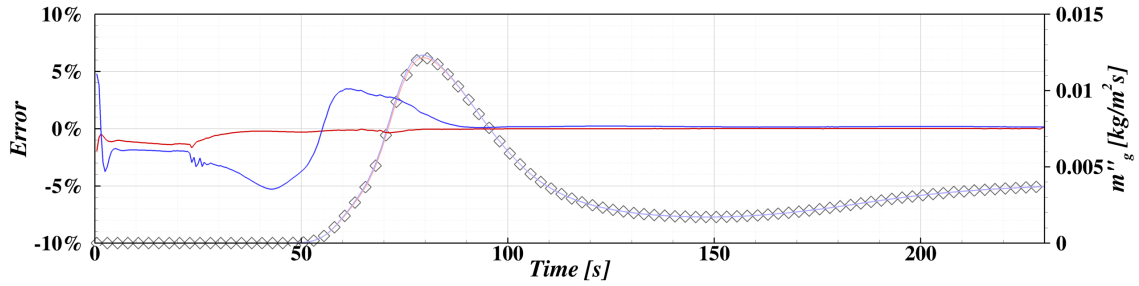

(c) *Dimensional Pyrolysis Gas Blowing Rate*

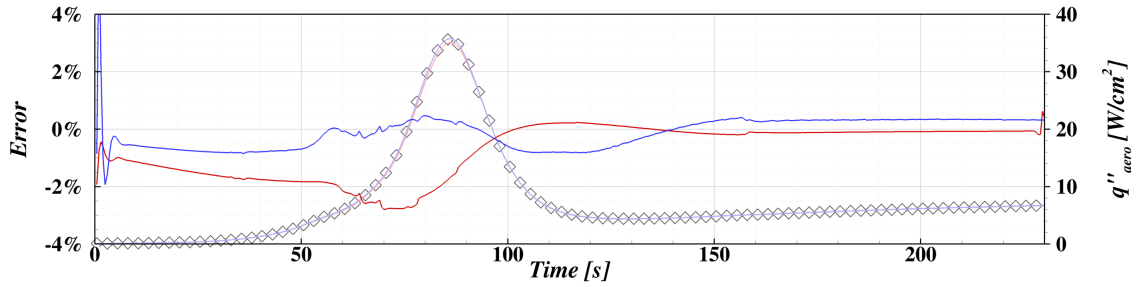

(d) *Aeroheating Flux*

Figure 6.21. Comparison of reconstruction method results on the diffusion limited TACOT case.

6.5 Summary

In this chapter, the theory for the decoupled SEB reconstruction approach is presented and discussed. The role of the ablator permeability on the internal pressure field is discussed and it is described how this could undermine the validity of a decoupled reconstruction. Following a description of the code used to execute the proposed algorithm, several examples are presented. The first shows that the decoupled SEB algorithm is capable of producing very accurate reconstructed film coefficients (better than 0.1%) on materials without internal decomposition and pyrolysis gas. Furthermore, the differences between explicit and implicit SEB reconstruction algorithms are demonstrated, although the apparent result that the explicit algorithm is more accurate is likely biased by an explicit assumption in *CHAR* which produced the simulated data for reconstruction. Incorporating pyrolysis gas decreases the accuracy of the reconstructions, although the film coefficient errors remained less than 3%. Several different models for accounting for the ablator permeability are assessed with the apparent result that there is no justifiable reason to use an artificial permeability in the decoupled reconstruction process if a physically-accurate value is available. Finally, the decoupled SEB reconstruction algorithm is compared to the conventional direct film coefficient reconstruction method, where it is shown that the decoupled SEB method is similarly accurate to the conventional method, but notably cheaper to evaluate.

Though not demonstrated here, one more key advantage of the decoupled SEB method is that it permits evaluation of multiple recession models using the same reconstructed temperature field. Considering that there is often significant uncertainty in the physical models describing recession and the dependence on the reconstructed flux to energy release in the recession process, it is reasonable to expect that an assessment of the sensitivity of reconstructions to the recession model parameters will be performed. Performing this type of assessment with a conventional direct film coefficient method would require recomputing the full reconstruction for every recession model, which can become prohibitively expensive. With the decoupled approach, many different recession models can be assessed (even

ones which cannot be described by a B' table) without duplicating the effort of solving for the response of the ablator interior. This capability is demonstrated in Chapter 7.

7. MEDLI FLIGHT DATA RECONSTRUCTION

This chapter applies the techniques presented in this document to two of the MEDLI thermocouple plugs previously discussed in Section 1.2. The SEB reconstruction results for a number of recession and environment assumptions are discussed. In some instances, models are shown to provide infeasible results thereby allowing some conclusions to be made regarding the applicability of certain assumptions. That said, it should be cautioned that this approach is not guaranteed to provide clear statements on the adequacy of specific models. The environment and surface thermochemistry form a tightly-coupled system, and the interdependence of each component means that no single aspect can be clearly addressed by one measure of the overall response. This is an unfortunate example of the possible non-uniqueness in the inverse problem. The proposed approach does, however, allow viewing the system response in a different light, providing another measure of the performance of each part of the complicated mechanism.

7.1 Flight Information

The layout of the temperature plugs and pressure ports are provided in Figure 7.1. Temperature data (shown in Figure 7.2(a)) from the nearest-surface thermocouples in MISP 1 ($2.65\,\mathrm{mm}$ deep, near the stagnation point) and MISP 7 ($2.39\,\mathrm{mm}$ deep, observed the highest temperatures and clear laminar/turbulent transition) are used for reconstruction. Pressure ports MEADS 2 and MEADS 5 are assumed to be close enough to MISP 1 and MISP 7, respectively, that the measured pressures are used as the respective reconstruction surface pressures without spatial interpolation. For the SEB reconstruction, the recovery enthalpy was taken to be the total enthalpy calculated using the altitude, velocity, and atmospheric properties reconstructed from MEADS and IMU (inertial measurement unit) data. The surface pressure and recovery enthalpy are shown in Figure 7.2(b).

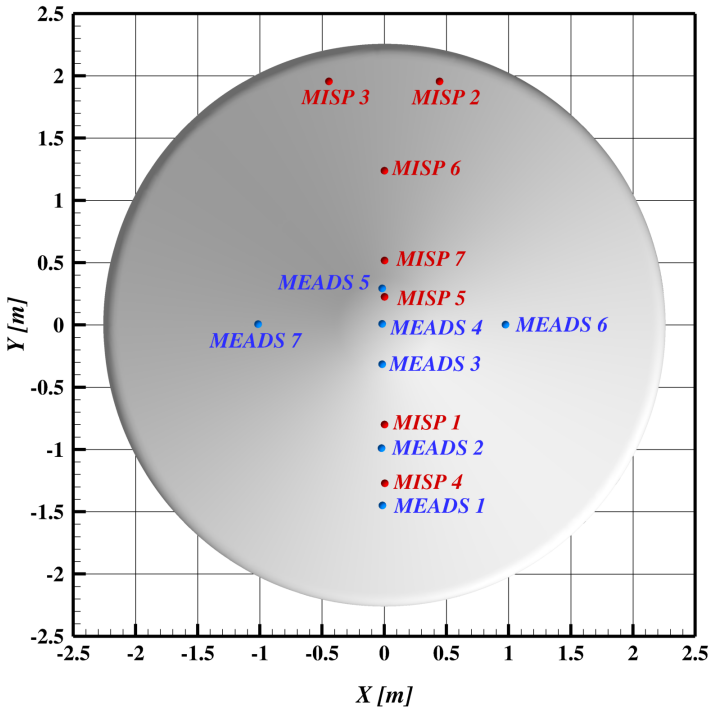

Figure 7.1. MEDLI instrumentation layout. The nominal stagnation point is in the vicinity of MISP 1 and MEADS 2.

Three assumptions of the shock-layer radiation profile are used in the present work. Figure 7.3 shows the shock-tube data corrected prediction of shock-layer radiation heating on the MSL stagnation point from Cruden et al. [8] along with uncertainty estimates. Two spline-fit curves are derived: the nominal profile in red that fits the indicated heating, and the minimum profile in green that fits the lower end of the uncertainty bound. These two curves and the assumption of no shock-layer radiation is used for the presented SEB reconstructions.

The temperature data in reference [2] is provided with a resolution of $0.1\,^{\circ}\mathrm{C}$. Aside from this quantization error, there is very little evidence of high-frequency noise in the TC data. As a result, the TC data was not filtered prior to the reconstruction. To assess the noise level that should be expected in the reconstruction, the TC data was filtered using a Savitsky-Golay [54] filter with filter coefficients for a 4^{th}-order polynomial calculated from

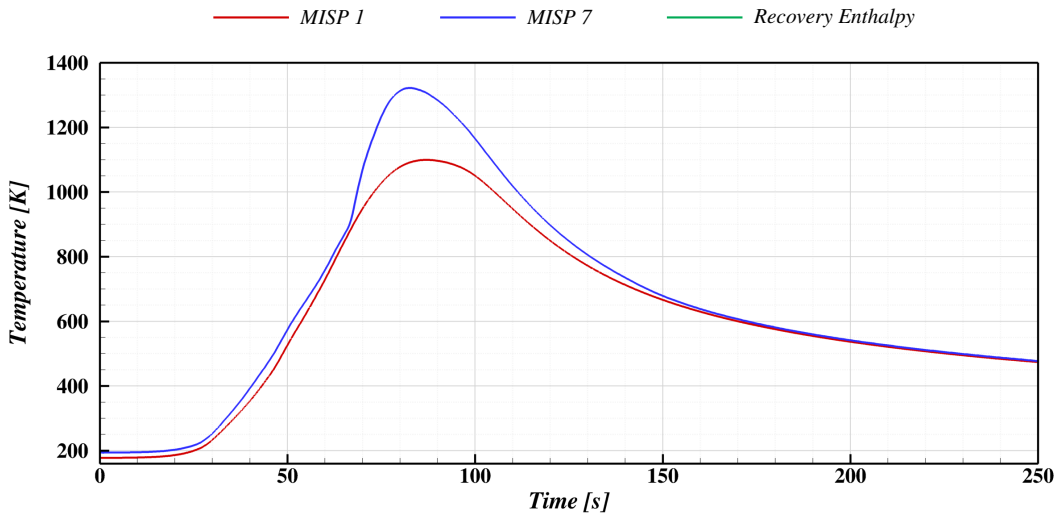

(a) TC 1 Temperature

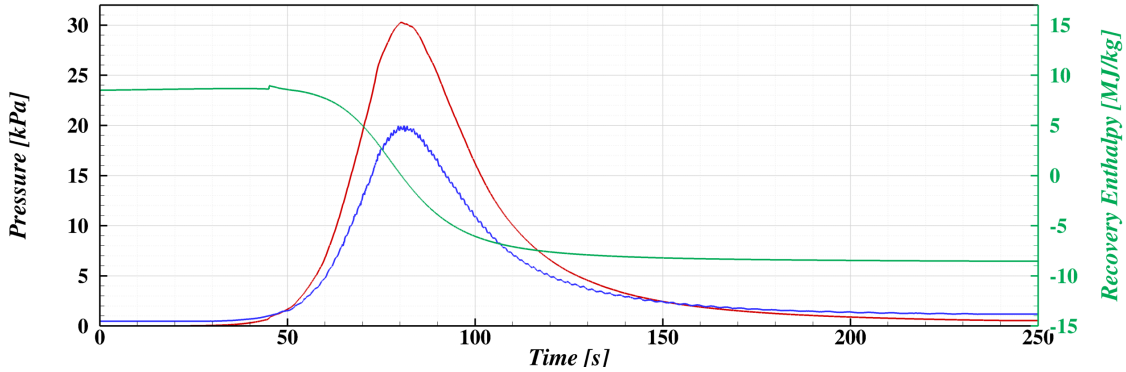

(b) Pressure and Recovery Enthalpy

Figure 7.2. Temperature, surface pressure, and recovery enthalpy used for reconstruction of MISP 1 and 7.

the Table II formula provided by Madden [55] for a filter half-width of 5 points to provide a baseline for comparison. Comparison to the filtered temperature samples yields standard deviations of $0.052\,\mathrm{K}$ and $0.102\,\mathrm{K}$ for MISP 1 and 7, respectively, with corresponding sum-squared temperature errors of $8.338\,\mathrm{K}^2$ and $5.579\,\mathrm{K}^2$.

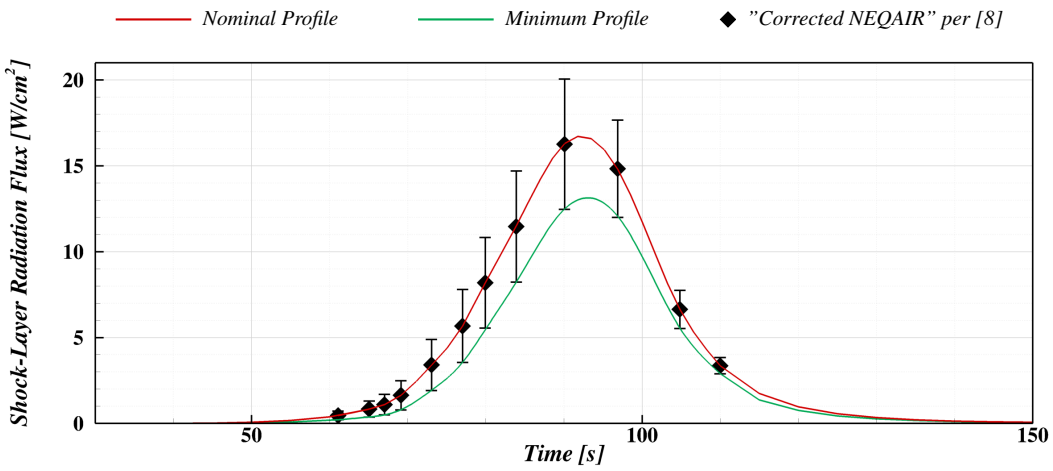

Figure 7.3. Shock layer radiation used for reconstruction of MISP 1 and 7.

7.2 Temperature Field Reconstructions

The SSD algorithm is used to produce the temperature field reconstructions. Publication limits on the PICA material model prevent showing the results of the sensitivity coefficients study performed for the present problem; however, it is sufficient to note that the general character is consistent with that of the TACOT examples shown previously in Section 4.2. Based on this study, the reconstruction future time window was taken to be $5\,\mathrm{s}$ long. The boundary conditions were reconstructed at frequencies for which data is available: $8\,\mathrm{Hz}$ for MISP 1, and $2\,\mathrm{Hz}$ for MISP 7.

The temperature field was reconstructed in 1-D using the full as-designed material stack-up thicknesses, including adhesive and substructure layers. Time was integrated with $0.0625\,\mathrm{s}$ time steps from a uniform initial condition that matched the temperature measurement at entry interface. A grid refinement study was performed regarding the density of elements required in the PICA layer. Temperature field reconstructions and SEB reconstructions (assuming diffusion limited recession) of MISP 1 were computed with grids ranging from 100 to 1000 elements in the PICA layer. Results of the reconstructed film coefficient are shown in Table 7.1. Based on these results, the grid consisting of 800 elements was used for the presented results.

Table 7.1. Grid convergence study results for MEDLI reconstructions.

Elements	$C_h^*[\mathrm{kg/m^2 s}]$	% Change
100	0.029248	-
200	0.029255	0.025%
400	0.029260	0.015%
600	0.029262	0.010%
800	0.029264	0.005%
1000	0.029265	0.002%

All values at time 70 s.

First-order regularization was used with locally-scaled regularization factors (Equation 3.18), with four scaling parameters from 1.0 to 0.001 considered. Figure 7.4(a) shows the reconstructed temperatures at peak heating and Figure 7.4(b) shows the difference between the reconstructed and measured temperatures (residual temperature error) for MISP 1. Results using the regularization scaling parameter $\texttt{a\_1} = 1.0$ visibly under-shoot the peak temperature in 7.4(a) and also demonstrate visible bias relative to the data and other reconstructions in 7.4(b). By contrast, results for the next largest value of the scaling parameter do not show these traits, therefore this value ($\texttt{a\_1} = 0.1$) is used for the presented results. Since the data rate is lower for MISP 7, it is possible that a different regularization parameter would perform better on that case. Figure 7.5 shows the equivalent data for MISP 7. In this case, $\texttt{a\_1} = 1.0$ and 0.1 both show characteristics of over-smoothing, so results for MISP 7 are presented using the reconstruction with $\texttt{a\_1} = 0.01$.

Reconstructed surface temperatures (neglecting recession) are shown in Figure 7.6, along with temperatures at the first two TC locations. As expected given the measurements at the TCs, the surface temperature for MISP 7 is quite a bit higher than that for MISP 1. The sharp temperature increase at approximately $65\,\mathrm{s}$ (that can be attributed to higher heating due to laminar to turbulent boundary layer transition) on MISP 7 is much more pronounced at the surface compared to the first TC depth, which is used as the reconstruction target. Furthermore, the good comparison of the modeled and measured temperatures at the second TC (blue line) show the relatively high-quality of the conduction and decom-

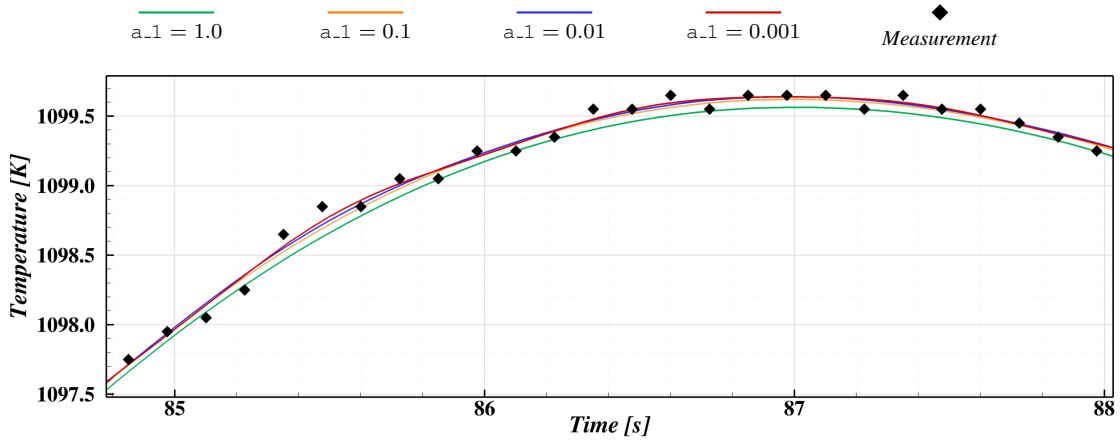

(a) Temperature

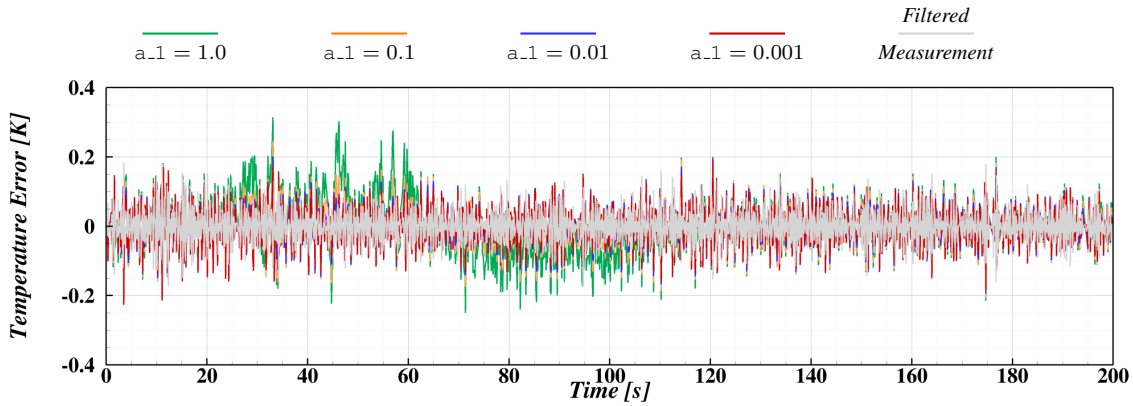

(b) Temperature Error

Figure 7.4. Reconstructed temperature and residual temperature error at $2.65\,\mathrm{mm}$ depth on MISP 1 using four different values of the first-order regularization scaling factor.

position components of the PICA thermal response model, since measurements from the second TC did not influence the reconstructed boundary conditions.

7.3 SEB Reconstruction

There are a large number of physical effects that contribute to the net response at the surface of an ablator. To help orient the reader, results on MISP 1 and 7 are shown in a progressive manner, with additional physical phenomena and recession models introduced gradually.

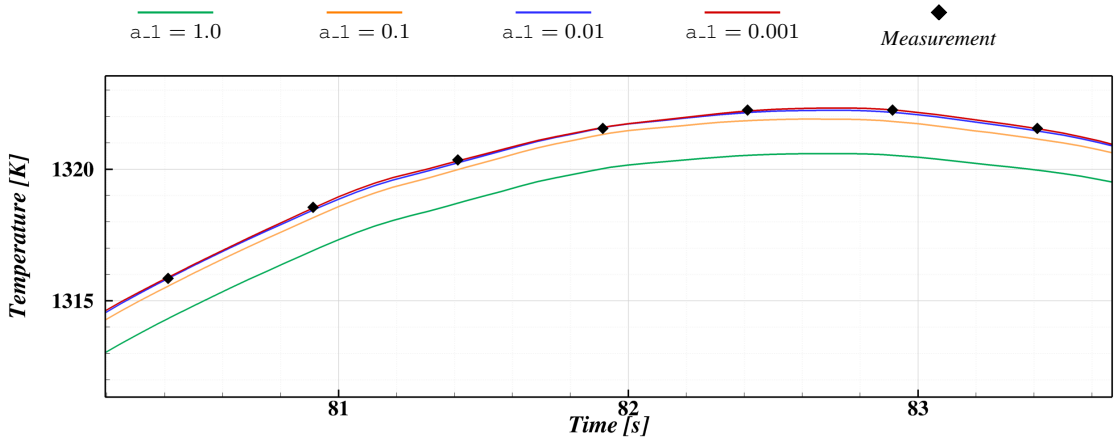

(a) Temperature

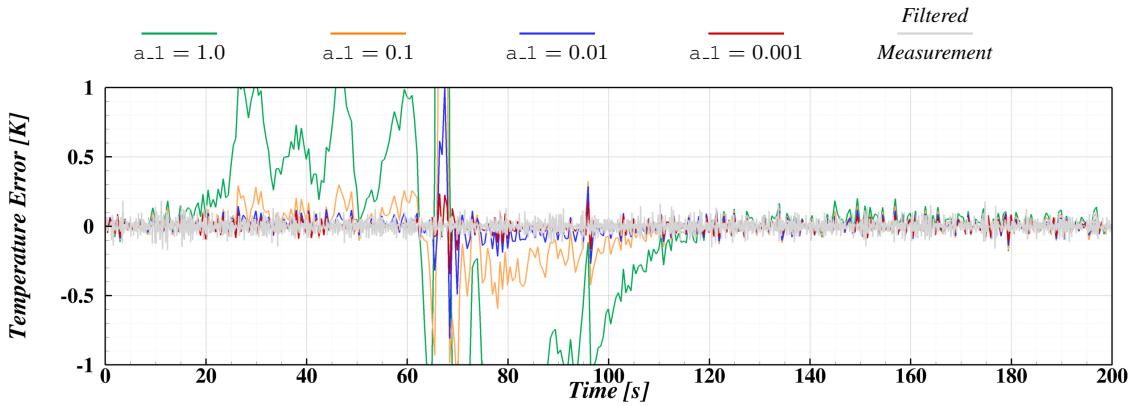

(b) Temperature Error

Figure 7.5. Reconstructed temperature and residual temperature error at $2.39\,\mathrm{mm}$ depth on MISP 7 using four different values of the first-order regularization scaling factor.

7.3.1 No Recession

The first reconstructions presented in Figures 7.7 and 7.8 show SEB reconstructions on MISP 1 and 7, respectively, assuming that surface recession does not occur (recession is forced to zero in the SEB reconstruction). Each figure consists of four time-synchronized plots that show the reconstructed aeroheating flux, the shock-layer radiation flux, the wall enthalpy (enthalpy of ablation products with the recovery enthalpy also shown), and finally the film coefficient. There are six curves shown, though only three are visible in the flux plots. Solid lines are used to denote the assumption of chemical equilibrium species

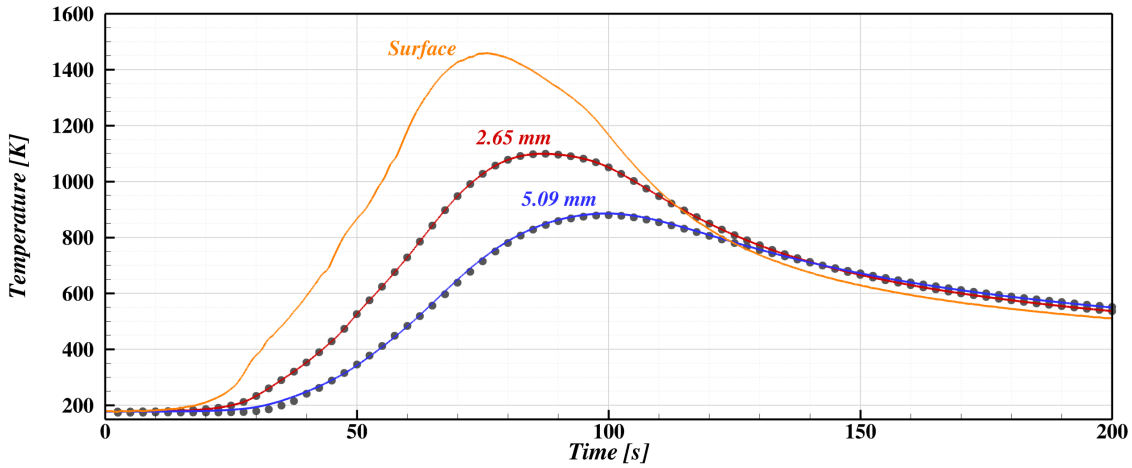

(a) MISP 1

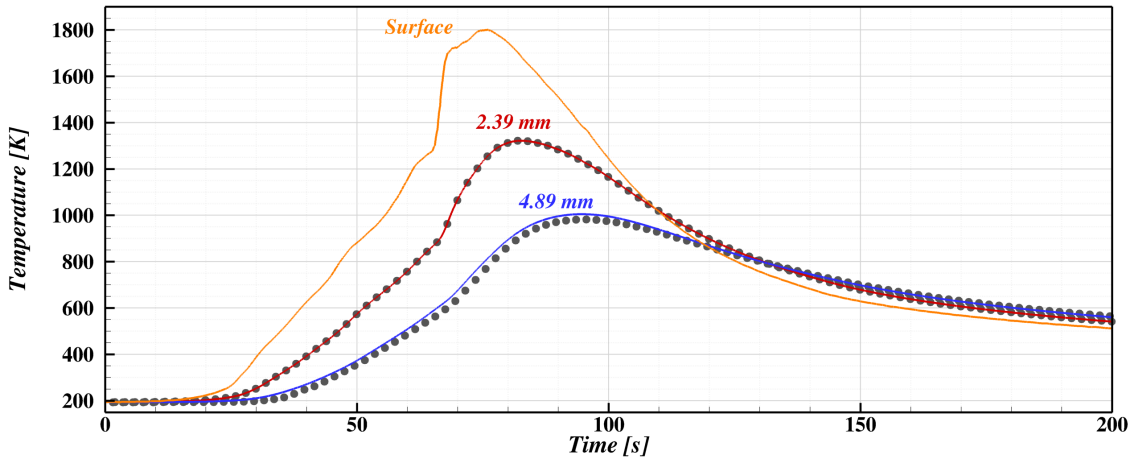

(b) MISP 7

Figure 7.6. Reconstructed surface temperatures and TC temperatures relative to measured data. A subset of the measured data is denoted by filled circles. Recall that the shallow TC (red line) is used as the reconstruction target.

composition in the surface gas mixture, dashed lines denote a frozen species composition (described more later). The line color identifies the shock-layer radiation profile assumed in the reconstruction (blue for no applied shock-layer radiation, red for the nominal profile, and green the minimum profile).

Based on the three equilibrium curves, two things are worth noting. First, the heat flux needed from the boundary layer to balance the SEB decreases when radiation is consid-

ered. This makes sense from a reconstruction point-of-view; the heat flux conducting into the heatshield is constant, so if more heat comes from one source (radiation) then less is required from another source (boundary layer). Second, the aeroheating flux on MISP 1 (Figure 7.7) is negative near $100\,\mathrm{s}$ with the assumed nominal radiation profile. This implies that there is more radiation absorbed in this case than is needed to produce the observed TC response. Examining the film coefficient and enthalpy curves in this figure, it is clear that the wall enthalpy exceeds the recovery enthalpy, permitting negative flux with a positive film coefficient, and that the film coefficient decreases to allow the wall enthalpy to increase. This second point may not be obvious. The Martian atmosphere is predominantly CO_2, which has a considerably negative heat of formation. Increasing the film coefficient increases the fraction of the wall gas mixture that is edge gas relative to the pyrolysis gas which is also present here. CO_2 from the boundary layer edge drives the wall enthalpy more negative, so the proportion of the edge gas must be reduced to allow the pyrolysis gas to bring the wall gas enthalpy up to the level that will permit the negative aeroheating flux needed. The negative flux is not seen in the MISP 7 reconstruction (Figure 7.8), although the film coefficient does have to drop (with its corresponding increase in wall enthalpy) to achieve the low aeroheating flux needed.

Considering the difference between equilibrium and frozen species composition, one must first clarify what the frozen composition represents. In this case, the species composition for the frozen case (dashed lines) is computed by evaluating, separately, the equilibrium species composition of the edge gas and pyrolysis gas at the surface temperature and pressure. These species mixtures are then combined into a mass-weighted average using the non-dimensional blowing rate, B'_g, as the weighting parameter before evaluation of the mixture enthalpy. The particular assumption of the species does not affect the net aeroheating flux, since this is the amount required to balance the other flux terms in the SEB. It does, however, affect how the aeroheating flux is generated, which can be seen in the different wall enthalpies and film coefficients shown with dashed lines. In general, the frozen composition yields a more negative wall enthalpy, likely because the CO_2 from the boundary layer edge is not allowed to react and form other species. As a result, the film

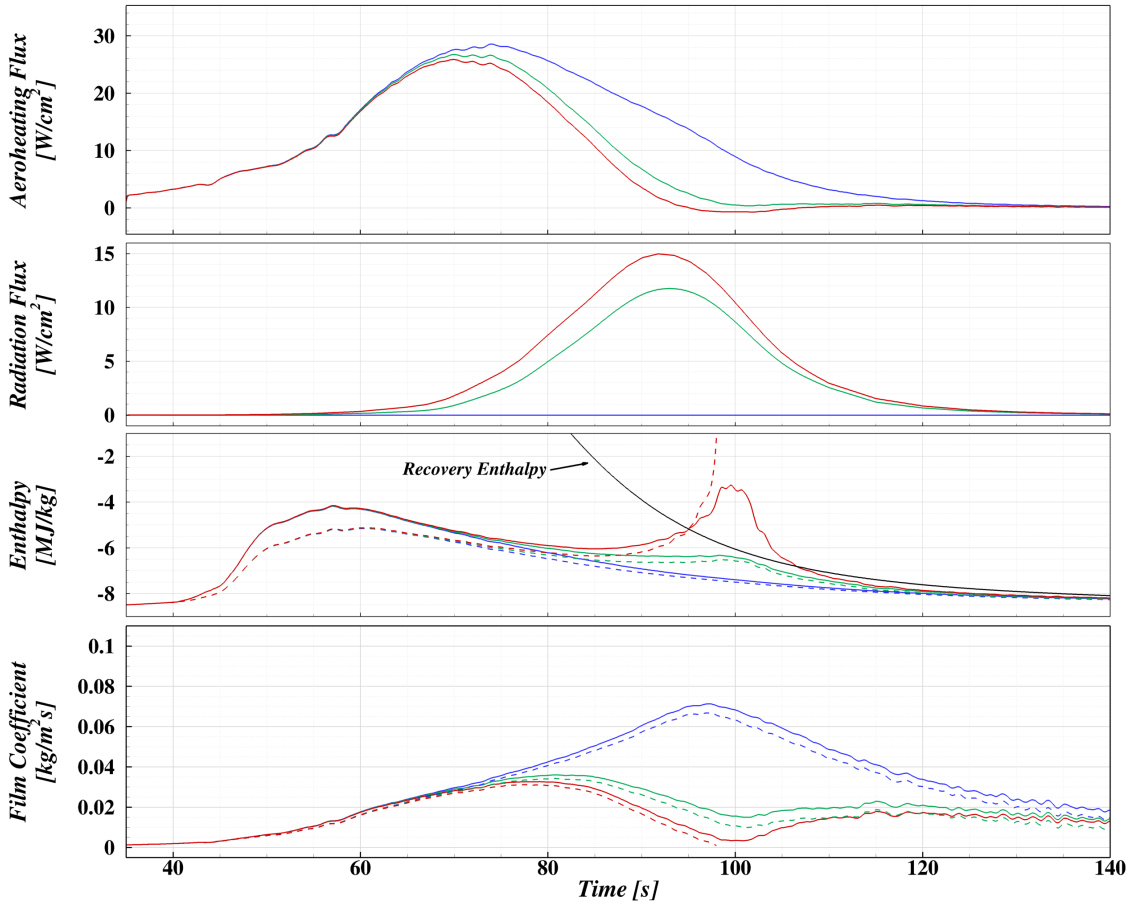

Figure 7.7. MISP 1 SEB reconstructions with no recession permitted. Line colors denote different shock-layer radiation assumptions (blue: no radiation, red: nominal predicted radiation, green: minimum predicted radiation), solid lines denote equilibrium chemistry assumption, dashed lines denote frozen chemistry assumption.

coefficients required to achieve the needed aeroheating flux are reduced. Note, however, in the case of MISP 1 with the nominal radiation profile, the required negative flux could not be produced with the frozen chemistry assumption, so the solution fails before $100\,\mathrm{s}$.

7.3.2 Scaled Diffusion Limit Recession

Effects of surface recession are introduced in Figures 7.9 and 7.10 for MISP 1 and 7, respectively. In these plots, the recession model considered is taken to be uniformly-scaled diffusion limited recession. At each point in the reconstruction, the diffusion limited B'_c

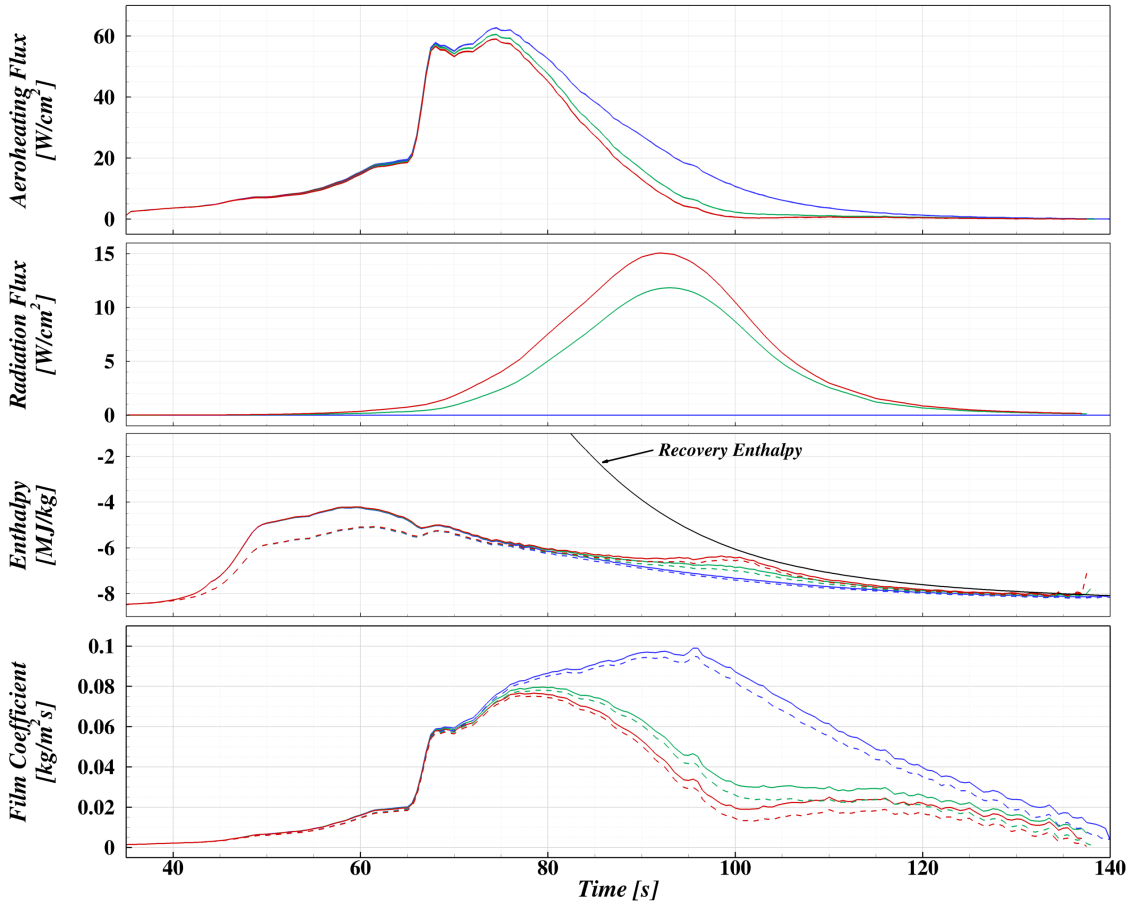

Figure 7.8. MISP 7 SEB reconstructions with no recession permitted. Line colors denote different shock-layer radiation assumptions (blue: no radiation, red: nominal predicted radiation, green: minimum predicted radiation), solid lines denote equilibrium chemistry assumption, dashed lines denote frozen chemistry assumption.

is evaluated (refer to Section 5.2), B'_c is then scaled by a number less than 1 to yield the scaled recession (values of 0, 0.1, 0.2, 0.3, 0.6, and 1.0 are shown), which is then used to evaluate the wall enthalpy (assuming chemical equilibrium)[1]. Two additional plots have been added to these figures, showing the dimensional char mass loss rate and the surface recession. The frozen chemistry assumption is not considered here; instead the dashed lines represent reconstructions that demonstrate clearly infeasible behavior (predicted recession

[1]Note that this is not the same thing done by Mazhari et al. in their original reconstructions. In their work, they evaluated the recession profile assuming the diffusion limit throughout, then scaled the resulting surface profile. These methods will yield different results as the surface temperature will be different at the differing surface locations.

greater than the first TC depth or failure to find a solution during the heat pulse). Since trends are consistent, arrows are included on the plots to denote the direction the result moves as the B'_c scale factor is increased from 0 to 1.

Considering the aeroheating flux in both figures, the effect of increasing recession is to decrease the amount of heat required from the boundary layer. The balance of energy is made up by the energy released in the exothermic recession process. Much like the no-recession cases with nominal radiation sometimes required negative aeroheating flux to balance out the flux due to radiation, increasing the surface recession leads to the need for negative heat fluxes. Increasing surface recession denoted by increasing B'_c leads to higher wall enthalpy (indicated by upward pointing arrows on enthalpy plots in Figures 7.9 and 7.10) as the additional carbon encourages the formation of more CO instead of CO_2 in the ablation products. This increase in wall enthalpy with increased recession means that film coefficients must be larger to produce the required aeroheating flux (indicated by upward pointing arrows on film coefficient plots in Figures 7.9 and 7.10). However, since the rate of recession scales with the film coefficient in diffusion limited (or derived) models, this can lead to a feedback loop, whereby the increased film coefficient to offset the energy released by recession leads to even more recession. As a result of this, reconstructions with B'_c scale factors in excess of 0.3 on MISP 1 and 0.2 on MISP 7 result in un-realistically high recession amounts or lead to solution failure prior to the end of the heat pulse. Shock-layer radiation does not appear to have a strong influence on this process above and beyond what it does for the no-recession case, however consideration of the lowest 'failed' B'_c curves in Figure 7.10 suggests that radiation is probably increasing the B'_c value at which the solution becomes unstable. Aside from the fact that none of the 'successful' reconstructions on MISP 7 show negative aeroheating flux, there are no substantial differences in observations between MISP 1 and MISP 7.

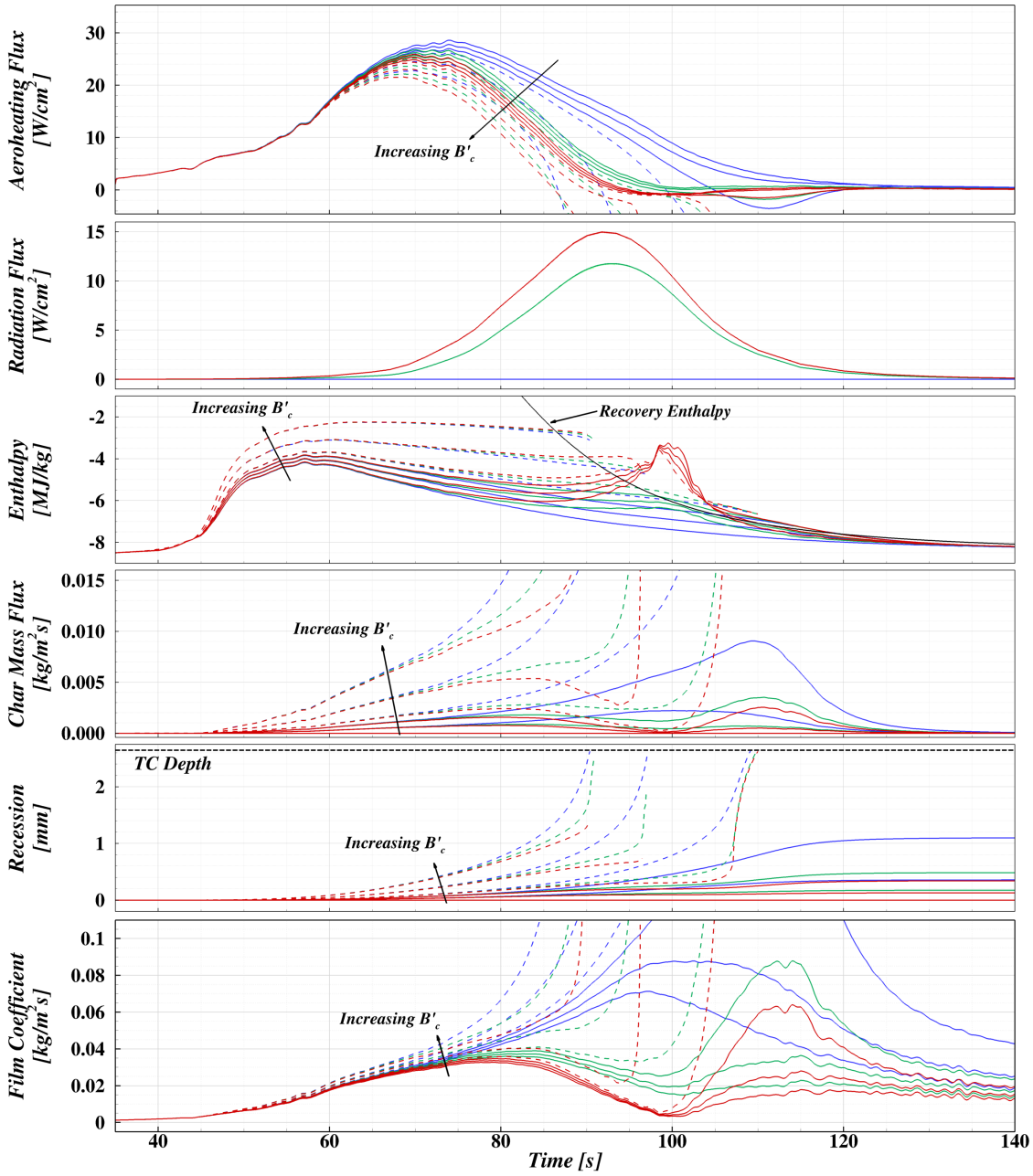

Figure 7.9. MISP 1 SEB reconstructions with B'_c evaluated as fixed percentages of the diffusion limit B'_c. Scale factors shown are 0, 0.1, 0.2, 0.3, 0.6, and 1.0. Line colors denote different shock-layer radiation assumptions (blue: no radiation, red: nominal predicted radiation, green: minimum predicted radiation), with infeasible reconstructions shown with dashed lines.

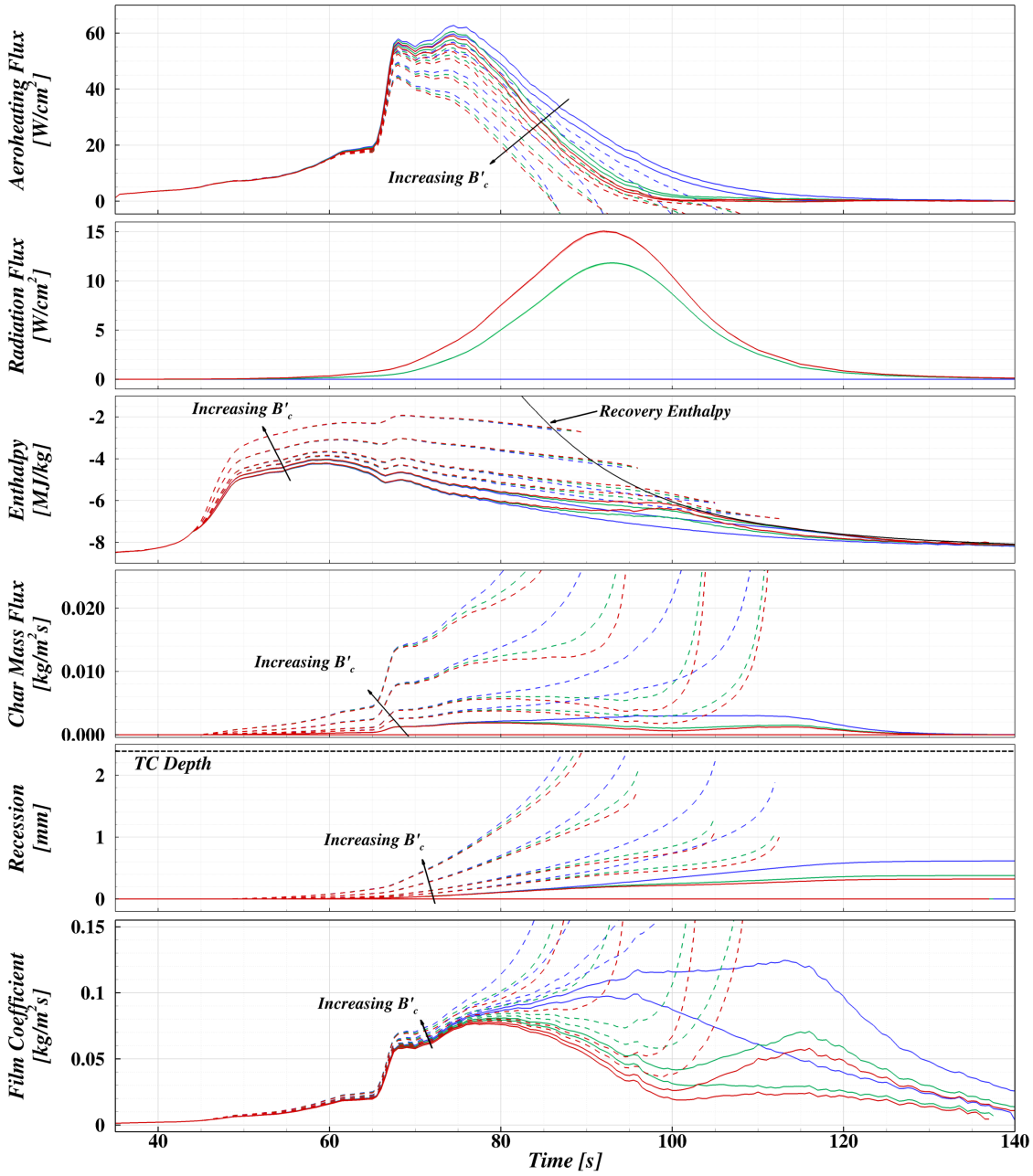

Figure 7.10. MISP 7 SEB reconstructions with B'_c evaluated as fixed percentages of the diffusion limit B'_c. Scale factors shown are 0, 0.1, 0.2, 0.3, 0.6, and 1.0. Line colors denote different shock-layer radiation assumptions (blue: no radiation, red: nominal predicted radiation, green: minimum predicted radiation), with infeasible reconstructions shown with dashed lines.

7.3.3 Kinetically Limited Recession

The uniformly scaled diffusion limit recession model is particularly easy to implement in the present framework and instructive in terms of identifying trends in behavior, but there is little theoretical or experimental basis for using such a model for design purposes. In the event that some kinetic mechanism is preventing recession from achieving the diffusion limit rate, the actual recession rate will likely vary with temperature and species composition. It is not likely that these trajectory-specific conditions will lead to recession rates that are a consistent factor below the diffusion limit rate. Therefore, the next step of this analysis is to incorporate, to the extent presently possible, more realistic kinetically limited reaction mechanisms. The qualification 'to the extent possible' in the previous sentence is a significant one; the present implementation of the decoupled SEB code only permits a single heterogeneous reaction with the gas phase in chemical equilibrium. Physically, this represents the assumption that all heterogeneous reactions are slow compared to one modeled reaction, which itself is slow compared to all gas-phase homogeneous reactions. While this assumption is likely insufficient to safely design a vehicle, single-reaction models will suffice to demonstrate the capability provided by the decoupled SEB reconstruction method and can provide some insight into how more complete kinetic mechanisms could behave under MSL flight-like conditions.

Three individual reactions are considered beyond the full diffusion limit: the Scala "fast" graphite ablation model[2] [46] (assuming $R_b = 1\,\mathrm{m}$), the Park atomic oxygen reaction with solid carbon [56], and a simple model for the reaction of CO_2 with graphite[3] based on the data of Gulbransen [57]. Table 7.2 presents the reaction rate coefficients used and Figure 7.11 shows the resulting forward rate (Equation 5.13) for each model as a function of temperature. Comparing the forward rates in Figure 7.11 reveals that the Park model

[2]It is worth noting the impracticality of using this recession model for design purposes. The Scala models are empirical in nature, so it is risky to apply them in contexts far removed from those for which they were developed. In this case, ablation of a lightweight carbon ablator in a CO_2 atmosphere on a 70° sphere-cone heatshield at an angle of attack is probably an unreasonable departure from spherical high-density graphite nose tips in air for which the models were developed.

[3]Note that this CO_2 model was developed (in Appendix A) for demonstration purposes in the present work and has neither been peer-reviewed nor validated against other data sets.

does not show nearly as much temperature dependence as the other two models, and that the CO_2 reaction is considerably slower than the oxygen reactions (which is a common reason for omitting this reaction from air-based multiple surface reaction mechanisms).

Table 7.2. Heterogeneous reaction models used for SEB reconstruction.

Model	Reaction	$B\left[\mathrm{mol}/\mathrm{m^2 s Pa^n}\right]$	$E_a\left[\mathrm{kJ}/\mathrm{mol}\right]$	$\phi[-]$
Scala "fast" [46]	$0.5O_2 + C(s) \rightarrow CO$	$8.593 \cdot 10^8$	184	0
Park [56]	$O + C(s) \rightarrow CO$	0.689	9.64	-0.5
Simple CO_2 [App. A]	$CO_2 + C(s) \rightarrow 2CO$	$3.356 \cdot 10^9$	341	-0.5

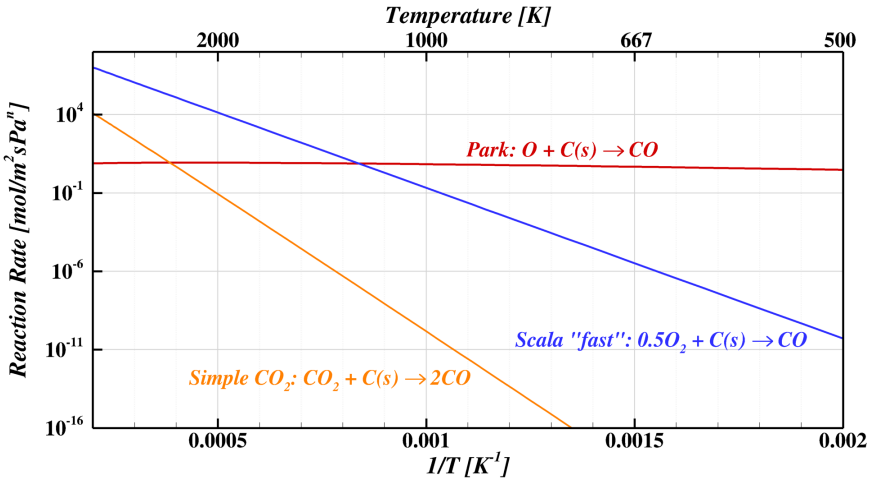

Figure 7.11. Temperature-dependent heterogeneous reaction rate models used for MEDLI SEB reconstruction.

Note that each model reacts a different gas-phase species with solid carbon to form carbon monoxide: the Scala model considers molecular oxygen, O_2; the Park model considers atomic oxygen, O; and the simple CO_2 model considers carbon dioxide. This is important as the different species are present at the surface in different amounts at different points in the entry trajectory, and recession is greatly limited if the required gas-phase species is not present in sufficient quantity. Figure 7.12 shows the mole fraction of these species for both plugs for the reconstructions assuming no recession and the nominal shock-layer radiation profile (reconstruction assumptions are necessary for this comparison since pyrolysis

gas and atmospheric gas are both present in proportions that scale with the film coefficient). The higher heating experienced by MISP 7 leads to considerably more molecular and atomic oxygen during peak heating than on MISP 1, and CO_2 is present in significant amounts through most of the trajectory, although dissociation and pyrolysis gas lead to lower CO_2 concentrations than might otherwise be expected in a mostly CO_2 atmosphere. As a result, it should be expected that the Scala and Park recession models will only show meaningful recession during the window between $60 - 100\,\mathrm{s}$, and that even though the reaction rate for CO_2 is considerably lower than the oxygen reactions, the abundance of CO_2 may yet lead to comparable recession via this mechanism.

SEB reconstruction results for MISP 1 and MISP 7 using the presented kinetic models are shown in Figures 7.13 and 7.14. Considering first MISP 1 in 7.13, it is seen that the two oxygen-based kinetic models (the Scala model shown with dashed lines and the Park reaction model shown with dashed-dot lines) show very little recession (note in particular the plot showing the char mass flux), especially compared to the full diffusion limit (shown with desaturated solid lines). The Scala model does show a very small amount of recession at about $75\,\mathrm{s}$, but it makes a relatively minor impact on the reconstructed film coefficient and aeroheating flux. On MISP 7 in 7.14, however, the Scala model shows quite a bit of recession between 65 and $90\,\mathrm{s}$, even approaching the diffusion limit rate in this time period. Based on Figure 7.12, this could easily be attributed to the increased amount of molecular oxygen present, although the surface temperatures on MISP 7 can be up to $400\,\mathrm{K}$ higher than MISP 1 (based on Figure 7.6), which can drive up the ablation rates as well. The Park model does not show significant recession on either plug, suggesting that the additional recession due to the Scala model is due to the increased surface temperature. Despite the abundance of CO_2 to drive the simple CO_2 recession model, it would seem that only the high temperatures during peak heating on MISP 7 are sufficient to drive notable recession.

None of the kinetic recession models considered allows for adequate recession to ablate through the first TC, so it is not possible to invalidate any of the models based on the flight data. It is interesting to note, however, that all models are in agreement that there is no recession prior to $65\,\mathrm{s}$, even though the ablation products are theoretically capable of

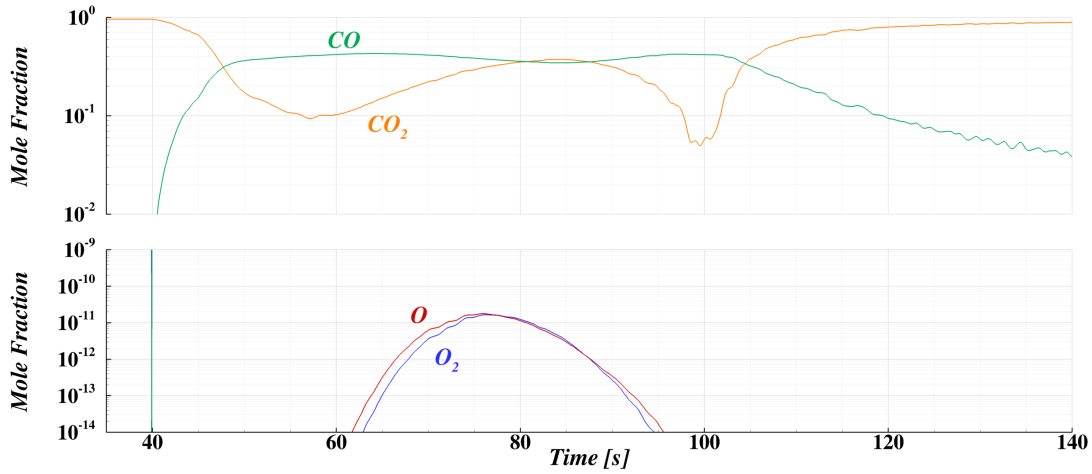

(a) MISP 1

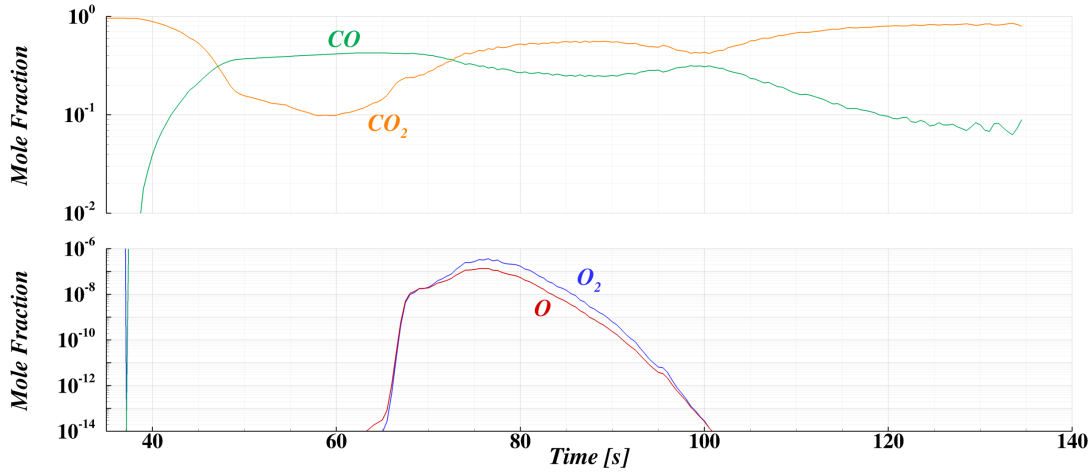

(b) MISP 7

Figure 7.12. Mole fraction of select gas-phase species in wall gas mixture of SEB reconstructions assuming no recession and the nominal shock-layer radiation profile. Note the split ordinate due to the considerable difference between oxygen and carbon species concentrations.

supporting more gas-phase carbon. It would seem that the surface temperatures are simply too low to drive this carbon from solid to gas phase.

Because all of the kinetic models predict that recession has largely stopped by the time the recovery enthalpy reaches the level of the wall enthalpy, the net impact on the aeroheating flux and film coefficient are slightly different than might be expected based on the uniformly scaled diffusion limit results in Figures 7.9 and 7.10. Since MISP 1 recorded very

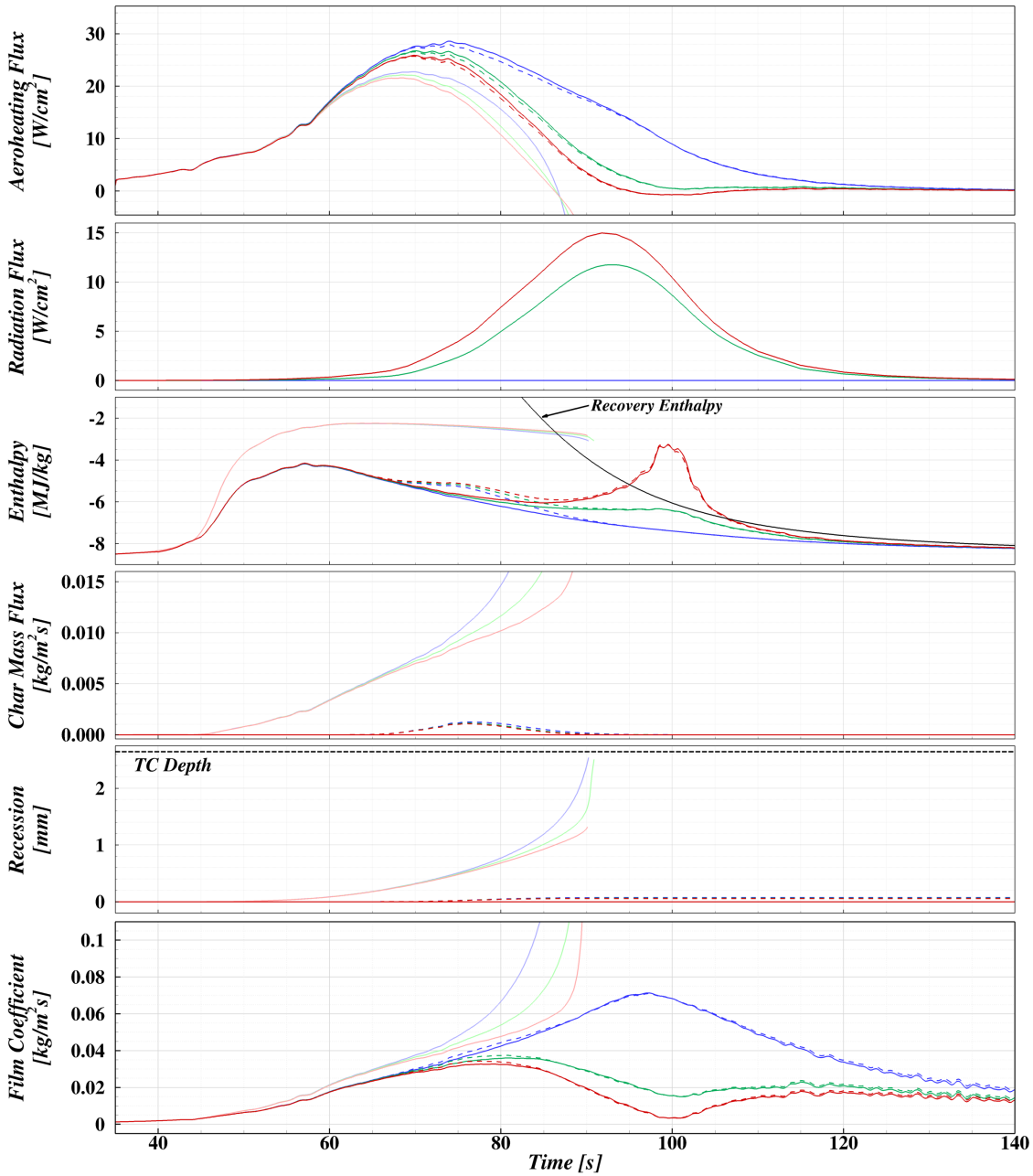

Figure 7.13. MISP 1 SEB reconstructions using Scala "fast" carbon oxidation model (dashed lines), Park atomic oxidation model (dash-dot lines), simple CO_2 model (solid lines), and the diffusion limit model (desaturated solid lines). Line colors denote different shock-layer radiation assumptions (blue: no radiation, red: nominal predicted radiation, green: minimum predicted radiation).

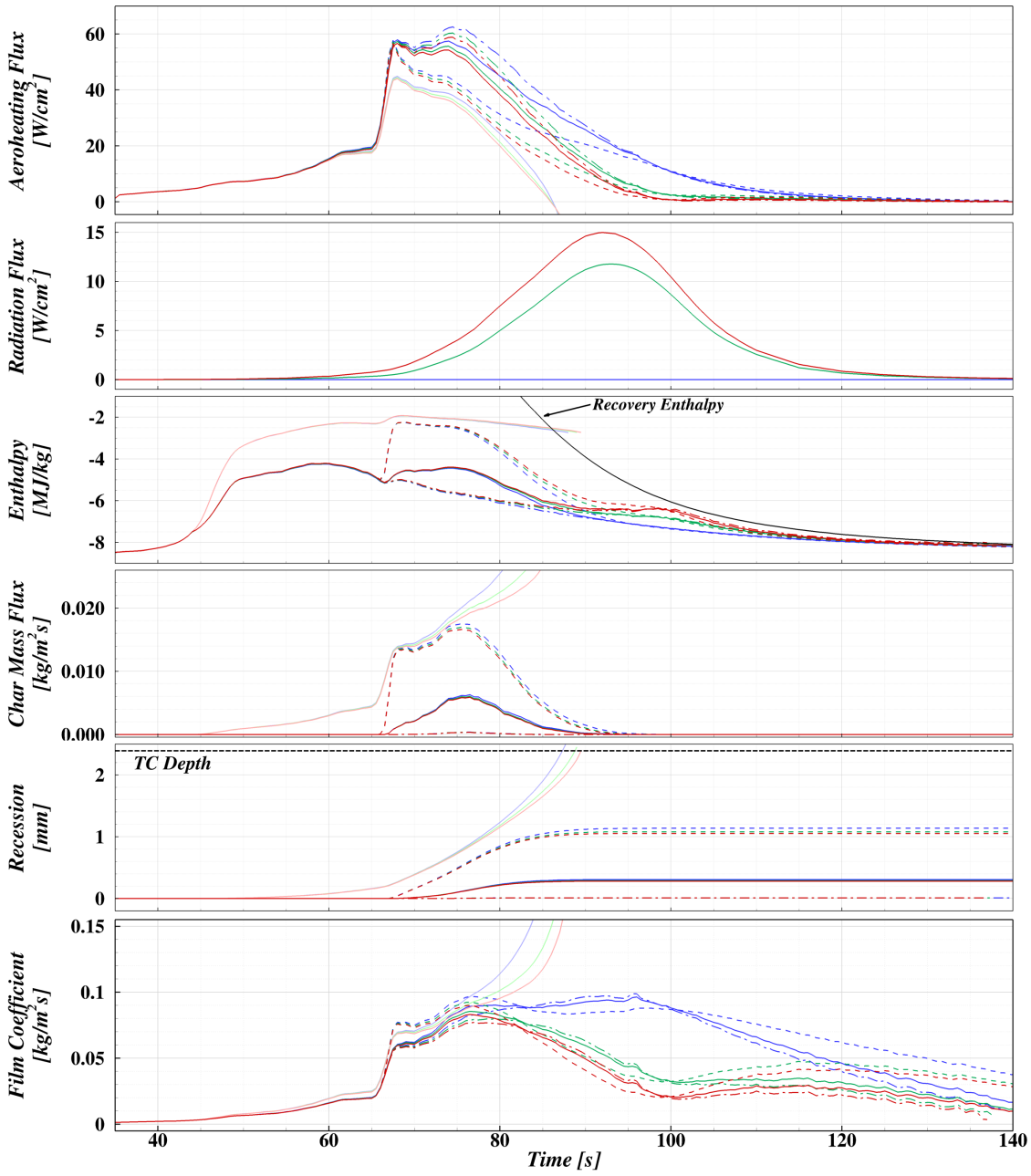

Figure 7.14. MISP 7 SEB reconstructions using Scala "fast" carbon oxidation model (dashed lines), Park atomic oxidation model (dash-dot lines), simple CO_2 model (solid lines), and the diffusion limit model (desaturated solid lines). Line colors denote different shock-layer radiation assumptions (blue: no radiation, red: nominal predicted radiation, green: minimum predicted radiation).

little kinetically-driven recession, the discussion here will focus on MISP 7 (Figure 7.14). Much like before, recession proportionally decreases the necessary aeroheating flux, as recession adds another energy source in the SEB that decreases the amount of energy required from the boundary layer. Also like before, adding ablated carbon to the ablation products leads to increased wall enthalpy. The reconstructed film coefficient, however, shows an increase in film coefficient prior to $80\,\mathrm{s}$, but a decrease after. Differences in the reconstructed terms after recession has ceased are due to variations in the location of the surface and the corresponding surface temperature.

The net effect of the isolated recession is a more exaggerated film coefficient profile, although it would seem that the only potentially unreasonable characteristic of the reconstructed profile (the peak or valley around $100\,\mathrm{s}$) is more strongly influenced by the shock-layer radiation assumption than by recession. While the author has not seen detailed CFD predictions of the MEDLI heatshield on the best estimated trajectory, given the sensitivity of the reconstructions to the shock-layer radiation input, it seems likely that comparison to CFD predictions around $100\,\mathrm{s}$ could lead to better estimates of the absorbed shock-layer radiation (by either changes in the assumed incident radiation or the absorptivity of the material model) particularly on MISP 1 where turbulence and recession do not play a significant role. However, given a desire to use flight environment reconstructions to validate CFD prediction tools for complicated entry flows, it may be inappropriate to incorporate CFD prediction into the reconstruction process in this manner.

It is an unfortunate result of the non-uniqueness of the inverse problem that without clear knowledge of what radiation profile and what recession model is most accurate, the specific film coefficient cannot be computed for a true validation of CFD predictions. Furthermore, recall that the film coefficient that balances the SEB represents the rough-surface, blown film coefficient, so comparison to smooth-wall CFD predictions requires the application of yet another empirical model for the effects of surface blowing (this model has been applied for presented results, yielding the presumed unblown film coefficient). For flight data of this nature to yield insight into the accuracy of high-fidelity prediction tools at flight conditions, the experiment must be designed differently such that more information

on recession and shock-layer radiation are obtained and incorporated into the reconstruction process. The presented decoupled SEB method should be able to incorporate additional recession and radiation information to produce refined estimates of the true film coefficient.

7.4 Summary

In this chapter, two plugs from the MEDLI flight data set are reconstructed using the techniques proposed in this document. Two key uncertainties that impact the reconstructed film coefficient are discussed: the shock-layer radiation experienced in flight, and the recession model. The shock-layer radiation sensitivity is addressed by carrying three assumed profiles through the full analysis process. The recession model sensitivity is addressed by observing the response of two classes of recession model: scaled diffusion limit models and single-reaction kinetic models. It is shown that for all of the shock-layer radiation assumptions, the diffusion limit recession model shows too much recession considering that at upper bound on recession is known. Uniformly scaling the diffusion limit B_c' down by a constant factor suggests that recession proceeded at no greater than 20% of the diffusion limit rate integrated over the whole entry. The three single-reaction kinetic models considered, each based on a different reacting gas-phase species, show that recession only occurs near peak heating when temperatures are high and reactive species are abundant. None of the kinetic models predict recession in excess of the depth of the first TC. The shock-layer radiation assumption is shown to have a considerable effect on the reconstructed film coefficient. Since an embedded TC is unable to distinguish heating to the TPS surface via radiation from heating through convection, future flights must incorporate sensors to quantify the radiation component if an accurate film coefficient reconstruction for CFD validation is desired.

For the present dataset, if reasonable bounds of the CFD uncertainty can be formed, it may be possible to use the present reconstruction techniques to refine the range of possible absorbed shock-layer radiation profiles due to the considerable sensitivity of the reconstructed film coefficient to this parameter. This is a notable finding permitted only by in-

verse reconstruction. It has been noted previously through direct comparisons of predicted environments to flight data that predictions fail to capture the full heating level observed, and radiation was proposed as a possible solution to the shortfall. The proposed radiation profiles, however, failed to completely make up for the shortage. By fixing the total environment heating to that necessary to match the thermal response at the TC locations, the surface thermochemistry models can be applied at more accurate conditions, and the impacts of the balance between radiation and convection can be identified more clearly. In this instance, the considerable sensitivity of the reconstructed film coefficients to the shock layer radiation near $100\,\mathrm{s}$ means that it may be possible to refine the radiation contribution estimate in this time period with an estimate of the film coefficient, even if the film coefficient estimate is reasonably uncertain. More work will be necessary to determine to what extent the radiation estimate can be confidently refined.

8. SUMMARY

An alternative approach for reconstructing surface heating environments in practical flight experiments with particular emphasis on reconstructions on ablative TPS materials is presented. Current methods are shown for several practical examples to be overly dissipative, computationally expensive, or subject to modeling errors for physically complicated systems. Two distinct methods are proposed to improve upon these limitations.

First, the hybrid Sequential Subdomain IHCP algorithm is developed and demonstrated to provide many of the computational benefits of sequential IHCP methods, while retaining the accuracy of whole domain methods for sensors moderately insensitive to the boundary condition. It is shown that the presented implementation is flexible enough to afford the user the freedom to fine-tune the regularization to optimize the accuracy and computational effort in a reconstruction. The local regularization scaling option implemented is shown to reduce the sensitivity of the end result to choices made by the user (leading to improved analyst-independence of the results) and accommodates problems where the sensitivity coefficients, and therefore the required regularization, vary considerably through the course of the flight. Improvements in run-time are demonstrated for non-linear reconstruction problems, and the capability to handle problems with multiple relevant time-scales is demonstrated. Finally, the specific implementation is shown to be capable of performing multi-component reconstructions with spatially-varying unknown boundary conditions.

Second, the decoupled SEB reconstruction approach is developed to separate the surface thermochemistry and the surface recession problems from the computationally expensive IHCP solution. The theoretical basis and limitations of the decoupling assumptions are presented, and a number of verification cases are presented to demonstrate the method with and without the presence of pyrolysis gas. The decoupled SEB reconstruction is compared to a conventional IHCP film coefficient reconstruction to demonstrate the advantages of the decoupled approach and the accuracy of the end result.

To demonstrate the capabilities of the proposed methods, two instrumented plugs from the MEDLI flight data set are reconstructed and two particular uncertain terms in the SEB are addressed: the shock-layer radiation and recession models. A number of scaled diffusion-limited recession models and kinetically-limited recession models are considered in the reconstructions, with the specific impact of each model on the reconstruction discussed. The reconstructions are seen to be particularly sensitive to the assumptions made regarding the shock-layer radiation. While the non-uniqueness of the inverse problem means that the specific instrumentation used is not able to distinguish between radiative and convective heating, the decoupled SEB reconstruction approach allows the rapid evaluation of multiple recession and radiation assumptions, and additional information can be incorporated to determine feasible and infeasible combinations of environment assumptions.

Two primary limitations of the present reconstruction tools are identified. First, while multi-component reconstructions can be performed and are demonstrated, the specific implementation is not optimized for efficient solution of a large number of unknown spatially-varying boundary conditions. Furthermore, the IHCP implementation is constrained to assuming piecewise-constant variation of the boundary conditions in time, whereas piecewise-linear would likely yield smoother results when the reconstruction frequency is low. Second, the decoupled SEB tool is limited by the fact that only very simple kinetically-limited recession models may be considered. Much more detailed heterogeneous reaction mechanisms are available in the literature, however more robust solution algorithms for the chemical equilibrium problem must be implemented and more advanced models may be required to incorporate more accurate species diffusion assumptions. Present needs in the aerothermal community suggest that improvements in reconstructions on ablators are probably more important than the improvements for multi-component reconstructions, so future efforts are going to be dedicated to improving the surface thermochemistry capabilities of the decoupled SEB tool.

The discussion in this work has focused primarily on the reconstruction of flight data to support design model validation. This is not to downplay the importance of well-designed

ground testing in the validation process. Many aspects of an aerothermal environment database can, and should, be validated using available wind tunnels where conditions can be more carefully controlled than in flight. Likewise, material response models can be validated using arc-jet and plasma torch facilities. Neither of these options will be able to match all of the relevant conditions and scaling conditions may not always be straightforward. Flight testing is necessary as a final check to verify that scaling assumptions required in ground testing do not result in insufficient heatshield designs.

Given the generally high costs of performing flight tests, it is desirable to maximize the amount of information that can be extracted from the data and use that information to improve the models and heatshield designs. It is towards this end that the methods described in this work have been developed. However, it is worth noting that these methods may also be used to augment the analysis of arc-jet test data. Decoupled SEB reconstruction from temperatures in an arc-jet tested ablator sample can permit efficient evaluation of different recession models, which is particularly helpful in model development as the true recession profile will likely be known. Furthermore, if the arc-jet flowfield is well characterized, the true film coefficient may be known well enough to provide insight into other aspects of the material response model. Flight and ground test data processed with these methods will be used in conjunction with more conventional data obtained in wind tunnels, arc-jets, and fundamental scientific experiments to advance the state-of-the-art in ablation and aerothermal environment modeling.

REFERENCES

REFERENCES

[1] D. B. Lee and W. D. Goodrich. The Aerothermodynamic Environment of the Apollo Command Module During Superorbital Entry. Technical Report NASA TN D-6792, Manned Spacecraft Center, Houston, TX 77058, 1972.

[2] F. M. Cheatwood, D. Bose, C. D. Karlgaard, C. A. Kuhl, J. A. Santos, and M. J. Wright. Mars Science Laboratory (MSL) Entry, Descent, and Landing Instrumentation (MEDLI): Complete Flight Data Set. Technical Report NASA/TM-2014-218533, NASA Langley Research Center, Langley Station, Hampton, VA, October 2014 2014.

[3] D. Bose, T. White, J. A. Santos, J. Feldman, M. Mahzari, M. Olson, and B. Laub. Initial Assessment of Mars Science Laboratory Heatshield Instrumentation and Flight Data. AIAA Paper 2013-0908, 51st AIAA Aerospace Sciences Meeting including the New Horizons Forum and Aerospace Exposition, Grapevine, TX, January 7-10, 2013.

[4] T. R. White, I. Cozmuta, J. A. Santos, B. Laub, and M. Mahzari. Proposed Analysis Process for Mars Science Laboratory Heat Shield Sensor Plug Flight Data. AIAA Paper 2011-3957, 42nd AIAA Thermophysics Conference, Honolulu, HI, June 27-30, 2011.

[5] T. R. White, M. Mahzari, D. Bose, and J. A. Santos. Post-flight Analysis of the Mars Science Laboratory Entry Aerothermal Environment and Thermal Protection System Response. AIAA Paper 2013-2779, 44th AIAA Thermophysics Conference, San Diego, CA, June 24-27, 2013.

[6] M. Mahzari and R. D. Braun. Time-Dependent Mars Entry Aeroheating Estimation from Simulated In-Depth Heat Shield Temperature Measurements. *Journal of Thermophysics and Heat Transfer*, 27(3):435–446, 2013.

[7] M. Mahzari, R. D. Braun, T. R. White, and D. Bose. Inverse Estimation of the Mars Science Laboratory Entry Aerothermal Environment and Thermal Protection System Response. AIAA Paper 2013-2780, 44th AIAA Thermophysics Conference, San Diego, CA, June 24-27, 2013, 2013.

[8] B. A. Cruden, A. M. Brandis, T. R. White, and M. Mahzari. Radiative Heating for MSL Entry : Verification of Simulations from Ground Test to Flight Data. AIAA Paper 2015-1894, 53rd AIAA Aerospace Sciences Meeting, Kissimmee, FL, January 5-9, 2015.

[9] K. A. Woodbury. Sequential function specification method using future times for function estimation. In Keith A. Woodbury, editor, *Inverse Engineering Handbook*, chapter 2. CRC Press, Boca Raton, FL, 2003.

[10] M. N. Ozisik and H. R. B. Orlande. *Inverse Heat Transfer: Fundamentals and Applications*. Taylor & Francis, Washington, D.C., 2000.

[11] W. J. Cook and E. J. Felderman. Reduction of Data from Thin-Film Heat-Transfer Gages: A Concise Numerical Technique. *AIAA Journal*, 4(3):561–562, 1966.

[12] S. Kuchi-Ishi. Uncertianty Evaluation of Thermocouple Aeroheating Measurements for Hypersonic Wind-Tunnel Tests. *Journal of Spacecraft and Rockets*, 43(3):698–700, 2006.

[13] K. A. Woodbury, J. V. Beck, and H. Najafi. Filter solution of inverse heat conduction problem using measured temperature history as remote boundary condition. *International Journal of Heat and Mass Transfer*, 72:139–147, 2014.

[14] J. V. Beck, B. F. Blackwell, and C. R. St. Clair. *Inverse Heat Conduction Problems*. Wiley-Interscience, New York, NY, 1985.

[15] S. Deng and Y. Hwang. Applying neural networks to the solution of forward and inverse heat conduction problems. *International Journal of Heat and Mass Transfer*, 49(25-26):4732–4750, December 2006.

[16] S. Deng and Y. Hwang. Solution of inverse heat conduction problems using Kalman filter-enhanced Bayesian back propagation neural network data fusion. *International Journal of Heat and Mass Transfer*, 50(11-12):2089–2100, June 2007.

[17] B. S. Elkins, M. Keyhani, and J. I. Frankel. Surface Heat Flux Prediction Through Physics-Based Calibration, Part A: Theory. *Journal of Thermophysics and Heat Transfer*, 27(2):189–205, 2013.

[18] J. I. Frankel and M. Keyhani. Inverse Ablation Analysis and the Calibration Integral Equation Method. *Journal of Thermophysics and Heat Transfer*, Posted online on September 16, 2015.

[19] M. Raynaud. Some comments on the sensitivity to sensor location of inverse heat conduction problems using Beck's method. *International Journal of Heat and Mass Transfer*, 29(5):815–817, 1986.

[20] Y. Jarny. The adjoint method to compute the numerical solutions of inverse problems. In Keith A. Woodbury, editor, *Inverse Engineering Handbook*, chapter 3. CRC Press, Boca Raton, FL, 2003.

[21] A. Carassos. Determining surface temperatures from interior observations. *SIAM Journal of Applied Mathematics*, 42(3):558–574, 1982.

[22] D. A. Murio. Mollification and space marching. In Keith A. Woodbury, editor, *Inverse Engineering Handbook*, chapter 4. CRC Press, Boca Raton, FL, 2003.

[23] B. Blackwell. Inverse Methods for Estimating Heat Flux from Temperature Measurements: Seminar at Purdue Univeristy School of Aeronautics and Astronautics, 2008.

[24] F. P. Incropera and D. P. DeWitt. *Fundamentals of Heat and Mass Transfer*. John Wiley & Sons, Hoboken, NJ, 5th edition, 2002.

[25] J. Lachaud, A. Martin, I. Cozmuta, and B. Laub. Ablation test-case series 1. *4th AFOSR/SNL/NASA Ablation Workshop*, 2010.

[26] P. Craven and G. Wahba. Smoothing noisy data with spline functions - Estimating the correct degree of smoothing by the method of generalized cross-validation. *Numerische Mathematik*, 31:377–403, 1979.

[27] C. H. Huang and M. N. Ozisik. Optimal regularization method to determine the strength of a plane surface heat source. *International Journal of Heat and Fluid Flow*, 12(2):173–178, 1991.

[28] A. van den Bos. *Parameter Estimation for Scientists and Engineers*. Wiley-Interscience, Hoboken, NJ, 2007.

[29] P. K. Lamm. Variable-smoothing local regularization methods for first-kind integral equations. *Inverse Problems*, 19(1):195–216, 2003.

[30] P. K. Lamm and Z. Dai. On local regularization methods for linear Volterra equations and nonlinear equations of Hammerstein type. *Inverse Problems*, 21(5):1773–1790, 2005.

[31] B. S. Kirk, J. W. Peterson, R. H. Stogner, and G. F. Carey. `libMesh`: A C++ Library for Parallel Adaptive Mesh Refinement/Coarsening Simulations. *Engineering with Computers*, 22(3):237–254, 2006.

[32] A. J. Amar, N. D. Calvert, and B. S. Kirk. Development and Verification of the Charring Ablating Thermal Protection Implicit System Solver. AIAA Paper 2011-144, 49th AIAA Aerospace Sciences Meeting, Orlando, FL, January 4-7, 2011.

[33] A. J. Amar, A. B. Oliver, B. S. Kirk, and G. Salazar. Overview of the CHarring Ablator Response (CHAR) Code. AIAA Paper 2016-3385, 46th AIAA Thermophysics Conference, Washington, DC, June 13-17, 2016.

[34] A. J. Amar and B. S. Kirk and A. B. Oliver and G. Salazar and J. C. Droba. Development and Verification of the CHarring Ablator Response (CHAR) Code. NASA Johnson Space Center, Houston, TX 77058, 2013.

[35] A. J. Amar. Modeling of One-Dimensional Ablation with Porous Flow Using Finite Control Volume Procedure. Master's thesis, North Carolina State University, 2006.

[36] C. B. Moyer and R. A. Rindal. An Analysis of the Coupled Chemically Reacting Boundary Layer and Charring Ablator, Part II: Finite Difference Solution for the In-Depth Response of Charring Materials Considering Surface Chemical and Energy Balances. Technical Report 66-7 Part II, Aerotherm, March 1967.

[37] S. D. Williams and D. M. Curry. Thermal protection materials: Thermophysical property data. Technical Report NASA-RP-1289, NASA Lyndon B. Johnson Space Center, Houston, TX, 1992.

[38] J. Congdon, R. Beck, and D. Prabhu. Ablation Analysis of Teflon Reference Samples Tested in the Arc-Jets of NASA/ARC. AIAA Paper 2008-3804, 40th Thermophysics Conference, June 23-26, 2008.

[39] R. M. Kendall, R. A. Rindal, and E. P. Bartlett. Thermochemical Ablation. AIAA Paper 65-642, AIAA Thermophysics Specialist Conference, Moneterey, CA, September 13-15, 1965.

[40] R. M. Kendall. An Analysis of the Coupled Chemically Reactiing Boundary Layer and Charring Ablator, Part V: A General Approach to the Thermochemical Solution of Mixed Equilibirum-Nonequilibrium , Homogeneous and Heterogeneous Systems. Technical Report 66-7 Part V, Aerotherm, June 1968.

[41] B. F. Blackwell and M. A. Howard. An Element Potential Based Chemical Equilibrium Solver for Gas / Surface Thermochemistry. AIAA Paper 2012-0815, 50th AIAA Aerospace Sciences Meeting including the New Horizons Forum and Aerospace Exposition, Nashville, TN, January 9-12, 2012.

[42] M. E. Ewing and D. A. Isaac. Mathematical Modeling of Multiphase Chemical Equilibrium. *Journal of Thermophysics and Heat Transfer*, 29(3):551–562, 2015.

[43] J. B. Scoggins and T. E. Magin. Gibbs function continuation for linearly constrained multiphase equilibria. *Combustion and Flame*, 162(12):4514–4522, 2015.

[44] F. S. Milos and J. Marschall. Thermochemical Ablation Model for TPS Materials with Multiple Surface Constituents. AIAA Paper 94-2042, 6th AIAA/ASME Joint Thermophysics and Heat Transfer Conference, Colorado Springs, CO, June 20-23, 1994.

[45] F. S. Milos and Y.-K. Chen. Comprehensive Model for Multicomponent Ablation Thermochemistry. AIAA Paper 97-0141, AIAA 35th Aerospace Sciences Meeting & Exhibit, Reno, NV, January 6-9, 1997.

[46] S. M. Scala. The Ablation of Graphite in Dissociated Air, Part I: Theory. IAS National Summer Meeting, Los Angeles, CA, June 19-22, 1962.

[47] W. E. Welsh Jr. and P. M. Chung. A Modified Theory for the Effect of Surface Temperature on the Combustion Rate of Carbon Surfaces in Air. Heat Transfer and Fluid Mechanics Institute, Pasadena, CA, June 12-14, 1963.

[48] S. V. Zhluktov and T. Abe. Viscous Shock-Layer Simulation of Airflow past Ablating Blunt Body with Carbon Surface. *Journal of Thermophysics and Heat Transfer*, 13(1):50–59, 1999.

[49] W. Kays, M.Crawford, and B. Weigand. *Convective Heat and Mass Transfer*. McGraw-Hill, 4th edition, 2005.

[50] Y.-K. Chen Frank Milos. Ablation and thermal response program for spacecraft heatshield design. *Journal of Spacecraft and Rockets*, 36(3):475–483, 1999.

[51] S. B. Pope. Gibbs function continuation for the stable computation of chemical equilibrium. *Combustion and Flame*, 139(3):222–226, 2004.

[52] J. B. Scoggins and T. E. Magin. Development of Mutation++: MUlticomponent Thermodynamics And Transport properties for IONized gases library in C++. AIAA Paper 2014-2966, 11th AIAA/ASME Joint Thermophysics and Heat Transfer Conference, Atlanta, GA, June 16-20, 2014.

[53] P. J. Roache. *Verification and Validation in Computational Science and Engineering*. Hermosa Publishers, Albuquerque, NM, 1998.

[54] A. Savitzky and M. J. E. Golay. Smoothing and Differentiation of Data by Simplified Least Squares Procedures. *Analytical Chemistry*, 36(8):1627–1639, 1964.

[55] H. H. Madden. Comments on the Savitzky-Golay convolution method for least-squares-fit smoothing and differentiation of digital data. *Analytical Chemistry*, 50(9):1383–1386, 1978.

[56] C. Park. Effects of Atomic Oxygen on Graphite Ablation. *AIAA Journal*, 14(11):1640–1642, 1976.

[57] E. Gulbransen, K. Andrew, and F. Brassart. Reaction of graphite with carbon dioxide at 1000-1600C under flow conditions. *Carbon*, 2(4):421–429, 1965.

APPENDICES

A. CO_2 RECESSION MODEL DERIVATION

Gulbransen et al. [57] measured the rate of consumption of spectroscopic-grade graphite by CO_2 gas at a range of elevated temperatures. A number of parameters were varied, but the most significant parameters were the temperature and gas flow rates. Ablation was measured by the weight of the solid specimen, and ablation rate was computed using a curve fit of weight vs. time at the initial time when the specimen surface area was best characterized. A high level summary of the observations is that ablation rate was seen to be insensitive to the gas flow rate at temperatures below $1350\,^{\circ}\mathrm{C}$, indicating reaction-rate controlled ablation, and the ablation rate could be correlated to gas flow rate above $1400\,^{\circ}\mathrm{C}$, indicating diffusion limited ablation. The pressure was held constant at approximately $2.5\,\mathrm{kPa}$, however the pressure was varied for a diffusion limited temperature with little change in the ablation rate noted. Carbon consumption rate was presented in a tabular form that permits further processing to construct a recession model that can be used to approximate how the Martian atmosphere might drive ablation of carbon heatshield materials.

The present recession model assumes a temperature-varying reaction probability on the kinetic gas theory expression for gas molecule collisions with the surface. The model takes the form

$$\dot{m}_i = K_{f,i}\rho_i, \quad \left[\mathrm{kg/m^2 s}\right] \tag{A.1}$$

where $\dot{m}_i$ is the consumption rate of solid due to gas phase species i, $K_{f,i}$ is the forward reaction rate due to species i, and ρ_i is the density of species i. The forward reaction rate has the form

$$K_{f,i} = \gamma(T)\sqrt{\frac{\mathcal{R}T}{2\pi\mathcal{M}_i}}, \quad \left[\mathrm{m/s}\right] \tag{A.2}$$

where $\gamma(T)$ is the reaction probability, $\mathcal{R}$ is the universal gas constant ($8.314\,{}^{\mathrm{J}}/_{\mathrm{mol-K}}$), $\mathcal{M}_i$ is the molecular weight of species i, and T is the temperature (K). The term in the radical is closely related to the kinetic theory of gases expression for the number of gas particle collisions with a surface per unit area (the *impingement rate*). If every surface collision resulted in reaction with a carbon atom from the surface, the atomic carbon consumption rate would match this rate. Heterogeneous reaction physics are much more complicated (often involving specific reaction sites and adsorbed species), so an empirical expression for the reaction probability is derived from test data to approximate the true behavior.

The ACE kinetics model implemented in this work takes the reaction parameters in a slightly different form than Equations A.1 and A.2. As was shown in Section 5.2, this model computes the ablation rate using the gas species partial pressure (Equation 5.12). Furthermore, the forward rate is given by an exponential model (Equation 5.13). The code is capable of taking the parameter B_n of Equation 5.13 in table form as an arbitrary function of temperature for more complicated models; however, if the only temperature dependence in $\gamma(T)$ is exponential, ACE inputs may be used directly. Substituting in the ideal gas law for the species density, the ACE model forward rate is given by

$$K_{f_n} = \frac{K_{f,i}}{\mathcal{R}T} = \frac{\gamma(T)}{\sqrt{2\pi\mathcal{R}\mathcal{M}_i T}}. \quad \left[{}^{\mathrm{mol}}/_{\mathrm{m^2 sPa}}\right] \tag{A.3}$$

If the individual ACE inputs are used, the ACE term ϕ_n takes a value of -0.5, E_{a_n} is defined to yield the appropriate exponential term in $\gamma(T)$, and B_n is defined to account for the remaining terms in Equation A.3.

The reaction probability of the ablation data was evaluated by dividing the experimentally observed ablation rate (atoms per second) by the corresponding impingement rate. Figure A.1 shows the resulting reaction probabilities of the dataset, along with a best fit exponential curve. It should be noted that this curve fit will yield reaction probabilities greater than unity for temperatures in excess of $2233\,\mathrm{K}$, so it is not expected that this will yield useful results beyond this. A more significant limitation of this model, however, is the assumption that only CO_2 molecules were present in the experiment. If CO_2 is allowed

to dissociate into CO and O_2, it will do so beginning at $1500\,\mathrm{K}$ based on equilibrium calculations. This was not taken into account in the presented evaluation of the experimental reaction probability and could lead to over- or under-prediction of the recession rate depending on the relative proportion of O_2 and CO_2 after dissociation in the experiment as compared to application at flight conditions.

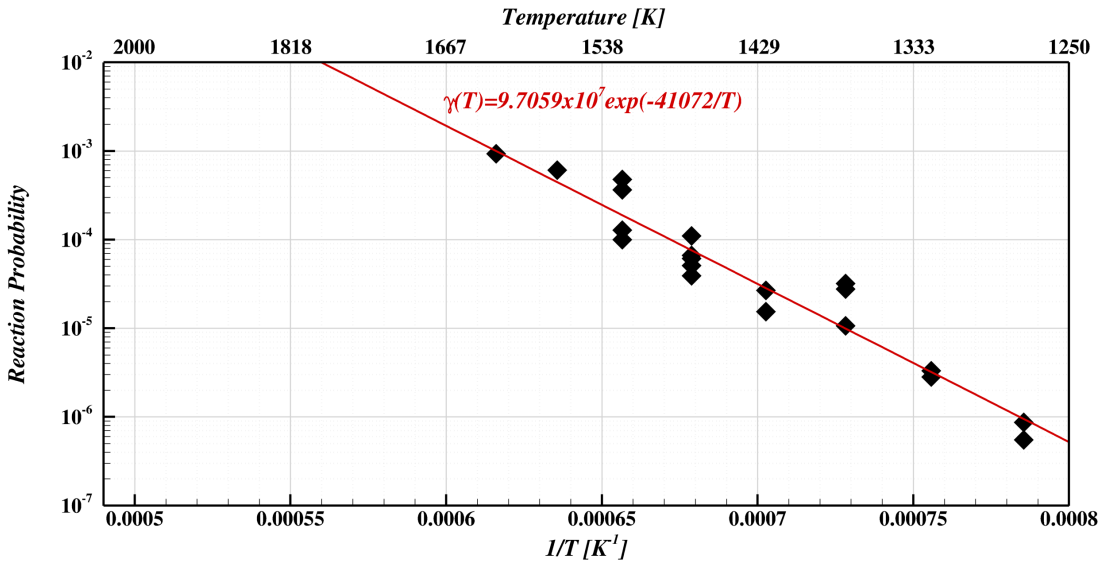

Figure A.1. Fit of reaction probability of Gulbransen et al. [57] ablation data.

Given the partial pressure of CO_2 and surface temperature, the reaction probability and impingement rate can be used to obtain the overall recession rate per unit area of carbon. Because PICA is a porous low density material, it is assumed that the actual surface area of carbon per unit of heatshield area is somewhat larger than unity. As such, the forward reaction rate is augmented by a factor of 50 to account for this fact. This factor is a rough estimate based on the surface areas of pure carbon cylinders of a diameter roughly equivalent to the fibers in PICA char with a density consistent with that of PICA char.

The final recession model coefficients used in the analysis representing the reaction of

$$CO_2 + C(s) \rightarrow 2CO \tag{A.4}$$

is given by

$$B_n = 3.356 \cdot 10^9 \, {}^{\mathrm{mol}}/_{\mathrm{m^2 s Pa}} \tag{A.5}$$

$$E_{a_n} = 341 \, {}^{\mathrm{kJ}}/_{\mathrm{mol}} \tag{A.6}$$

$$\phi_n = -0.5. \tag{A.7}$$

It should be noted again that this model was developed simply for demonstration purposes in this work to approximate how CO_2 driven ablation might behave. This model has not been peer-reviewed, nor has any attempt yet been made to validate this model against any other data sources.

VITA

VITA

Oliver received his Bachelors of Science in Mechanical Engineering in the spring of 2004 from the University of Denver with an emphasis in robotics, data acquisition, and fluid dynamics. His studies continued at the School of Aeronautics and Astronautics at Purdue University under Professor Gregory Blaisdell and Professor Anastasios Lyrintzis. His research funded by the Applied Aeroscience and CFD branch (EG3) at the NASA Johnson Space Center focused on RANS turbulence modeling in shock-boundary layer interactions typically seen on launch vehicle protuberances. After completing his masters degree in the spring of 2006, he continued on to the Ph.D. program and helped EG3 with a protuberance heating test effort through CFD support and consultation on how to make the test useful for CFD validation. Upon completion of his classwork, qualifying, and preliminary exams in March 2008, Oliver took a full-time position in EG3 and continued his Ph.D. research in absentia. In the 8 years at NASA, he was involved primarily in aerothermodynamic environment characterization for ascent vehicles and the Orion entry capsule. He continued work on the protuberance heating test investigating measurement interference and conduction losses. This experience led him to be named the aerothermal DFI reconstruction lead for the Multi-Purpose Crew Vehicle Aeroscience Program. This assignment steered his continuing Ph.D. research towards addressing deficiencies in reconstruction techniques on ablative heatshield materials needed to process heatshield measurements for the 2014 Orion EFT-1 mission. Upon completion of his Ph.D., he will continue in his role as the aerothermal DFI reconstruction lead in preparation for the Orion EM-1 mission.